

Ali Poursaeidesfahani

# Zeolite-Based Separation and Production of Branched Hydrocarbons

Delft University of Technology



# **Zeolite-Based Separation and Production of Branched Hydrocarbons**

Proefschrift

ter verkrijging van de graad van doctor  
aan de Technische Universiteit Delft,  
op gezag van de Rector Magnificus Prof.dr.ir. T.H.J.J. van der Hagen,  
voorzitter van het College voor Promoties,  
in het openbaar te verdedigen op  
25 februari 2019

Door

Ali Poursaeidesfahani  
Werktuigkundig ingenieur  
geboren te Teheran, Iran.

This dissertation has been approved by the  
promotor: Prof. dr. ir. T. J. H. Vlugt  
copromotor: Dr. D. Dubbeldam

Composition of the doctoral committee:

Rector Magnificus	Chairman
Prof. dr. ir. T.J.H. Vlugt	Promotor, Delft University of Technology
Dr. D. Dubbeldam	Copromotor, University of Amsterdam

Independent members:

Prof. dr. ir. Earl Goetheer	Delft University of Technology
Prof. dr. Titus S. van Erp	Norwegian University of Science and Technology
Prof. dr. ir. Michiel T. Kreutzer	Delft University of Technology
Prof. dr. Erik Zuidema	Shell Global solution, Amsterdam
Prof. dr. ir. Krijn P. de Jong	Utrecht University



This work was sponsored by NWO Exakte Wetenschappen (Physical Sciences) for the use of supercomputer facilities, with financial support from the Nederlandse Organisatie voor Wetenschappelijk Onderzoek (Netherlands Organization for Scientific Research, NWO). We also gratefully acknowledge the financial support from Shell Global Solutions B.V..

Copyright © 2019 by A. Poursaeidesfahani  
ISBN: 978-94-6384-014-9  
Printed by: Ridderprint B.V.

*Dedicated to my beloved parents*



# Contents

<b>1</b>	<b>Introduction</b>	<b>1</b>
1.1	Overview . . . . .	1
1.2	Outline . . . . .	6
<b>2</b>	<b>Breakthrough Curves and Adsorption Isotherms</b>	<b>11</b>
2.1	Introduction . . . . .	11
2.2	Experiments . . . . .	13
2.2.1	Adsorbents . . . . .	13
2.2.2	Measurement of pure component adsorption isotherms . . . . .	13
2.2.3	Breakthrough experiments . . . . .	14
2.3	Mathematical model . . . . .	15
2.3.1	Estimation of adsorption properties . . . . .	20
2.4	Results . . . . .	21
2.4.1	Mass transfer coefficient and Péclet number . . . . .	21
2.4.2	Estimation of Henry coefficients . . . . .	24
2.4.3	Estimation of Langmuir isotherms . . . . .	26
2.5	Conclusions . . . . .	30
<b>3</b>	<b>Heat and Entropy of Adsorption Near Saturation Conditions</b>	<b>33</b>
3.1	Introduction . . . . .	33
3.2	Enthalpy and entropy of adsorption . . . . .	36

3.3	Computational methods . . . . .	39
3.4	Simulation details . . . . .	45
3.5	Results and comparison of different methods . . . . .	46
3.6	Energy Slope Method for mixtures . . . . .	54
3.7	Conclusions . . . . .	58
<b>4</b>	<b>Product Shape Selectivity in the Catalytic Hydroconversion of Heptane</b>	<b>61</b>
4.1	Introduction . . . . .	61
4.2	Simulations . . . . .	63
4.3	Experiments . . . . .	65
4.4	Results and discussion . . . . .	66
4.4.1	Reaction scheme and production of dibranched isomers	66
4.4.2	Distribution of dibranched isomers . . . . .	71
4.4.3	MFI-type with different crystal sizes . . . . .	78
4.5	Conclusions . . . . .	80
<b>5</b>	<b>Catalytic Hydroconversion of Heptane Using Large Pore Zeolite Catalysts</b>	<b>83</b>
5.1	Introduction . . . . .	83
5.2	Experiments . . . . .	85
5.3	Simulations . . . . .	85
5.3.1	Adsorption isotherms . . . . .	85
5.3.2	Reaction network . . . . .	86
5.3.3	Rate equations . . . . .	88
5.3.4	Gibbs free energy of reaction . . . . .	89
5.3.5	Reactor model . . . . .	90
5.4	Results and discussion . . . . .	92
5.5	Conclusions . . . . .	97
<b>6</b>	<b>Continuous Fractional Component Monte Carlo in the Gibbs Ensemble</b>	<b>99</b>
6.1	Introduction . . . . .	99
6.2	The Gibbs Ensemble . . . . .	101

6.3	Methodology . . . . .	103
6.3.1	Computation of the pressure . . . . .	116
6.4	Simulation details . . . . .	120
6.5	Lennard-Jones particles . . . . .	121
6.5.1	Densities and acceptance probabilities . . . . .	121
6.5.2	Properties corresponding to the conventional GE . .	126
6.6	Water . . . . .	129
6.7	Conclusions . . . . .	130
<b>7</b>	<b>Continuous Fractional Component Monte Carlo in the Reaction Ensemble</b>	<b>133</b>
7.1	Introduction . . . . .	133
7.2	Conventional RxMC and parallel Rx/CFC . . . . .	137
7.3	Serial Rx/CFC . . . . .	140
7.3.1	Partition function . . . . .	140
7.3.2	Trial moves . . . . .	141
7.3.3	Biasing the probability distribution $p(\lambda, \delta)$ . . . . .	147
7.3.4	Free energy calculations . . . . .	149
7.4	Simulation details . . . . .	151
7.5	Results . . . . .	153
7.6	Conclusions . . . . .	163
<b>A</b>	<b>Appendix</b>	<b>167</b>
A.1	Details on serial Rx/CFC . . . . .	169
A.1.1	Partition function of Serial Rx/CFC . . . . .	169
A.1.2	Partition function of the reaction ensemble with CFCMC for the ideal gas case . . . . .	175
A.1.3	Trial moves and acceptance rules . . . . .	177
A.1.4	Changing the value of $\lambda$ . . . . .	177
A.1.5	Reaction for fractional molecules . . . . .	178
A.1.6	Reaction for whole molecules . . . . .	180
A.2	Chemical potentials of mixtures in the conventional Gibbs ensemble . . . . .	182
A.3	Chemical potentials in serial Rx/CFCMC . . . . .	188

A.4 Extension to constant pressure . . . . .	196
A.5 Thermodynamic modeling of the ammonia synthesis reaction	197
A.6 Molecular interactions for modelling the ammonia synthesis reaction . . . . .	202
<b>References</b>	<b>206</b>
<b>Summary</b>	<b>233</b>
<b>Samenvatting</b>	<b>237</b>
<b>Conclusions</b>	<b>241</b>
<b>Acknowledgements</b>	<b>245</b>
<b>Curriculum Vitea</b>	<b>251</b>
<b>List of Publications</b>	<b>253</b>

# Chapter 1

## Introduction

### 1.1 Overview

There is an excessive demand for the production of cleaner fuels with high energy efficiency [1, 2]. In the past decades, toxic components such as sulfur and aromatics were present in fuels. Aromatics are added to the fuels to increase their octane/cetance number [3, 4]. A high concentration of aromatics increases CO emissions [5]. Currently, many countries have limited the concentration of aromatics in gasoline, in particular for benzene. In the EU, for automotive gasoline, the concentration of benzene cannot exceed 1% in volume [5, 6]. Increasing the concentrations of branched hydrocarbons can increases the octane number of a fuel without causing any additional environmental concerns [7, 8]. However, the processes for selective production and separation of branched isomers are very complex and challenging [9]. The environmental regulations have forced refineries to explore different ways of increasing the octane number of fuels, making the industrial production of hydrocarbon isomers more important than ever [1, 2].

Zeolite-based catalysts and separation are crucial for selective production and separation of branched hydrocarbons [10, 11]. Zeolites contain a network of pores that only allows the adsorption of molecules with sizes

comparable to or smaller than the pore dimensions [12]. The remarkable stability and accessibility of their pores from the outside have made zeolites valuable for many industrial applications [12, 13]. Separation processes based on adsorption are becoming increasingly popular [14–16]. This is mainly due to the recent sharp growth in the number of potential adsorbents [17]. To date, more than 200 zeolites are successfully synthesized, while the number of theoretical zeolites is virtually unlimited [18]. The capacity, selectivity and energy consumption during the desorption process are crucial for designing an efficient adsorption-based separation process [19]. Adsorption isotherms and breakthrough curves are used to assess the capacity and selectivity of an adsorption-based separation process [20, 21]. The modelling of the transient adsorption process is one of the most efficient ways to study the adsorption capacity and selectivity of an adsorption based separation at different operating conditions. During the past decades, several models with various simplifications have been proposed to reproduce and predict experimental breakthrough curves for different systems [22–26]. Most of these studies are using experimental adsorption isotherms as an input to predict breakthrough curves. However, the experimental measurement of breakthrough curves is faster and requires less experiments compared to experimental measurement of adsorption isotherms. Therefore, it would be more beneficial to use these models to predict adsorption isotherms from breakthrough curves.

Thermodynamic properties such as the heat of adsorption and the entropy of adsorption are also very important for the characterizing the performance of adsorption-based separation processes [19, 25, 27]. The heating demand of the process is determined by the heat of adsorption [19, 25, 28]. At high loadings, the entropies of adsorption of different adsorbates determine the selectivity of the adsorption process [29–31]. To improve the capacity and cost efficiency of the separation process, most industrial process take place at high loadings. Therefore, comprehensive knowledge concerning the heat and entropy of adsorption at high loadings is of great industrial importance [32]. It is very challenging to measure the entropy and heat of adsorption of a gas mixture experimentally. Recent advancements in computing power have made molecular simulation a powerful tool

for computing heats and entropies of adsorption of hydrocarbons [12, 33–37]. There are several methods to compute the heat of adsorption with molecular simulations (*e.g.* energy differences in canonical ensemble and energy/particle fluctuations in grand-canonical ensemble [33]). However, most of these methods are inefficient for computation of the heat and entropy of adsorption at high loadings [38]. Therefore, new simulation techniques are needed for this purpose.

Selective production of branched hydrocarbons by zeolite-based catalysts is even more challenging compared to the adsorption-based separation of hydrocarbons (see Fig. 1.1). This process involves several steps such as adsorption, diffusion, and chemical conversion of hydrocarbons within the pores of zeolites [11, 39, 40]. Structural details of the pores can lead to enhanced or reduced adsorption, formation, and diffusion of certain reactants or reaction products. These effects are known as shape selectivity [12, 41]. There are basically three forms of shape selectivity [12]: (1) reactant shape selectivity: adsorption and/or diffusion of (some of the) reactant molecules to the reaction sites is inhibited by the confinement created by the zeolite pores; (2) transition state shape selectivity: formation of some products is hindered by the shape of the zeolites pores simply because these molecules are too large to fit inside the pore structure; (3) product shape selectivity: diffusion limitations prohibit desorption of some product molecules that are too bulky to diffuse sufficiently fast along the channels of the zeolite. Understanding this process requires information on the adsorption and desorption of reactants/products, diffusion of these molecules to and from active sites, and the chemical conversion on the active site [41, 42]. Due to the industrial importance of this process, many studies focused on hydroconversion of linear alkanes by zeolite catalysts. These include investigating the influence of the zeolite crystal size and activity [9, 43, 44], comparison of performance of different zeolite catalysts [10, 11, 45, 46], and the development of kinetic models [40, 47, 48]. These studies have been very useful to qualitatively explain the product distributions based on differences in pore geometry [10, 45]. However, a quantitative approach explicitly including all steps (*e.g.* adsorption, diffusion and reaction) is missing. As most of the steps take place within the zeolite, it is very

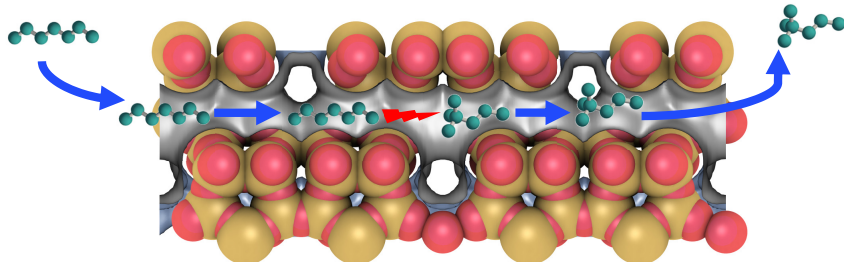


Figure 1.1: Schematic representation of the zeolite-based hydroconversion process. This process involves adsorption and diffusion of the reactant molecules to the reaction site, formation of the reaction products at the reactions site, and diffusion and desorption of the reaction product molecules. This figure is created with the iRASPA software [51].

difficult to perform experiments that can provide detailed information at the atomistic level [12, 41]. Molecular simulation can be used to provide information on the adsorption, transport, and reaction of hydrocarbons at the molecular scale [12, 33–37]. Therefore, a more quantitative treatment can be obtained by integrating experimental observations, process modelling and molecular simulations.

Monte Carlo (MC) simulations in open ensembles (such as grand-canonical, Gibbs, and the reaction ensemble) can be used to study the adsorption and reaction of hydrocarbons within the zeolites [12, 35, 36, 49]. However, simulations in open ensembles critically rely on a sufficient number of molecule exchanges. Unfortunately, the acceptance probabilities for these exchanges can be close to zero when molecules are large or when the system is at high loading, making the simulations useless [38, 50]. As the industrial hydroconversion of hydrocarbons takes place at high loading, new advanced simulation techniques are need to study the adsorption and reaction of hydrocarbons at the industrial conditions.

In this thesis, molecular simulation is used to calculate thermodynamic properties of systems in the adsorbed phase. There are two different classes of molecular simulations: simulations based on classical and quantum mechanics. Simulations based on quantum mechanics are very accurate but they are extremely computer intensive for typical system sizes required for

simulations of zeolite adsorption. In classical simulations, the explicit treatment of the electronic structures are neglected, therefore, these simulations are computationally fast and suitable for studying large systems. Monte Carlo (MC) and Molecular Dynamics (MD) simulations are different categories of classical molecular simulations. In MD simulations, the average properties of the system are computed by following the system in time and averaging over time. In Monte Carlo simulations, properties are computed as averages over different microstates. Moving from one microstate to another is accepted or rejected according to an acceptance criteria. In this way, the probability of visiting a mircostate is proportional to the Boltzmann weights of that mircostate. MC simulations are widely used for studying adsorption and phase equilibria [12, 35].

The goals of this thesis are: (1) to introduce methods and techniques that can provide detailed information regarding relevant adsorption information for the adsorption-based separation processes of hydrocarbons at industrial conditions; (2) to integrate experimental observations, process modelling and molecular simulations to improve our understanding of the complex process of catalytic hydroconversion of hydrocarbons; (3) to introduce advanced simulation techniques which are capable of providing information on the adsorption and reaction of hydrocarbons at the molecular scale at the industrial conditions. In this thesis, a mathematical model to reduce the number of adsorption experiments is introduced. A reliable simulation technique to compute the heat of adsorption at any loading is developed. Combining our experimental findings with insights obtained from simulations at the molecular level, the crucial steps in zeolite shape selectivity are identified. New advanced simulation techniques to study the phase equilibria, adsorption, and reactions of dense systems (e.g. hydrocarbons inside zeolites at high loadings) are introduced. These methods can be used to facilitate future simulation research on this topic.

## 1.2 Outline

As shown in Fig. 1.2, zeolite-based separation process are the subject of chapters 2 and 3 of this thesis. Adsorption isotherms and breakthrough curves are essential in design of an efficient adsorption process. In chapter 2, a method is introduced to obtain the complete pure component adsorption isotherms for all the components in the system with limited a number of breakthrough experiments. Obtaining an experimental adsorption isotherm is, in general, more time consuming (and involves more experiments) compared to obtaining a breakthrough curve for the same system. In this way, one can reduce the number of adsorption experiments. In this chapter, a mathematical model is used for estimating adsorption isotherms from breakthrough curves. As a case study, the adsorption of a equimolar mixture of CO<sub>2</sub>/CH<sub>4</sub> in ITQ-29 is investigated. The effects of mass transfer and gas phase dispersion on the shape of breakthrough curves are studied. The Henry coefficients and the complete adsorption isotherm obtained from our approach are in excellent agreement with those measured experimentally from equilibrium adsorption experiments.

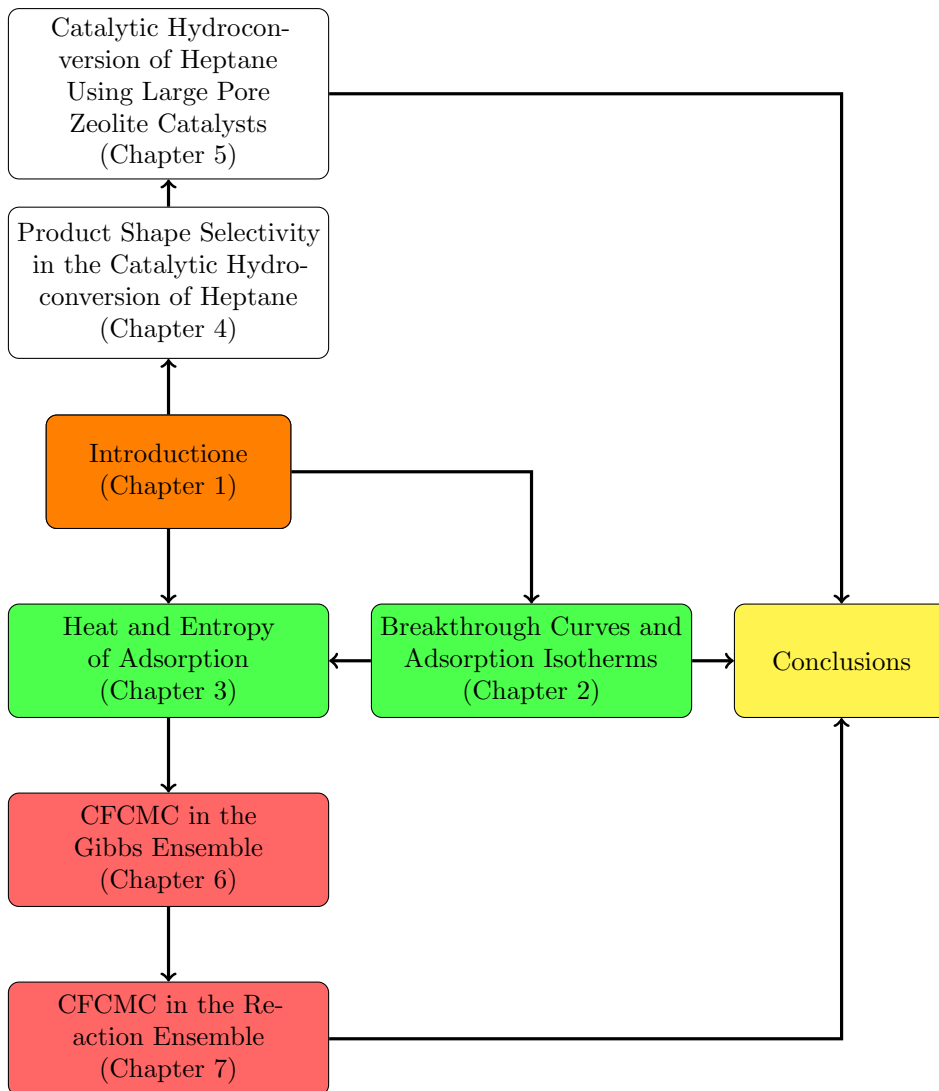


Figure 1.2: Schematic representation of the structure of this thesis. Chapters on the adsorption-based separation of hydrocarbons are shown in green. Chapters about the zeolite-based catalytic hydroconversion hydrocarbons are shown in white. Chapters on advanced simulation techniques for molecular simulation of adsorption as reaction of hydrocarbons are shown in red.

The heat of adsorption determines the energy demand of an adsorption-based separation process. The entropy of adsorption can be considered as a driving force for these processes [52]. The heat and entropy of adsorption are functions of loading [30]. In chapter 3, molecular simulation is used to study the adsorption of different heptane isomers in MFI- and MEL-type zeolites. The performance of current methods in molecular simulation for computing the heat and entropy of adsorption as a function of loading is examined. It is shown that at high loadings, all conventional methods fail to compute the heat or entropy of adsorption of bulky molecules in the zeolites studied in chapter 3. As an alternative, the so-called "Energy Slope" method is introduced, which outperforms the present techniques at high loadings. In this method, the heat and entropy of adsorption are estimated from the slope of the line fitted to the variation of the total internal energy of the system as a function of loading. The Energy Slope method is validated by comparing the heats of adsorption computed with this method for a butane/isobutane mixture and the ones computed based on the energy/particle fluctuations in the grand-canonical ensemble.

The zeolite-based catalytic hydroconversion of linear hydrocarbons into branched ones is studied in chapters 4 and 5. In these chapters, an integration of molecular simulations, process modelling, and experimental observations are used to quantitatively study the shape selective behaviour of zeolites. In chapter 4, the influence of product shape selectivity on the bifunctional conversion of n-C<sub>7</sub> by zeolite catalysts is studied. Experiments were performed with three different zeolite catalysts with different pore sizes (MFI-type (pore size≈ 4.7 Å), MEL-type (pore size≈ 5.2 Å), and BEA-type (pore size≈ 6 Å) zeolites ) [53]. For all three zeolites, heptane is isomerized to monobranched isomers which are further isomerized into dibranched isomers, and these dibranched molecules are converted into cracking products. The production of dibranched isomers as a function of the crystal size of the MFI-type zeolite is analyzed. It is observed that larger crystals produce more cracking products and less dibranched isomers. The adsorption isotherms and free energy barriers for diffusion of dibranched isomers in MFI-type, MEL-type, and BEA-type zeolites are computed using molecular simulation. By combining experimental and simulation results, it is

shown that although transition state shape selectivity fails to explain the distribution of dibranched molecules, product shape selectivity explains the experimental observations in this respect.

To identify important factors other than product shape selectivity that affect the distribution of products, systems where product shape selectivity is not expected are considered in chapter 5. In this chapter, the reaction network for the catalytic hydroconversion of heptane is identified, by analysing a series of precise experiments. A complete mechanistic model considering all components and reactions is described. Since only large pore zeolites are considered in this chapter, it is assumed that there are no diffusion limitations and the gas phase and the adsorbed phase are in equilibrium. The Gibbs free energies of reactions in the adsorbed phase are computed using the Gibbs free energies of formation of reactants and reaction products in the gas phase and the mixed Langmuir adsorption isotherms. A large set of experimental data from three large pore catalysts (FAU-type, MRE-type, and BEA-type zeolites) is used to estimate the rates of different reactions by fitting the model outputs to the experimental results. By comparing the product distributions and reaction rates estimated for these three catalysts, it is shown that in the absence of product shape selectivity, the product distribution obtained from different catalysts are very similar. However, various catalysts show different activity levels.

In chapters 6 and 7, advanced simulation techniques are introduced that can significantly improve the performance of molecular simulations at high loadings. This can facilitate simulation of the zeolite-based catalytic hydroconversion of hydrocarbons at the molecular scale. In general, the grand-canonical ensemble, the Gibbs Ensemble (GE), and the reaction ensemble [38] can be used for studying this process. In chapter 6, the serial Continuous Fractional Component Monte Carlo [54, 55] method in the Gibbs Ensemble (serial GE/CFC) is presented. In chapter 7, serial Rx/CFC, a new formulation of the Reaction Ensemble Monte Carlo (RxMC) technique combined with the Continuous Fractional Component Monte Carlo method is introduced. In serial GE/CFC, only a single fractional molecule per component is used (compared to the previous formulation by Maginn and co-workers [55]). This has the following advantages: (1) the chemi-

cal potentials of all components are obtained directly, without using test particles; (2) independent biasing is applied to each simulation box. This significantly enhances the acceptance probability of the molecule exchanges; (3) the maximum changes of the scaling parameter of intermolecular interactions can be chosen differently for each component and each simulation box. Therefore, the maximum change in the scaling parameter can be much larger in the gas phase compared to the liquid phase, leading to more efficient molecule exchanges. The key feature of serial Rx/CFC is that chemical reactions always involve fractional molecules and fractional molecules of either reactants or products are present in the system. The advantages of serial Rx/CFC compared to other approaches include: (1) direct calculation of chemical potentials of all reactants and products; (2) significant increase in the efficiency of the algorithm by independent biasing for the fractional molecules of reactants and products; (3) reduction of the number of fractional molecules.

## Chapter 2

# Breakthrough Curves and Adsorption Isotherms

This chapter is based on the following paper: Poursaeidesfahani, A; Andres-Garcia, E.; de Lange, M. F.; Torres-Knoop, A.; Rigutto, M.; Nair, N.; Kapteijn, F.; Gascon, J.; Dubbeldam, D.; Vlugt, T. J. H.; Prediction of adsorption isotherms from breakthrough curves, *Microporous and Mesoporous Materials*, 2019, 277, 237-244.

### 2.1 Introduction

Separation processes based on adsorption are becoming increasingly popular [14–16]. This is mainly due to the recent sharp growth in the number of potential adsorbents [17]. Traditionally, the best adsorbent for a process is selected by conducting several experiments [56, 57]. During the last decades, several models with various simplifications have been proposed to reproduce and predict the experimental breakthrough curves for different systems [20–26]. Breakthrough curves estimated by many of these models are in good agreement with the experimental breakthrough curves [25, 26, 58]. However, the application of an efficient model for simulating transient

adsorption processes is not limited to the prediction of the breakthrough curves.

In this chapter, we use a mathematical model for estimating the adsorption isotherms from breakthrough curves and investigating the effects of mass transfer and gas phase dispersion on the shape of breakthrough curves. Obtaining an experimental adsorption isotherm is, in general, more time consuming (and involves more experiments) compared to obtaining a breakthrough curve for the same system. Consequently, it would be beneficial if one can obtain both the breakthrough curve and the adsorption isotherm only by performing breakthrough experiments. The idea of predicting adsorption isotherms from experimentally measured breakthrough curves has attracted many researchers for decades [59–63]. One of the mostly used approaches to determine adoption isotherms from the breakthrough curves is based on the classical equilibrium theory [62, 63]. Many excellent papers have been published on the application of this theory [64–67]. This theory neglects all the kinetic effects and just considers convection and equilibrium distribution between the phases which is defined by thermodynamics. The nice feature of this approach is that, by the exclusion of kinetics, the dynamic measurements (breakthrough curves) and thermodynamic predictions (adsorption isotherms) are directly related [68, 69]. This is also the main limitation of the approach which prohibits its application for the cases with significant kinetic effects causing band broadening. If the breakthrough curves are significantly eroded due to kinetic effects it is difficult to calculate the retention times and estimate the intermediate plateau concentrations. Moreover, one needs to perform several experiments to obtain the entire adsorption isotherm. In this chapter, an approach is introduced to obtain the complete pure adsorption isotherms for all the components in the system with limited number of breakthrough experiments. Together with IAST it can be used to compute the equilibrium loading for each component in the mixture at any composition and condition. We used our approach to obtain adsorption isotherms from significantly eroded breakthrough curves when equilibrium theory is not applicable.

This chapter is organized as follows. Experimental details are provided in section 2.2 In section 2.3, the mathematical model used for modeling

the transient adsorption process and its main assumptions are summarized. Estimation of adsorption isotherms from experimentally measured breakthrough curves is described as an optimization problem. In section 2.4, the effects of mass transfer resistance and dispersion in the gas phase on the shape of breakthrough curves are investigated. The Henry coefficients obtained from our approach, using experimentally measured breakthrough curves at pressure of 2 bar, are compared with the experimental values. The same procedure is applied to predict the complete adsorption isotherm from breakthrough curves at higher pressures. Our findings are summarized in section 2.5.

## 2.2 Experiments

### 2.2.1 Adsorbents

Pure-silica (Al-free) ITQ-29 is a hydrophobic 8MR zeolite, able to sieve small organic molecules with a high precision, even in the presence of water [70]. The complete absence of acidity allows separations even in the presence of olefins. This is not possible with Al-containing zeolites due to oligomerization and pore blocking [71]. This pure-silica zeolite, analysed with SEM (Scanning Electron Microscopy), presents a homogeneous distribution of cubic particles of  $2.00\text{ }\mu\text{m}$  (see Fig. 2.1).

### 2.2.2 Measurement of pure component adsorption isotherms

The adsorbent (ITQ-29 powder) is weighed and outgassed overnight under vacuum condition at 473 K. Gas adsorption is performed by the volumetric method, using a high-pressure gas adsorption system BELSORP-HP (BEL Japan, INC). The adsorption isotherms for  $\text{CO}_2$  and  $\text{CH}_4$  are obtained by an equilibration time of 1200 s between different pressure steps. All experiments are performed at 298 K.

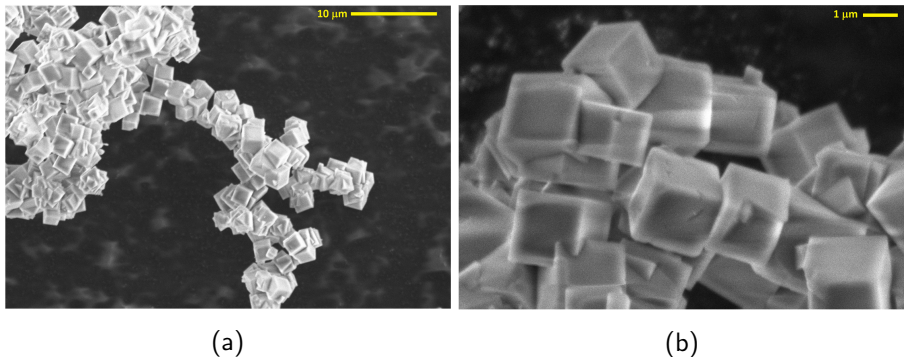


Figure 2.1: SEM images of ITQ-29 zeolite used in this study.

### 2.2.3 Breakthrough experiments

Breakthrough experiments are carried out to study the performance of a packed bed of ITQ-29 pellets for separating CO<sub>2</sub>/CH<sub>4</sub> mixtures. 220 mg of ITQ-29 self-sustained pelletized (pellet density 1016 kg m<sup>-3</sup>, particles size between 500 and 720 μm, pelletizing pressure 5 ton cm<sup>-2</sup>) are placed inside the column. To control the composition of the gas mixture, separate flow controllers are used to adjust the flow rate of different components upstream of the mixing section. In this mixing section, CO<sub>2</sub> and CH<sub>4</sub> with equal flow rates of 5 ml min<sup>-1</sup> are mixed with hydrogen. Hydrogen, with the flow rate of 1 ml min<sup>-1</sup>, is used as a non-adsorbing tracer. The total pressure of the gas mixture is controlled at the outlet of the adsorption column. The pressure of the system is maintained at 2 bar. At these conditions, the pressure drop across the column is negligible. An adsorption column with an inner diameter of 0.4 cm and a length of 7 cm is placed inside an oven to ensure isothermal condition throughout the experiment. Before starting the experiments the column is filled with He at the pressure of the experiment and 298 K. The temperature of the column is kept at 298 K throughout the experiments. A Quadrupole Mass Spectrometer (QMS200-PRISMATM with GSD 300 O/T, using Electron Ionization) is used to analyse the composition of the gas mixture breaking through the column.

At the column exit a flow of  $100 \text{ ml min}^{-1}$  He is added to avoid gas stand still in case of adsorption of both components, and to allow calculation of component flow rates exiting the column based on MS analysis [57]. More details regarding the experimental setup can be found elsewhere [57, 72].

## 2.3 Mathematical model

Our mathematical model is mainly formed by the transient material balance of the fluid phase and the adsorbed phase and the momentum balance (Ergun equation) [73], neglecting heat transfer effects [74] (see Fig. 2.2). The material balance of the fluid phase includes the spatial (axial) and temporal variations of concentrations of all components in the fluid phase. The adsorbed phase material balance describes the variations in the loading of each component along the column. The fluid and adsorbed phase material balances are coupled by the mass transfer between the two phases.

The migration of adsorbate molecules from the gas phase into the adsorbent and vice versa are described by Linear Driving Force model (LDF-model) [75–77]. Sircar and Hufton compared LDF-model with the more rigorous Fickian diffusion [78]. These authors showed that all details regarding the intra-pore diffusion are lost, when modeling breakthrough curves using Fickian diffusion. Therefore, the LDF-model is a sufficient and efficient approximation for computing breakthrough curves [78]. The LDF-model is formulated as follows:

$$\frac{\partial \bar{q}_{i,\text{ads}}}{\partial t} = k_{L,i} (q_{i,\text{eq}} - \bar{q}_{i,\text{ads}}) \quad (2.1)$$

Here,  $\bar{q}_{i,\text{ads}}$  is the average loading in the adsorbent as a function of time,  $k_{L,i}$  is the effective mass transfer coefficient of component  $i$  ( $s^{-1}$ ), and  $q_{i,\text{eq}}$  is the equilibrium loading of component  $i$  for given gas phase conditions. By definition, when the adsorbed phase is in equilibrium with the gas phase, there is no net mass transfer between the phases. The equilibrium loadings ( $q_{i,\text{eq}}$ ) for components present in the mixture are computed using the Ideal

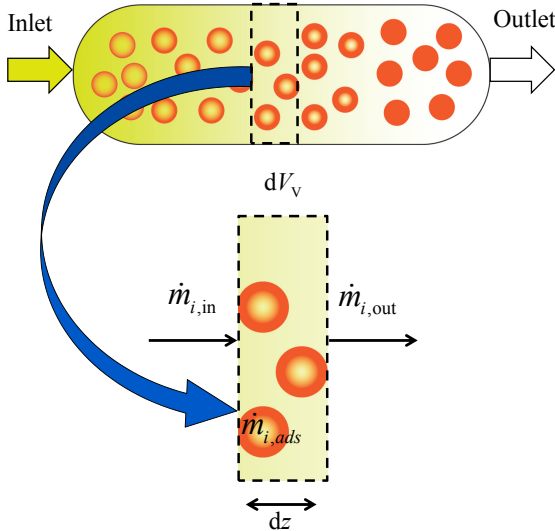


Figure 2.2: Schematic representation of mathematical model used to simulate breakthrough experiments. In this model, the reactor is divided into number of slices. For each slice, the material balance of the fluid phase and the adsorbed phase are solved using finite difference method.

Adsorption Solution Theory (IAST) [79–81]. IAST makes use of pure component isotherms to estimate the equilibrium loading of each component in a mixture. To facilitate the application of IAST, based on the shape of the experimentally measured pure component isotherms, a functional form (e.g. Langmuir, Langmuir-Freundlich [56]) is fitted to each pure component isotherm data. In this way, it is trivial to obtain an analytical expression for the spreading pressure of each component. Spreading pressures are then used to compute the equilibrium loading of each component in the gas mixture. Note that IAST fails to provide accurate estimation of equilibrium loadings when there is a strong segregation in the preferable adsorption sites for different components [82, 83]. This is not the case for the system under study. For more information about IAST, readers are referred to the original publications [79–81, 84]. Assuming ideal gas behaviour for the

gas phase, the material balance for each component in the gas phase is described by [77, 85]

$$\frac{1}{RT} \frac{\partial p_i}{\partial t} = -\frac{1}{RT} \frac{\partial (up_i)}{\partial z} + \frac{1}{RT} D_i \frac{\partial^2 p_i}{\partial z^2} - \left( \frac{1-\varepsilon}{\varepsilon} \right) \rho_P k_{L,i} (q_{i,\text{eq}} - \bar{q}_{i,\text{ads}}) \quad (2.2)$$

where  $p_i$  is the partial pressure of component  $i$  in the gas phase,  $u$  is the interstitial velocity of the gas phase,  $D_i$  is the axial dispersion coefficient for component  $i$ , and  $\varepsilon$  is the void fraction of the column packing. The first term on the right hand side of Eq. 2.2 accounts for the effect of convective mass transport. The second term on the right shows the effect of axial dispersion on the overall mass balance of the gas phase and the last term takes in to account the influence of mass transfer between the adsorbed phase and the gas phase. Radial gradients are assumed absent. Velocity profiles in packed beds due to radial packing gradients can be neglected for sufficiently small particles compared to the column diameter. One can rewrite Eq. 2.2 using dimensionless parameters:

$$\frac{1}{RT} \frac{\partial p_i}{\partial \tau} = -\frac{1}{RT} \frac{\partial (vp_i)}{\partial \zeta} + \frac{1}{RTPe_i} \frac{\partial^2 p_i}{\partial \zeta^2} - \left( \frac{1-\varepsilon}{\varepsilon} \right) \rho_P k'_{L,i} (q_{i,\text{eq}} - \bar{q}_{i,\text{ads}}) \quad (2.3)$$

where

$$\begin{aligned} \tau &= t \frac{u_{\text{in}}}{L} \\ \zeta &= \frac{z}{L} \\ v &= \frac{u}{u_{\text{in}}} \\ \frac{1}{Pe_i} &= D'_i = \frac{D_i}{Lu_{\text{in}}} \\ k'_{L,i} &= k_L \frac{L}{u_{\text{in}}} \end{aligned} \quad (2.4)$$

Here,  $L$  is the length of the column,  $u_{\text{in}}$  is the interstitial velocity at the inlet of the column, and  $Pe$  is the Péclet number. In literature, the Péclet

number is commonly used to refer to the dimensionless dispersion coefficient [86]. It is important to note that the characteristic length of particle and not the length of the column is sometimes used in the definition of the Péclet number. The pressure drop along the fixed bed follows from the momentum balance and can be estimated using the Ergun equation [73]. It is assumed that the pressure gradient (if any) is constant and not affected by the adsorption process. As a result, the pressure varies linearly along the length of the column and remains constant with time. Therefore, the overall mass balance equation can be summarized as:

$$\frac{\partial p_t}{\partial \tau} = 0, \frac{\partial p_t}{\partial \zeta} = \text{constant} \quad (2.5)$$

$$\frac{1}{RT} \left( p_t \frac{\partial v}{\partial \zeta} + v \frac{\partial p_t}{\partial \zeta} \right) = - \sum_{i=1}^N \left[ \left( \frac{1-\varepsilon}{\varepsilon} \right) \rho_P k'_L (q_{i,\text{eq}} - \bar{q}_{i,\text{ads}}) - \frac{1}{RTPe} \frac{\partial^2 p_i}{\partial \zeta^2} \right] \quad (2.6)$$

In this equation,  $p_t$  is the total pressure of the gas phase and  $N$  is the number of components in the gas phase. Eq. 2.6 can be rearranged to obtain an expression for the term  $\frac{\partial v}{\partial z}$

$$\frac{\partial v}{\partial \zeta} = \frac{1}{p_t} \left[ -RT \left( \sum_{i=1}^N \left[ \left( \frac{1-\varepsilon}{\varepsilon} \right) \rho_P k'_L (q_{i,\text{eq}} - \bar{q}_{i,\text{ads}}) - \frac{1}{RTPe} \frac{\partial^2 p_i}{\partial \zeta^2} \right] \right) - v \frac{\partial p_t}{\partial \zeta} \right] \quad (2.7)$$

The mathematical model consists of a system of Partial Differential Equations subject to following boundary and initial conditions:

Initial conditions:

$$\begin{aligned} p_i(0, \zeta) &= 0 \\ p_{He}(0, \zeta) &= p_t(0, \zeta) \\ \bar{q}_{i,\text{ads}}(0, \zeta) &= 0 \end{aligned} \quad (2.8)$$

Boundary conditions:

$$\begin{aligned} v(\tau, 0) &= 1 \\ p_i(\tau, 0) &= p_{i,\text{in}} \\ p_t(\tau, \zeta) &= p_t(0, \zeta) \\ \frac{\partial p_i}{\partial \zeta}(\tau, 0) &= 0 \end{aligned} \tag{2.9}$$

The system of equations is discretized in time and space using finite difference approximations and solved step wise in time. Spatial partial derivatives are approximated by second order upwind method. In each time step, a system of  $2N \times n$  equations is solved, where  $N$  is the number of components and  $n$  is the number of grid points in the axial directions. The numerical method of lines with the implicit trapezoidal rule is used to perform integration in time [87]. The values for partial pressures and loadings of each component in the next time step are first approximated using the first order forward approximation. These values are used in an iterative scheme using the implicit trapezoidal rule. Our model is implemented in MATLAB and has been validated by comparing the simulation results with other existing breakthrough models developed independently by other groups [52, 88]. The code can handle the adsorption of multi-component mixtures as well as pure gases with various functional forms for the adsorption isotherm. In summary, the following assumptions are made: (1) the gas phase behaves as an ideal gas; (2) the system is isothermal (this assumption is valid when the heat of adsorption is not too high. If required the none isothermal case can be modelled by including an energy balance); (3) radial variations in concentration are negligible compared to axial variations in the bed; (4) mass transfer between the gas phase and the adsorbed phase can be described by the effective LDF-model; (5) the adsorbed phase is homogeneous; (6) IAST is applicable.

### 2.3.1 Estimation of adsorption properties

It is assumed that the adsorption isotherms for CO<sub>2</sub> and CH<sub>4</sub> in zeolite ITQ-29 are unknown. Instead, the experimental breakthrough curves for the equimolar mixture of CO<sub>2</sub> and CH<sub>4</sub> passing through a fixed bed of zeolite ITQ-29, at total pressures of 2-16 bar and temperature of 298 K, are available. The mathematical model is used to estimate the adsorption isotherms by fitting the theoretical breakthrough curves to the experimental ones. The Mean Sum of Squared of Residuals (MSSR) is the natural objective function for this optimization problem. The residual at each data point is defined as the difference between the experimental and theoretical concentration of component *i*. The objective function is

$$MSSR = \frac{\sum_{j=0}^n (C_{i,j,\text{out,model}} - C_{i,j,\text{out,exp}})^2}{n - n_p} \quad (2.10)$$

where *n* is the number of data points available from the breakthrough experiment, *n<sub>p</sub>* is the number of estimated parameters, and *C<sub>i,j,out,model</sub>* is the concentration of component *i* at the outlet of the column predicted by model. Input parameters for the mathematical model include specifications of the adsorption column (length and inner diameter), density and amount of adsorbent placed inside the adsorption column, gas phase composition and flow rate, pressures at the inlet and outlet of the adsorption column, mass transfer coefficient, and the Péclet number. The main output of the mathematical model are absolute adsorption isotherms for each of the components up to the pressure of the experiment.

Breakthrough curves are generated by collecting the last points of the instantaneous spatial concentration profiles in the gas phase throughout the experiment (or calculation). As the adsorbing gases proceed through the column, the partial pressures at different points of the column change differently from zero to partial pressures at the inlet and even higher (for the less adsorbing component when it is displaced by a more adsorbing component). Therefore, during the breakthrough experiment each point of the column experiences the whole pressure range of the adsorption isotherm

from zero to the inlet partial pressure (or even higher). For the case of mixture, the equilibrium loading of each component depends on the partial pressures of all components. By fitting to the breakthrough curves and using the adsorption isotherms as variables, information from the breakthrough curves are extracted and used more efficiently and the adsorption isotherms of all components can be estimated more accurately.

## 2.4 Results

### 2.4.1 Mass transfer coefficient and Péclet number

The estimation of the effective mass transfer coefficient and the Péclet number requires detailed information regarding the properties of the system and it is not always straightforward [89]. This information is not always available and even if it is, experimental correlations and can only provide an estimation of the effective mass transfer coefficient and the Péclet number. Therefore, it is advantageous to investigate the influence of these parameters on the theoretical breakthrough curves and eventually the adsorption isotherms fitted by the model. To investigate the effect of  $k'_L$  and  $Pe$  on the shape of the theoretical breakthrough curves, the theoretical breakthrough curves corresponding to different mass transfer coefficients and the Péclet numbers are compared in Fig. 2.3. In some studies, it is assumed that the value of effective mass transfer coefficient is identical for all components. This assumption does not necessarily hold for components with very different sizes, specially when micropore diffusion is important. Therefore, in this section, separate mass transfer coefficients but identical Péclet numbers are considered for different components. In Fig. 2.3,  $t = 0$  is the breakthrough time of hydrogen (defined as the time at which hydrogen partial pressure at the outlet of the column reaches 10% of its inlet partial pressure). He content is excluded while calculating the mole fractions. In both cases (Figs. 2.3a and 2.3b), increasing the mass transfer coefficient results in steeper breakthrough curve, while delaying the breakthrough time. Due to the increase in the mass transfer rate, larger mass transfer coefficients result in steeper concentration profile of the adsorbing gases along

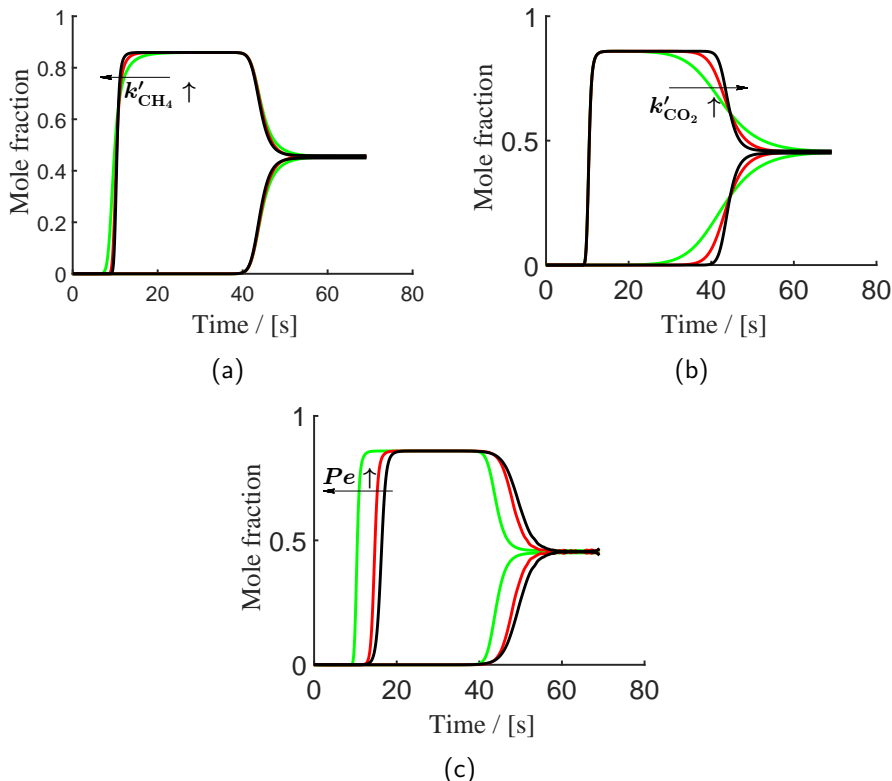


Figure 2.3: Theoretical breakthrough curves obtained for different sets of mass transfer coefficient and Pélet number (a)  $Pe = \infty$ ,  $k'_{\text{CO}_2} = 15$  and  $k'_{\text{CH}_4} = 15$  black, 7 red, 3 green (b)  $Pe = \infty$ ,  $k'_{\text{CH}_4} = 15$  and  $k'_{\text{CO}_2} = 15$  black, 7 red, 3 green (c)  $k'_{\text{CO}_2} = 15$ ,  $k'_{\text{CH}_4} = 15$  and  $Pe = 250$  black, 500 red,  $\infty$  green. An equimolar mixture of  $\text{CO}_2$  and  $\text{CH}_4$  is adsorbed by ITQ-29 zeolite at 2 bar and 298 K. The experimentally measured Henry coefficients are used in these breakthrough calculations ( $K_{H,\text{CO}_2}^{\text{exp}} = 1.2 \text{ [mol kg}^{-1} \text{ bar}^{-1}\text{]}$ ,  $K_{H,\text{CH}_4}^{\text{exp}} = 0.3 \text{ [mol kg}^{-1} \text{ bar}^{-1}\text{]}$ ).

the column. Therefore, the first traces of both gases are observed later for cases where the mass transfer coefficient is higher, and the mole fractions at the outlet of the column increase more rapidly compared to cases with a lower mass transfer coefficient (see Fig. 2.3). Comparing Figs. 2.3a and 2.3b, two important points are observed: (1) preferentially adsorbed component has a more gradual (less steep) breakthrough curve even for the cases that identical mass transfer coefficients are assumed for the two components; (2) mass transfer coefficient of the component which is preferentially adsorbed has a more pronounced influence on the shape of the breakthrough curves. There are two parameters that can influence the steepness of breakthrough curves: (1) the average velocity of the Mass Transfer Zone (MTZ) and (2) the steepness of the concentration profile along the column. For the average velocity of the Mass Transfer Zone  $V_{\text{MTZ}}$  one can write

$$V_{\text{MTZ}} \propto \frac{\dot{Q}_{i,\text{in}}}{a \times q_{i,\text{eq}}^{\text{in}} + b} \quad (2.11)$$

where  $\dot{Q}_{i,\text{in}}$  is the volume flow rate of component  $i$  and  $q_{i,\text{eq}}^{\text{in}}$  is the equilibrium loading of component  $i$  at the inlet conditions.  $a$  and  $b$  are constants defined by the void fraction, density of the adsorbent and conditions of the experiment. Higher values of  $V_{\text{MTZ}}$  can be interpreted as shorter time difference between the breakthrough time and the time that the concentration at the outlet reaches its plateau. Therefore, higher values of  $V_{\text{MTZ}}$  leads to steeper breakthrough curve. For the limiting case when  $q_{i,\text{eq}}^{\text{in}} = 0$ , breakthrough curve will be the steepest. As the two components have identical flow rates and same inlet conditions (50-50 mixture), the component with the higher value of  $q_{i,\text{eq}}^{\text{in}}$  (higher Henry coefficient) is expected to have the lower values of  $V_{\text{MTZ}}$  and less steep breakthrough curve (Figs. 2.3a and 2.3b). As  $q_{i,\text{eq}}^{\text{in}}$  increases, the influence of the second parameter, the steepness of the concentration profile, becomes more important. The steepness of the concentration profile is reduced by decreasing the mass transfer coefficient (Figs. 2.3a and 2.3b). It should be mentioned that unlike the thermodynamic properties (e.g. adsorption isotherm) kinetic properties (e.g. mass transfer coefficient) strongly depend on the crystal size and other

physical properties of the adsorbent. Therefore, it is important to estimate the kinetic parameters for each situation. Simulated breakthrough curves for different values of Péclet number are shown in Fig. 2.3c. Increasing the value of Péclet number (lowering the dispersion coefficient) shifts both breakthrough curves to the left. That is mainly due to displacement of  $t = 0$  (the breakthrough time of hydrogen). Higher dispersion coefficient makes the concentration profile less steep and more gradual. The concentration gradient along the axis of the column is the driving force for the axial dispersion. Consequently, axial dispersion smooths the breakthrough curves and makes the changes in mole fraction (with respect to time and space) more gradual. In general, a larger axial dispersion coefficient (lower value for  $Pe$ ) results in larger deviations from plug flow and more gradual changes in concentrations. This can have a considerable effect on the breakthrough time of none-adsorbing component. Therefore, for higher values of dispersion coefficient, hydrogen reaches the outlet of the column faster which shifts the  $t = 0$  to the left and results in longer breakthrough times for the adsorbing components. The analysis above is in agreement with general theory on this topic [90–92]. Assuming that the film resistance and macropore diffusion are the limiting steps for the mass transfer between the two phases, the dimensionless effective mass transfer coefficient is roughly estimated by ( $k'_L \approx [10^0 - 10^1]$ ). Empirical correlations are used to estimate the effective mass transfer coefficients ( $k_{L,i}$ ). It is assumed that the molecular diffusivity ( $D_M$ ) is of the order of magnitude  $10^{-7} \text{ m}^2/\text{s}$  [93].

#### 2.4.2 Estimation of Henry coefficients

Experiments are performed at total pressure of 2 bar. To compute the theoretical breakthrough curves, the adsorption isotherms of pure components are required only up to the pressure of 2 bar. At this pressure, the loading is so low that it can be safely assumed that the enthalpy of adsorption is independent of loading. In this region and for this system, the loading is a linear function of external pressure and normally described by

the Henry coefficient:

$$q_{i,\text{eq}} = K_{H,i} p_i \quad (2.12)$$

where  $p_i$  is the partial pressure of the component  $i$  and  $K_{H,i}$  is the Henry coefficient. The pure component adsorption isotherms are measured experimentally and it has been confirmed that the loading is a linear function of external pressure. It is important to note that experimental breakthrough curves cannot provide any information regarding the pure components equilibrium loadings at pressures larger than the pressure of the experiment. By fitting the theoretical breakthrough curves to the experimental ones, the adsorption isotherms can only be estimated up to the pressure of the experiment. Since, in this region, the pure component equilibrium loadings of both components ( $\text{CO}_2$  and  $\text{CH}_4$ ) are linear functions of pressure, the Henry adsorption coefficients and mass transfer coefficients of the two components are the parameters that are estimated by the model. To investigate the importance of initial values, the optimization process is started with several initial values for the dimensionless mass transfer coefficients of two components within the range of (1-15) and Henry coefficients for  $\text{CO}_2$  in range of ( $0.5\text{-}1.5$  [mol kg $^{-1}$  bar $^{-1}$ ]) and for  $\text{CH}_4$  in range of ( $0.1\text{-}0.5$  [mol kg $^{-1}$  bar $^{-1}$ ]).

In total, 192 different optimization processes are performed. For each optimization, the Henry coefficient and dimensionless mass transfer coefficient for both components ( $\text{CH}_4$  and  $\text{CO}_2$ ) are fitted to the experimental breakthrough curves. In Fig. 2.4, the distribution of Henry coefficients obtained for  $\text{CO}_2$  in different runs are shown. Different colors represent different fixed values of Péclet number. As shown in Fig. 2.4, there is a clear distinction between the results obtained for different fixed values of Péclet number. For cases with the low Péclet number (high dispersion coefficient), Henry coefficient of  $\text{CO}_2$  is underestimated. This under estimation reduces by increasing the Péclet number. As discussed in the previous section, by reducing the Péclet number the breakthrough time of hydrogen reduces leading to the shift of breakthrough curves to the right. The objective of the optimization algorithm is to minimize the deviation between the

theoretical and experimentally measured breakthrough curves by varying the values of mass transfer and Henry coefficients of the two components. Therefore, in the optimization algorithm, the shift to the right due to the under estimation of Péclet number is compensated by the underestimation of the Henry coefficients which shifts the breakthrough curves to the left. The highest value of Péclet number (no dispersion) leads to the most accurate estimation of Henry coefficient of CO<sub>2</sub>. An other observation from Fig. 2.4 is that for each Péclet number, as the value of objective function reduces the estimated Henry coefficients are converging to a certain value. One would expect the lowest absolute difference between the estimated Henry coefficients and those measured experimentally to occur when the global minimum is found. The data presented in Fig. 2.4 shows exactly the expected shape. For the case with highest value of Péclet number, the global minimum corresponds to the lowest absolute difference between the estimated Henry coefficients and the experimental ones. Therefore, one can conclude that  $Pe = \infty$  is an appropriate value for the Péclet number of the system under study. Independent of the value of the mass transfer coefficients, the Henry coefficients predicted by the model are close to the values measured experimentally. This shows even without detailed information regarding the characteristics of a system, one should be able to estimate the Henry coefficients for all components with only rough estimations for the mass transfer coefficients. However, the value of the objective function (quality of the fit) is a function of the estimated mass transfer coefficient. Therefore, better estimations of mass transfer coefficient will result in lower values of objective function and as a consequence better agreement between the theoretical and experimental breakthrough curves. The experimental breakthrough curves and the fitted breakthrough curves for the lowest values of the objective functions are shown Fig. 2.5. The obtained Henry coefficients are presented in Table 2.1.

### 2.4.3 Estimation of Langmuir isotherms

In this section, the capability of the proposed method for predicting adsorption isotherms beyond the Henry region is investigated. For this purpose

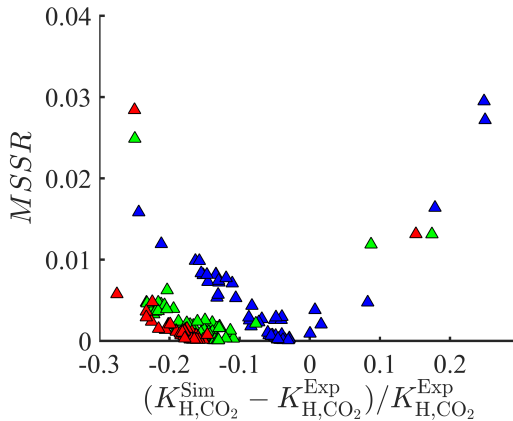


Figure 2.4: Distribution of the values of  $MSSR$  as a function of obtained Henry coefficients for  $\text{CO}_2$  for different fixed values of Péclet number  $Pe = \infty$  (blue),  $Pe = 500$  (green) and  $Pe = 250$  (red). Fitted Henry coefficients are obtained by fitting the theoretical breakthrough curves to the experimental breakthrough curves. An equimolar mixture of  $\text{CO}_2$  and  $\text{CH}_4$  is adsorbed by ITQ-29 zeolite at 2 bar and 298 K.

experimental breakthrough curves at 11 and 16 bar are used. Experimental conditions, except the pressure of the column, are identical to those of the breakthrough experiments at 2 bar. The experimental adsorption isotherms for  $\text{CO}_2$  and  $\text{CH}_4$  in ITQ-29 at 298 K are described very well by Langmuir functional forms. To facilitate the use of IAST, Langmuir adsorption isotherms are assumed for pure  $\text{CO}_2$  and  $\text{CH}_4$ . It should be noted that any other functional forms (e.g. Freundlich or Langmuir-Freundlich) can also be used depending on the system under study. The procedure for predicting the Langmuir adsorption isotherms is similar to the procedure used for predicting the Henry coefficients. Therefore, in this case, the Henry coefficient, the saturation loading corresponding to the adsorption of  $\text{CO}_2$  and  $\text{CH}_4$  in ITQ-29, dimensionless mass transfer coefficients of the two components and Péclet number are the possible variables for the fitting process. Assuming no dispersion for high pressure case reduces the number of fitting parameters to 6: Henry coefficients, saturation loadings and dimensionless mass transfer

Table 2.1: Henry coefficients, mass transfer coefficients and saturation loadings estimated by the mathematical model for low (2 [bar]) and high (11, 16 [bar]) pressure cases ( $K_{H,\text{CO}_2}^{\text{exp}} = 1.2 \text{ [mol kg}^{-1} \text{ bar}^{-1}\text{]}$ ,  $K_{H,\text{CH}_4}^{\text{exp}} = 0.3 \text{ [mol kg}^{-1} \text{ bar}^{-1}\text{]}$ , These values are calculated from independent equilibrium adsorption experiments. )

Component	Pressure [bar]	$k'_L$	$K_H$ [mol kg <sup>-1</sup> bar <sup>-1</sup> ]	$q_{\text{sat}}$ [mol kg <sup>-1</sup> ]
CO <sub>2</sub>	2	4.35 +/- 0.004	1.16 +/- 0.01	-
CH <sub>4</sub>	2	1.47 +/- 0.064	0.36 +/- 0.01	-
CO <sub>2</sub>	11,16	6.3 +/- 0.36	1.50 +/- 0.13	6.56 +/- 0.01
CH <sub>4</sub>	11,16	2.6 +/- 0.15	0.48 +/- 0.08	3.20 +/- 0.004

coefficients of the two components. The experimental breakthrough curves and the fitted breakthrough curves for the lowest values of the objective functions  $MSSR=0.0021$  are shown Figs. 2.6a and 2.6b. In Fig. 2.7, the predicted adsorption isotherms corresponding to the lowest value of the objective function among all different simulations are compared with the experimentally measured adsorption isotherms for the adsorption of CO<sub>2</sub> and CH<sub>4</sub> in ITQ-29 at 298 K. The method is well capable of predicting the whole adsorption isotherm for both CO<sub>2</sub> and CH<sub>4</sub> ( $MSSR_{\text{CO}_2}=0.16$  and  $MSSR_{\text{CH}_4}=0.023$ ). As discussed in previous sections, accurate estimation of mass transfer coefficients is not always straightforward. Therefore, it is important to examine the influence of the mass transfer coefficients on the breakthrough curves and corresponding estimated adsorption isotherms. For the case of estimation of Langmuir adsorption isotherms, although mass transfer coefficients are distributed in a wide range, they do not have a noticeable influence on the estimated adsorption isotherms and their agreement with the experimental ones. Therefore, it can be concluded that for the proposed approach a rough estimation of mass transfer coefficients is sufficient. It is not always known whether the conditions of the experiment are within the Henry region or beyond that. Therefore, it is important to investigate the possibility to verify the adequacy of the function form used for the fitting process. In the interest of assessing that, instead of Langmuir adsorption isotherm Henry adsorption isotherm is assumed for the fitting of the theoretical breakthrough curves to the experimental ones at pressures of 11 and 16 bar. It is realized that in this case, the lowest values of

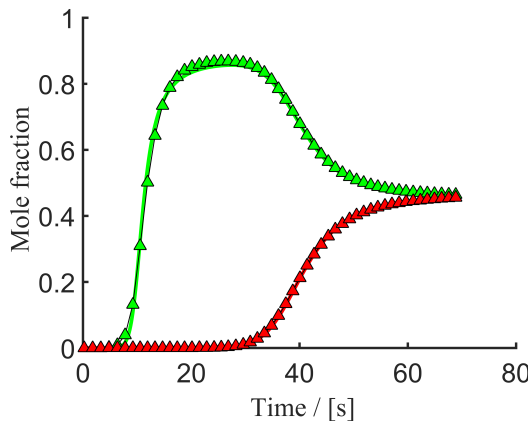


Figure 2.5: Experimental breakthrough data (symbols) and theoretical breakthrough curves (lines) obtained for the optimized estimated parameter,  $Pe = \infty$ . An equimolar mixture of  $\text{CO}_2$  (red) and  $\text{CH}_4$  (green) is adsorbed by ITQ-29 zeolite at 2 bar and 298 K.

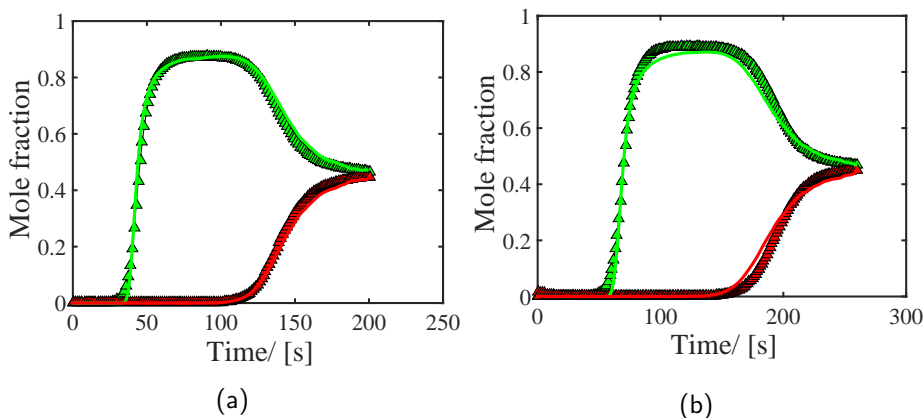


Figure 2.6: Experimental breakthrough data (symbols) and theoretical breakthrough curves (lines) obtained for the optimized estimated parameter,  $Pe = \infty$ . An equimolar mixture of  $\text{CO}_2$  (red) and  $\text{CH}_4$  (green) is adsorbed by ITQ-29 zeolite (a) at 11 bar (b) at 16 bar and 298 K.

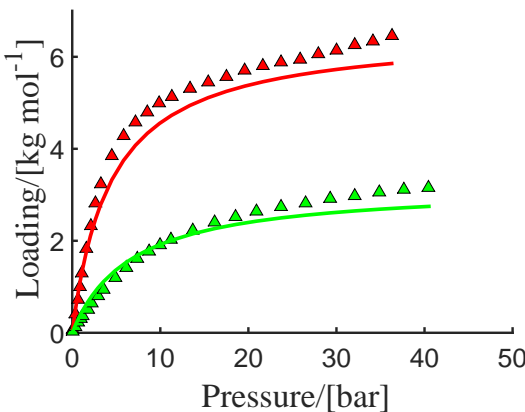


Figure 2.7: Isotherms based the parameter values estimated from the breakthrough fitting (lines) and experimental data from independently measured isotherms (symbols) adsorption isotherms obtained for the adsorption of pure CO<sub>2</sub> (red) and CH<sub>4</sub> (green) by ITQ-29 zeolite at 298 K.  $MSSR_{CO_2}=0.16$  and  $MSSR_{CH_4}=0.023$ .

the objective functions ( $MSSR=0.023$ ) is an order of magnitude greater than the lowest values of the objective functions ( $MSSR=0.0021$ ) for the case where appropriate functional forms were used for the two components. There are also noticeable differences between the fitted and experimental breakthrough curves. These could indicate that the functional form used for the adsorption isotherms is not appropriate.

## 2.5 Conclusions

In this chapter, we applied a mathematical model describing transient adsorption processes to investigate the effect of the mass transfer rate and dispersion in the gas phase on the shape of breakthrough curves. Higher mass transfer rate between the gas phase and adsorbed phase results in steeper breakthrough curves and longer breakthrough times, while higher dispersion in the gas phase has the opposite effect. The application of an appropriate model is not limited only to prediction of the breakthrough curves.

We estimated the Henry coefficients and complete Langmuir adsorption isotherm by minimizing the deviation between the theoretical breakthrough curves (computed by model) and those measured experimentally. The adsorption isotherms obtained from our approach are in excellent agreement with the experimental values. Using our approach, one is capable of estimating the adsorption isotherms even without detailed knowledge regarding the mass transfer characteristics of the system. Rough estimations of the mass transfer and dispersion coefficients are sufficient to reproduce the absolute adsorption isotherm from the breakthrough curves. Our approach has the following advantages over the conventional method of extracting adsorption data from breakthrough experiments by equilibrium theory: (1) integration is always accompanied by a level of uncertainty which can result in deviations between the calculated amount of adsorption and real adsorption. This is eliminated in our approach by the direct use of breakthrough curves; (2) the number of experiments which are required to estimate the adsorption isotherms are significantly reduced in our approach. (3) in contrast to the conventional equilibrium theory, our method is suitable for the cases with significantly eroded breakthrough curves (significant kinetic effects). (4) Our approach is applicable for mixture of gases and one can obtain the single component adsorption isotherms from experiments performed for a mixture of gases. This is a very important advantage since one can compute the mixture adsorption isotherms at any composition from pure component adsorption isotherms using IAST. Although computational algorithms used in this work are readily extendible to multicomponent mixtures, accurate measurement of multicomponent breakthrough curves might be more complicated. Therefore, future studies are needed to assess the accuracy of the proposed method for multicomponent mixtures.



# **Chapter 3**

## **Heat and Entropy of Adsorption Near Saturation Conditions**

This chapter is based on the following paper: Poursacidesfahani, A.; Torres-Knoop, A.; Rigutto, M.; Nair, A.; Dubbeldam , D.; Vlugt, T. J. H.; Computation of the heat and entropy of adsorption in proximity of inflection points, Journal of Physical Chemistry C, 2016, 120, 1727-1738.

### **3.1 Introduction**

In the previous chapter, the adsorption isotherms and the importance of kinetic effects were discussed. In this chapter, the thermodynamic properties of adsorbate molecules and their dependency on the loading, as well as simulation methods to calculate these properties are studied in detail. Thermodynamic properties such as the heat of adsorption and the entropy of adsorption are crucial for the characterization of the performance of adsorption based separation processes [19, 25, 27]. These properties are sometimes held responsible for the shape selective behaviour of zeolites.

The heat of adsorption determines the thermal energy released during the adsorption step (exothermic) and the heating demand through the desorption step (endothermic) [19, 25, 28]. It is well known that the entropic differences can influence the selectivity of the adsorption process and can be used as the driving force for the separation of similar molecules [29–31]. Consequently, comprehensive knowledge concerning the heat and entropy of adsorption is of great industrial importance. Zeolite 5A is used for the industrial separation of linear and branched alkanes [94] and several other zeolites are suggested by the literature for this task [94–97]. Zeolites usually provide different adsorption sites. As branched hydrocarbons are more bulky than their linear isomers they are preferentially located at very specific adsorption sites [7, 49, 98, 99]. As the loading increases, the molecules are eventually forced to fill the less favourable adsorption sites as well. The thermodynamic properties of adsorbate molecules can be highly influenced by the topology of the adsorption site [12, 100]. The difference between the topologies of the less favorable adsorption sites and the sites that were initially preferred by the branched molecules can cause significant changes in the adsorption properties of hydrocarbons [30, 101].

Although there are several methods to compute the heat of adsorption with Monte Carlo simulations (*e.g.* energy difference in canonical ensemble and energy/particle fluctuations in grand-canonical ensemble [33]), a systematic comparison of the different methods is missing. For instance, a technique that is suitable for computation of the heat of adsorption at low loadings might not be efficient or applicable for calculating the same property near the inflection point. The main focus of this chapter is on the calculation of the heat and entropy of adsorption at various loadings and investigation of the important aspects of each method. Although this chapter is focused on the adsorption of hydrocarbons by zeolites, the proposed methods are by no means restricted to this case and can be applied to other porous materials such as Metal Organic Frameworks.

This chapter is organized as follows. In section 3.2, the heat and entropy of adsorption are defined and the relevant thermodynamic correlations for calculating these properties are derived. In section 3.3, various methods used in molecular simulations to compute the heat and entropy of adsorp-

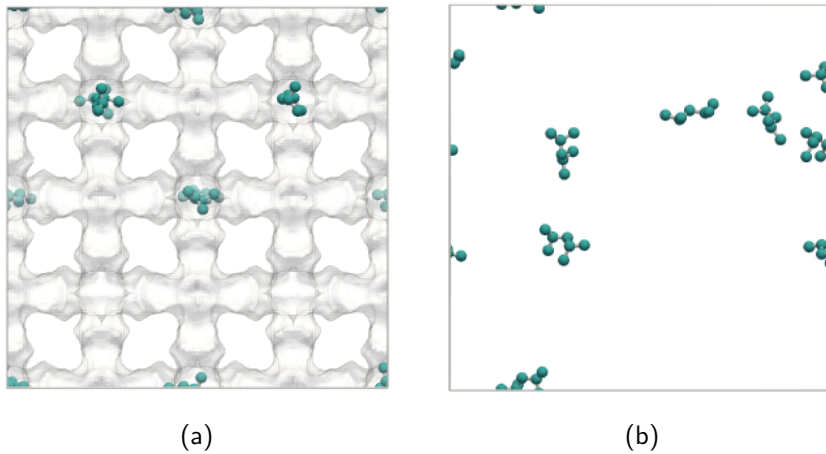


Figure 3.1: (a)  $2 \times 2 \times 2$  unit cells of MEL-type zeolite with adsorbed 2,4-dimethylpentane at 400K (b) the same number of 2,4-dimethylpentane molecules as in Figure 2 (a) at 400K with a volume equal to  $2 \times 2 \times 2 \times$  unit cells of MEL-type, in the absence of zeolite (Reference State 2).

tion for pure components and mixtures are reviewed. The advantages and disadvantages of each method are discussed. The energy slope method is introduced which outperforms the other approaches in the computation of the heat and entropy of adsorption of large molecules near the inflection point. The results of different methods for the system described in section 3.4 are compared in section 3.5. In section 3.6, values for the heat of adsorption of butane/isobutane mixture computed using the energy slope method are presented. These result are compared with the ones computed by the method based on the energy/particle fluctuations for the adsorption of equimolar gas mixture of butane and isobutane at different pressures. The main findings are summarized in section 3.7.

### 3.2 Enthalpy and entropy of adsorption

During an adsorption process, molecules are removed from the reference state and transported into the zeolite. It is important to have a clear definition of the reference state. In this paper, the gas phase in chemical equilibrium with the adsorbed phase is used as the reference state for the calculation of the enthalpy and entropy of adsorption [102]. Moreover, the gas phase is assumed to be ideal, only to simplify the equations. Not using this assumption results in small but trivial changes in upcoming equations. The heat of adsorption of component  $i$  is defined as the change in the total enthalpy of the system as a molecule of component  $i$  is removed from the gas phase (which is in equilibrium with the zeolite) and transported into the zeolite at constant temperature. Here, the system includes the gas phase, zeolite and the guest molecules. Therefore,

$$\Delta H_{i,\text{ads}} = \left( \frac{\partial H}{\partial N_i} \right)_{T,N_j \neq i,z} - \left( \frac{\partial H}{\partial N_i} \right)_{T,N_j \neq i,g} \quad (3.1)$$

where  $H$  is the total enthalpy of the system,  $N_i$  and  $\Delta H_{i,\text{ads}}$  are the number of guest molecules and the heat of adsorption of component  $i$ . The subscripts "z" and "g" refer to the zeolite and the gas phase, respectively. In Eq. 5.1, the heat of adsorption is divided into two contributions: the changes in the enthalpy of the zeolite with guest molecules caused by the addition of a single molecule, and the change in the enthalpy of the gas phase when a molecule is removed from it. The enthalpy of adsorption can be written as the sum of the change in the internal energy and the change in product of the pressure and the volume of the system.

$$\Delta H_{i,\text{ads}} = \Delta U_{i,\text{ads}} + \Delta(PV)_{\text{ads}} \quad (3.2)$$

$\Delta U_{i,\text{ads}}$  is the total internal energy change of the system, due to adsorption of an additional molecule of component  $i$ . The term  $\Delta(PV)_{\text{ads}}$  in Eq. 3.2 requires a closer look. The conditions under which the removal of a molecule from the ideal gas phase and its addition to the zeolite take place should be specified. Generally, the volume and the temperature of

the zeolite are assumed to be constant during this process. For the gas phase, usually the pressure and the temperature are kept constant. Similar to the heat of adsorption, the  $\Delta(PV)_{\text{ads}}$  in Eq. 3.2 is expanded into an ideal gas phase contribution and an adsorbed phase contribution. The ideal gas phase contribution is computed utilizing the ideal gas law. The zeolite is acknowledged as a solid structure with microscopic openings where pressure is not defined and the volume of adsorbate is zero [103]. With this assumption, the contribution of the adsorbed phase to the  $\Delta(PV)_{\text{ads}}$  term of Eq. 3.2 would vanish and the enthalpy of adsorption of component  $i$  can be computed from

$$\Delta H_{i,\text{ads}} = \Delta U_{i,\text{ads}} - k_B T \quad (3.3)$$

Here,  $k_B$  is the Boltzmann factor. The entropy of adsorption is defined in a similar way, starting from the Gibbs free energy. The Gibbs free energy of adsorption of component  $i$  is the change in the total Gibbs free energy of the adsorption system when an additional molecule of component  $i$  is transferred from the ideal gas phase inside the zeolite,

$$\Delta G_{i,\text{ads}} = \left( \frac{\partial G}{\partial N_i} \right)_{T,V,N_j \neq i,z} - \left( \frac{\partial G}{\partial N_i} \right)_{T,P,N_j \neq i,g} \quad (3.4)$$

where  $G$  is the total Gibbs free energy of the system. The first term on the right hand side of Eq. 3.4 is, by definition, equal to the chemical potential of component  $i$  in the adsorbed phase and the second one is the chemical potential of component  $i$  in the ideal gas phase. Chemical equilibrium implies that the chemical potential of component  $i$  in the adsorbed phase is equal to the one in the gas phase. Consequently, at equilibrium, the Gibbs free energy of the adsorption system remains unchanged. Then, the entropy of adsorption of component  $i$  is given by

$$\Delta G_{i,\text{ads}} = \Delta H_{i,\text{ads}} - T \Delta S_{i,\text{ads}} = 0 \quad (3.5)$$

$$\Delta S_{i,\text{ads}} = \frac{\Delta H_{i,\text{ads}}}{T} \quad (3.6)$$

In Eq. 3.6, the gas phase in equilibrium with the adsorbed phase (denoted by Reference State 1) is used as the reference state for the calculation of the entropy of adsorption [102]. However, sometimes a different reference state is used: the gas phase with the temperature and number density equal to the adsorbed phase (denoted by Reference State 2) [46, 104, 105]. In this approach, the entropy of the adsorbate molecules inside the zeolite is compared to the entropy of the adsorbate molecules in the absence of the zeolite (Figs. 3.1a and 3.1b). In this case, the Helmholtz free energy is the natural starting point for the computation of the entropy of adsorption. The change in the total Helmholtz free energy of the system is given by

$$\Delta A_{i,\text{ads}} = \Delta U_{i,\text{ads}} - T\Delta S_{i,\text{ads}} \quad (3.7)$$

$\Delta A_{i,\text{ads}}$  is the total change in the Helmholtz free energy of the system, subjected to adsorption of an additional molecule of component  $i$ . The value of  $\Delta A_{i,\text{ads}}$  in Eq. 3.7 is given by the difference in the chemical potential of component  $i$  in the adsorbed phase and in the gas phase. Due to the choice of the reference state, the chemical potentials are not identical. The chemical potential can be expressed as the sum of the ideal gas part and the excess part. The ideal gas part is defined by the number density. Since the number densities of the Reference State 2 and the adsorbed phase are equal, the ideal gas parts cancel each other out. Assuming ideal gas behaviour at Reference State 2, the excess chemical potential of component  $i$  in the Reference State 2 would be zero. Therefore, the total changes in the Helmholtz free energy of the system can be estimated by the excess chemical potential of component  $i$  in the adsorbed phase. The Widom's test particle method is conventionally used to compute the excess chemical potential in molecular simulations. For chain molecules, conformation of a test chain is normally generated using the Rosenbluth algorithm [106]. Considering Widom's test particle method with Rosenbluth algorithm, the excess chemical potential

of component  $i$  in the adsorbed phase and, therefore, the total change in the Helmholtz free energy of the system is given by [38]

$$\Delta A_{i,\text{ads}} = \mu_{i,\text{ex,z}} = -k_B T \ln \frac{\langle W_{i,z} \rangle}{\langle W_{i,\text{id}} \rangle} \quad (3.8)$$

where  $\langle W_{i,z} \rangle$  is the average Rosenbluth factor of a test chain of component  $i$  in the adsorbed phase and  $\langle W_{i,\text{id}} \rangle$  is the average Rosenbluth factor of an isolated chain of component  $i$ .  $\mu_{\text{ex,z}}$  is the excess chemical potential of component  $i$  in the adsorbed phase.

Using Eqs. 3.7 and 3.8, considering the fact that the chemical potential of the Reference State 1 (not Reference State 2) and the chemical potential of the adsorbed phase are equal, the entropy of adsorption for component  $i$ , using Reference State 2, can be computed from Eq. 3.9.

$$\Delta S_{i,\text{ads}} = \frac{\Delta U_{i,\text{ads}}}{T} - k_B \ln \frac{\rho_{i,\text{ref.1}}}{\rho_{i,\text{ref.2}}} \quad (3.9)$$

where  $\rho_{i,\text{ref.1}}$  and  $\rho_{i,\text{ref.2}}$  are the number densities of component  $i$  in the Reference State 1 and Reference State 2. As reflected in Eqs. 3.3, 3.6 and 3.9, choosing different reference states can lead to different expressions for the entropy of adsorption. However, the difference between these expressions is only caused by the entropy difference between the reference states (last term on the right hand side of Eq. 3.9 and a term  $k_B T$ ). Therefore, the values computed by the two approaches can be compared after including the entropy difference between the reference states.

The computational steps needed to compute the entropy of adsorption and the enthalpy of adsorption are identical. Therefore, in the remainder of this paper, to compare various computational methods, only the enthalpy of adsorption is considered explicitly.

### 3.3 Computational methods

The partial derivative of the total internal energy of an ideal gas phase with respect to the number of molecules of component  $i$  is independent

from the pressure. This value is equal to the average internal energy of a single isolated molecule of component  $i$  at the corresponding temperature and needs to be calculated only once. As a result, the heat of adsorption is given by

$$\Delta H_{i,\text{ads}} = \left( \frac{\partial U}{\partial N_i} \right)_{T,V,N_j \neq i,z} - \langle U_{g,i} \rangle - k_B T \quad (3.10)$$

In which  $\langle U_{g,i} \rangle$  is the average internal energy of a single isolated molecule of component  $i$  in the gas phase. There are various methods for computing the change in the total internal energy of the zeolite and adsorbates upon the adsorption of an additional molecule (the partial derivative in Eq. 3.10) in molecular simulations. In this section, the most commonly used methods are reviewed and their advantages and disadvantages are discussed. The "Energy Slope" method is also introduced as an improved method to compute the partial derivative in Eq. 3.10. The subscript "z" is skipped for the partial derivatives and they all apply to the zeolite phase.

### 1. Energy/Particle fluctuations in the grand-canonical ( $\mu VT$ ) ensemble:

The partial derivatives with respect to chemical potential can be expressed as a function of averages in the grand-canonical ensemble [107–110]. Consequently, for a single-component system, the partial derivative in Eq. 3.10 is computed from

$$\left( \frac{\partial U}{\partial N} \right)_{T,V,z} = \frac{\left( \frac{\partial U}{\partial \mu} \right)_{T,V,z}}{\left( \frac{\partial N}{\partial \mu} \right)_{T,V,z}} = \frac{\langle UN \rangle_\mu - \langle U \rangle_\mu \langle N \rangle_\mu}{\langle N^2 \rangle_\mu - \langle N \rangle_\mu \langle N \rangle_\mu} \quad (3.11)$$

where  $\langle \dots \rangle_\mu$  presents an average in grand-canonical ensemble. The heat of adsorption of a single-component system is therefore expressed as [33, 110, 111]

$$\Delta H_{\text{ads}} = \frac{\langle UN \rangle_\mu - \langle U \rangle_\mu \langle N \rangle_\mu}{\langle N^2 \rangle_\mu - \langle N \rangle_\mu \langle N \rangle_\mu} - \langle U_g \rangle - k_B T \quad (3.12)$$

The energy/particle fluctuations in the grand-canonical ensemble can also be used to compute the heat/entropy of adsorption of gas mixtures. In this case, the partial derivative in Eq. 3.10 is given by [111]

$$\left( \frac{\partial U}{\partial N_i} \right)_{T,V,N_j \neq i,z} = \sum_{k=1}^{N_C} \left( \frac{\partial U}{\partial \mu_k} \right)_{T,V,\mu_j \neq k} \left( \frac{\partial \mu_k}{\partial N_i} \right)_{T,V,N_j \neq i} \quad (3.13)$$

where  $N_C$  is the number of components in the gas mixture. As the partial derivative in Eq. 3.10 indicate, the change in the total internal energy of the adsorbed phase should be calculated. This value should be computed while only the loading of component  $i$  is changed and the loadings of all other components are unchanged. The change in the chemical potential of component  $i$  results in changes in the chemical potentials of all other components and therefore, their loadings. Consequently, as shown in Eq. 3.13, the chemical potentials of all other components should change in such a way that their loadings remain constant. To find the correct values for the last term on the right hand side of Eq. 3.13, a system of linear algebraic equations should be solved. For the most simple case of a binary mixture, the system of equations can be written as [111]

$$I = \begin{bmatrix} \left( \frac{\partial N_1}{\partial \mu_1} \right)_{T,V,\mu_2} & \left( \frac{\partial N_2}{\partial \mu_1} \right)_{T,V,\mu_2} \\ \left( \frac{\partial N_1}{\partial \mu_2} \right)_{T,V,\mu_1} & \left( \frac{\partial N_2}{\partial \mu_2} \right)_{T,V,\mu_1} \end{bmatrix} \begin{bmatrix} \left( \frac{\partial \mu_1}{\partial N_1} \right)_{T,V,N_2} & \left( \frac{\partial \mu_1}{\partial N_2} \right)_{T,V,N_1} \\ \left( \frac{\partial \mu_2}{\partial N_1} \right)_{T,V,N_2} & \left( \frac{\partial \mu_2}{\partial N_2} \right)_{T,V,N_1} \end{bmatrix} \quad (3.14)$$

Here,  $I$  is the identity matrix. As mentioned before, the partial derivatives with respect to the chemical potential can be written as a function of averages in the grand-canonical ensemble:

$$\begin{aligned} \left( \frac{\partial U}{\partial \mu_k} \right)_{T,V,\mu_j \neq k} &= \langle UN_k \rangle_\mu - \langle U \rangle_\mu \langle N_k \rangle_\mu \\ \left( \frac{\partial N_i}{\partial \mu_k} \right)_{T,V,\mu_j \neq k} &= \langle N_i N_k \rangle_\mu - \langle N_i \rangle_\mu \langle N_k \rangle_\mu \end{aligned} \quad (3.15)$$

The main disadvantage of this method is that calculating the energy/particle fluctuations is computationally very expensive, requiring many successive particle insertion/removal. The acceptance rate for the complete insertion of branched molecules can be quite low, even when advanced sampling methods, such as the Configurational-Bias Monte Carlo (CBMC), are used. Generally, the fraction of accepted trial moves decreases as the loading increases and near the inflection point, where all the suitable adsorption sites are already filled. Therefore, significantly long simulations are needed to obtain accurate statistics.

## 2. Energy difference of two simulations in the canonical ensemble:

The partial derivative in Eq. 3.10 can be estimated by

$$\left(\frac{\partial U}{\partial N_i}\right)_{T,V,N_j \neq i,z} = \langle U \rangle_{N_1, N_2, \dots, (N_i+1), \dots, N_C} - \langle U \rangle_{N_1, N_2, \dots, (N_i), \dots, N_C} \quad (3.16)$$

$$N_T = \sum_{k=1}^{N_C} N_k \quad (3.17)$$

where  $\langle U \rangle_{N_1, N_2, \dots, (N_i), \dots, N_C}$  denotes the average total internal energy of the zeolite plus  $N_T$  adsorbate molecules at constant temperature, volume, and loading of all  $N_C$  components. the last term is the average total internal energy when the loadings of all the components are the same as the former case, except for the component  $i$ . As a result, the total number of adsorbed molecules in this case is  $N_T + 1$ . The canonical ensemble is the natural choice for calculating these averages. The heat of adsorption can be computed by substituting Eq. 3.16 in Eq. 3.10.

This method is mostly used to estimate the heat of adsorption at zero-loading. Usually, rigid zeolite structures are used in simulations, [112] therefore, the average internal energy of zeolite without any guest molecule is zero. At zero-loading, only one simulation in  $NVT$  ensemble is needed to compute the partial derivative in Eq. 3.10 [95,

113, 114]. This approach is rarely utilized for the calculation of the heat of adsorption at higher loadings. The reason behind is that as the loading increases, the values of the two average internal energies in Eq. 3.16 increase. At higher loadings, these values can become significantly larger than their difference. Therefore, even a small relative error in the calculation of average internal energies can cause a noticeable relative error in the energy difference and eventually in the calculated value for the heat of adsorption.

### 3. Widom's test particle in the canonical ensemble:

In principle, the two averages on the right hand side of Eq. 3.16 can be computed in a single simulation in the canonical ensemble. Using Widom's test particle method with Rosenbluth algorithm,  $\langle U \rangle_{N_1, N_2, \dots, (N_i+1), \dots, N_C}$  is computed in the *NVT* simulation with  $N_T$  adsorbate molecules:

$$\langle U \rangle_{N_1, N_2, \dots, (N_i+1), \dots, N_C} = \frac{\langle (U + u_i^+) W_i \rangle_{N_1, N_2, \dots, (N_i), \dots, N_C}}{\langle W_i \rangle_{N_1, N_2, \dots, (N_i), \dots, N_C}} \quad (3.18)$$

$u_i^+$  and  $W_i$  are the internal energy and the Rosenbluth factor of a test chain of component  $i$  in the adsorbed phase. Substituting Eq. 3.18 into Eq. 3.16 leads to the following expression for the partial derivative in Eq. 3.10

$$\left( \frac{\partial U}{\partial N_i} \right)_{T, V, N_j \neq i, z} = \frac{\langle (U + u_i^+) W_i \rangle_{N_1, N_2, \dots, (N_i), \dots, N_C}}{\langle W_i \rangle_{N_1, N_2, \dots, (N_i), \dots, N_C}} - \langle U \rangle_{N_1, N_2, \dots, (N_i), \dots, N_C} \quad (3.19)$$

In Eq. 3.19, the adsorbed phase contribution to the variation of the total internal energy of the adsorption system is computed in a single simulation. The same parameter is computed with two different simulations using the energy differences in *NVT* ensemble.

#### 4. Energy slope method:

It is shown in the next section that by increasing the number of adsorbed hydrocarbon chains, the enthalpy of adsorption of C<sub>7</sub> isomers in MFI- and MEL-type zeolites remains roughly constant. The sizable variations in the enthalpy of adsorption only occur when the more energetically favorable adsorption sites are filled and additional molecules are located in the less energetically favourable adsorption site. This observation has been used to develop the energy slope method for computing the heat and entropy of adsorption. For the adsorption of C<sub>7</sub> isomers in MFI- and MEL-type zeolites, it is assumed that the enthalpy of adsorption is not a function of the loading as long as the hydrocarbon chains are adsorbed in the particular adsorption sites. By increasing the loading, as soon as the most favorable adsorption site is completely filled and the next molecule is forced to sit within the less favorable adsorption site, the heat/entropy of adsorption suddenly changes to a new value. Considering the partial derivative in Eq. 3.10, this assumption suggests that while the molecules are filling a particular adsorption site, the total internal energy of the zeolite plus the guest molecules should be a linear function of the loading. In the energy slope method, the partial derivative in Eq. 3.10 is estimated by the slope of the line describing the variation of the total internal energy of the zeolite plus the guest molecules as a function of the loading. When the most favorable adsorption site is completely filled (molecules are forced to fill the second favorable adsorption site), the slope of this line is expected to suddenly change to a new value. This new value corresponds to the zeolite contribution to the enthalpy of adsorption associated with the second adsorption site. The fact that the enthalpy of adsorption of C<sub>7</sub> isomers in MFI- and MEL-type zeolites is a piecewise constant function of loading is the main reason for using a straight line to describe the changes in the total internal energy of the zeolite as a function of loading. However, in general, any analytical function that nicely fits to the total internal energy of the zeolite as a function of loading can be used in the energy slope method.

In summary, to compute the heat and entropy of adsorption using the energy slope method the total internal energy of zeolite and adsorbed molecules should be calculated as a function of loading. This can be easily obtained by simulations in canonical ensemble. An analytical function which accurately describes the variations in the total internal energy of zeolite and adsorbed molecules as a function of loading should be fitted to the data. The partial derivative in Eq. 3.10 as a function of loading is obtained by computing the derivative of fitted analytical function with respect to the number of adsorbed molecules.

### 3.4 Simulation details

The adsorption of linear (heptane), mono-branched (2-methylhexane), geminal di-branched (2,2-dimethylpentane), and non-geminal di-branched (2,4-dimethylpentane) C<sub>7</sub> isomers in MFI- and MEL-type zeolites is studied. The RASPA software is used for the simulations [115, 116]. A cutoff radius of 12 Å is applied and no tail corrections are used. The simulation box is made by  $2 \times 2 \times 2$  rigid unit cells with periodic boundary conditions to ensure that the distance of two periodic images is at least twice the cutoff radius. The unit cell of MFI-type zeolite consists of four identical intersections connected by zigzag and straight channels, while the unit cell of MEL-type zeolite is formed by two large intersections and two small intersections and there are only straight channels in between [53]. Simulations were performed in the grand-canonical and canonical ensemble at 400K. At each Monte Carlo step of grand-canonical simulations an attempt is made to either displace, regrow, rotate, insert, or remove a randomly chosen hydrocarbon chain. Hydrocarbon chains are inserted/regrown using the Configurational-Bias Monte Carlo (CBMC) technique. For the simulations in the canonical ensemble, the number of hydrocarbon chains is fixed and there is no insertion or removal move. The number of Monte Carlo steps in a cycle is equal to the total current number of adsorbates in the system with the minimum of 20. Typical simulations are started with 0.2 to 0.5 million Monte Carlo cycles to equilibrate the system, followed by 0.5 to 5 million production

cycles. The total production run is divided into five blocks and the standard deviation of the block averages is used for the calculation of the error in computed properties. More details regarding the simulations can be found elsewhere [49, 95].

### 3.5 Results and comparison of different methods

In Figs. 3.2a and 3.2b, the enthalpy of adsorption of 2,4-dimethylpentane computed using the energy/particle fluctuations in the grand-canonical ensemble is plotted as a function of loading. The method works quite accurately at lower loadings, however, although all simulations have the same number of cycles, errors increase as the loading is increased. The width of the error bars expands significantly around the loading of four molecules per unit cell. This is due to the fact that MC moves to place a bulky molecule like 2,4-dimethylpentane inside the narrow channels of these structures are accompanied by very unfavorable changes in the energy of the system and are rarely accepted. Therefore, when all the available intersections (four intersections per unit cell for both MFI-type and MEL-type zeolite) are filled, the acceptance rate for the insertion/removal move drops significantly. This results in poor statistics in the computation of fluctuations of Eq. 3.11 and eventually large error bars for the reported enthalpy of adsorptions. For loadings higher than four molecules per unit cell, it is not even possible to compute the fluctuations in some of the simulations even after 10 million MC cycles. It is instructive to study in more details the variations in the enthalpy of adsorption as a function of loading. It is shown in Fig. 3.2b that when less than four hydrocarbon chains per unit cell are present inside MFI-type zeolite, the enthalpy of adsorption of 2,4-dimethylpentane weakly depends on loading. However, in Fig. 3.2a, there are two plateaus below the loading of four molecules per unit cell. The first plateau lasts until the loading of roughly two molecules per unit cell. Then, the enthalpy of adsorption rises to the value of the second plateau and remains approximately constant up to the loading of four molecules per unit cell. The existence of only single type of intersections in MFI-type zeolite and two

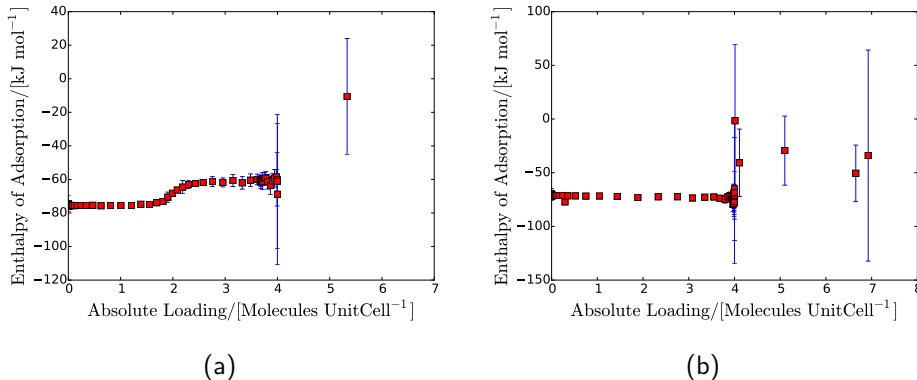


Figure 3.2: Enthalpy of adsorption of 2,4-dimethylpentane computed using energy/particle fluctuations in grand-canonical ensemble at 400K. (a) MEL-type and (b) MFI-type zeolite. The error bars indicate the 95% confidence interval.

different types of intersections in MEL-type zeolite is the source of different behaviour. The large intersections of MEL-type zeolite are the most favorable adsorption site for the adsorption of 2,4-dimethylpentane. Therefore, the 2,4-dimethylpentane molecules are preferentially located in these intersections (Fig. 3.3a). As soon as all the large intersections are filled (loading of two molecule per unit cell), additional molecules are forced to occupy the energetically less favourable adsorption sites (small intersections). The first plateau in Fig. 3.2a corresponds to the adsorption in the favorable (large) intersections and the second one is associated with the adsorption in less favorable (small) intersections. Accordingly, one can conclude that the intersections are far enough from each other that when the molecules are adsorbed only within them, the adsorbate-adsorbate interactions are negligible compared to the host-adsorbate interactions. Therefore, the enthalpy of adsorption weakly depends on loading. The enthalpy of adsorption is mainly determined by the topology of the particular adsorption site and the shape of adsorbate molecules. Consequently, the enthalpy of adsorption changes considerably only when the additional molecule is located in a new adsorption site. This explains why the enthalpy of adsorption of

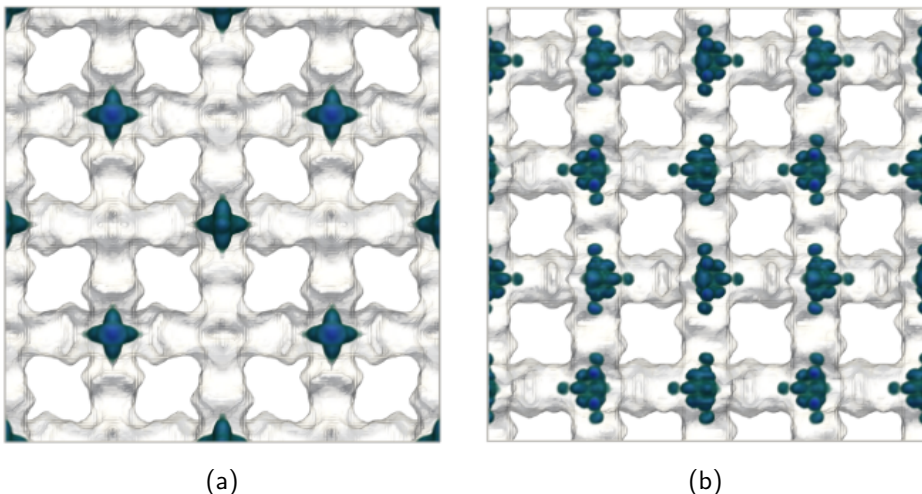


Figure 3.3: 3D histogram (density plot) of 2,4-dimethylpentane atomic positions at 400K and 10Pa in (a) MEL-type and (b) MFI-type zeolite.

2,4-methylpentane in MFI-type zeolite, with four identical intersections per unit cell, remains almost constant below the loading of four molecules per unit cell. It also explains why there are two plateaus below the loading of four molecules per unit cell in the plot of the enthalpy of adsorption versus loading of 2,4-methylpentane in MEL-type zeolite with two large and two small intersections per unit cell. The effect of this key feature of MEL-type zeolite can also be seen in the isotherm of 2,4-dimethylpentane (Fig. 3.4a). There is a noticeable inflection in the 2,4-dimethylpentane isotherm, around the loading of two molecules per unit cell (Fig. 3.4a). In Figs. 3.4a and 3.4b, fugacity is converted to pressure using the Peng-Robinson equation of state. In Figs. 3.5a and 3.5b, the enthalpy of adsorption for 2,4-dimethylpentane computed from the energy difference of two simulations in the canonical ensemble is plotted as a function of loading. It is shown that as the loading is increased, errors associated with the enthalpy of adsorption, calculated with this method, are sharply increased. As the loading rises, the difference between the two average internal energies in Eq. 3.16 becomes substan-

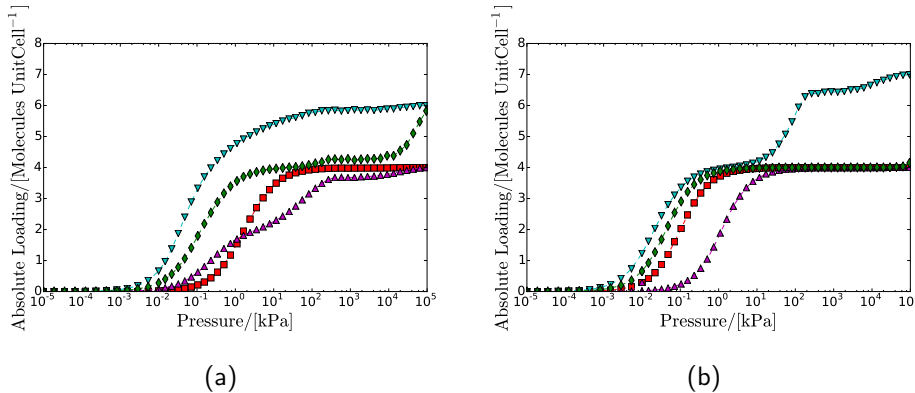


Figure 3.4: Adsorption isotherms of pure heptane ( $\nabla$ ), 2-methylhexane ( $\diamond$ ), 2,2-dimethylpentane ( $\square$ ) and 2,4-dimethylpentane ( $\triangle$ ) at 400K as computed with CBMC simulations. (A) MEL-type and (B) MFI-type zeolite.

tially smaller than either of them and approaches the typical fluctuations of the two averages. Hence, it is not surprising that the energy difference method performs poorly at higher loadings. Just as the method based on the energy/particle fluctuation, this method is not capable of providing an accurate estimation of the enthalpy of adsorption , at loadings that due to lack of more favourable adsorption sites, molecules are located in the channels (the least favorable adsorption site). Due to the large error bars associated with this method, it is hardly possible to notice the change in the enthalpy of adsorption as the molecules start to fill a new adsorption site. As a result, the different adsorption regions that can be seen in Figs. 3.2a and 3.2b, cannot be distinguished easily when the energy difference is used instead of the energy/particle fluctuations method. In Figs. 3.6a and 3.6b, the values obtained for the enthalpy of adsorption of 2,4-dimethylpentane at various loadings using the Widom's test particle method are presented. In the same way as the method based on the energy difference, the error bars associated with the Widom's test particle method are evidently larger when the loading is higher. This difficulty arises from the fact that even when the structure is empty, most of the randomly chosen positions for the

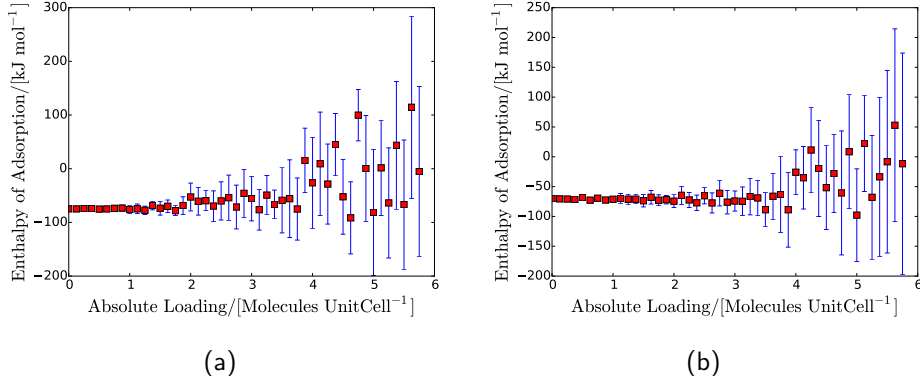


Figure 3.5: Enthalpy of adsorption of 2,4-dimethylpentane computed using energy difference between two simulations in canonical ensemble at 400K. (a) MEL-type and (b) MFI-type zeolite. The error bars indicate the 95% confidence interval.

test hydrocarbon chain result in an overlap with the host atoms. These positions have very low Rosenbluth weight and consequently very limited contribution to the overall averages in Eq. 3.19. This problem becomes more significant as the length of the chain increases and as the loading is increased. At high loadings, most of the randomly selected positions for the insertion of a molecule result in an overlap with the host atoms or adsorbate molecules that are already present in the system. Therefore, it becomes very difficult to find a cavity that a molecule can fit in. Simulations in the open ensembles (grand-canonical, Gibbs, and reaction ensemble) suffer from the same problem. New simulation techniques that does not rely on the occurrence of spontaneous cavities for the insertion of a molecule are introduced in Chapters 6 and 7. Various methods to compute the heat of adsorption at nonzero-loadings have been investigated. Comparison between the results of different approaches coherently showed that the method based on energy/particle fluctuations in the grand-canonical ensemble can provide the best estimate for the heat and entropy of adsorption of C<sub>7</sub> isomers. However, even this approach was not appropriate to compute the aforementioned thermodynamic properties at loadings higher than four

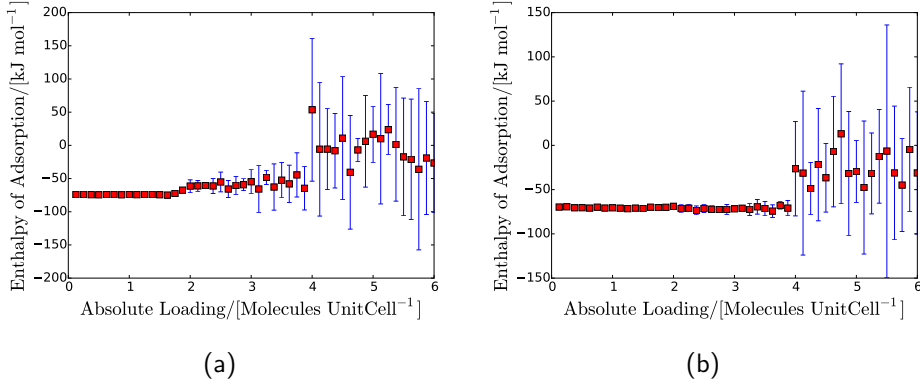


Figure 3.6: Enthalpy of adsorption of 2,4-dimethylpentane computed using the Widom test particle method in canonical ensemble at 400K. (a) MEL-type and (b) MFI-type zeolite. The error bars indicate the 95% confidence interval.

molecules per unit cell in MFI- and MEL-type zeolites. In this part, the energy slope method is used to enhance our estimation of the heat and entropy of adsorption after the inflection.

In Figs. 3.7a and 3.7b, the total internal energies of MFI- and MEL-type zeolites systems as a function of the loading of 2,4-dimethylpentane are plotted. The plot of the total internal energy of the structure and the guest molecules as a function of the loading is divided into a number of blocks (Figs. 3.7a and 3.7b). Since MEL-type zeolite consists of three different adsorption sites, three blocks are considered in Fig. 3.7a. The first block includes the total internal energy of MEL-type zeolite with 0-2 molecules per unit cell. The second block contains the data for loadings between 2 to 4 molecules per unit cell and the last one presents the data for the loadings higher than 4 molecules per unit cell. In the same way, two blocks are considered in Fig. 3.7b. The first one considering the data for the loadings below four molecules per unit cell and the second one including the data for the loadings larger than four molecules per unit cell. As shown in Figs. 3.7a and 3.7b, in each block, the total internal energy of the structures and guest molecules varies approximately linearly with the loading. More

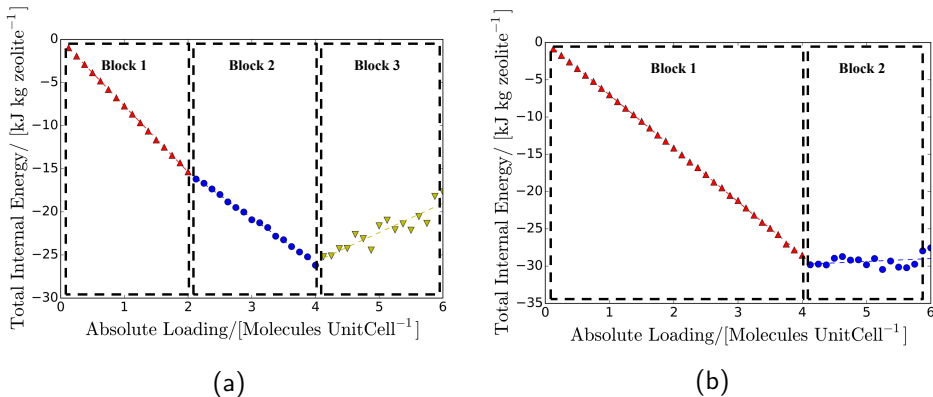


Figure 3.7: The total internal energy of zeolite as a function of loading of 2,4-dimethylpentane at 400K. Different symbols (and colors) correspond to adsorption in different adsorption sites and the dashed lines are the line fitted to the data associated with each adsorption site. (a) MEL-type and (b) MFI-type zeolite.

interestingly, there is a clear difference between the slope of the lines fitted to the data in the different blocks.

All above can confirm the theory that the enthalpy of adsorption of 2,4-dimethylpentane is roughly constant at each block. As a result, noticeable variations in the value of the enthalpy of adsorption occur only when the more energetically favorable adsorption sites are filled and additional molecules start to fill the less energetically favourable adsorption site. This is along the same line with what was expected from the enthalpy of adsorption data computed from the energy/particle fluctuations. There, below the loading of four molecules per unit cell, two plateaus for the enthalpy of adsorption of 2,4-dimethylpentane in MEL-type zeolite and only one for the enthalpy of adsorption of 2,4-dimethylpentane in MFI-type zeolite have been perceived. In the energy slope method, the zeolite contribution to the enthalpy of adsorption is computed from the slope of the best line fitted to the series of data points describing the variation of total internal energy of structure and guest molecules as a function of loading at each block. In Figs. 3.8a and 3.8b, the results obtained from the energy slope

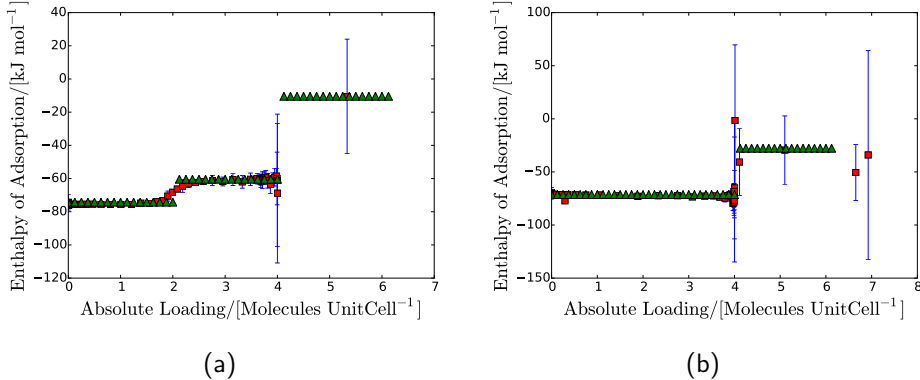


Figure 3.8: Comparison between the enthalpy of adsorption of 2,4-dimethylpentane computed from energy/particle fluctuations in grand-canonical ensemble ( $\square$ ) and using the energy slope in canonical ensemble at 400K ( $\triangle$ ). (a) MEL-type and (b) MFI-type zeolite. The error bars indicate the 95% confidence interval.

method are compared with the ones computed from the method based on the energy/particle fluctuations. The values computed with the energy slope method are in good agreement with the results obtained from the energy/particle fluctuations method. The main advantage of the energy slope method over the energy/particle fluctuations method appear at loading near and above the inflection point where the method based on energy/particle fluctuations performs poorly. As discussed in previous sections, the performance of energy/particle fluctuations method is directly related to the acceptance rate of the insertion/removal move. Significantly low acceptance rate of the insertion/removal move results in an inadequate performance of energy/particle fluctuations method at loading near and above the inflection point. Using the energy slope method, all simulations are performed in canonical ensemble where the number of adsorbate molecules is fixed (no insertion/removal move). Moreover, in the energy slope method, the main disadvantage of the energy difference method (which is the difference in scales of the two averages in Eq. 3.16 and their difference) is eliminated. In the energy slope method, instead of using the difference between the two

average internal energies in Eq. 3.16 (which is highly vulnerable to even limited errors in computation of the average internal energies), the slope of the best fitted line to the set of data points corresponding to each block is used to compute the partial derivative in Eq. 3.10 . The slope of this line is much less affected by the computational error in calculation of any of the average internal energies. Therefore, even at loading higher the inflection point, where the computational error in the calculation of average energies in the canonical ensemble is considerably high (Figs. 3.7a and 3.7b), the energy slope method is still capable of providing an accurate estimation of the enthalpy of adsorption.

### 3.6 Energy Slope Method for mixtures

The adsorption of the equimolar mixture of butane and isobutane at 400K by MFI-type zeolite is considered to compare the different methods. While using the energy slope method, it is necessary to consider the total internal energy of the zeolite at series of points, where the loadings of all of the components are constant except the one that its heat/entropy of adsorption should be computed. Therefore, a two dimensional grid of data points is required to compute the heat/entropy of adsorption of each component in a binary mixture at different loadings. In the same way, if one is interested in computing the heat/entropy of adsorption at various loading of either of components in a binary mixture, using the method based on the energy/particle fluctuation, a two dimensional grid including different partial pressures of each component is needed. In contrast to the pure heptane isomers, by increasing the pressure of the gas phase the variations in the heat of adsorption of each component in the binary mixture of butane and isobutane occur gradually. The reason is that these molecules are much smaller than heptane isomers. Therefore, they are not as tightly fitted within the different adsorption sites as the heptane isomers are. As a result, the difference between the heats of adsorption corresponding to different adsorption sites is less significant in this case. Moreover, in the case of the binary mixture, at low loadings, there are enough adsorption sites for both

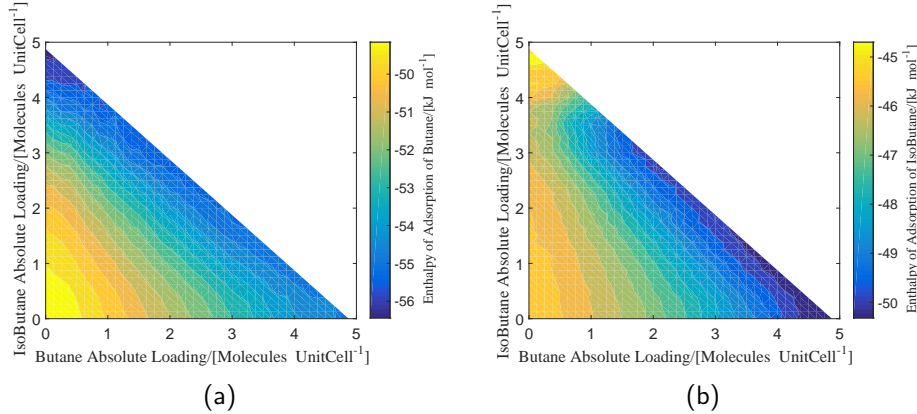


Figure 3.9: The enthalpy of adsorption of butane (a) and isobutane (b) computed with the energy slope method in the canonical ensemble at 400K in MFI-type zeolite.

components to site freely at their favorable adsorption sites. There is no competition between the different molecules to occupy the adsorption site. Consequently, their heats of adsorption in the mixture are almost equal to their heats of adsorption in the case of pure gas. As the total loading increases, molecules start to compete over the available adsorption sites. The molecule that fits better within the zeolite and has the higher stacking efficiency will occupy more adsorption sites. This component gradually takes over the adsorption sites that were occupied by the other component at lower loadings. This results in a gradual change in the heat of adsorption of both components. Considering all above, to compute the enthalpy of adsorption at each grid point with the energy slope method, the slope of the best fitted straight line passing through the grid point in question and its neighbours in the corresponding direction are used.

In Figs. 3.9a and 3.9b, the heat of adsorption of butane and isobutane at various loadings of each component is presented. The enthalpy of adsorption of butane is always lower (more negative) than isobutane, implying that butane molecules fit better within the confinements provided by MFI-type zeolite and that they have more favourable stacking efficiency. Consequently,

it can be concluded that MFI-type zeolite prefers the adsorption of butane over isobutane (Figs. 3.10a and 3.10b). There is an agreement between the values for the heat of adsorption of both components computed with the energy slope method and the ones calculated from the method based on the energy/particle fluctuations (Figs. 3.10a and 3.10b). For each data point, discrepancy between the values computed with two methods is less than each of their uncertainties (not shown here). The data presented in Figs. 3.10a and 3.10b shows that the applications of the energy slope method are not limited to the adsorption of pure gases. This method can also be used for the computation of the heat/entropy of mixtures. However, since an  $N$  dimensional grid of data points is needed to compute the heat/entropy of adsorption of all  $N$  components in a mixture, the computational effort associated with this method increases sharply with the number of components. Therefore, it might not be the most computationally-efficient method while the heat of adsorption of all the components in a multi-component mixture with single set of partial pressures is of interest. In this case, if the acceptance rate for the insertion/removal move is high enough, the method based on energy particle fluctuations would be more computationally-efficient.

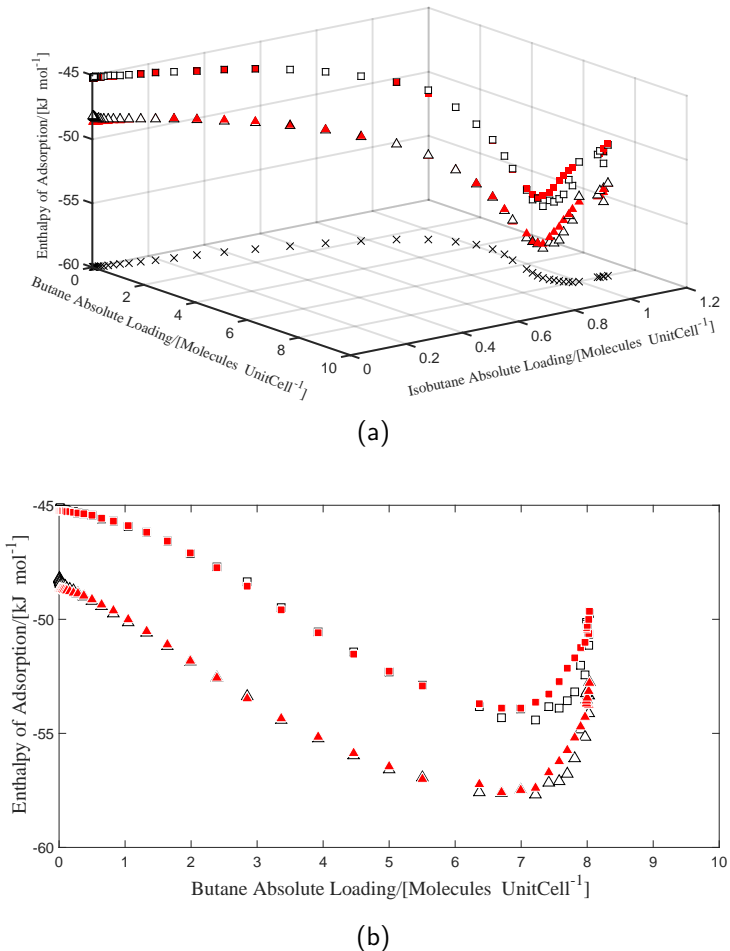


Figure 3.10: (a) Comparison between the enthalpy of adsorption of butane ( $\triangle$ ) and isobutane ( $\square$ ) computed with energy/particle fluctuations in grand-canonical ensemble (open symbols) and using the energy slope in canonical ensemble (closed symbols) at 400K in MFI-type zeolite. Data points correspond to adsorption of equimolar gas mixture of butane and isobutane at various pressures of the gas phase. The symbol ( $\times$ ) shows the loading of the components at each point. (b) 2D representation of Fig. 3.10a.

### 3.7 Conclusions

We systematically compared the effectiveness of various methods to compute the heat and entropy of adsorption at different loadings. We showed that at low loadings, the method based on the energy/particle fluctuation in the grand-canonical ensemble is the most efficient method to compute the equilibrium enthalpy of adsorption of relatively large molecules such as C<sub>7</sub> isomers. However, none of the conventional methods discussed in the first part of this chapter exhibited a satisfactory performance around the inflection point. We showed that the enthalpy of adsorption of C<sub>7</sub> isomers is a weak function of the loading and the value of the enthalpy of the adsorption of C<sub>7</sub> isomers is mainly determined by the host-adsorbate interactions at the adsorption site which is being filled at the particular loading. Therefore, large changes in the value of the enthalpy of adsorption occurs only when a more favourable adsorption site is completely filled and additional molecules are forced to fill the less favourable adsorption site. Based on this observation, we introduced the "Energy Slope" method to compute the enthalpy of adsorption. In this method, the variations in the total internal energy of zeolite with respect to the hydrocarbon loading are divided into different blocks. Each of these blocks correspond to the adsorption of hydrocarbon chains in a particular adsorption site. Then, at each block the enthalpy of adsorption is computed using the slope of the best fitted straight line describing the variations in the total internal energy of zeolite as a function of the loading. Compared to commonly used energy difference method, the energy slope method is far less sensitive to the computational error in calculation of the average energies. We showed that this method has the best performance amongst the currently available methods for the computation of the enthalpy of adsorption near the inflection point. We also investigated the application of the energy slope method for the calculation of the enthalpy of mixtures. We showed that the use of either the energy slope method or the method based on the energy/particle fluctuations lead to identical results for the enthalpy of adsorption of a binary mixture of butane and isobutane. From the computational point of view, the energy/particle fluctuations method appears to be more efficient, when

the acceptance rate for insertion/removal move is sufficiently high (loadings lower than the inflection point). This is due to the fact that, using the energy slope method, the number of simulations to compute the enthalpy of adsorption of all components in a mixture increases significantly as the number of mixture component increases.



## **Chapter 4**

# **Product Shape Selectivity in the Catalytic Hydroconversion of Heptane**

This chapter is based on the following paper: Poursaeidesfahani, A.; de Lange. M. F.; Khodadadian, F.; Dubbeldam , D.; Rigutto, M.; Nair, A.; Vlugt, T. J. H.; Product shape selectivity of MFI-type, MEL-type, and BEA-type zeolites in the catalytic hydroconversion of heptane, Journal of Catalysis, 2017, 353, 54-62.

### **4.1 Introduction**

In the previous chapters, the kinetic and thermodynamic properties of adsorption of hydrocarbons by zeolites and method to calculate these properties were discussed. This information can also be used to study various forms of shape selectivity and assessing their influences on the distribution of products in hydroconversion process. In this chapter, the zeolite based catalytic hydroconversion of heptane and product shape selectivity in particular are considered. Zeolite based catalysts are crucial to the production of fuels, lubricants and petrochemicals, in oil refining and, increasingly, in

gas to liquids (GTL) technology [9, 43, 44, 117]. As a key example, a very large and steadily increasing fraction of today's clean transportation fuels is produced through zeolite-catalyzed hydrocracking, with a global capacity of over 500 million tons per annum. Due to the industrial importance of this process, many studies focused on hydroconversion of linear alkanes by zeolite catalysts. These include investigating the influence of zeolite crystal size and activity [9, 43, 44], comparison of performance of different zeolite catalysts [10, 11, 45, 46], and the development of kinetic models [40, 47, 48]. The hydroconversion process of linear hydrocarbons can be seen as a chain of reactions [11, 39, 40, 44, 47, 118]. First, linear hydrocarbons are adsorbed and subsequently dehydrogenation occurs at the metal sites of the catalyst forming alkenes. These alkenes migrate to the acid sites where alkylcarbenium ions are formed through protonation. The alkylcarbenium ions can undergo isomerization and cracking. Finally, these ions are transferred to metal sites where they are transformed into alkanes via hydrogenation. Zeolite shape selectivity influences most of these steps and results in vastly different product distributions when different catalysts are used. There are basically three forms of shape selectivity [12, 41]: (1) Reactant shape selectivity: Adsorption and/or diffusion of (some of the) reactant molecules to the reaction sites is inhibited by the confinement created by the zeolite pores; (2) Transition state shape selectivity: Formation of some products is hindered by the shape of the zeolites pores simply because they are too large to fit inside the pore structure; (3) Product shape selectivity: Diffusion limitations prohibit desorption of some product molecules that are too bulky to diffuse sufficiently fast along the channels of the zeolite. If the reactants have limited mobility they will stay longer at the active sites and the probability for the consecutive reactions to take place and convert these molecules is increased [12, 41, 95, 119]. Due to the complexity of the reaction mechanism, it is particularly difficult to study the influence of different forms of shape selectivity on individual steps of the hydroconversion process. During the past decades, a significant number of studies tried to improve the understanding of the shape selective behaviour of zeolite catalysts in bifunctional conversion of alkanes [10, 45, 104, 120–122]. Whereas concepts of shape selectivity in zeolite catalysis have been very

useful in qualitatively explaining product distributions based on differences in pore geometry [10, 45] and in assisting catalyst development in a qualitative fashion, quantitative treatments of reaction kinetics in shape selective reactions allowing unambiguous interpretation of shape selectivity in terms of reactant selectivity, transition state, and product shape selectivity have been scarce [104, 123].

In this chapter, a quantitative treatment of competitive adsorption and diffusion of reactants and products is presented in a very relevant model reaction: the hydroisomerization/hydrocracking of n-heptane by three zeolite catalysts (BEA-type, MFI-type, and MEL-type zeolites). The results are combined with experimental observations and used to explain trends in the reaction kinetics, as a step towards a full quantitative treatment. In this chapter and following chapter, to simplify the assessment of this complex process it is assumed that alkanes and alkenes behave identically within a zeolite. It should be mentioned that diffusion of alkenes between the metal and acid sites might have an important effect on the shape selective behaviour of a zeolite [124].

This chapter is organized as follows. In section 4.2, molecular simulations methods and simulation details used to compute adsorption isotherms and free energy landscapes of reactants and product molecules are described. Experimental details are provided in section 4.3. The product distributions obtained with different catalysts and crystal sizes (for MFI-type) are discussed in details in section 4.4. Our main findings are summarized in section 4.5.

## 4.2 Simulations

The adsorption isotherms and free energy profiles of different heptane isomers are computed using force field based Monte Carlo Simulations. Adsorption isotherms show the strength of adsorption of different components and can be directly used to study transition state shape selectivity. Free energy profile shows the relative free energy of a molecule as a function of its location inside channels. The free energy landscape of reactant and

product molecules within the pores of the zeolite show the mobility of these molecules inside the zeolites can be used in more quantitative investigation of product shape selectivity of zeolite catalysts. The RASPA software package is used for the simulations [115, 116]. Heptane isomers are modelled using the TraPPE force field [125, 126]. A cutoff radius of 12 Å is applied for Lennard-Jones interactions and no tail corrections are used. The simulation box consists of  $2 \times 2 \times 1$  rigid unit cells for BEA-type zeolite and  $2 \times 2 \times 2$  for MFI-type and MEL-type zeolites with periodic boundary conditions. Zeolite structure were taken from the IZA database [53]. Adsorption isotherms are obtained by performing simulations in the grand-canonical ensemble at  $T = 227^\circ\text{C}$  and  $T = 303^\circ\text{C}$ . At each Monte Carlo step of grand-canonical simulations an attempt is made to either displace, regrow, rotate, insert, or remove a randomly chosen hydrocarbon chain. Hydrocarbon chains are regrown/inserted using the Configurational-Bias Monte Carlo (CBMC) technique [49, 127, 128]. The free energy profile of different heptane isomers along the channels of these structures at zero loading are computed from Monte Carlo simulations in the canonical ensemble. The length of the channels are divided into 1000 slices and the probability of being in each of these slices is calculated using only a single molecule. To compute the free energy profiles along a channel, the possible positions for the molecule are restricted to a single channel and trial moves attempting to move the molecule outside the channel are automatically rejected. The free energy of the molecule at each slice is given by:

$$F_i = -k_B T \ln p_i \quad (4.1)$$

where  $T$  is the temperature,  $k_B$  is the Boltzmann factor, and  $F_i$  and  $p_i$  are the average free energy at slice  $i$  and the probability of molecule being in slice  $i$ , respectively. The free energy profile can have very low local minima. When the molecule reaches these local minima, the energy penalty for the trial move that transfers the molecule out of local minima would be very high. Therefore, these translational trial moves are rarely accepted. This results in very poor sampling of the configurations in which the molecules is not in local minima. To improve the sampling, a biasing factor ( $\exp[w_i]$ )

is added to statistical weight for each slice [129]. These biasing factors are computed iteratively so that the observed probability for the molecule being in any of the slices is the same. In this case, the free energy of the molecule at each slice is given by:

$$F_i = -k_B T (\ln p_i - w_i) \quad (4.2)$$

The RASPA software is used for simulations [115, 116]. More details regarding the simulations techniques can be found in Chapter 3 and elsewhere [49, 95].

### 4.3 Experiments

Three samples of zeolite MFI-type were used with different crystal sizes: (1) a large-crystal material (denoted by MFI-bulk) with composition Si/Al=20 and BET surface area 373 m<sup>2</sup>/g described by Zhu et al. [130] ; (2) CBV-8014G, a commercial MFI-type (denoted by MFI-reference)with Si/Al= 40 and BET surface area of 425 m<sup>2</sup>/g consisting of aggregates of 40-150 nm primary crystals, obtained from Zeolyst International; (3) a MFI-type nanosheet material (denoted by MFI nanosheet) with Si/Al=20 and approximately 20 nm long and 4 nm thick sheets, described by Zhu et al. [130] (sample ZMS-5-F(3,20,423)). Samples of zeolite BEA-type with Si/Al=50 BET and a surface area of 700 m<sup>2</sup>/g and a crystal size of approximately 400 nm and of MEL-type with Si/Al=23 and BET surface area of 440 m<sup>2</sup>/g were also obtained from Zeolyst International. The crystal size of the MFI-bulk is much larger than the MFI nanosheet and MFI-reference and the crystal size of the MEL-type is sufficiently small and of the same order as BEA-type and MFI-reference. All three structure are formed by three-dimensional pore networks. The pore network of BEA-type zeolite is formed by 12-membered-rings straight pores while the pore networks of MFI-type and MEL-type zeolites contain 10-membered-rings.

Hydroconversion of heptane was carried out on Pd-loaded zeolites as described previously [131]. The dried support was shaped in a sieve fraction (177-420 μm) and loaded with 0.4 wt% Pd via incipient wetness impreg-

nation with a solution of appropriate concentration of  $\text{Pd}(\text{NH}_3)_4(\text{NO}_3)_2$ . The resulting materials were calcined at 300°C. Prior to testing, the catalysts were reduced at 320°C at 30 bar in flowing hydrogen. Hydroconversion of n-heptane was carried out at 30 bar using 300 mg of catalyst and H<sub>2</sub>/hydrocarbon ratio of 24 mol/mol. Experiments are conducted in a flow reactor and the flow rate of hydrogen is set to 25 ml min<sup>-1</sup>. To investigate various conversion levels (5% - 95%), the reaction temperature was lowered from 320°C to 200°C at a rate of 0.2 °C min<sup>-1</sup>, and products were analyzed by online GC.

## 4.4 Results and discussion

### 4.4.1 Reaction scheme and production of dibranched isomers

For all catalysts, normal C<sub>7</sub> is transformed into monobranched isomers (M), multibranched isomers (T), and cracking products (C). No secondary cracking is observed in this temperature range (200-320°C) and the only observed cracking products are i-C<sub>4</sub>, n-C<sub>4</sub>, and C<sub>3</sub>. The monobranched isomers mainly consist of methylhexanes. The fraction of ethylpentane in total monobranched isomers was lower than 5% for all catalysts and for all conversion levels. No traces of trimethylbutane were detected for MFI-type and MEL-type zeolites, and for BEA-type zeolite, less than 1% of heptane is converted to trimethylbutane. In Fig. 4.1, the yields of monobranched isomers (M) and multibranched isomers (T) and cracking products (C) are shown as a function of the conversion of n-C<sub>7</sub>. It can clearly be seen that the monobranched isomers are the primary reaction products and cracking products and multibranched isomers are secondary reaction products. Heptane isomers are consecutively cracked to either i-C<sub>4</sub> + C<sub>3</sub> or n-C<sub>4</sub> + C<sub>3</sub>. Cracking of monobranched isomers exclusively produces n-C<sub>4</sub> + C<sub>3</sub>, while cracking of most of the multibranched isomers (except 2,3-dimethylpentane) results in production of i-C<sub>4</sub> + C<sub>3</sub>. Therefore, the i-C<sub>4</sub>/n-C<sub>4</sub> ratio indicates whether monobranched or multibranched isomers are the main reactants in the cracking reactions. The i-C<sub>4</sub>/n-C<sub>4</sub> ratio is larger than 15 for all the

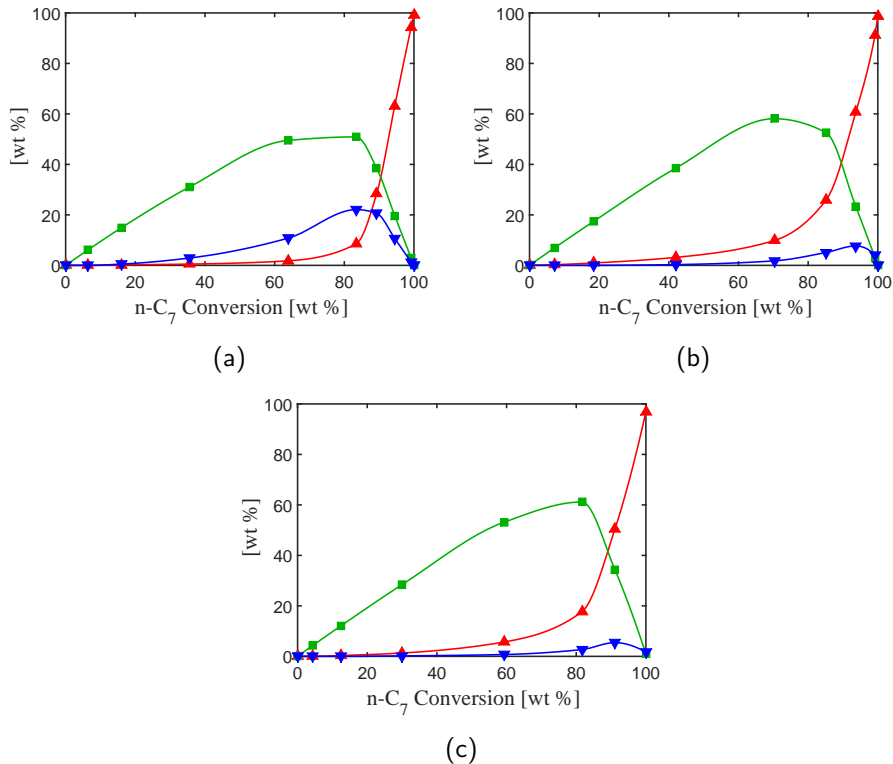


Figure 4.1: The experimental yields of monobranched isomers (green  $\square$ ) and multibranched isomers (blue  $\triangledown$ ) and cracking products (red  $\triangle$ ) are plotted as a function of the conversion of n-C<sub>7</sub> for (a) BEA, (b) MFI, and (c) MEL. Different conversion levels are obtained by changing the temperature of the reactor between 200°C and 320°C. Lines are guide to the eye.

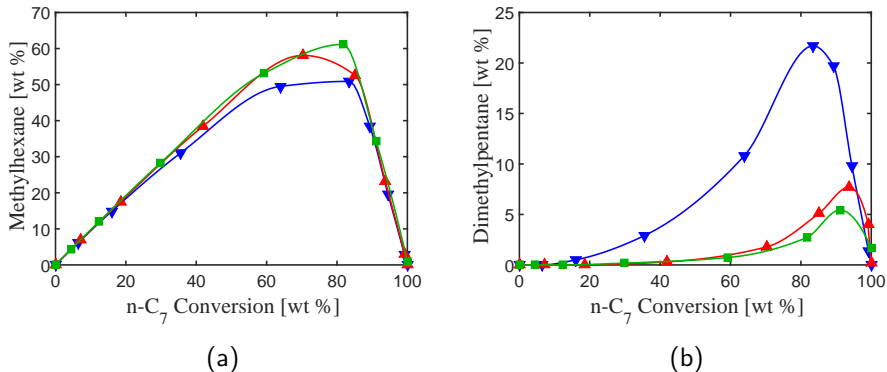


Figure 4.2: The experimental yields of (a) methylhexane and (b) dimethylpentane are plotted as a function of the conversion of n-C<sub>7</sub> for BEA (blue  $\bigtriangledown$ ), MFI (red  $\triangle$ ), and MEL (green  $\square$ ). Different conversion levels are obtained by changing the temperature of the reactor between 200°C and 320°C. Lines are a guide to the eye.

catalysts and for the entire conversion range. This shows that the main reaction scheme for the hydroconversion of n-C<sub>7</sub> on all three catalysts is:



Methylhexanes and dimethylpentanes have by far the highest share in the produced monobranched and multibranched isomers, respectively. In Figs. 4.2a and 4.2b, the yields of methylhexanes and dimethylpentanes for the three catalysts are compared for the entire range of n-C<sub>7</sub> conversion, respectively. The yield of methylhexanes for the three zeolites are almost the same, regardless of the conversion level. BEA-type zeolite produces slightly less methylhexanes compared to MFI-type and MEL-type zeolites in the conversion range (60-80%). However, these catalysts behave very differently while considering the production of dimethylpentanes (Fig. 4.2b). BEA-type zeolite has by far the highest rate of production for dimethylpentanes. The experimental data presented in Fig. 4.3 shows the ratio between the yield of dimethylpentanes and i-C<sub>4</sub>. Considering the main reaction scheme (Reaction.1), this ratio essentially mimics the ratio of dimethylpentanes

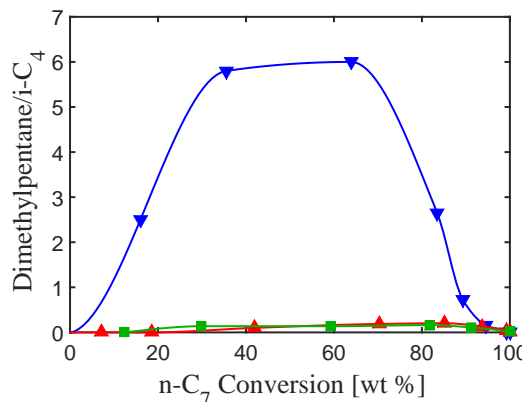


Figure 4.3: The ratio between the yield of dimethylpentanes and i-C<sub>4</sub> plotted as a function of the conversion of n-C<sub>7</sub> BEA (blue  $\triangledown$ ), MFI (red  $\triangle$ ), and MEL (green  $\square$ ). Different conversion levels are obtained by changing the temperature of the reactor between 200°C and 320°C. Lines are a guide to the eye.

that transferred to the gas phase to dimethylpentanes which are cracked to i-C<sub>4</sub> + C<sub>3</sub> and then transferred to the gas phase. It is clear that this ratio is always larger than one for BEA-type zeolite and larger than 3 in the conversion range (10-80%). This means that on average three out of four dimethylpentane molecules that are formed in BEA-type zeolite are transferred into the gas phase, and only one is cracked. This shows that most of the dimethylpentanes that are produced in BEA-type zeolite can leave the structure before undergoing cracking into i-C<sub>4</sub>. However, the ratio between the yield of dimethylpentanes and i-C<sub>4</sub> is always lower than one (around 0.1) for MFI-type and MEL-type zeolites. This means that on average nine out of ten dimethylpentane molecules that are formed in MFI-type and MEL-type zeolites are cracked and only one is transferred into the gas phase. This suggests that diffusion rate for dimethylpentane molecules is much higher in channels of BEA-type zeolite compared to that of MFI-type and MEL-type zeolites. To validate this argument, one should have knowledge on the diffusion of different heptane isomers within these three catalysts.

This is achieved by computing the free energy profiles of different heptane isomers along the channels of the three structures. MEL-type and BEA-type zeolites have only single type of straight channels in two perpendicular directions while MFI-type has two types of channels straight and zigzag in two perpendicular directions. In Fig. 4.4, the free energy profiles of different heptane isomers in the straight channels of MFI-type, MEL-type, and BEA-type zeolites are shown. When considering diffusion, only the relative free energies as a function of the position along the channels are important. Therefore, the free energy profiles shown in Fig. 4.4 are shifted in such a way that the minimum of free energy is always zero. The free energy barrier for diffusion can be defined as the difference between the maximum and minimum of the free energy profiles. These values are listed in Table 5.2. It is clear that there is almost no free energy barrier for diffusion of all heptane isomers in large pores of BEA-type zeolite (see Fig. 4.5). The free energy barriers of different heptane isomers in MFI-type and MEL-type zeolites are  $2\text{-methylhexane} \approx 3\text{-methylhexane} < 24\text{-dimethylpentane} < 23\text{-dimethylpentane} \ll 22\text{-dimethylpentane} \approx 33\text{-dimethylpentane}$ . Therefore, due to the absence of any considerable free energy barrier for diffusion of dimethylpentane molecules in BEA-type zeolite, most of dimethylpentane molecules can move to the gas phase before cracking. However, in MFI-type and MEL-type zeolites, dimethylpentane molecules must overcome significant free energy barriers before they can move to the gas phase. Therefore, most of the dimethylpentane molecules that are produced in MFI-type and MEL-type zeolites are trapped inside the zeolite and cannot diffuse to the gas phase. Dimethylpentane molecules are more likely to undergo cracking and form  $\text{i-C}_4 + \text{C}_3$  which can diffuse out of the zeolite much faster than dimethylpentane molecules. This also explains why BEA-type zeolite has a higher production rate for dimethylpentanes. The difference between BEA-type zeolite and the other two zeolites is that in BEA-type zeolite dimethylpentanes can move to the gas phase. Moreover, the channels of BEA-type zeolite are large enough so that dimethylpentane molecules can be formed almost anywhere inside the structure. However, dimethylpentane molecules can only fit within the intersections of MFI-type and MEL-type zeolites [132] (see Fig. 4.5). As a result, in the case of BEA-type zeolite,

more dimethylpentane molecules are produced and more methylhexanes are consumed compared to the cases of MFI-type and MEL-type zeolites. Therefore, as in the case in Fig. 4.2a, one would expect to have lower concentration of monobranched isomers when BEA-type zeolite is used as a catalyst.

#### 4.4.2 Distribution of dibranched isomers

Dimethylpentanes with geminal methyl groups (22,33-dimethylpentane) have very high free energy barriers for diffusion in the channels of MFI-type and MEL-type zeolites (see Table 5.2 and Fig. 4.4). This suggests that dimethylpentanes with the geminal methyl groups can only fit within the intersections of the two channels (where free energy is minimal). Hence, it is almost impossible for these molecules to move to the gas phase. Therefore, they are trapped inside the intersections until they are cracked. Among all dimethylpentanes, 24-dimethylpentane has the lowest free energy barrier for diffusion. The free energy barrier for the diffusion of 24-dimethylpentane is closer to that of the methylhexanes than to the other dimethylpentanes. Therefore, it is expected that the yield of dimethylpentanes obtained from MFI-type and MEL-type zeolites predominantly consists of 24-dimethylpentane. The yields of different dimethylpentane isomers as a function of the conversion of n-C<sub>7</sub> for the three structures are shown in Fig. 4.6.

It can be seen that 24-dimethylpentane is the most produced dimethylpentane on MFI-type and MEL-type zeolites, followed by 23-dimethylpentane. This is exactly what is expected from the analysis of the free energy profiles. The fastest diffusing dimethylpentane (the one with the lowest free energy barrier) has the largest share in the total production of dimethylpentanes. As shown in Fig. 4.4 and Table 5.2, free energy barriers of all heptane isomers are higher and the differences between them are more significant in the straight pores of MEL-type compared to straight pores of MFI-type. This can explain the higher yield of dimethylpentanes on MFI-type. For BEA-type zeolite, 23-dimethylpentane has the highest yield among dimethylpentanes for the entire conversion range of n-C<sub>7</sub> (see Fig. 4.6). The yield of

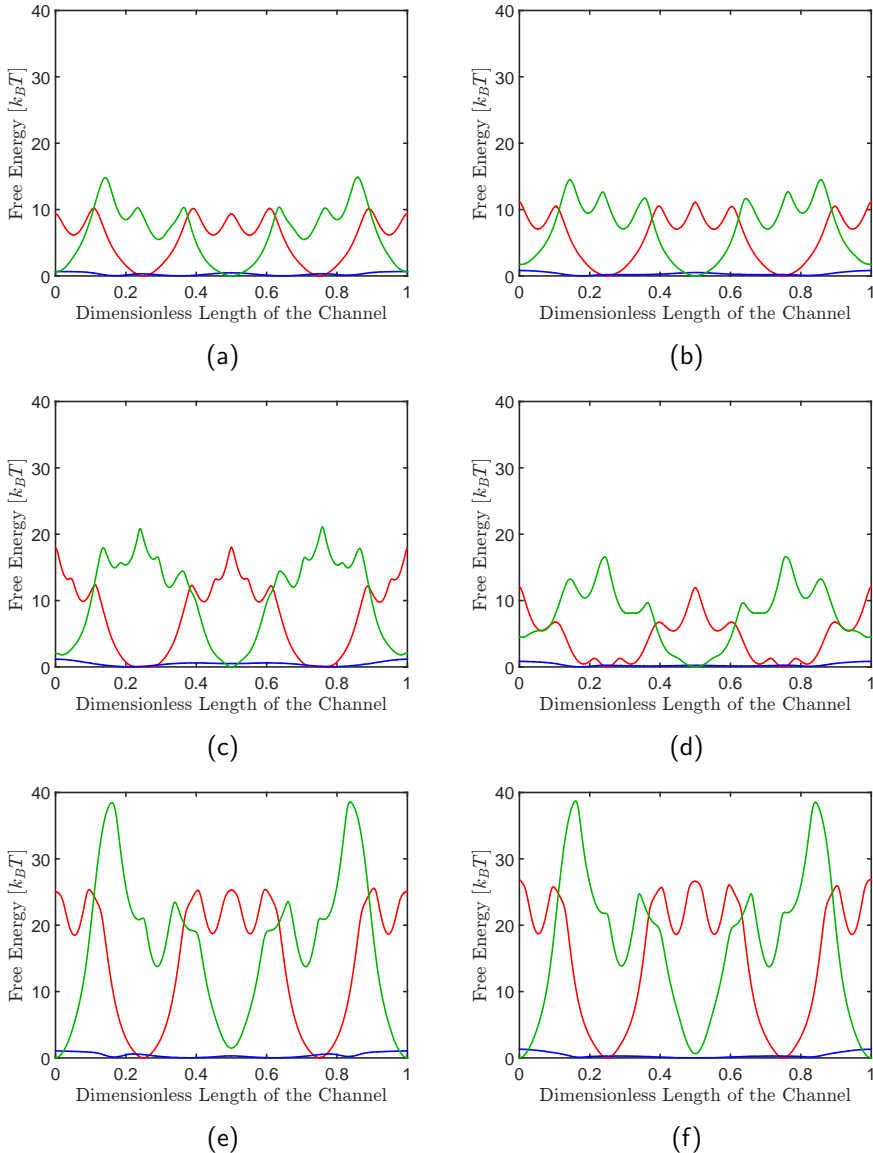


Figure 4.4: The free energy profiles of (a) 2-methylhexane, (b) 3-methylhexane, (c) 23-dimethylpentane, (d) 24-dimethylpentane, (e) 22-dimethylpentane, (f) 33-dimethylpentane at zero loading are plotted as a function of the position of the molecule in straight channels of for BEA (Blue), MFI (Red), and MEL (Green) at  $T = 227^\circ\text{C}$ . The free energy profiles are shifted in such a way that the minimum of free energy is always zero.

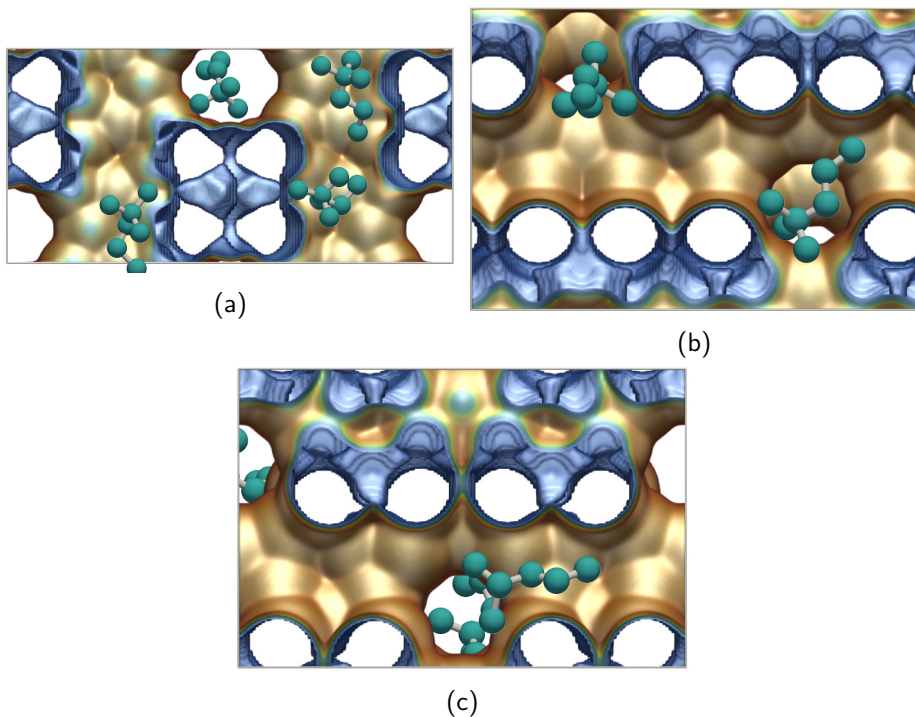


Figure 4.5: Visualization of 22-dimethylpentane molecules within the pore structure of zeolite (a) BEA, (b) MFI, and (c) MEL. 22-dimethylpentane molecules can be everywhere within the pore structure of BEA. However, in pore structures of MFI and MEL, 22-dimethylpentane molecules are mostly at the intersection and only very rarely at the middle of the channels.

Table 4.1: Free energy barriers for diffusion of different heptane isomers in straight channels of MFI, MEL, and BEA-type zeolites at zero loading and at 227°C, as computed by CBMC simulations.

Molecule	Free Energy Barrier/ [k <sub>B</sub> T]		
	BEA	MFI	MEL
2-Methylhexane	0.68	10.2	14.9
3-Methylhexane	0.82	11.1	14.5
23-Dimethylpentane	1.17	18.0	21.1
24-Dimethylpentane	0.85	12.0	16.6
22-Dimethylpentane	1.06	25.6	38.6
33-Dimethylpentane	1.32	26.8	38.7

22-dimethylpentane and 24-dimethylpentane are almost the same for all conversions and 33-dimethylpentane has always the lowest fraction among dimethylpentanes. Interestingly, the fraction of different dimethylpentanes in the total dimethylpentanes produced remains roughly constant and corresponds to the equilibrium distribution of dimethylpentanes in the gas phase. From the free energies of formation of different dimethylpentanes, one can compute the equilibrium constants for the methyl-shift reactions in the gas phase:

$$K_{\text{eq}} = \exp \left[ \frac{-\Delta G^\circ}{RT} \right] \quad (4.3)$$

where  $\Delta G^\circ$  is the Gibbs free energy of the reaction which is obtained by subtracting the Gibbs free energy of formation of products from those of reactants. The values for the Gibbs free energies of formation of heptane isomers reported by D. W. Scott [133] are used to compute the equilibrium constants for the methyl-shift reactions of dimethylpentanes in the gas phase. The equilibrium distribution of dimethylpentanes in the gas phase and the distribution of dimethylpentanes produced by BEA-type zeolite are shown in Table 4.2. As BEA-type zeolite imposes no free energy barrier for diffusion of any of the dimethylpentanes and the methyl-shift reaction are very fast compare to isomerization reactions [11, 44], the distribution

Table 4.2: Equilibrium distribution of dimethylpentanes in the gas phase and the distribution of dimethylpentanes produced by BEA-type zeolite. The equilibrium distribution in the gas phase is obtained from the free energies of formation of dimethylpentanes at the mean temperature of the experiments ( $260^{\circ}\text{C}$ ). The values for the Gibbs free energies of formation of heptane isomers reported by D. W. Scott [133] are used to compute the equilibrium distribution of dimethylpentanes in the gas phase. Numbers in brackets are uncertainties in the last digit, i.e., 0.25 (2) means  $0.25 \pm 0.02$ .

	Equilibrium (Gas phase)	Produced by BEA
22-dimethylpentane	0.25(2)	0.26(1)
24-dimethylpentane	0.24(2)	0.25(1)
23-dimethylpentane	0.35(2)	0.32(1)
33-dimethylpentane	0.17(2)	0.16(2)

of dimethylpentanes by BEA-type zeolite is equilibrium limited.

To investigate the influence of transition state shape selectivity, the adsorption isotherms of different dibranched isomers are studied. One should be cautious using equilibrium adsorption isotherms to study the transition-state shape selectivity. The main assumption here is that the transition-state and product have almost the same shape, size and interactions with the zeolite structure. For the isomerization reactions, this assumption is not far from reality [12, 41]. Dibranched molecules that fit better within the channels and intersections of a structure should have a higher loading. Those isomers with a lower loading fit more difficult inside the pore network of the zeolite and, according to transition state shape selectivity, have lower probability of formation [12, 41]. In Fig. 4.7, the adsorption isotherms of 23-dimethylpentane, 24-dimethylpentane, 22-dimethylpentane, and 33-dimethylpentane at  $T = 227^{\circ}\text{C}$  and  $T = 303^{\circ}\text{C}$  are shown for the three zeolite catalysts. For the entire pressure range, 24-dimethylpentane has the lowest loading in MFI-type (Fig. 4.7b), and still 24-dimethylpentane is the dibranched molecule that is preferentially produced. One can argue that a molecule which is weakly adsorbed by the catalyst has higher mobility compared to strongly adsorbed molecules and desorbs faster. As shown for MEL-type in Fig. 4.7c, 24-dimethylpentane has the highest loading at the pressure range of the experiments. However,

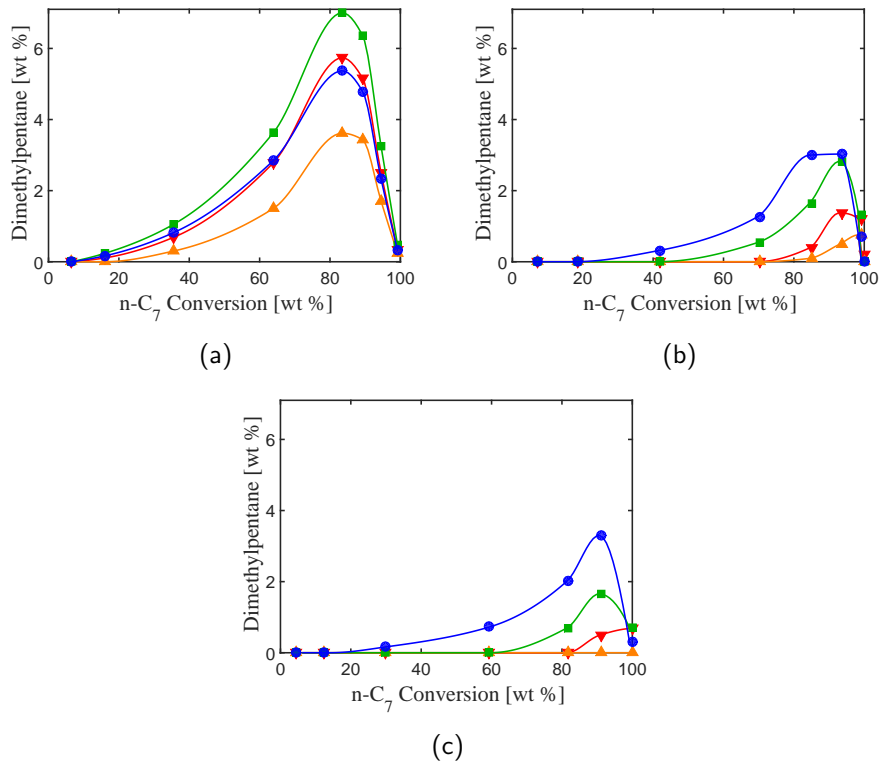


Figure 4.6: The experimental yields of dimethylpentanes are plotted as a function of the conversion of n-C<sub>7</sub> for (a) BEA, (b) MFI, and (c) MEL. 23-dimethylpentane (green □), 24-dimethylpentane (blue ○), 22-dimethylpentane (red ▽), and 33-dimethylpentane (orange △). Different conversion levels are obtained by changing the temperature of the reactor between 200°C and 320°C. Lines are a guide to the eye.

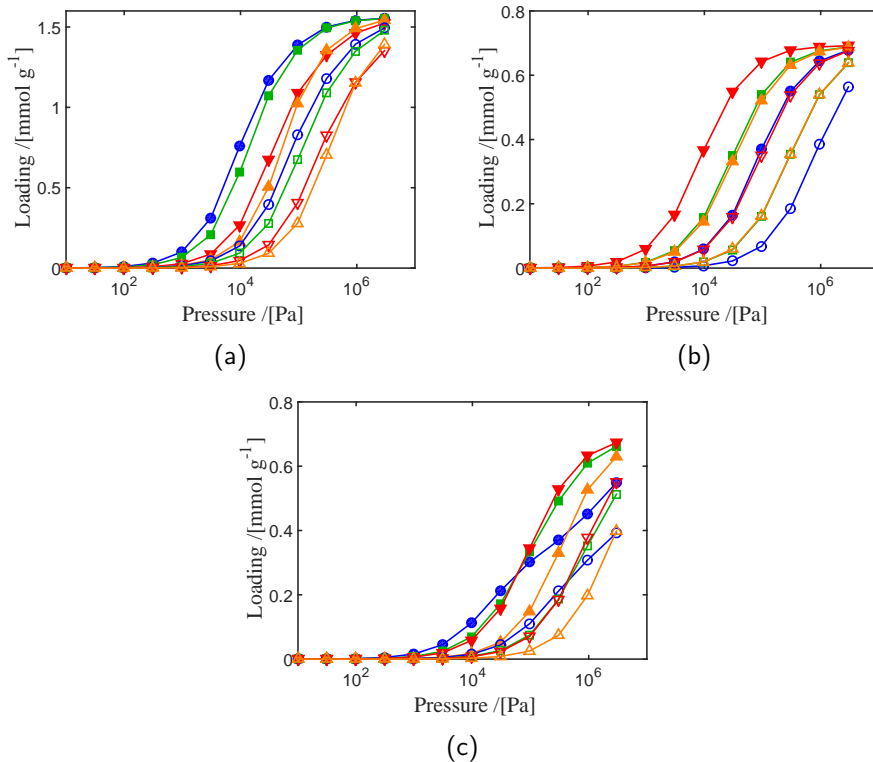


Figure 4.7: The adsorption isotherms of 23-dimethylpentane (green  $\square$ ), 24-dimethylpentane (blue  $\circ$ ), 22-dimethylpentane (red  $\triangledown$ ), and 33-dimethylpentane (orange  $\triangle$ ) at  $T = 227^\circ\text{C}$  (close symbols) and at  $T = 303^\circ\text{C}$  (open symbols) as computed with CBMC simulations. (a) BEA, (b) MFI, and (c) MEL. Lines are a guide to the eye.

this molecule is still produced with the highest concentration among all dimethylpentanes by MEL-type. While following the above argument, one would expect 24-dimethylpentane to have limited contribution in production of dimethylpentanes by MEL-type, due to the preferential adsorption of 24-dimethylpentane and consequently its lower tendency for desorption. Moreover, 22-dimethylpentane which is adsorbed preferentially by MFI-type and MEL-type zeolite has one of the lowest fractions in produced dimethylpentanes by these structures. This clearly shows that although the effect of adsorption strength can be interpreted in different ways, neither of these interpretations can explain the distribution of dimethylpentanes for these three catalysts. Therefore, transition state shape selectivity is not the underlying reason for the sharp difference between the distributions of dimethylpentanes in these three structures. The product shape selectivity can explain the difference between the distributions of dimethylpentanes very well. For MFI-type and MEL-type zeolites, the free energy barriers that different dimethylpentanes molecules need to overcome to reach the gas phase are significantly different. For these catalysts, the dibranched molecule that has to overcome lower diffusion barrier is produced with a higher yield. Channels of BEA-type zeolite are large enough that practically do not impose any free energy barrier for diffusion of any of the dibranched molecules. Therefore, in this case there is no product shape selectivity and the distributions of dimethylpentanes molecules can reach the equilibrium distribution in the gas phase.

#### 4.4.3 MFI-type with different crystal sizes

The observations from the previous subsections suggest that product shape selectivity is the dominant form of shape selectivity in distribution of dimethylpentanes obtained from conversion of n-C<sub>7</sub> by MFI-type. It is shown that dimethylpentanes have a limited mobility inside the pore network of MFI-type. Therefore, one would expect that by increasing the crystal size dimethylpentane molecules are forced to stay longer inside the structure and in proximity of active sites. This increases the probability of consecutive cracking reactions to take place and convert these molecules

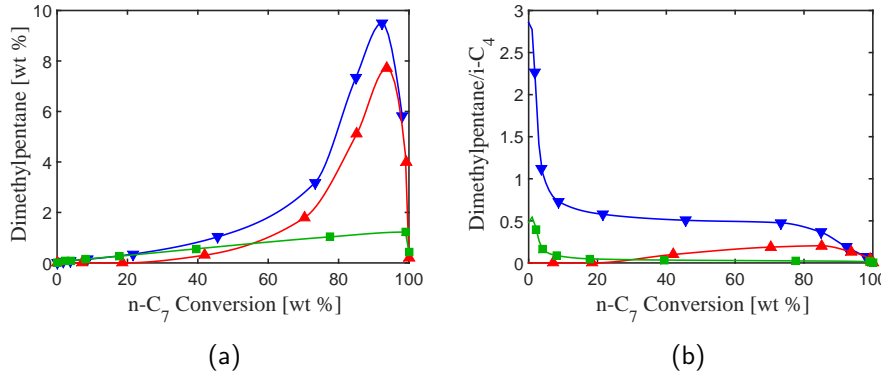


Figure 4.8: The experimental yields of (a) dimethylpentane and (b) the ratio between the yield of dimethylpentanes and  $i\text{-C}_4$  are plotted as a function of the conversion of  $n\text{-C}_7$  for MFI nanosheet (blue  $\nabla$ ), MFI reference (red  $\triangle$ ), and MFI bulk (green  $\square$ ). Different conversion levels are obtained by changing the temperature of the reactor between 200°C and 320°C. Lines are a guide to the eye.

to cracking products which can diffuse faster through the pores of MFI-type. Consequently, the yield of dimethylpentanes is expected to reduce by increasing the crystal size of MFI-type. To support the claims and arguments made in the previous sections, experiments have been conducted on three samples of zeolite MFI-type with different crystal sizes: (1) a large-crystal material (denoted by MFI-bulk) with composition Si/Al=20 and BET surface area 373 m<sup>2</sup>/g described by Zhu et al. [130]; (2) CBV-8014G, a commercial MFI-type with Si/Al= 40 and BET surface area of 425 m<sup>2</sup>/g consisting of aggregates of 40-150 nm primary crystals, obtained from Zeolyst International; (3) a MFI-type nanosheet material (denoted by MFI nanosheet) with Si/Al=20 and approximately 20 nm long and 4 nm thick sheets, described by Zhu et al. [130] (sample ZMS-5-F(3,20,423)). In Fig. 4.8, it can be seen that by increasing the crystal size, the production of dimethylpentanes and the ratio of produced dimethylpentanes to the cracking products decrease. Similar observations have been reported by other groups [134]. This shows that diffusion of dimethylpentanes (product shape selectivity) has significant influence on the product distribution of

n-C<sub>7</sub> conversion, when MFI-type is used as catalyst.

## 4.5 Conclusions

For all catalysts investigated in this study, n-C<sub>7</sub> is first converted into monobranced isomers. Monobranced isomers are further isomerized to dibranched isomers, and dibranched isomers are the main reactants for the cracking reactions. The free energy barriers for diffusion of different heptane isomers in MFI-type and MEL-type zeolites are ordered as 2-methylhexane ≈ 3-methylhexane < 24-dimethylpentane < 23-dimethylpentane ≪ 22-dimethylpentane ≈ 33-dimethylpentane. Significant free energy barriers for diffusion of dibranched isomers in MFI-type and MEL-type zeolites inhibit transfer of these molecules to the gas phase. Therefore, most of the formed dibranched isomers remain inside the zeolite until they are cracked and fast diffusing cracking products are transferred to the gas phase. For MFI-type and MEL-type zeolites, the dibranched molecule that has to overcome lower diffusion barrier is produced with a higher yield. Clearly showing the importance of product shape selectivity for these catalysts, the shares of different dimethylpentane molecules in the total production of dibranched isomers are ordered as 24-dimethylpentane > 23-dimethylpentane ≫ 22-dimethylpentane ≈ 33-dimethylpentane. BEA-type zeolite catalyst showed the highest selectivity towards production of dibranched isomers. The free energy barriers computed for heptane isomers at zero loading show that all heptane isomers can diffuse through the large pores of BEA-type zeolite without encountering diffusion barriers. As BEA-type zeolite imposes no free energy barrier for diffusion of any of the dimethylpentanes, the distribution of dimethylpentanes by BEA-type zeolite is equilibrium limited. It can be concluded that product shape selectivity is the main source of sharp differences between the product distribution of BEA-type zeolite compared to MFI-type and MEL-type zeolites. The influence of product shape selectivity on distribution of dibranched products increases as the pore size decreases from almost no effect for BEA-type zeolite (equilibrium distribution) to completely dominant for MFI-type and MEL-type zeolites.

It should be mentioned that in reality alkenes (and not alkanes) are involved in the isomerization and cracking reactions catalyzed by zeolites. However, to simplify the models we did not distinguish between alkenes corresponding alkanes. However, the kinetics and thermodynamics of alkenes might also be important for better understanding of the catalytic hydroconversion of hydrocarbons.



## Chapter 5

# Catalytic Hydroconversion of Heptane Using Large Pore Zeolite Catalysts

This chapter is based on the following manuscript: Poursaeidesfahani, A.; Rigoutto, M.; Nair, N.; Dubbeldam, D.; Vlugt, T. J. H.; Experimental and Theoretical Study of Catalytic Hydroconversion of Heptane Using Large Pore Zeolite Catalysts, in preparation.

### 5.1 Introduction

In the previous chapter, product shape selectivity was identified as the most important form of shape selectivity for the studied systems (catalytic hydroconversion of heptane in MFI-, MEL-, and BEA-type zeolites). The main aims of this chapter are to (1) investigate the shape selective behaviour of zeolites in the absence of product shape selectivity; (2) introduce a model that can simulate the catalytic hydroconversion of heptane by large pore zeolites. In the catalytic hydroconversion of hydrocarbons, zeolites are used as bifunctional catalysts containing both Lewis metal sites and Brønsted acid

sites [135]. In the past decades, many studies are focused on hydroconversion processes [10, 45, 104, 120–122]. Studies strive for superior comprehension of isomerized and cracked product distribution through modeling to achieve desired product properties. Major types of reaction models are based on Lumping and Mechanistic approaches [135, 136]. Early studies of catalytic hydrocracking of complex feedstock were mostly focused on development of lumped kinetic models. In these models, feedstock is divided into pseudo-components known as 'lumps'. These lumps are formed of components on the basis of their boiling point range, degree of branching, carbon number, and molecular weight [48, 137–139]. To increase the accuracy of models, larger number of lumps were considered. The number of parameters to be estimated increases as the number of lumps increases leading to greater computational complexity [140]. Mechanistic models take into account the chemistry of individual components and reactions in a network. Adsorption data and identification of an appropriate reaction network are crucial inputs for these models [141, 142].

In this chapter, the entire reaction network for the hydroconversion of heptane is considered and all main alkanes are modelled explicitly. The reaction network is identified by analysing series of precise experiments and fundamental information regarding the adsorption and diffusion properties of reactants and products are obtained from molecular simulation [12, 33–37, 95, 132]. This chapter is organized as follows. In section 5.1, the reaction network and the key assumptions are explained. In section 5.2, details regarding the molecular simulations to compute adsorption isotherms and free energy barriers are explained. The equation used for the reaction rate and the justification of that are explained. The mathematical model used for modeling the hydroconversion process and its main assumptions are described. The estimation of reaction rates by fitting the model output to the experimental results is described as an optimization problem. Experimental details are provided in section 5.3. In section 5.4, our modeling results are compared with experimental observations. The product distributions obtained for different catalysts are discussed. Our findings are summarized in section 5.5.

## 5.2 Experiments

A sample of zeolite BEA with Si/Al=50 BET and a surface area of 700 m<sup>2</sup>/g and a crystal size of approximately 400 nm and of zeolite Y with Si/Al=23 and BET surface area of 440 m<sup>2</sup>/g were also obtained from Zeolyst International. Hydroconversion of heptane was carried out on Pd-loaded zeolites as described previously [131]. The dried support was shaped in a sieve fraction (177-420 µm) and loaded with 0.4 wt% Pd via incipient wetness impregnation with a solution of appropriate concentration of  $\text{Pd}(\text{NH}_3)_4(\text{NO}_3)_2$ . The resulting materials were calcined at 300°C. Prior to testing, the catalysts were reduced at 320°C at 30 bar in flowing hydrogen. The hydroconversion of n-heptane was carried out at 30 bar using 300 mg of catalyst and a H<sub>2</sub>/hydrocarbon ratio of 24 mol/mol. Experiments are conducted in a flow reactor, and the flow rate of hydrogen is set to 25 ml min<sup>-1</sup>. To investigate various conversion levels (5% - 95%), the reaction temperature was lowered from 320°C to 200°C at a rate of 0.2 °C min<sup>-1</sup>, and reaction products were analyzed by online Gas Chromatography.

## 5.3 Simulations

### 5.3.1 Adsorption isotherms

The adsorption isotherms and free energy profiles of heptane isomers are computed using force field based Monte Carlo Simulations in the grand-canonical ensemble [12, 36, 37]. The RASPA software package is used for the simulations [115, 116]. Heptane isomers are modeled using the TraPPE force field which contains intramolecular and intermolecular Lennard-Jones interactions, and intramolecular bond bending and torsion interactions [125, 126]. The TraPPE-zeo force field is used to model the interactions between the hydrocarbons and zeolites [143]. A cutoff radius of 12 Å is applied for Lennard-Jones interactions and no tail corrections are used. The simulation box consists of  $2 \times 2 \times 1$  rigid unit cells for BEA-type zeolite,  $1 \times 1 \times 1$  for FAU-type zeolite and  $3 \times 2 \times 2$  MRE-type zeolite with periodic boundary conditions. Zeolite structures were taken from the IZA database [53, 112].

Hydrocarbon chains are regrown/inserted using the Configurational-Bias Monte Carlo (CBMC) technique [49, 127, 128, 144]. For more details, the reader is referred to Refs. [49, 145, 146].

### 5.3.2 Reaction network

In previous studies, it has been shown that the lumped reaction scheme for the catalytic hydroconversion of C<sub>7</sub> is:



where M, D and C are referring to monobranched isomers, dibranched isomers and cracking products, respectively. To distinguish between different monobranched isomers, dibranched isomers, and cracking products, this simple reaction scheme should be refined. To identify the appropriate reaction network, the experimental product slate obtained for catalytic hydroconversion of heptane is studied. Considering Eq. 5.1, one can define conversion of monobranched isomers as:

$$X_{mC_6} = \frac{1 - [C_7] - [mC_6]}{1 - [C_7]} \quad (5.2)$$

In the compact notation used in this work, 2,3-dimethylpentane is denoted by 2,3 – dmC<sub>5</sub>, where dmC<sub>5</sub> indicates that the main branch is made of 5 carbon atoms with 2 additional methyl groups, and 2,3 show the positions of methyl groups. One can identify the primary dibranched isomer by looking at the distribution of the dibranched isomers as a function of conversion of monobranched isomers. This is shown in Fig. 5.1.

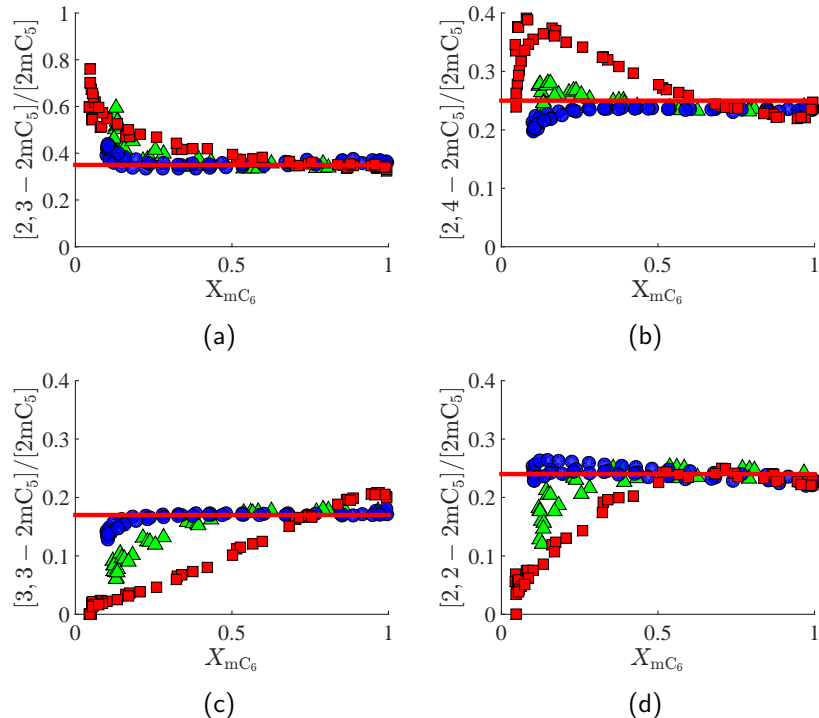


Figure 5.1: The experimental distribution of different dibranched isomers of heptane as a function of the conversion of monobranched isomers by zeolite BEA (green triangles), zeolite Y (Blue circles) and MRE-type zeolite (red squares): (a) 2,3-dmC<sub>5</sub>, (b) 2,4-dmC<sub>5</sub>, (3) 3,3-dmC<sub>5</sub> and (d) 2,2-dmC<sub>5</sub>.

As the conversion of monobranched isomers approach zero, the contribution of all dibranched isomers except 2,3-dmC<sub>5</sub> approach zero, regardless of the type of catalyst. Therefore, it can be concluded that for all catalysts considered in this study, 2,3-dmC<sub>5</sub> is the primary dibranched isomer formed from isomerization of monobranched isomers. It is assumed that all other dibranched isomers, namely 2,2-dmC<sub>5</sub>, 2,4-dmC<sub>5</sub>, 3,3-dmC<sub>5</sub>, are formed by the methyl shift reactions from 2,3-dmC<sub>5</sub>. As all zeolite catalysts considered in this study contain structures with only large pores ( $d_{\min} > 5.6 \text{ \AA}$ ),

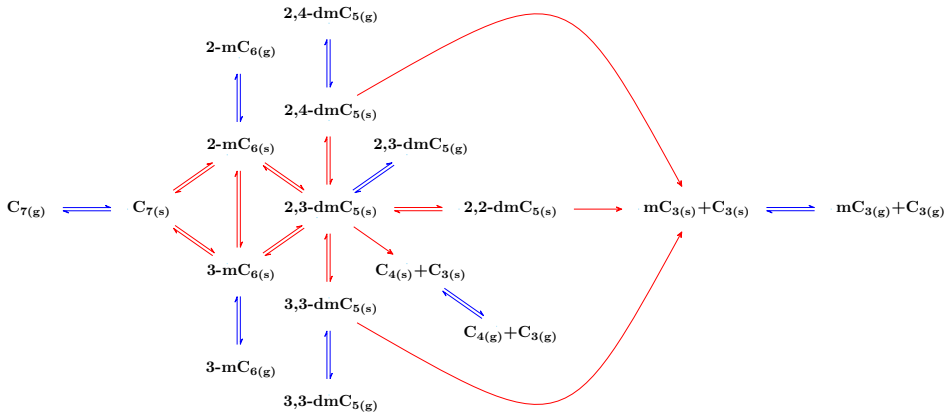


Figure 5.2: Reaction scheme for the catalytic hydroconversion of heptane by large pore zeolites. Blue arrows indicate steps that are in equilibrium and red arrows are used to show reaction that are not in equilibrium. Only the adsorption and desorption steps are assumed to be in equilibrium. Components in the gas phase and adsorbed phase are indicated by subscripts "g" and "s", respectively.

no significant mass transfer limitation for the transformation of molecules between the gas phase and the adsorbed phase is expected. Therefore, it is assumed that the adsorbed phase and gas phase are in equilibrium. The expanded reaction network for the catalytic hydroconversion of n-C<sub>7</sub> is shown in Fig. 5.2. In this reaction network, the formation of heptane isomers with more than two branches is neglected. This is supported by the very limited concentration of these components in the experimental product slate obtained for catalytic hydroconversion of heptane [147].

### 5.3.3 Rate equations

Three different categories are considered in the reaction network of this work: (1) isomerization reactions with changes in the degree of branching; (2) methyl-shift reactions; (3) cracking reactions. As discussed earlier, it is assumed that the adsorbed phase and the gas phase are in equilibrium. The concentrations of components in the adsorbed phase in equilibrium with

the gas phase are computed using a mixed Langmuir adsorption isotherm, and we have verified that for this system it yields identical results as Ideal Adsorption Solution Theory (IAST). At low temperatures where the conversion is low, zeolite catalysts are mainly loaded by the linear alkanes. As the conversion increases, the loading decreases and the composition of the adsorbed phase changes. Initially, branched alkanes and alkenes are formed. At higher conversions, shorter chain alkanes and alkenes are produced. The following rate equation is used to describe the individual isomerization and cracking reactions shown in Fig. 5.2

$$k_f = A \exp \left[ \frac{-E_a}{RT} \right] \quad (5.3)$$

where  $R$  is the universal gas constant,  $T$  is the absolute temperature,  $A$  is the frequency factor,  $k_f$  and  $E_a$  are the rate constant and activation energy. For reactions in each category, identical frequency factors  $A$  are used. The rate constant of the reverse reactions are given by:

$$k_b = A \exp \left[ \frac{-E_a + \Delta G^\circ}{RT} \right] \quad (5.4)$$

where  $\Delta G^\circ$  is the Gibbs free energy of reaction.

### 5.3.4 Gibbs free energy of reaction

The Gibbs free energy of the reaction can be obtained by subtracting the Gibbs free energy of formation of the reactants from those of the reaction products. The values for the Gibbs free energies of formation of heptane isomers as reported by D. W. Scott [133] are used to compute the Gibbs free energies of reaction for isomerization and methyl-shift reactions in the gas phase (see also section 4.4.2). These free energies are reported in Table 5.1. In the reaction network considered in this study, isomerization and methyl-shift reactions are taking place in the adsorbed phase and not in the gas phase. Therefore, the Gibbs free energies of these reaction in the adsorbed phase are of interest. To compute the the Gibbs free

Table 5.1: Gibbs free energies of formation of different heptane isomers at different temperatures as reported by D. W. Scott [133].

Molecule	Free Energy of formation/ [kJ mol <sup>-1</sup> ]			
	400K	500K	600K	700K
2-Methylhexane	72.7	143.9	216.7	290.4
3-Methylhexane	73.2	143.5	215.9	288.7
2,3-Dimethylpentane	75.7	147.3	220.5	295.0
2,4-Dimethylpentane	74.9	148.1	222.6	298.3
2,2-Dimethylpentane	73.2	146.9	222.2	298.3
3,3-Dimethylpentane	76.6	149.8	224.7	300.4

energies of isomerization and methyl-shift reactions, first, the equilibrium constants in the gas phase are calculated, see Eq. 4.3. Since the gas phase and adsorbed phase are assumed to be in equilibrium, mixed Langmuir adsorption isotherms are used to compute the equilibrium loading of all heptane isomers using the equilibrium distribution of these components in the gas phase. The temperature dependency is explicitly taken into account. Using the equilibrium distribution in the adsorbed phase, the Gibbs free energies of reaction in the adsorbed phase are calculated using Eq. 4.3.

### 5.3.5 Reactor model

Our reactor model is formed by the mas balance of the gas phase. Assuming steady state conditions, the material balance includes the spatial (axial) variations of concentrations of all components in the gas phase. Therefore, the mass balance can be written as

$$\begin{aligned} U \frac{dn_{i,z}}{dz} &= r_{i,z} \\ r_{i,z} &= \frac{1 - \varepsilon}{\varepsilon} \frac{V_{\text{reactor}}}{n} \rho_P r_{\text{ads},i,z} \end{aligned} \quad (5.5)$$

where  $U$  is the average velocity of the gas phase,  $n_{i,z}$  is the number of moles of component  $i$  at the slice in a distance  $z$  from the inlet of the reactor,  $r_{i,z}$

and  $r_{\text{ads},i,z}$  are the total production rates of component  $i$  in units of  $\text{mol s}^{-1}$  and  $\text{mol kg}^{-1} \text{ s}^{-1}$ , respectively.  $\varepsilon$  is the void fraction of the reactor,  $U$  is the average velocity of the gas,  $V_{\text{reactor}}$  is the volume of the reactor,  $n$  is number of grid points in the axial direction and  $\rho_p$  is the density of the catalyst. The mathematical model consists of a system of Ordinary Differential Equations (ODE) subject to following boundary conditions:

$$\begin{aligned} U(z) &= U_{\text{in}} \\ p_i(0) &= p_{i,\text{in}} \end{aligned} \tag{5.6}$$

As in all this reactions, the number of moles of the reactant and the number of the moles the reaction products are the same, the total number of moles remains unchanged. Therefore, it is assumed that the velocity remains constant along the reactor. At each grid point, it is assumed that the gas phase and the adsorbed phase are in equilibrium. Therefore, using the partial pressures of components in the gas phase, the loading of each component in the adsorbed phase follows from a mixed Langmuir adsorption isotherm. There are 10 different components present in the reactor, therefore, a system of 10 equations is solved to calculate the total production rate of each component in the corresponding grid point. The production rate is converted into units of  $\text{mol s}^{-1}$ . Using a first order upwind finite difference approximation, the gas phase composition in the next grid point is calculated. In total, a system of  $N = 10$  equations is solved  $n = 1000$  times, where  $N$  is the number of components and  $n$  is the number of grid points in the axial direction. By fitting the theoretical concentration of different product at different conditions to those obtained experimentally, the activation energies and frequency factors for different reactions are estimated. The Mean Sum of Squared of Residuals (MSSR) is the natural objective function for this optimization problem. The residual at each data point is defined as the difference between the experimental and

theoretical concentration of component  $i$ . The objective function equals

$$MSSR = \frac{\sum_{i=0}^N \sum_{j=0}^n (y_{i,j,out,model} - y_{i,j,out,exp})^2}{N \times n - n_P} \quad (5.7)$$

where  $N$  is the number of components,  $n$  is the number of experiments,  $n_P$  is the number of estimated parameters, and  $y_{i,j,out,model}$  and  $y_{i,j,out,exp}$  are the mole fractions of component  $i$  at experimental conditions  $j$  at the outlet of the reactor predicted by model and measured experimentally. The input parameters for the mathematical model include specifications of the reactor, the density and amount of catalyst placed inside the reactor, the gas phase composition, flow rate, and pressure of the reactor. In total, 12 activation energies and 3 frequency factors are estimated.

## 5.4 Results and discussion

As shown in parity diagrams in Fig. 5.3, an excellent fit of the experimental data is obtained for all components. Heptane, methylhexanes, and cracking products are observed with high mole fractions. Therefore, even small relative errors in estimation of mole fractions of these components will significantly affect the objective function. Excellent fits are obtained for these components. In our large pore structures, dimethylpentanes are produced with mole fractions up to 0.1. This is considerably lower than the mole fractions of methylhexanes. As a result, the fit for these components is slightly less accurate than those of methylhexanes. The optimal values of the fitting parameters are shown in Table 5.2. Clearly, the activation energy depends on the type of zeolite structure, although the fitted values are of similar magnitude. This is expected, because the structure influences both the adsorption equilibrium and the energy of the transition state. The frequency factors for the large-pore zeolite (FAU) are large for isomerization, while for the small-pore zeolite (MRE) these are large for cracking reactions. In BEA-type zeolite (intermediate pore size), the frequency factors for isomerization and cracking are very similar.

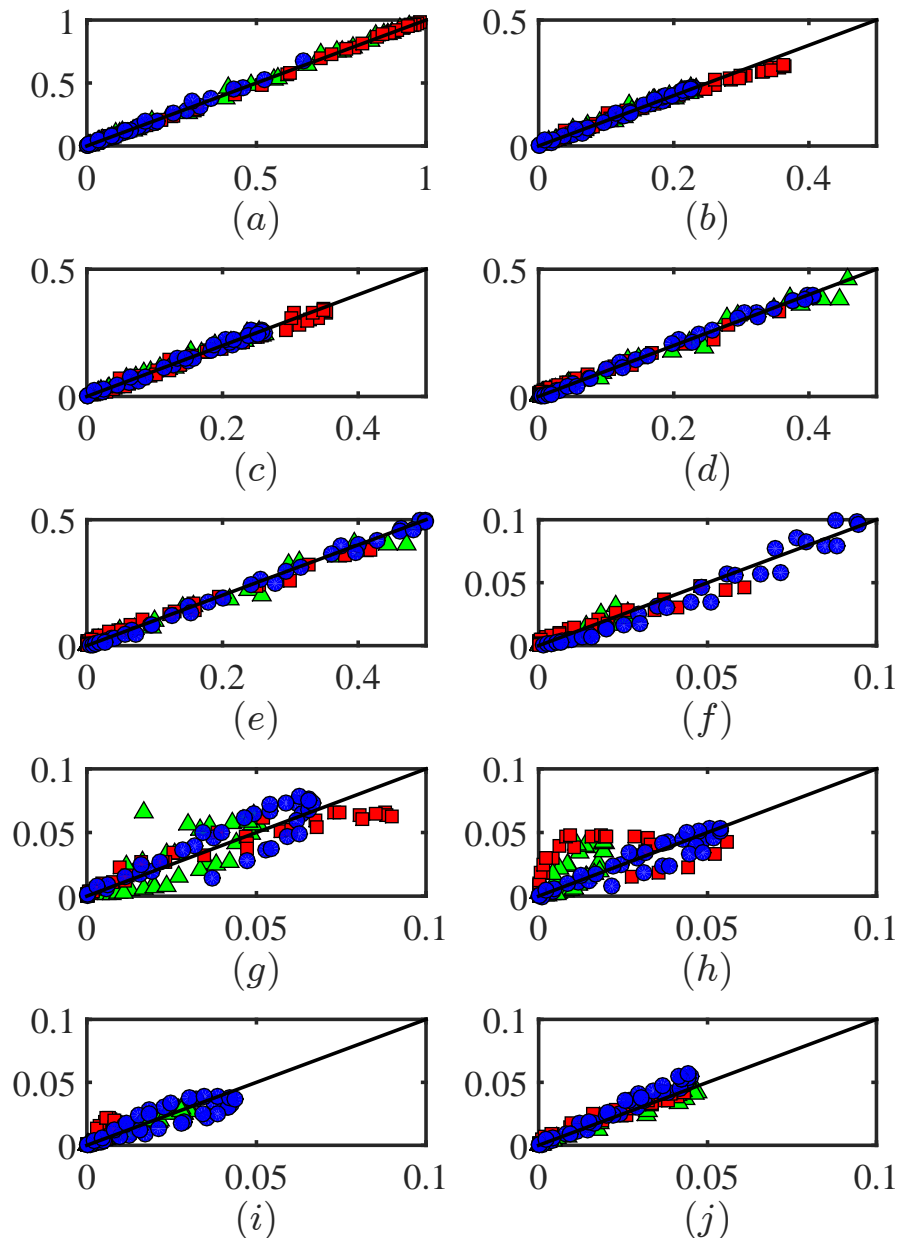


Figure 5.3: Parity plots experimental (vertical axis) and predicted (horizontal axis) mole fractions of heptane (a), 2-mC<sub>6</sub> (b), 3-mC<sub>6</sub> (c), mC<sub>3</sub> (d), C<sub>3</sub> (e), C<sub>4</sub> (f), 2,3-2mC<sub>5</sub> (g), 2,4-2mC<sub>5</sub> (h), 3,3-2mC<sub>5</sub> (i), and 2,2-2mC<sub>5</sub> (j) in the reactor outlet produced by zeolite BEA (green triangles), zeolite Y (blue circles) and by MRE zeolite (red squares).

Table 5.2: Optimal values for activation energies and frequency factors for different reactions in FAU, BEA, and MRE-type zeolites.

Reaction	BEA		MRE		FAU	
	$E_a^0/[\text{kJ mol}^{-1}]$	$A/[\text{s}^{-1}]$	$E_a^0/[\text{kJ mol}^{-1}]$	$A/[\text{s}^{-1}]$	$E_a^0/[\text{kJ mol}^{-1}]$	$A/[\text{s}^{-1}]$
$\text{C}_7(\text{s}) \rightleftharpoons 2\text{-mC}_6(\text{s})$	175.5	$7.58 \times 10^{11}$	149.0	$1.35 \times 10^{12}$	154.7	$1.78 \times 10^{13}$
$\text{C}_7(\text{s}) \rightleftharpoons 3\text{-mC}_6(\text{s})$	145.3	$7.58 \times 10^{11}$	150.6	$1.35 \times 10^{12}$	176.9	$1.78 \times 10^{13}$
$2\text{-mC}_6(\text{s}) \rightleftharpoons 2,3\text{-2mC}_5(\text{s})$	134.6	$7.58 \times 10^{11}$	158.5	$1.35 \times 10^{12}$	150.3	$1.78 \times 10^{13}$
$3\text{-mC}_6(\text{s}) \rightleftharpoons 2,3\text{-2mC}_5(\text{s})$	132.2	$7.58 \times 10^{11}$	179.1	$1.35 \times 10^{12}$	141.3	$1.78 \times 10^{13}$
$2\text{-mC}_6(\text{s}) \rightleftharpoons 3\text{-mC}_6(\text{s})$	157.0	$7.58 \times 10^{11}$	183.9	$1.35 \times 10^{12}$	200.6	$1.78 \times 10^{13}$
$2,3\text{-2mC}_5(\text{s}) \rightleftharpoons 2,2\text{-2mC}_5(\text{s})$	158.4	$3.71 \times 10^{12}$	138.5	$3.63 \times 10^{13}$	169.5	$7.25 \times 10^{12}$
$2,3\text{-2mC}_5(\text{s}) \rightleftharpoons 2,4\text{-2mC}_5(\text{s})$	154.8	$3.71 \times 10^{12}$	126.5	$3.63 \times 10^{13}$	167.3	$7.25 \times 10^{12}$
$2,3\text{-2mC}_5(\text{s}) \rightleftharpoons 3,3\text{-2mC}_5(\text{s})$	135.4	$3.71 \times 10^{12}$	111.1	$3.63 \times 10^{13}$	140.9	$7.25 \times 10^{12}$
$2,2\text{-2mC}_5(\text{s}) \rightarrow \text{mC}_3(\text{s}) + \text{C}_3(\text{s})$	156.8	$1.70 \times 10^{12}$	186.3	$8.70 \times 10^{13}$	175.2	$8.3 \times 10^{11}$
$2,4\text{-2mC}_5(\text{s}) \rightarrow \text{mC}_3(\text{s}) + \text{C}_3(\text{s})$	158.5	$1.70 \times 10^{12}$	190.0	$8.70 \times 10^{13}$	159.5	$8.3 \times 10^{11}$
$3,3\text{-2mC}_5(\text{s}) \rightarrow \text{mC}_3(\text{s}) + \text{C}_3(\text{s})$	140.8	$1.70 \times 10^{12}$	135.5	$8.70 \times 10^{13}$	149.6	$8.3 \times 10^{11}$
$2,3\text{-2mC}_5(\text{s}) \rightarrow \text{C}_3(\text{s}) + \text{C}_3(\text{s})$	162.2	$1.70 \times 10^{12}$	161.9	$8.70 \times 10^{13}$	159.6	$8.3 \times 10^{11}$

In Fig. 5.4, the conversion of methylhexanes as a function of the conversion of heptane is shown. There is an excellent agreement between the model and the experimental findings. BEA-type and FAU-type zeolites are very similar in terms of conversion of methylhexanes. For MRE-type zeolite, conversion of methylhexane stays low up to very high conversions of heptane. To investigate the underlying reason for this difference one can study the pore structure of these zeolites. The pores of BEA- and FAU-type zeolites are large enough that none of the heptane isomers experience any energy barrier for diffusion within the pore network of these structures [147]. However, the pores of MRE-type zeolite are slightly narrower compared to BEA-type zeolite. As a result, in the pores of MRE-type zeolite, only the bulkiest isomers (dimethylpentanes with geminal methyl groups) experience moderate energy barriers to reach the gas phase. These free energy barriers are listed in Table 5.3. Free energy barriers for diffusion of methylhexanes and dimethylpentanes with non-geminal methyl groups are almost the same while the free energy barriers for dimethylpentanes with geminal methyl groups are more than two times higher. Therefore, it can be argued that at lower conversion of heptane (lower temperatures), these components stay inside the channels of MRE-type zeolites. These molecules can either crack and convert into fast diffusing cracking products, or stay inside the zeolite structure. Since cracking does not start

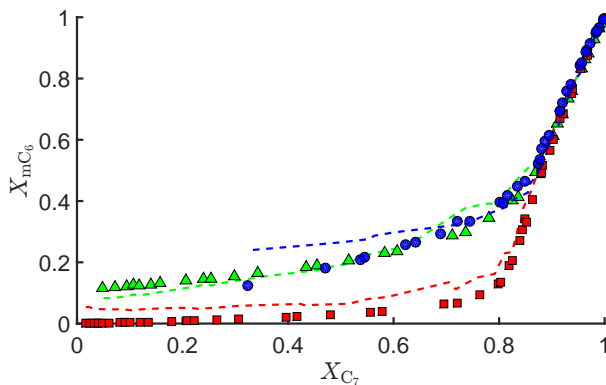


Figure 5.4: Caparison between the experimental (lines) and predicted conversion of methylhexanes as a function of the conversion of heptane in the reactor outlet produced by zeolite BEA (green triangles), zeolite Y (blue circles) and by MRE zeolite (red squares).

until high conversion of heptane (roughly 80%), up to this conversion level dimethylpentanes with geminal methyl groups will stay inside the zeolite structure. This will shift the methyl shift reactions and isomerization reactions in favour of methylhexanes and dimethylpentanes with non-geminal methyl groups. This results, in a lower conversion of methylhexanes and a higher fraction of dimethylpentanes with non-geminal methyl groups. This is supported by the experimental finding presented in Fig. 5.1. While for FAU- and BEA-type zeolites, the distribution of dimethylpentanes reaches the equilibrium level at very low conversion of methylhexane, for MRE-type zeolite the equilibrium between the dimethylpentanes is only reached after 50% conversion of methylhexane. It can also clearly be seen that at low conversions dimethylpentanes with geminal groups are not detected in the gas phase. As conversion increases (higher temperatures), the contribution of these component in the dimethylpentanes production increases. This indicates that at low temperature dimethylpentanes with geminal methyl groups, although produced, cannot overcome the free energy barrier for diffusion and reach the gas phase. As temperature increases, these molecules become more mobile and can reach the gas phase. It is shown in previous

Table 5.3: Free energy (Helmholtz) barriers for diffusion of different heptane isomers in straight channels of MFI, MEL, and MRE-type zeolites at zero loading and at 227°C, as computed by CBMC simulations. The length of the channels are divided into 1000 slices and the probability of being in each of these slices is calculated using only a single molecule. The molecule is restricted to a single channel and trial moves attempting to move the molecule outside the channel are automatically rejected [147].

Molecule	Free Energy Barrier/ [ $k_B T$ ]		
	MRE	MFI	MEL
2-Methylhexane	4.7	10.2	14.9
3-Methylhexane	3.9	11.1	14.5
2,3-Dimethylpentane	2.8	18.0	21.1
2,4-Dimethylpentane	3.8	12.0	16.6
2,2-Dimethylpentane	12.7	25.6	38.6
3,3-Dimethylpentane	9.1	26.8	38.7

chapter that for MFI and MEL-types of zeolites, due to diffusion limitations, 2,4-dimethylpentane is the main dibranched product for the catalytic hydroconversion of heptane. While for BEA-type zeolite, branched molecules are distributed according to the equilibrium distribution. The presence of large pores of BEA-type zeolite and, therefore, high mobility of all dibranched isomers within the pore network of BEA-type zeolite was identified as the underlying reason for the equilibrium distribution of dibranched isomers in BEA-type zeolite. In addition to BEA-type zeolite, two other large pore structures, one with larger pore size (FAU-type zeolite) and one with slightly narrower pores (MRE-type zeolite), are studied in this work. For BEA- and FAU-type zeolite, the distribution of dibranched is the same as what is estimated from the equilibrium distribution in the gas phase except for very low conversion levels where 2,3-dimethylpentane is produced preferentially. However, for MRE-type zeolite equilibrium and for conversion levels below 50%, 2,3-dimethylpentane has the highest contribution in production of dibranched isomers followed by 2,4-dimethylpentane. This behaviour can also be explained by the product shape selectivity. In MRE-type zeolite, 2,3-dimethylpentane and 2,4-dimethylpentane have to overcome much lower

free energy barriers compared to dimethylpentanes with geminal methyl groups. Therefore, at low conversion levels (low temperatures), these component can diffuse much faster within the pores of MRE-type zeolite and desorb into the gas phase. The free energy barriers for dimethylpentanes with geminal methyl groups are much higher than those of dimethylpentanes with non-geminal methyl groups, however, these values are still significantly lower than those experienced by the same molecules in MFI- and MEL-type zeolites. Therefore, these molecules are significantly more mobile within the pores of MRE-type zeolite compared to the pores of MFI- and MEL-type zeolites. As temperature increase, the mobility of these molecules improves and as a result contribution of dimethylpentanes with geminal methyl groups in total production of dibranched molecules increase until it reached the equilibrium around 50% conversion of methylhexanes. Considering the above discussion and data showed in Table 5.3, one can categorizes the free energy barriers between 0 to 5  $k_B T$  as low between 5 to 15  $k_B T$  as moderate, and above 15  $k_B T$  as high.

## 5.5 Conclusions

Three large pore catalyst are considered in this chapter. Dibranched molecules produced from catalytic hydroconversion of heptane using BEA-type zeolite are distributed according to the equilibrium distribution. Except for BEA-type zeolite, we considered a catalyst with a larger pore size (FAU-type zeolite) and a catalyst with a narrower pores (MRE-type zeolite). We showed that as the pore size increases the equilibrium distribution of dibranched molecules is reached at a lower conversion of heptane. For FAU-type zeolite, the equilibrium distribution is almost immediately reached as the first dibranched molecules are formed. For MRE-type zeolite, this is only achieved after 50% conversion of methylhexanes. A complete reaction network for the hydroconversion of heptane on large pore catalysts is identified. This is used as to simulate the catalytic hydroconversion of heptane in a packed bed. The reaction rates for different reactions are estimated by fitting the simulated results to an extended set of experimental data.

The excellent agreement between the modeling results and experimental data indicates that an appropriate reaction network and description of kinetics are used. It is important to note that the model presented here is a simplification of the actual experiments. Using thermodynamic data from the gas phase, and computed adsorption isotherms, we have separated the effect of confinement on adsorption and reaction, and found reaction rates that depend on the pore size. In smaller pores, cracking is favoured while in large-pore zeolites, isomerization is more preferential. This can be explained by size differences of the transition states. It appears that confinement influences both adsorption behaviour and the reaction rates. It is interesting to speculate whether or not this also implies a direct relation between the adsorption isotherm and the reaction rate. This could imply that adsorption and reaction may be lumped into a single (much simpler) model, at the expense of a clear physical interpretation.

# **Chapter 6**

# **Continuous Fractional Component Monte Carlo in the Gibbs Ensemble**

This chapter is based on the following papers: (1) Poursaeidesfahani, A.; Torres-Knoop, A.; Dubbeldam , D.; Vlugt, T. J. H., Direct free energy calculation in the continuous fractional component Gibbs ensemble: Journal of Chemical Theory and Computation, 2016, 12, 1481-1490; (2) Poursaeidesfahani, A.; Rahbari, A.; Torres-Knoop, A.; Dubbeldam , D.; Vlugt, T. J. H.; Computation of thermodynamic properties in the Continuous Fractional Component Monte Carlo Gibbs ensemble: Molecular Simulation, 2016, 43, 189-195.

## **6.1 Introduction**

In this part of this thesis, advanced simulation techniques are introduced to simulate dense fluids at the molecular scale. This can be used for simulating zeolite-based separation and catalytic production of branched hydrocarbons at industrial conditions. In general, the osmotic ensemble [148, 149], the grand-canonical ensemble [38, 150], Gibbs ensemble (GE) [151–

153], and the reaction ensemble [154–156] can be used for studying these processes. The GE and grand-canonical ensemble are based on the same concept (simulating chemical equilibrium by molecule exchanges between the two phases). Both ensembles can be used for the adsorption of hydrocarbons inside zeolites. Simulations in these ensembles can provide information regarding the adsorbed phase in equilibrium with a gas or liquid phase. In the GE, a separate simulation box is used to simulated explicitly the gas or liquid phase. In the grand-canonical ensemble, the gas phase is simulated implicitly using an equation of state. The GE and grand-canonical ensembles are designed to simulated an equilibrium between two phases. Therefore, in these simulations, the conditions of phase equilibria should be satisfied. One of these conditions is the equality of chemical potentials between the two phases for all the species in the systems. In practice, this condition is reached by sufficient number of molecule exchanges between the phases. Unfortunately, the acceptance probabilities for the molecule exchanges can be close to zero. This is typically the case when molecules are large or when densities or loading are high [38]. As mentioned in the previous chapters (sections 1.1 and 3.1), branched hydrocarbons are bulky and industrial separation and production of these molecules takes place at high loadings. Therefore, it is important to use advanced simulation that can increase the acceptance probability of the molecular exchanges. There are two classes of solutions to overcome the problem of low acceptance probabilities for molecule exchanges: methods based on the insertion of molecules in a single step such as Configurational-Bias Monte Carlo (CBMC) or related methods [144–146, 157, 158], and methods inspired by expanded-ensembles [159–161] such as the Continuous Fractional Component Monte Carlo (CFCMC) method developed by Shi and Maginn [54, 55]. The advantage of the latter approach is that molecules are not inserted in a single trial move such as in CBMC, but in a gradual way. Therefore, the method does not depend on the occurrence of spontaneous cavities in the system that have the same size as the exchanged molecule. CFCMC is frequently used for computing solubilities of various gases in Ionic Liquids [55, 162–168] and this method is often significantly more efficient than CBMC, even for small molecules such as CO<sub>2</sub> and CH<sub>4</sub> [169]. The CFCMC approach can also be combined

with Reaction Ensemble Monte Carlo [116, 154, 170, 171] to simulate the zeolite-based production of hydrocarbons at high loadings. In this chapter, an advanced simulation method based on the CFCMC approach is introduced to facilitate molecule exchanges in the GE. In the next chapter, a similar method is discussed for the reaction ensemble.

## 6.2 The Gibbs Ensemble

Monte Carlo simulation in the Gibbs Ensemble (GE), introduced in the 80s of the last century by Panagiotopoulos [151–153], is widely applied for simulating phase coexistence of pure components and mixtures [172–176]. Frenkel showed that the densities obtained for the two simulation boxes in GE are corresponding to the densities of two phases at equilibrium [38]. Smit and Frenkel also showed that it is possible to compute the chemical potential of the system at equilibrium from simulations in GE [177]. Equilibrium is achieved when the pressures and chemical potentials are equal in both simulation boxes [38]. The GE provides a straightforward route to determine accurate coexistence densities and critical parameters using relatively small system sizes [176]. In the Gibbs Ensemble version of CFCMC, the conventional GE is expanded with two fractional molecules per component, one in each simulation box [54, 55]. Interactions of the fractional molecule with the surrounding are scaled by a coupling parameter  $\lambda$ , such that  $\lambda = 0$  means no interactions with the surroundings (the fractional molecule is an ideal gas molecule), and  $\lambda = 1$  means full interactions with the surroundings (the fractional molecule has the same interactions as other molecules of the same component). The coupling parameters of fractional molecules in two boxes are constrained by  $\lambda_{\text{box } 1} + \lambda_{\text{box } 2} = 1$  [55]. In addition to conventional trial moves in the GE, attempts are made to change the coupling parameters, using  $\lambda_{n,\text{box } 1} = \lambda_{o,\text{box } 1} + \Delta\lambda$ . Here,  $n$  and  $o$  denote the new and old configurations, respectively. Due to the constraint  $\lambda_{\text{box } 1} + \lambda_{\text{box } 2} = 1$ , the coupling parameter of the fractional molecule in the other simulation box also changes according to  $\lambda_{n,\text{box } 2} = \lambda_{o,\text{box } 2} - \Delta\lambda$ . When  $\lambda_{n,\text{box } 1} > 1$  or  $\lambda_{n,\text{box } 1} < 0$ , molecule transfer between

the simulation boxes occurs. For more details, we refer the reader to the original publication by Shi and Maginn [55]. Although the CFCMC GE algorithm significantly facilitates the exchange of molecules between the simulation boxes, one cannot directly obtain chemical potentials, and hence no direct check for chemical equilibrium is possible. Moreover, due to the constraint  $\lambda_{\text{box } 1} + \lambda_{\text{box } 2} = 1$  the two fractional molecules have to adapt to their surrounding molecules simultaneously. This may reduce the efficiency of the method when the density of at least one of the phases is high.

In this chapter, an alternative formulation for CFCMC GE with only a single fractional molecule per component is introduced. As a proof of principle, our method is tested and validated for LJ particles and the TIP3P-Ew water model [178]. The reason to choose these simple systems is that conventional GE yields accurate results for coexistence densities and chemical potentials, so a detailed numerical comparison can be made. In the new method, the chemical potential of each box is directly obtained without using test particles and therefore chemical equilibrium between the two phases can be checked directly. We show analytically that the chemical potentials obtained are identical to those in the conventional GE, but no test particles are required and hence the approach will be efficient for dense fluids. Knowledge of the chemical potentials facilitates thermodynamic modeling using the simulation results (e.g. fugacity coefficients and activity coefficient follow directly from the simulations). In addition, the issue regarding how to compute average properties in the expanded ensemble is studied. The relevant equations for computing the pressures in the conventional GE, the CFCMC GE. [38], and the pressure corresponding to the conventional GE calculated in CFCMC GE are derived, Also, guidelines for computing averages corresponding to the conventional GE and computed in the CFCMC GE are presented. The pressures and densities of the two coexisting phases of LJ particles at various temperatures computed in the conventional GE and the CFCMC GE are presented. Our formulation of CFCMC GE is added to the RASPA software package [115, 116].

## 6.3 Methodology

In our new formulation of the CFCMC GE method, we consider a single component system consisting of  $N_T$  whole molecules. These molecules are indistinguishable and are referred to as whole molecules as they interact via the full unscaled interaction potential. The total volume  $V_T$  of the simulation boxes is fixed while the boxes can exchange volume. Molecules can be distributed between the two simulation boxes. In addition to the  $N_T$  whole molecules, there is a single fractional molecule present in the system that is distinguishable from the whole molecules. This fractional molecule can be located in either of the two simulation boxes (see Fig. 6.1). The interactions of the fractional molecule with the whole molecules are scaled with a coupling parameter  $\lambda \in [0, 1]$  (hence the name “fractional molecule”). For the LJ potentials it is convenient to scale interactions as [55]:

$$u_{\text{LJ}}(r) = \lambda 4\epsilon \left( \frac{1}{\left[ \frac{1}{2}(1-\lambda)^2 + \left(\frac{r}{\sigma}\right)^6 \right]^2} - \frac{1}{\left[ \frac{1}{2}(1-\lambda)^2 + \left(\frac{r}{\sigma}\right)^6 \right]} \right) \quad (6.1)$$

Electrostatic interactions are scaled according to [54, 55, 169]

$$u_{\text{Coul}}(r) = \begin{cases} r > 2A & \lambda^5 \frac{1}{4\pi\epsilon_0} \frac{q_i q_j}{r} \\ r \leq 2A & \lambda^5 \frac{1}{4\pi\epsilon_0} \frac{q_i q_j}{r+A(1-\lambda)} \end{cases} \quad (6.2)$$

where  $\epsilon_0$  is the dielectric constant in vacuum,  $q_i$  is the partial charge of atom  $i$ , and  $A = 0.5\text{\AA}$ . Note that other choices for scaling the interactions of fractional molecule are also possible [179–182].

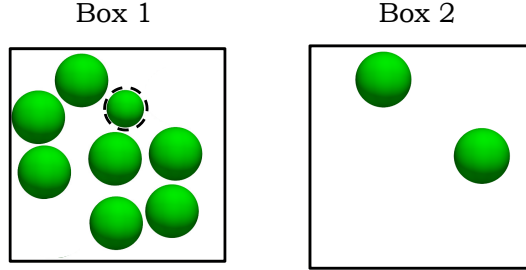


Figure 6.1: Schematic representation of serial GE/CFC for the combination of Gibbs ensemble with CFCMC. In serial GE/CFC, there is a single fractional molecule present in the system that is distinguishable from the whole molecules. This fractional molecule can be located in either of the two simulation boxes.

Following the guidelines presented in the work of Frenkel and Smit [38, 177] and Shi and Maginn [54, 55], the partition function of such a system is:

$$\begin{aligned}
 Q_{\text{CFCMC}} = & \frac{1}{\Lambda^{3(N_T+1)} (N_T)!} \sum_{i=1}^2 \sum_{N_1=0}^{N_T} \int_0^1 d\lambda \int_0^{V_T} dV_1 V_1^{N_1+\delta_{i,1}} (V_T - V_1)^{N_T-N_1+\delta_{i,2}} \\
 & \frac{(N_T)!}{(N_1)! (N_T - N_1)!} \times \int ds^{N_1} \exp[-\beta U_{\text{int},1}(s^{N_1})] \\
 & \int ds^{N_T-N_1} \exp[-\beta U_{\text{int},2}(s^{N_T-N_1})] \times \\
 & \left( \delta_{i,1} \int ds_{\text{frac}}^1 \exp[-\beta U_{\text{frac},1}(s_{\text{frac}}^1, s^{N_1}, \lambda)] + \right. \\
 & \left. \delta_{i,2} \int ds_{\text{frac}}^2 \exp[-\beta U_{\text{frac},2}(s_{\text{frac}}^2, s^{N_T-N_1}, \lambda)] \right)
 \end{aligned} \quad (6.3)$$

in which  $\beta = 1/(k_B T)$  and  $\Lambda$  is the thermal wavelength. The parameter  $i$  indicates the box in which the fractional molecule is located.  $U_{\text{int},i}$  indicates the energy of the indistinguishable whole molecules in box  $i$ , and  $U_{\text{frac},i}$  indicates the interaction energy of the fractional molecule in box  $i$  with the indistinguishable (whole) molecules in box  $i$ . The scaled coordinates

of molecules are indicated by the symbol  $s$ . The function  $\delta_{i,j}$  equals 1 when  $i = j$  and zero otherwise. As the fractional molecule can be located in either of the simulation boxes, we need to consider both possibilities in Eq. 6.3. In principle, one could reformulate the partition function with more than one fractional molecule per component. This increases the number of combinations in the last term of Eq. 6.3 and therefore this is not considered here.

In MC simulation in the GE ensemble, we have 3 different categories of trial moves: displacement of a randomly selected molecule (including the fractional molecule), volume changes (in such a way that the total volume  $V_T$  is conserved), and molecule exchanges between the simulation boxes. It is trivial to show that the acceptance rule for molecule displacements is the same as in the conventional GE [38, 183]. For volume changes, one should take care that the fractional molecule is taken into account. From Eq. 6.3, it immediately follows that the acceptance criterion for random volume changes equals [38]

$$\text{acc}(o \rightarrow n) = \min \left( 1, \frac{(V_1^n)^{N_1 + \delta_{i,1}} (V_T - V_1^n)^{N_T - N_1 + \delta_{i,2}}}{(V_1^o)^{N_1 + \delta_{i,1}} (V_T - V_1^o)^{N_T - N_1 + \delta_{i,2}}} \exp [-\beta \Delta U] \right) \quad (6.4)$$

in which  $\Delta U$  is the total energy change resulting from the trial move, and the symbols  $n$  and  $o$  are used to denote the new and old configurations, respectively. An extended derivation for the chemical potentials of different components in a mixture is shown in Appendix 2. For ergodic sampling of the ensemble of Eq. 6.3, three different types of trial moves are devised for exchanging molecules (that are schematically illustrated in Figs. 6.2 to 6.4). Changing the parameter  $\lambda$  by adding a uniformly distributed random value from the interval  $[-\Delta\lambda, \Delta\lambda]$ , while the fractional molecule stays in the same simulation box at the same position (see Fig. 6.2). Assume here that the fractional molecule is in box 1 (the resulting acceptance rule when the fractional molecule is in the other box is similar). As the parameter  $\lambda$  is constrained to the interval between 0 and 1, trial moves that take  $\lambda$  outside this range are automatically rejected.

The probabilities for the system to be in the old ( $o$ ) and new ( $n$ ) configurations are respectively

$$\begin{aligned} p_o &= \frac{1}{Q_{\text{CFCMC}}} \frac{1}{\Lambda^{3(N_T+1)} (N_T)!} V_1^{N_1+1} (V_T - V_1)^{N_T - N_1} \frac{(N_T)!}{(N_1)! (N_T - N_1)!} \times \\ &\quad \exp[-\beta U_{\text{int},1}(s^{N_1})] \exp[-\beta U_{\text{int},2}(s^{N_T - N_1})] \exp[-\beta U_{\text{frac},1}(s_{\text{frac}}, s^{N_1}, \lambda_o)] \\ p_n &= \frac{1}{Q_{\text{CFCMC}}} \frac{1}{\Lambda^{3(N_T+1)} (N_T)!} V_1^{N_1+1} (V_T - V_1)^{N_T - N_1} \frac{(N_T)!}{(N_1)! (N_T - N_1)!} \times \\ &\quad \exp[-\beta U_{\text{int},1}(s^{N_1})] \exp[-\beta U_{\text{int},2}(s^{N_T - N_1})] \exp[-\beta U_{\text{frac},1}(s_{\text{frac}}, s^{N_1}, \lambda_n)] \end{aligned} \quad (6.5)$$

in which  $\lambda_n$  is the new value of the coupling parameter and  $\lambda_o$  is the old one. From this it follows that the ratio of these probabilities equals

$$\frac{p_n}{p_o} = \exp \left[ -\beta (U_{\text{frac},1}(s_{\text{frac}}, s^{N_1}, \lambda_n) - U_{\text{frac},1}(s_{\text{frac}}, s^{N_1}, \lambda_o)) \right] \quad (6.6)$$

and therefore the acceptance rule reduces to the conventional Metropolis acceptance rule [38, 183]

$$\begin{aligned} \text{acc}(o \rightarrow n) &= \min \left( 1, \exp \left[ -\beta (U_{\text{frac},1}(s_{\text{frac}}, s^{N_1}, \lambda_n) - U_{\text{frac},1}(s_{\text{frac}}, s^{N_1}, \lambda_o)) \right] \right) \\ &= \min \left( 1, \exp [-\beta \Delta U] \right) \end{aligned} \quad (6.7)$$

in which  $\Delta U$  is the energy change resulting from the trial move. It is important to note that the maximum change in  $\lambda$  (denoted by  $\Delta\lambda$ ) can be chosen differently for each simulation box. The value of  $\Delta\lambda$  can be much larger in the gas phase than in the liquid phase.

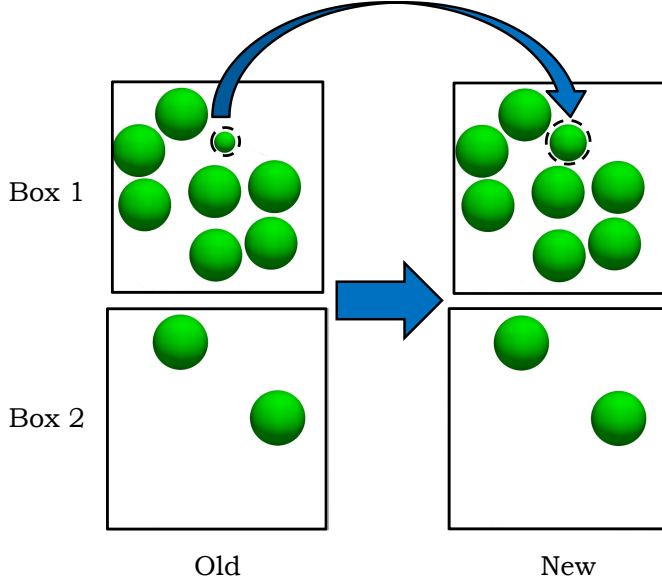


Figure 6.2: Schematic representation of the trial move attempting to change the coupling parameter  $\lambda$  while the fractional molecule stays in the same simulation box. The dashed sphere represents fractional molecules. In this example, the interactions of the fractional molecule in box 1 are increased. These trial moves are accepted or rejected according to Eq. 6.7 (or Eq. 6.16 when a weight function is used).

Swapping the fractional molecule between the simulation boxes, while keeping the value of  $\lambda$  fixed (see Fig. 6.3). Assume that the fractional molecule is removed from its current position  $s_{\text{frac}}$  in box 1 and inserted at a random position  $s_{\text{frac}}^n$  in box 2. The probabilities to be in the old and new configuration are respectively:

$$\begin{aligned}
 p_o &= \frac{1}{Q_{\text{CFCMC}}} \frac{1}{\Lambda^{3(N_T+1)} (N_T)!} V_1^{N_1+1} (V_T - V_1)^{N_T - N_1} \frac{(N_T)!}{(N_1)! (N_T - N_1)!} \times \\
 &\quad \exp[-\beta U_{\text{int},1}(s^{N_1})] \exp[-\beta U_{\text{int},2}(s^{N_T-N_1})] \exp[-\beta U_{\text{frac},1}(s_{\text{frac}}, s^{N_1}, \lambda)] \\
 p_n &= \frac{1}{Q_{\text{CFCMC}}} \frac{1}{\Lambda^{3(N_T+1)} (N_T)!} V_1^{N_1} (V_T - V_1)^{N_T - N_1 + 1} \frac{(N_T)!}{(N_1)! (N_T - N_1)!} \times \\
 &\quad \exp[-\beta U_{\text{int},1}(s^{N_1})] \exp[-\beta U_{\text{int},2}(s^{N_T-N_1})] \exp[-\beta U_{\text{frac},2}(s_{\text{frac}}^n, s^{N_T-N_1}, \lambda)]
 \end{aligned} \tag{6.8}$$

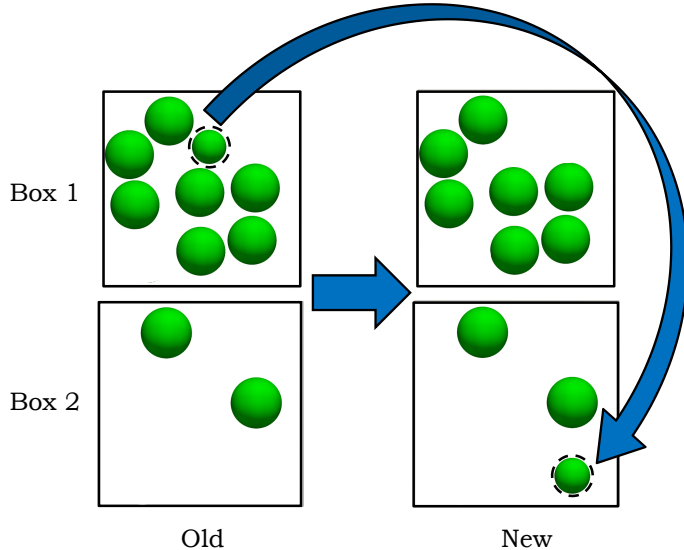


Figure 6.3: Schematic representation of the trial move attempting to swap the fractional molecule between the simulation boxes. The dashed sphere represents fractional molecules. In this example, the fractional molecule is moved from box 1 to a randomly selected position in box 2, while keeping the value of  $\lambda$  fixed. These trial moves are accepted or rejected according to Eq. 6.10 (or Eq. 6.17 when a weight function is used).

The ratio of these probabilities equals

$$\frac{p_n}{p_o} = \frac{V_T - V_1}{V_1} \exp \left[ -\beta \left( U_{\text{frac},2}(s_{\text{frac}}^n, s^{N_T - N_1}, \lambda) - U_{\text{frac},1}(s_{\text{frac}}, s^{N_1}, \lambda) \right) \right] \quad (6.9)$$

and therefore the acceptance probability equals

$$\begin{aligned} \text{acc}(o \rightarrow n) &= \min \left( 1, \frac{V_T - V_1}{V_1} \exp \left[ -\beta \left( U_{\text{frac},2}(s_{\text{frac}}^n, s^{N_T - N_1}, \lambda) - U_{\text{frac},1}(s_{\text{frac}}, s^{N_1}, \lambda) \right) \right] \right) \\ &= \min \left( 1, \frac{V_T - V_1}{V_1} \exp [-\beta \Delta U] \right) \end{aligned} \quad (6.10)$$

It is important to note that when  $\lambda$  is very small, this equation reduces to

$$\text{acc}(o \rightarrow n) = \min \left( 1, \frac{V_T - V_1}{V_1} \right) \quad (6.11)$$

This result is expected, as the distribution of an ideal gas molecule over two volumes equals the ratio of the two volumes. Changing the fractional molecule into a whole molecule while keeping its position fixed, and, simultaneously, changing a (randomly selected) whole molecule in the other simulation box into a fractional molecule while not changing the value of  $\lambda$  (see Fig. 6.4). Consider here the situation that the fractional molecule is initially located in box 1. This molecule is transformed into a whole molecule and a randomly selected molecule in box 2 is transformed into a fractional molecule. We can write for the probabilities for being in the old and new configuration respectively

$$\begin{aligned} p_o &= \frac{1}{Q_{\text{CFCMC}}} \frac{1}{\Lambda^{3(N_T+1)} (N_T)!} V_1^{N_1+1} (V_T - V_1)^{N_T-N_1} \\ &\quad \times \frac{(N_T)!}{(N_1)! (N_T - N_1)!} \exp[-\beta U_{\text{int},1}(s^{N_1})] \\ &\quad \exp[-\beta U_{\text{int},2}(s^{N_T-N_1})] \exp[-\beta U_{\text{frac},1}(s_{\text{frac}}^1, s^{N_1}, \lambda)] \\ p_n &= \frac{1}{Q_{\text{CFCMC}}} \frac{1}{\Lambda^{3(N_T+1)} (N_T)!} V_1^{N_1+1} (V_T - V_1)^{N_T-N_1} \\ &\quad \times \frac{(N_T)!}{(N_1 + 1)! (N_T - N_1 - 1)!} \exp[-\beta U_{\text{int},1}(s^{N_1+1})] \times \\ &\quad \exp[-\beta U_{\text{int},2}(s^{N_T-N_1-1})] \exp[-\beta U_{\text{frac},2}(s_{\text{frac}}^2, s^{N_T-N_1}, \lambda)] \end{aligned} \quad (6.12)$$

The ratio of these probabilities equals

$$\frac{p_n}{p_o} = \frac{N_T - N_1}{N_1 + 1} \exp[-\beta \Delta U] \quad (6.13)$$

in which  $\Delta U$  is the energy change of the two simulation boxes due to the

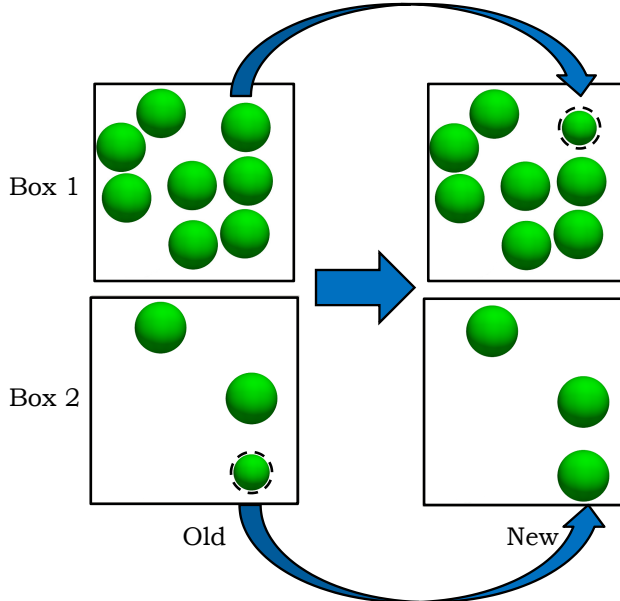


Figure 6.4: Schematic representation of the trial move attempting to change the fractional molecule into a whole molecule while keeping its position fixed, and, simultaneously, changing a (randomly selected) whole molecule in the other simulation box into a fractional molecule while not changing the value of  $\lambda$ . In this example, the fractional molecule (dashed sphere) in box 1 is exchanged with a whole molecule in box 2. These trial moves are accepted or rejected according to Eq. 6.14 (or Eq. 6.18 when a weight function is used).

trial move. The acceptance probability then becomes

$$\text{acc}(o \rightarrow n) = \min \left( 1, \frac{N_T - N_1}{N_1 + 1} \exp [-\beta \Delta U] \right) \quad (6.14)$$

For  $\lambda$  close to 1, the energy change  $\Delta U$  is small and hence the acceptance criterion reduces to

$$\text{acc}(o \rightarrow n) = \min \left( 1, \frac{N_T - N_1}{N_1 + 1} \right) \quad (6.15)$$

It is convenient to bias the probability distribution of  $\lambda$  in such a way that the sampled probability distributions  $p_i(\lambda)$  are flat and that the fractional molecule is equally likely to be in box 1 and box 2 (in principle by changing the applied bias one could tune this ratio to any desired value). In practice, this is realized by multiplying the statistical weight of each system state by a factor  $\exp[W(\lambda, i)]$  ( $i$  being the box in which the fractional molecule is located). It is important to note that as the fractional molecule can be located in two boxes, the weight function  $W(\lambda, i)$  is a two-dimensional function that depends both on  $\lambda$  and the box the fractional molecule is located in ( $i$ ). The acceptance criterion for changing the parameter  $\lambda$  (Fig. 6.2) then becomes

$$\text{acc}(o \rightarrow n) = \min(1, \exp[-\beta\Delta U + W(\lambda_n, i) - W(\lambda_o, i)]) \quad (6.16)$$

The acceptance criterion for swapping the fractional molecule (Fig. 6.3) becomes

$$\text{acc}(o \rightarrow n) = \min\left(1, \frac{V_T - V_1}{V_1} \exp[-\beta\Delta U + W(\lambda, 2) - W(\lambda, 1)]\right) \quad (6.17)$$

The acceptance criterion for the trial move of Fig. 6.4 changes to

$$\text{acc}(o \rightarrow n) = \min\left(1, \frac{N_T - N_1}{N_1 + 1} \exp[-\beta\Delta U + W(\lambda, 2) - W(\lambda, 1)]\right) \quad (6.18)$$

To obtain the correct Boltzmann averages, the ensemble average of an observable  $X$  should be computed using

$$\langle X \rangle_{\text{Boltzmann}} = \frac{\langle X \exp[-W(\lambda, i)] \rangle_{\text{modified}}}{\langle \exp[-W(\lambda, i)] \rangle_{\text{modified}}} \quad (6.19)$$

The weight function  $W(\lambda, i)$  can be determined iteratively [38] or by the Wang-Landau algorithm [184, 185]. The algorithm can be easily extended to mixtures [186] and the NPT version of the Gibbs ensemble [153]. For molecules with intramolecular degrees of freedom, the trial move of Fig. 6.3 can be performed by inserting the fractional molecule at a random position

with a random orientation in the new simulation box, while keeping the internal configuration of the molecule the same as in the old configuration. For ergodic sampling, trial moves that attempt to change the internal configuration of flexible molecules should be added to the MC scheme [38, 187, 188]. In Ref. [177], it is shown that the chemical potential of molecules in box  $i$  of the conventional GE equals

$$\mu_i = -k_B T \ln \left\langle \frac{V_i/\Lambda^3}{N_i + 1} \exp[-\beta \Delta U_i^+] \right\rangle_{\text{GE}} \quad (6.20)$$

in which  $\Delta U_i^+$  is the energy change when a molecule is inserted at a random position in box  $i$ . In Eq. 6.20, the reference state chemical potential ( $\mu_i^0$ ) is disregarded for simplicity.  $\mu_i^0$  is identical for both phases. Therefore, disregarding this value does not affect the condition of equality of chemical potentials. How to compute  $\mu_i^0$  is discussed in the next chapter and Appendix. We will show that the term  $\left\langle \frac{V_i/\Lambda^3}{N_i + 1} \exp[-\beta \Delta U_i^+] \right\rangle_{\text{GE}}$  corresponding to the conventional GE can be computed using simulation in the ensemble of Eq. 6.3, but without using test particles. This can be done as follows for box 1 (using the brackets  $\langle \dots \rangle$  to indicate averages in the ensemble of

Eq. 6.3, and  $\langle \cdots \rangle_{\text{GE}}$  to indicate averages in the conventional GE):

$$\begin{aligned}
 \left\langle \frac{\delta_{\lambda,0}\delta_{i,1}}{V_1/\Lambda^3} \right\rangle &= \frac{1}{Q_{\text{CFCMC}}} \frac{1}{\Lambda^{3(N_T+1)} (N_T)!} \sum_{N_1=0}^{N_T} \int_0^{V_T} dV_1 V_1^{N_1+1} (V_T - V_1)^{N_T - N_1} \\
 &\quad \frac{(N_T)!}{(N_1)! (N_T - N_1)!} \frac{1}{V_1/\Lambda^3} \int ds^{N_1} \exp[-\beta U_{\text{int},1}(s^{N_1})] \\
 &\quad \int ds^{N_T - N_1} \exp[-\beta U_{\text{int},2}(s^{N_T - N_1})] \\
 &= \frac{1}{Q_{\text{CFCMC}}} \frac{1}{\Lambda^{3N_T} (N_T)!} \sum_{N_1=0}^{N_T} \int_0^{V_T} dV_1 V_1^{N_1} (V_T - V_1)^{N_T - N_1} \\
 &\quad \frac{(N_T)!}{(N_1)! (N_T - N_1)!} \int ds^{N_1} \exp[-\beta U_{\text{int},1}(s^{N_1})] \\
 &\quad \int ds^{N_T - N_1} \exp[-\beta U_{\text{int},2}(s^{N_T - N_1})]
 \end{aligned} \tag{6.21}$$

$$\begin{aligned}
\left\langle \frac{\delta_{\lambda,1}\delta_{i,1}}{N_1+1} \right\rangle &= \frac{1}{Q_{\text{CFCMC}}} \frac{1}{\Lambda^{3(N_T+1)} (N_T)!} \sum_{N_1=0}^{N_T} \int_0^{V_T} dV_1 V_1^{N_1+1} (V_T - V_1)^{N_T - N_1} \\
&\quad \frac{(N_T)!}{(N_1)! (N_T - N_1)!} \frac{1}{N_1 + 1} \int ds^{N_1} \exp[-\beta U_{\text{int},1}(s^{N_1})] \\
&\quad \int ds^{N_T - N_1} \exp[-\beta U_{\text{int},2}(s^{N_T - N_1})] \\
&\quad \int ds_{\text{frac}}^1 \exp[-\beta U_{\text{frac},1}(s_{\text{frac}}^1, s^{N_1}, 1)] \\
&= \frac{1}{Q_{\text{CFCMC}}} \frac{1}{\Lambda^{3N_T} (N_T)!} \sum_{N_1=0}^{N_T} \int_0^{V_T} dV_1 V_1^{N_1} (V_T - V_1)^{N_T - N_1} \\
&\quad \frac{(N_T)!}{(N_1)! (N_T - N_1)!} \int ds^{N_1} \exp[-\beta U_{\text{int},1}(s^{N_1})] \\
&\quad \int ds^{N_T - N_1} \exp[-\beta U_{\text{int},2}(s^{N_T - N_1})] \\
&\quad \frac{V_1/\Lambda^3}{N_1 + 1} \int ds_{\text{frac}}^1 \exp[-\beta U_{\text{frac},1}(s_{\text{frac}}^1, s^{N_1}, 1)]
\end{aligned} \tag{6.22}$$

In these equations, the notations  $\langle \delta_{\lambda,1} \rangle$  and  $\langle \delta_{\lambda,0} \rangle$  are used for  $\lim_{\lambda \uparrow 1} p_1(\lambda)$  and  $\lim_{\lambda \downarrow 0} p_1(\lambda)$ , respectively. It is important to note that in the limit where the value of  $\lambda$  approaches one, the fractional molecule is still distinguishable from the whole molecules. As the partition function of the conventional GE equals [177]

$$\begin{aligned}
Q_{\text{GE}} &= \frac{1}{\Lambda^{3N_T} (N_T)!} \sum_{N_1=0}^{N_T} \int_0^{V_T} dV_1 V_1^{N_1} (V_T - V_1)^{N_T - N_1} \frac{(N_T)!}{(N_1)! (N_T - N_1)!} \times \\
&\quad \int ds^{N_1} \exp[-\beta U_{\text{int},1}(s^{N_1})] \int ds^{N_T - N_1} \exp[-\beta U_{\text{int},2}(s^{N_T - N_1})]
\end{aligned} \tag{6.23}$$

we have

$$\frac{\left\langle \frac{\delta_{\lambda,1}\delta_{i,1}}{N_1+1} \right\rangle}{\left\langle \frac{\delta_{\lambda,0}\delta_{i,1}}{V_1/\Lambda^3} \right\rangle} = \left\langle \frac{V_1/\Lambda^3}{N_1+1} \exp[-\beta\Delta U_i^+] \right\rangle_{\text{GE}} \quad (6.24)$$

and therefore

$$\mu_{\text{CFCMC},1} = -k_B T \ln \frac{\left\langle \frac{\delta_{\lambda,1}\delta_{i,1}}{N_1+1} \right\rangle}{\left\langle \frac{\delta_{\lambda,0}\delta_{i,1}}{V_1/\Lambda^3} \right\rangle} \quad (6.25)$$

This means that the chemical potential in box 1 for CFCMC GE simulations directly follows from the probabilities that  $\lambda$  approaches zero or one, and that the obtained result is identical to that in the conventional GE. For sufficiently large systems, the volume and number of whole molecules in box 1 is uncorrelated to the value of  $\lambda$  and hence Eq. 6.25 reduces to

$$\mu_{\text{CFCMC},1} \approx -k_B T \ln \frac{\left\langle \frac{\delta_{i,1}}{N_1+1} \right\rangle}{\left\langle \frac{\delta_{i,1}}{V_1/\Lambda^3} \right\rangle} - k_B T \ln \left( \frac{p_1(\lambda \uparrow 1)}{p_1(\lambda \downarrow 0)} \right) \quad (6.26)$$

$$\approx -k_B T \ln \left\langle \frac{V_1/\Lambda^3}{N_1+1} \right\rangle - k_B T \ln \left( \frac{p_1(\lambda \uparrow 1)}{p_1(\lambda \downarrow 0)} \right) \quad (6.27)$$

Eq. 6.27 is identical to the chemical potential obtained by thermodynamic integration in the canonical ensemble [171, 189, 190]. As  $p_i(\lambda)$  can be steep for the liquid phase in the region  $\lambda \approx 1$ , extrapolation to  $\lambda \rightarrow 1$  may be required. We found that in practice a linear extrapolation is sufficiently accurate.

For computing ensemble average energies and densities of the simulation boxes, it is not obvious how to deal with the fractional molecule. For example, consider a system with  $N_1$  molecules and the fractional molecule in box 1. One could define the instantaneous density as  $N_1/V_1$ , but also as  $(N_1 + \lambda)/V_1$  [54], or, in general as  $(N_1 + f(\lambda))/V_1$  in which  $f(\lambda)$  is an arbitrary function of  $\lambda$ . Similarly, for the average energy of the total system

we can compute the ensemble average of the quantity  $[U_{\text{int}} + g(\lambda)]$  in which  $g(\lambda)$  is a similar arbitrary function. At the first sight, logical choices may be to set  $g(\lambda) = U_{\text{frac}}$  or  $g(\lambda) = 0$ . In Refs. [32, 191], it is shown that it is best no to count the fractional molecules, i.e.  $f(\lambda) = 0$  and  $g(\lambda) = 0$ . This will also be used in chapter 7.

### 6.3.1 Computation of the pressure

In molecular simulations, the thermodynamic pressure is usually computed by averaging over the instantaneous microscopic pressures. In any NVT ensemble, the general expression for the thermodynamic pressure  $P$  is [183, 192, 193]

$$P = k_B T \left( \frac{\partial \ln Q}{\partial V} \right)_T \quad (6.28)$$

Considering the fact the Gibbs ensemble is a special case of the NVT ensemble, Eq. 6.28 is applicable to the GE and CFCMC GE. The pressure in the conventional GE is obtained by the conventional virial equation [38, 183]:

$$P_{\text{GE},j} = k_B T \left\langle \frac{N_j}{V_j} \right\rangle_{\text{GE}} + \left\langle \frac{\sum_{a < b} f_j(r_{ab,j}) r_{ab,j}}{3V_j} \right\rangle_{\text{GE}} \quad (6.29)$$

where  $r_{ab,j}$  and  $f_j(r_{ab,j})$  are the distance and the force acting between particles "a" and "b" in box "j" (assuming pair potentials). The first term on the right hand side of Eq. 6.29 is the ideal gas contribution and the second term is commonly known as the virial contribution [183]. The labeling of the boxes is arbitrary, therefore, the same equation is obtained for the other box. Since there is only one thermodynamic pressure for the system, the pressures of the two boxes are on average equal.

The thermodynamic pressure in the CFCMC GE is computed from [194]:

$$\begin{aligned} P_{\text{CFCMC},j} &= k_B T \left( \frac{\partial \ln Q_{\text{CFCMC}}}{\partial V_T} \right)_T \\ &= k_B T \left\langle \frac{N_j + \delta_{i,j}}{V_j} \right\rangle_{\text{CFCMC}} + \left\langle \frac{\sum_{a < b} f_j(r_{ab,j}) r_{ab,j}}{3V_j} \right\rangle_{\text{CFCMC}} \end{aligned} \quad (6.30)$$

In this equation, the contribution of the fractional molecule is included in the ideal gas part and in the virial part. The thermodynamic pressures in the CFCMC GE (Eq. 6.30) and conventional GE (Eq. 6.29) are clearly not identical. However, it is possible to compute the properties corresponding to the conventional GE while performing simulations in the CFCMC GE. One can write the following ensemble averages in CFCMC GE:

$$\begin{aligned} \left\langle \delta_{\lambda=0,i=1} \frac{1}{V_1} \right\rangle_{\text{CFCMC}} &= \frac{1}{Q_{\text{CFCMC}}} \frac{1}{\Lambda^{3(N_T+1)} (N_T)!} \sum_{N_1=0}^{N_T} \binom{N_T}{N_1} \int_0^{V_T} dV_1 V_1^{N_1} (V_T - V_1)^{N_T - N_1} \\ &\times \int ds^{N_1} \exp(-\beta U_{\text{int},1}(s^{N_1}, V_1)) \int ds^{N_T - N_1} \exp(-\beta U_{\text{int},2}(s^{N_T - N_1}, (V_T - V_1))) \end{aligned} \quad (6.31)$$

$$\begin{aligned} \left\langle \delta_{\lambda=0,i=1} \frac{N_1}{V_1^2} \right\rangle_{\text{CFCMC}} &= \frac{1}{Q_{\text{CFCMC}}} \frac{1}{\Lambda^{3(N_T+1)} (N_T)!} \sum_{N_1=0}^{N_T} \binom{N_T}{N_1} \int_0^{V_T} dV_1 V_1^{N_1} (V_T - V_1)^{N_T - N_1} \\ &\times \left( \frac{N_1}{V_1} \right) \int ds^{N_1} \exp(-\beta U_{\text{int},1}(s^{N_1}, V_1)) \int ds^{N_T - N_1} \exp(-\beta U_{\text{int},2}(s^{N_T - N_1}, (V_T - V_1))) \end{aligned} \quad (6.32)$$

Dividing Eq. 6.31 by Eq. 6.32, the  $Q_{\text{CFCMC}}$  terms cancel, and we obtain

$$\frac{\left\langle \delta_{\lambda=0,i=1} \frac{N_1}{V_1^2} \right\rangle_{\text{CFCMC}}}{\left\langle \delta_{\lambda=0,i=1} \frac{1}{V_1} \right\rangle_{\text{CFCMC}}} = \frac{\sum_{N_1=0}^{N_T} \binom{N_T}{N_1} \int_0^{V_T} dV_1 V_1^{N_1} (V_T - V_1)^{N_T - N_1} \left( \frac{N_1}{V_1} \right) \left[ \begin{array}{l} \int ds^{N_1} \exp(-\beta U_{\text{int},1}(s^{N_1}, V_1)) \\ \int ds^{N_T - N_1} \exp(-\beta U_{\text{int},2}(s^{N_T - N_1}, (V_T - V_1))) \end{array} \right]}{\sum_{N_1=0}^{N_T} \binom{N_T}{N_1} \int_0^{V_T} dV_1 V_1^{N_1} (V_T - V_1)^{N_T - N_1} \left[ \begin{array}{l} \int ds^{N_1} \exp(-\beta U_{\text{int},1}(s^{N_1}, V_1)) \\ \int ds^{N_T - N_1} \exp(-\beta U_{\text{int},2}(s^{N_T - N_1}, (V_T - V_1))) \end{array} \right]} \quad (6.33)$$

This yields the average density in the Gibbs ensemble

$$\frac{\left\langle \delta_{\lambda=0,i=1} \frac{N_1}{V_1^2} \right\rangle_{\text{CFCMC}}}{\left\langle \delta_{\lambda=0,i=1} \frac{1}{V_1} \right\rangle_{\text{CFCMC}}} = \left\langle \frac{N_1}{V_1} \right\rangle_{\text{GE}} \quad (6.34)$$

In general, for any thermodynamic property  $X_j$  in box  $j$ , we can calculate  $\langle X \rangle_{\text{GE}}$  from the CFCMC GE simulations. Repeating the same mathematical steps for any thermodynamic property property  $X$ , yields:

$$\langle X_j \rangle_{\text{GE}} = \frac{\left\langle \delta_{\lambda=0,i=j} \frac{X}{V_j} \right\rangle_{\text{CFCMC}}}{\left\langle \delta_{\lambda=0,i=j} \frac{1}{V_j} \right\rangle_{\text{CFCMC}}} \quad (6.35)$$

The pressure of box  $j$  corresponding to the conventional GE but computed in CFCMC GE becomes

$$P_{\text{GE},j}^* = k_B T \frac{\left\langle \delta_{\lambda=0,i=j} \frac{N_j}{V_j^2} \right\rangle_{\text{CFCMC}}}{\left\langle \delta_{\lambda=0,i=j} \frac{1}{V_j} \right\rangle_{\text{CFCMC}}} + \frac{\left\langle \delta_{\lambda=0,i=j} \frac{\sum_{a < b} f_j(r_{ab,j}) r_{ab,j}}{3V_j^2} \right\rangle_{\text{CFCMC}}}{\left\langle \delta_{\lambda=0,i=j} \frac{1}{V_j} \right\rangle_{\text{CFCMC}}} = P_{\text{GE},j} \quad (6.36)$$

The difficulty associated with computing  $P_{\text{GE},j}^*$  using Eq. 6.36 is that only the states in which the value of  $\lambda$  equals zero are contributing to the ensemble average. Therefore, long simulations may be required to obtain reliable pressures especially for the liquid phase. Assuming that there is no

correlation between the volume and the number of whole molecules, and also no correlation between the volume and the virial part of the pressure, Eq. 6.36 reduces to

$$P_{\text{GE},j}^{**} = k_B T \left\langle \frac{N_j}{V_j} \right\rangle_{\text{CFCMC}} + \left\langle \frac{\sum_{a < b, a, \neg\text{frac}} f_j(r_{ab,j}) r_{ab,j}}{3V_j} \right\rangle_{\text{CFCMC}} \quad (6.37)$$

where the notation “ $\neg\text{frac}$ ” indicates that contribution of fractional molecule in virial part of the pressure should be disregarded. It is important to note that  $P_{\text{GE}}^{**}$  is an approximation for the pressure corresponding to the GE, and unlike  $P_{\text{GE}}^*$ ,  $P_{\text{GE}}$ , and  $P_{\text{CFCMC}}$ , the quantity  $P_{\text{GE}}^{**}$  may not be equal for both simulation boxes. In the gas phase, particles are usually far enough from each other that the contribution of the virial part in the total pressure is limited and not correlated with the volume of the box. However, in the liquid phase, stronger correlation between the contribution of the viral part of the pressure and the volume of the box is expected. The validity of the simplification of Eq. 6.37 is numerically investigated in section 6.5. One can use the exact same approach to define different densities:

$$\rho_{\text{GE},j} = \left\langle \frac{N_j}{V_j} \right\rangle_{\text{GE}} \quad (6.38)$$

$$\rho_{\text{CFCMC},j} = \left\langle \frac{N_j + \delta_{i,j}}{V_j} \right\rangle_{\text{CFCMC}} \quad (6.39)$$

$$\rho_{\text{GE},j}^* = \frac{\left\langle \delta_{\lambda=0, i=j} \frac{N_j}{V_j^2} \right\rangle_{\text{CFCMC}}}{\left\langle \delta_{\lambda=0, i=j} \frac{1}{V_j} \right\rangle_{\text{CFCMC}}} \quad (6.40)$$

$$\rho_{\text{GE},j}^{**} = \left\langle \frac{N_j}{V_j} \right\rangle_{\text{CFCMC}} \quad (6.41)$$

where  $\rho_{\text{GE},j}$  is the average density of box  $j$  computed in the conventional GE,  $\rho_{\text{CFCMC},j}$  is the average density of box  $j$  computed in the CFCMC GE (including the fractional molecule),  $\rho_{\text{GE},j}^*$  is the average density of box  $j$

computed in the CFCMC GE only when the value of  $\lambda$  equals zero excluding contribution of the fractional molecule, and  $\rho_{\text{GE},j}^{**}$  is the average density of box  $j$  computed in the CFCMC GE excluding the fractional molecule and averaged over all values of  $\lambda$ .

## 6.4 Simulation details

As a proof of principle, simulations are performed in the conventional GE and the proposed CFCMC GE to study the vapor liquid equilibria of Lennard-Jones particles. All properties are defined in reduced units (i.e. the Lennard-Jones parameters  $\sigma$  and  $\epsilon$  are set as units of length and energy, respectively) and for convenience the thermal wavelength  $\Lambda$  is set to 1 [38]. The interactions are truncated and shifted at  $2.5\sigma$ . Interactions of the fractional molecule are scaled according to Eq. 6.1. Two system sizes (256 and 512 molecules) and four reduced temperatures ( $T = 0.7, 0.8, 0.9$ , and 0.95) are considered. The weight function is determined iteratively such that the probability distributions  $p_i(\lambda)$  in the proposed CFCMC GE ensemble are flat and the fractional molecule is equally likely to be in the two simulation boxes. Ensemble averages are computed using Eq. 6.19 and the fractional molecule is not counted when computing average densities. Simulations are started with 0.2 million Monte Carlo cycles to equilibrate the system, followed by 2 million production cycles. To reduce the uncertainties in the values computed for pressures (Eqs. 6.29, 6.30, 6.36 and 6.37), after 2 million equilibration cycles, a long production (500 million cycles) run is carried out. The number of Monte Carlo steps per cycle equals the total number of molecules in the system, with a minimum of 20. In each Monte Carlo step, a trial move is selected at random with the following probabilities: 1% volume changes, 49,5% molecule displacements, 49,5% molecule exchanges. In the conventional GE, there is only one type of trial move for molecule exchange. In contrast, the proposed CFCMC GE requires three types of trial moves for facilitating molecule transfers: 50% changes in the  $\lambda$  space (Fig. 6.2), 25% swapping the fractional molecule to the other simulation box (Fig. 6.3), and 25% changing the fractional molecule with a whole molecule

in the other simulation box (Fig. 6.4). Maximum displacements in volume, positions, and  $\lambda$  were set such that on average 50% of the trial moves are accepted. 100 bins are used to store the probability distribution of  $\lambda$ . In the CFCMC GE method, the chemical potentials of the two simulation boxes are computed from Eq. 6.27. In the conventional GE, the chemical potentials are computed from the average energy change using the particle insertions (Eq. 6.20) [101].

To validate the proposed method for systems with partial charges, the VLE of the TIP3P-Ew water model at three different temperatures (400K, 450K, and 473K) is investigated. The TIP3P-Ew is a rigid water model with three point charges optimized for the Ewald summation [178]. A cutoff radius of 13 Å is used for both Lennard-Jones and electrostatic interactions. LJ interactions are truncated and smoothed and no tail corrections are used. The Ewald summation with a relative precision of  $10^{-6}$  is used for the electrostatic interactions [195]. Typically, around 800 water molecules are distributed over the two simulation boxes. Additional trial moves to rotate water molecules are used. Simulations are started with 0.1 million equilibration cycles followed by 2 million production cycles. 41 bins are used to store the probability distributions of  $\lambda$ . Uncertainties reported for the chemical potential of water include the uncertainties due to extrapolation to  $\lambda \rightarrow 1$  as well. The value of the thermal wavelength  $\Lambda$  is set to 1 Å for all temperatures.

## 6.5 Lennard-Jones particles

### 6.5.1 Densities and acceptance probabilities

In Table 6.1, the average densities and chemical potentials of the two coexisting phases computed using the conventional GE and the proposed CFCMC GE are compared. The values obtained from the two methods are in excellent agreement. This comparison shows that the algorithm is correctly implemented. The chemical potential computed from Eqs. 6.25 to 6.27 yield nearly identical values (not shown). We have confirmed numerically that CFCMC GE simulation results do not depend on the weight

Table 6.1: Coexistence densities and chemical potentials for Vapor-Liquid Equilibria of LJ particles for different system sizes and reduced temperatures computed with the conventional GE and the proposed CFCMC GE methods. Numbers in brackets are uncertainties in the last digit, i.e., -3.52 (1) means  $-3.52 \pm 0.01$ . A weight function was used in the CFCMC GE simulations to flatten the probability distribution of the coupling parameter  $\lambda$  and to ensure that the fractional molecule is equally likely to be in both simulation boxes. The total volume  $V_T$  equals  $2 \cdot 8^3$  for  $N_T = 256$  and  $2 \cdot 10^3$  for  $N_T = 512$ .

$N_T=256$								
GE				CFCMC GE				
$T$	$\rho_l$	$\rho_g$	$\mu_l$	$\mu_g$	$\rho_l$	$\rho_g$	$\mu_l$	$\mu_g$
0.7	0.788 (2)	0.0074 (1)	-3.52 (1)	-3.51 (1)	0.786 (2)	0.0074 (2)	-3.52 (2)	-3.52 (2)
0.8	0.731 (1)	0.0198 (2)	-3.34 (1)	-3.34 (1)	0.729 (1)	0.0198 (3)	-3.35 (1)	-3.35 (1)
0.9	0.664 (1)	0.0450 (3)	-3.20 (1)	-3.20 (1)	0.662 (1)	0.0451 (5)	-3.21 (1)	-3.22 (1)
0.95	0.623 (1)	0.0659 (8)	-3.14 (1)	-3.14 (1)	0.621 (1)	0.0660 (8)	-3.15 (1)	-3.16 (1)
$N_T=512$								
GE				CFCMC GE				
$T$	$\rho_l$	$\rho_g$	$\mu_l$	$\mu_g$	$\rho_l$	$\rho_g$	$\mu_l$	$\mu_g$
0.7	0.788 (2)	0.0074 (1)	-3.52 (1)	-3.52 (1)	0.786 (1)	0.0075 (1)	-3.52 (1)	-3.52 (1)
0.8	0.731 (1)	0.0199 (1)	-3.34 (1)	-3.33 (1)	0.730 (1)	0.0199 (3)	-3.34 (1)	-3.34 (1)
0.9	0.664 (1)	0.0451 (2)	-3.20 (1)	-3.20 (1)	0.663 (1)	0.0449 (2)	-3.21 (1)	-3.21 (1)
0.95	0.624 (1)	0.0661 (6)	-3.14 (1)	-3.14 (1)	0.623 (1)	0.0665 (4)	-3.14 (1)	-3.15 (1)

function. The easiest way to compare the efficiency of the two approaches is to compare the acceptance probabilities for exchanging molecules between the two simulation boxes. In Table 6.2, the acceptance probability for the exchange trial move in the conventional GE (moving one molecule from one simulation box to the other) is compared to the probability of changing the fractional molecule into a whole molecule while keeping its position fixed, and, at the same time, changing a (randomly selected) whole molecule in the other simulation box into a fractional molecule, while not changing the value of  $\lambda$  (Fig. 6.4). These trial moves both result in the exchange of whole molecules between the simulation boxes. The data presented in Table 6.2 shows that the acceptance probability for exchanging molecules between the two simulation boxes is considerably higher when the proposed CFCMC GE is used (more than two orders of magnitude at  $T = 0.7$ ). In other words, molecule exchange between the two simulation boxes is significantly facilitated in the proposed CFCMC GE approach. When in-

Table 6.2: Acceptance probabilities for the molecule exchange trial moves in the conventional GE and the CFCMC GE methods for different reduced temperatures and system sizes, for the simulations reported in Table 6.1 (LJ particles). The acceptance probabilities of swap trial moves in the conventional GE are compared to the acceptance probabilities of exchanging the fractional molecule with a whole molecule in the other simulation box (Fig. 6.4), using the proposed CFCMC GE method (Eq. 6.18). A weight function was used in the CFCMC GE simulations to flatten the probability distribution of the coupling parameter  $\lambda$  and to ensure that the fractional molecule is equally likely to be in both simulation boxes.

$N_T=256$			$N_T=512$	
$T$	$P_{\text{acc}}(\text{Swap})_{\text{GE}}$	$P_{\text{acc}}(\text{Change})_{\text{CFCMC GE}}$	$P_{\text{acc}}(\text{Swap})_{\text{GE}}$	$P_{\text{acc}}(\text{Change})_{\text{CFCMC GE}}$
0.7	$8.93 \times 10^{-4}$	$4.20 \times 10^{-1}$	$9.12 \times 10^{-4}$	$4.38 \times 10^{-1}$
0.8	$3.59 \times 10^{-3}$	$4.66 \times 10^{-1}$	$3.60 \times 10^{-3}$	$4.76 \times 10^{-1}$
0.9	$1.18 \times 10^{-2}$	$4.96 \times 10^{-1}$	$1.17 \times 10^{-2}$	$5.04 \times 10^{-1}$
0.95	$2.07 \times 10^{-2}$	$5.00 \times 10^{-1}$	$2.04 \times 10^{-2}$	$5.12 \times 10^{-1}$

sertions/deletions are considered as the bottleneck of the simulations, using CFCMC GE instead of conventional GE increases the efficiency of the simulation significantly. The average acceptance probability for the change trial moves in CFCMC GE (Fig. 6.4) is slightly reduced from ca. 0.4 to ca. 0.2 when  $W(\lambda, i) = 0$ , showing that an appropriate biasing improves the efficiency of the method. In Fig. 6.5, the acceptance probabilities of swapping the fractional molecule between the two simulation boxes (Fig. 6.3) and exchanging the fractional with a randomly chosen whole molecule in the other simulation box (Fig. 6.4), are plotted as a function of the coupling parameter  $\lambda$ . No biasing was used in the simulation reported in Figs. 6.5a and 6.5c. In comparison, the probability distribution of  $\lambda$  was flattened by adding a weight function, see Figs. 6.5b and 6.5d. Without biasing and  $\lambda$  being close to 0, almost 50% of the attempts to swap the fractional molecule from the gas phase to the liquid phase are accepted. We verified that this ratio is exactly equal to the ratio of the volumes of the two boxes, see Eq. 6.11. By increasing the coupling parameter  $\lambda$ , interactions of the fractional molecule with the surrounding molecules increase and therefore this trial move becomes more similar to the swap trial move in conventional GE. It is not surprising that the acceptance probability for swapping the fractional molecule reduces when the value of the coupling parameter is in-

creased. When no biasing is used and  $\lambda$  is close to 1, all attempts to change the fractional molecule in the gas phase into a whole molecule and simultaneously changing a whole molecule in the liquid phase into a fractional molecule are accepted. This is due to the fact that the energy change associated with this trial move is almost zero when  $\lambda$  is close to 1. Therefore, the acceptance rule reduces to Eq. 6.15 and, since more molecules are present in the liquid phase, this trial move is always accepted. When  $\lambda$  is close to 0, the energy change associated with this trial move is almost identical to the energy change associated with a swap trial move in conventional GE. Hence, such a trial move is rarely accepted at  $\lambda$  close to 0. In Fig. 6.5c, the acceptance probabilities of the same trial moves are plotted as a function of  $\lambda$ , in the case where the fractional molecule is initially located in the liquid phase. The acceptance probability for the change trial move (Fig. 6.4) first increases and subsequently decreases with increasing coupling parameter. When  $\lambda$  is close to 0, surrounding molecules in the liquid phase are very closely positioned to the fractional molecule. As a result, changing the fractional molecule into a whole molecule leads to repulsive interactions between the new whole molecule and surrounding molecules. As a consequence, this trial move is rarely accepted for  $\lambda$  close to 0. By increasing  $\lambda$ , the effective volume occupied by the fractional molecule increases, and changing it to a whole molecule results in less repulsive and more attractive interactions. For large values of  $\lambda$ , the energy change associated with this trial move is limited and the prefactor in Eq. 6.14 becomes increasingly important. As a result, for high values of  $\lambda$ , the acceptance probability of the change trial move (with fractional molecule initially in the liquid phase) reduces. In Fig. 6.6, the probability distributions of  $\lambda$  ( $p_i(\lambda)$ ) and the optimized weight functions for the gas and the liquid phase are shown. The shape of  $p_i(\lambda)$  is similar to the original CFCMC GE formulation [55]. The weight function for the gas phase is almost independent of the value of  $\lambda$ . This is due to the fact that the average distance between molecules in the gas phase is much larger than in the liquid phase. We verified that changing the total volume  $V_T$  in the simulations only results in a shift of the weight functions, while their shape remains the same. From Fig. 6.6 it becomes clear that maximum changes in  $\lambda$  can be much larger in the gas phase than in the

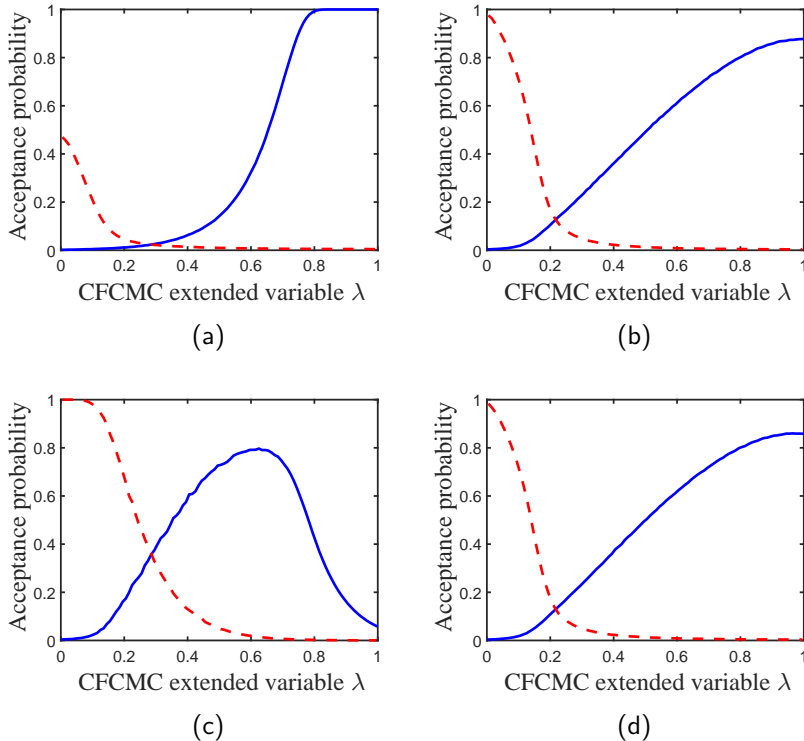


Figure 6.5: Acceptance probabilities for swapping the fractional LJ molecule between the two simulation boxes, while keeping  $\lambda$  constant (dashed line, Fig. 6.3), and changing the fractional molecule with a randomly chosen whole molecule in the other simulation box (solid line, Fig. 6.4) as a function of  $\lambda$ , for CFCMC GE at  $T = 0.8$ . (a) without weight function ( $W(\lambda, i) = 0$ ), fractional molecule in the gas phase (old configuration) (b) with weight function such that the observed distribution of  $\lambda$  is flat, fractional molecule in the gas phase (old configuration) (c) without weight function ( $W(\lambda, i) = 0$ ), fractional molecule in the liquid phase (old configuration) (d) with weight function such that the observed distribution of  $\lambda$  is flat, fractional molecule in the liquid phase (old configuration).

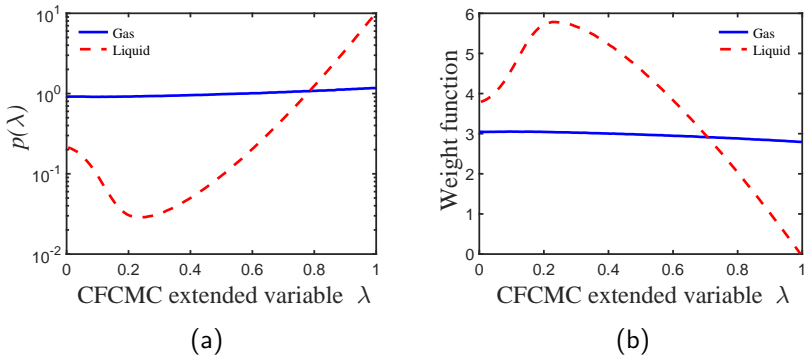


Figure 6.6: (a) Probability distribution of  $\lambda$  for the gas and the liquid phase as used in CFCMC GE of LJ particles at  $T = 0.8$ ; (b) Weight functions to flatten the corresponding probability distributions of  $\lambda$  (as in (a)) and to ensure that the fractional molecule is equally likely to be in both simulation boxes.

liquid phase, and this is an advantage compared to the original CFCMC GE formulation with two fractional molecules. In the acceptance rule for the changing and swapping the fractional molecule (Eqs. 6.17 and 6.18), the term " $\exp [W(\lambda, 2) - W(\lambda, 1)]$ " accounts for the biasing. Graphically, this corresponds to the deference between the weight functions in Fig. 6.6b at a constant value of  $\lambda$ . From Fig. 6.5, it is clear that this biasing significantly enhances molecule transfers.

### 6.5.2 Properties corresponding to the conventional GE

To compute the pressures and densities, simulations are performed in the conventional GE and the CFCMC GE. In Tables 6.3 and 6.4, the average pressures derived in Eqs. 6.29, 6.30, 6.36 and 6.37 and corresponding densities for the gas and liquid phases are shown for three different reduced temperatures ( $T = 0.7, 0.8, 0.95$ ) and for two system sizes (256 and 512 particles). An important point in Tables 6.3 and 6.4 is the fact that the thermodynamic pressures of the two phases computed in the conventional GE ( $P_{\text{GE}}$ ) are equal. The thermodynamic pressures of the two phases

computed in CFCMC GE ( $P_{\text{CFCMC}}$ ) are also equal. However, the thermodynamic pressures of the two ensembles, CFCMC GE and the conventional GE ( $P_{\text{CFCMC}}$ , and  $P_{\text{GE}}$ ) are clearly not equal. As discussed in the previous section, the presence of the fractional molecule in the CFCMC GE simulations results in an increase in the thermodynamic pressure. However, the computed values for  $P_{\text{GE}}^*$  and  $P_{\text{GE}}$  are nearly identical. In the same way, densities computed in CFCMC GE including the fractional molecule ( $\rho_{\text{CFCMC}}$ ) are not equal to those computed in the conventional GE ( $\rho_{\text{GE}}$ ). However, densities corresponding to the conventional GE but computed in CFCMC GE ( $\rho_{\text{GE}}^*$ ) are equal to densities computed in the conventional GE ( $\rho_{\text{GE}}$ ). This numerically confirms the validity of the derivations provided for computing properties corresponding to the conventional GE in the CFCMC GE. Only the states in which the value of  $\lambda$  is zero are contributing to the  $P_{\text{GE}}^*$ . As a result, the uncertainties associated with  $P_{\text{GE}}^*$  values are much larger than the other ensemble averages. The values of  $P_{\text{GE}}^{**}$  computed for the gas phase are very close to the values computed for  $P_{\text{GE}}$  and  $P_{\text{GE}}^*$  (deviation less than 0.2%). This is not the case for  $P_{\text{GE}}^{**}$  computed for the liquid phase (deviation up to 4%). The gas phase density of the conventional GE can be accurately estimated using  $\rho_{\text{GE}}^{**}$  (see Tables 6.3 and 6.4). Since the contribution of the virial part in the pressure of the gas phase is negligible and the ideal gas part is defined by the density,  $P_{\text{GE}}^{**}$  for the gas phase can be used as an estimate of  $P_{\text{GE}}^*$  and  $P_{\text{GE}}$ .

Table 6.3: Computed pressures and densities in the conventional GE and the CFCMC GE at different reduced temperatures for 256 LJ particles.  $P_{\text{GE}}$  (Eq. 6.29) and  $P_{\text{CFCMC}}$  (Eq. 6.30) are the pressures in the conventional GE and the CFCMC GE, respectively.  $P_{\text{GE}}^*$  (Eq. 6.36) indicates the pressure corresponding to that in the conventional GE and computed in the CFCMC GE.  $P_{\text{GE}}^{**}$  (Eq. 6.37) is the computed pressure in the CFCMC GE, not counting the contributions of the fractional molecule. The exact same definitions apply to the computed densities (Eqs. 6.38 to 6.41). Statistical uncertainties in the last digit are shown in brackets, i.e.,  $14.21(1)$  means  $14.21 \pm 0.01$ . The weight function in the CFCMC GE is calculated iteratively so that the probability distribution  $p(\lambda, j)$  is uniform. The total volume for  $T = 0.8$  and  $T = 0.95$  is  $V_T = 2 \times 8^3$  and for  $T = 0.7$  is  $V_T = 2 \times 12.5^3$ .

[Average Pressure]/ $10^{-3}$			[Average Density]/ $10^{-3}$	
$T = 0.7$	Gas	Liquid	Gas	Liquid
$P_{\text{CFCMC}}$	4.89(1)	4.90(10)	$\rho_{\text{CFCMC}}$	7.42(1)
$P_{\text{GE}}$	4.78(1)	4.75(5)	$\rho_{\text{GE}}$	7.25(1)
$P_{\text{GE}}^*$	4.78(1)	4.70(60)	$\rho_{\text{GE}}^*$	7.26(1)
$P_{\text{GE}}^{**}$	4.77(1)	5.10(50)	$\rho_{\text{GE}}^{**}$	7.26(1)
$T = 0.8$	Gas	Liquid	Gas	Liquid
$P_{\text{CFCMC}}$	14.21(1)	14.20(10)	$\rho_{\text{CFCMC}}$	20.31(2)
$P_{\text{GE}}$	13.86(0)	13.87(6)	$\rho_{\text{GE}}$	19.84(0)
$P_{\text{GE}}^*$	13.87(1)	13.80(50)	$\rho_{\text{GE}}^*$	19.83(3)
$P_{\text{GE}}^{**}$	13.87(1)	14.20(10)	$\rho_{\text{GE}}^{**}$	19.84(2)
$T = 0.95$	Gas	Liquid	Gas	Liquid
$P_{\text{CFCMC}}$	45.02(3)	45.02(4)	$\rho_{\text{CFCMC}}$	66.80(10)
$P_{\text{GE}}$	44.44(3)	44.42(6)	$\rho_{\text{GE}}$	66.02(7)
$P_{\text{GE}}^*$	44.42(6)	44.40(50)	$\rho_{\text{GE}}^*$	65.90(20)
$P_{\text{GE}}^{**}$	44.50(7)	44.81(3)	$\rho_{\text{GE}}^{**}$	66.10(10)

Table 6.4: Computed pressures and densities in the conventional GE and the CFCMC GE at different reduced temperatures for 512 LJ particles.  $P_{\text{GE}}$  (Eq. 6.29) and  $P_{\text{CFCMC}}$  (Eq. 6.30) are the pressures in the conventional GE and the CFCMC GE, respectively.  $P_{\text{GE}}^*$  (Eq. 6.36) indicates the pressure corresponding to that in the conventional GE and computed in the CFCMC GE.  $P_{\text{GE}}^{**}$  (Eq. 6.37) is the computed pressure in the CFCMC GE, not counting the contributions of the fractional molecule. The exact same definitions apply to the computed densities (Eqs. 6.38 to 6.41). Statistical uncertainties in the last digit are shown in brackets, i.e., 14.10(1) means  $14.10 \pm 0.01$ . The weight function in the CFCMC GE is calculated iteratively so that the probability distribution  $p(\lambda, j)$  is uniform. The total volume for  $T = 0.7$  is  $V_T = 2 \times 14.5^3$  and for  $T = 0.8$ ,  $V_T = 2 \times 10^3$  and for  $T = 0.95$ , the total volume is  $V_T = 2 \times 8.65^3$ .

[Average Pressure]/ $10^{-3}$			[Average Density]/ $10^{-3}$	
$T = 0.7$	Gas	Liquid	Gas	Liquid
$P_{\text{CFCMC}}$	4.95(1)	4.95(6)	$\rho_{\text{CFCMC}}$	7.53(2)
$P_{\text{GE}}$	4.89(0)	4.89(4)	$\rho_{\text{GE}}$	7.44(1)
$P_{\text{GE}}^*$	4.89(1)	4.80(50)	$\rho_{\text{GE}}^*$	7.44(2)
$P_{\text{GE}}^{**}$	4.88(1)	5.01(3)	$\rho_{\text{GE}}^{**}$	7.44(2)
$T = 0.8$	Gas	Liquid	Gas	Liquid
$P_{\text{CFCMC}}$	14.10(1)	14.14(3)	$\rho_{\text{CFCMC}}$	20.17(2)
$P_{\text{GE}}$	13.92(1)	13.91(2)	$\rho_{\text{GE}}$	19.92(1)
$P_{\text{GE}}^*$	13.93(1)	13.90(20)	$\rho_{\text{GE}}^*$	19.92(1)
$P_{\text{GE}}^{**}$	13.92(1)	14.10(10)	$\rho_{\text{GE}}^{**}$	19.92(2)
$T = 0.95$	Gas	Liquid	Gas	Liquid
$P_{\text{CFCMC}}$	44.88(3)	44.86(5)	$\rho_{\text{CFCMC}}$	66.67(7)
$P_{\text{GE}}$	44.51(2)	44.51(2)	$\rho_{\text{GE}}$	65.00(90)
$P_{\text{GE}}^*$	44.50(1)	44.60(10)	$\rho_{\text{GE}}^*$	66.10(10)
$P_{\text{GE}}^{**}$	44.53(2)	44.76(8)	$\rho_{\text{GE}}^{**}$	66.20(7)

## 6.6 Water

In Table 6.5, the average densities and chemical potentials computed using the conventional GE and the proposed CFCMC GE method for the two coexisting phases of TIP3P-Ew water at different temperatures are compared. Values obtained with the two approaches are in excellent agree-

Table 6.5: Coexistence densities and chemical potentials for Vapor-Liquid Equilibria of TIP3P-Ew water for different temperatures, computed with the conventional GE and the proposed CFCMC GE method. The acceptance probabilities of swap trial moves in the conventional GE are compared to the acceptance probabilities of exchanging the fractional molecule with a whole molecule in the other simulation box (Fig. 6.4). Numbers in brackets are uncertainties in the last digit, i.e., 882 (2) means  $882 \pm 2$ . A weight function was used in the CFCMC GE simulations to flatten the probability distribution of the coupling parameter  $\lambda$  and to ensure that the fractional molecule is equally likely to be in both simulation boxes. The total number of water molecules in the simulations is typically around 800. The value of the thermal wavelength  $\Lambda$  is set to 1 Å for all temperatures.

GE					
T /[K]	$\rho_l$ / [kg m <sup>-3</sup> ]	$\rho_g$ / [kg m <sup>-3</sup> ]	$\mu_l$ / [kJ mol <sup>-1</sup> ]	$\mu_g$ / [kJ mol <sup>-1</sup> ]	$P_{\text{acc}}(\text{Swap})_{\text{GE}}$
400	882 (2)	1.7 (1)	-32 (2)	-33.1 (1)	$2.86 \times 10^{-3}$
450	798 (2)	6.8 (1)	-32.2 (8)	-32.9 (2)	$6.83 \times 10^{-3}$
473	754 (5)	12.2 (5)	-32.4 (7)	-33.0 (3)	$9.52 \times 10^{-3}$
CFCMC GE					
T /[K]	$\rho_l$ / [kg m <sup>-3</sup> ]	$\rho_g$ / [kg m <sup>-3</sup> ]	$\mu_l$ / [kJ mol <sup>-1</sup> ]	$\mu_g$ / [kJ mol <sup>-1</sup> ]	$P_{\text{acc}}(\text{Change})_{\text{CFCMC GE}}$
400	882 (2)	1.7 (1)	-33.2 (6)	-33.0 (1)	$7.75 \times 10^{-2}$
450	798 (2)	6.7 (1)	-33.3 (5)	-32.8 (1)	$8.71 \times 10^{-2}$
473	753 (2)	12.2 (2)	-33.4 (5)	-32.9 (1)	$1.01 \times 10^{-1}$

ment, showing the applicability of the proposed method for systems with partial charges. For liquid water, the computed excess chemical potential at 400K equals 21.5 kJ mol<sup>-1</sup>, which agrees very well with the value of 21.8 kJ mol<sup>-1</sup> reported in Ref. [196]. In Table 6.5, the acceptance probabilities for the swap move in the conventional GE are compared with the acceptance probabilities of the change move (Fig. 6.4) in the proposed CFCMC GE. It is clear that the particle exchange between the two simulation boxes is significantly improved by using the proposed CFCMC GE instead of the conventional GE.

## 6.7 Conclusions

We introduced an alternative formulation for the Gibbs Ensemble (GE) combined with the Continuous Fractional Component Monte Carlo (CFCMC) method. The main advantages of this method over the original formulation of CFCMC GE by Shi and Maginn [55] are: (1) the direct calculation of

chemical potentials in both simulation boxes, without the use of test particles; (2) the biasing is applied to each simulation box independently; (3) the maximum change of the  $\lambda$  parameter ( $\Delta\lambda$ ) can be different for each simulation box. We verified our method for a system of LJ particles and molecules with partial charges (water using the TIP3P-Ew force field). Densities and chemical potentials obtained with the proposed method are in excellent agreement with those computed in the conventional GE. We showed that the CFCMC GE significantly increases the acceptance probability for exchanging molecules between the two simulation boxes, and that the use of appropriate weight functions can facilitate molecule exchanges further. We showed that there are differences between the averages computed in the CFCMC GE and those computed in the conventional GE. Although these differences may be limited for many properties, it is important to know that they exist. We also introduced guidelines for computing ensemble averages corresponding to the conventional GE and computed in the CFCMC GE. We showed analytically and numerically that one can compute ensemble averages that are identical to values computed in the conventional GE. As an example, we computed the pressure and density in the conventional GE and CFCMC GE. The pressure and densities corresponding to the conventional GE and computed in the CFCMC GE are equal to the pressure and densities computed in the conventional GE. However, due to the limited sampling (only when  $\lambda = 0$ ) of these averages in CFCMC GE, long simulations are required to obtain accurate results. It was shown that it is best not to count the fractional molecule while computing averages such as the average energy per molecule and the density. Similar conclusions were made in our more recent work for computing the enthalpy of adsorption using CFCMC in the grand-canonical ensemble [32]. Our approach can easily be extended to mixtures and molecules with intramolecular interactions. For the latter systems, one could consider using Molecular Dynamics to sample the degrees of freedom of each simulation box, while using the three proposed trial moves for molecule transfers. The simulation method is added to the RASPA software package [115, 116].



## **Chapter 7**

# **Continuous Fractional Component Monte Carlo in the Reaction Ensemble**

This chapter is based on the following paper: Poursaeidesfahani, A.; Hens, R.; Rahbari, A.; Ramdin, M.; Dubbeldam, D.; Vlugt, T. J. H.; Efficient Application of Continuous Fractional Component Monte Carlo in the Reaction Ensemble, *Journal of Chemical Theory and Computation*, 2017, 13, 4452-4466.

### **7.1 Introduction**

In the previous chapter, serial GE/CFC was introduced to simulate the adsorption and phase equilibria. This can be used to efficiently simulate adsorption of mixture of hydrocarbons at high loadings. In this chapter, serial Rx/CFC is introduced as an efficient method to study the reaction equilibria at high density and loading. This can be used to investigate the reaction equilibrium for the zeolite-based production of branched hydrocarbons at high loadings. Substantial efforts have been made by scientists and engineers to study chemical reactions in non-ideal environments [154–

156]. An optimal design and operation of many chemical processes relies on accurate information regarding reaction equilibria [197, 198].

It is not always possible to measure reaction equilibria experimentally. The main reasons for this are: (1) extreme conditions may not be accessible experimentally; (2) kinetic limitation may prohibit reaching chemical equilibrium on accessible timescales; (3) large-scale experimental screening of solvents for chemical reactions may not be feasible. Therefore, there is a demand for theoretical methods that can accurately predict reaction equilibria. Molecular simulation is a natural tool for this as interactions between atoms and molecules are explicitly taken into account. One can perform Molecular Dynamics (MD) with a forcefield that can handle chemical reactions, e.g. DFT-based [199], Car-Parrinello [200, 201], or ReaxFF based MD [202, 203]. The main disadvantage of these approaches is that reactions may not occur within the limited timescale of MD simulations. Therefore, advanced simulation techniques such as metadynamics [204–206] or transition path sampling [207–214] may be required. These types of simulation techniques are not considered further in this chapter. One of the most commonly used approaches in molecular simulation is to simulate the reaction equilibria in the Reaction Ensemble (RxMC) [154, 197, 215–221]. In this approach, the chemical reaction is carried out by a Monte Carlo (MC) trial move. Beside thermalization (translation, rotation, etc), trial moves are carried out in which reactants are removed and reaction products are inserted in the system, in such a way that an equilibrium distribution of reactants and reaction products is obtained. The mechanism and the transition state of the reaction are not considered as this approach is purely thermodynamic and reaction kinetics are not considered. As a result, the efficiency of this simulation technique is not affected by the height of the activation energy barrier of the reaction as reaction kinetics are not considered. For a detailed review of RxMC techniques, the reader is referred to Ref. [197]. RxMC struggles when insertions/removals of molecules are difficult e.g. at high loadings and high densities. During the past few years, significant progress has been made in Monte Carlo techniques for the insertion and deletion of molecules [132, 144, 157, 161, 222]. The combination of CFCMC in RxMC was first proposed by Rosch and Maginn [170] (from now on referred to as "parallel

Rx/CFC”). Balaji et al. used parallel Rx/CFC to compute the equilibrium concentrations of the different species in CO<sub>2</sub>/monoethanolamine solutions for different CO<sub>2</sub> loadings [154]. In this method, fractional molecules of reaction products are gradually changed into whole reaction product molecules, while the fractional molecules of reactants are gradually removed, and vice versa. This algorithm is shown schematically in Fig. 7.1a. A key ingredient of parallel Rx/CFC is that the fractional molecules of both all reactants and reaction products are always present in the system. This CFCMC version of RxMC improves the acceptance probability of molecule insertions/removals significantly compared to the conventional RxMC algorithm [170]. It does not allow direct calculation of chemical potentials and it is not possible to directly check if the reaction is at equilibrium. Additional free energy calculations are needed to compute the chemical potentials of reactant and reaction product molecules. The fractional molecules of reactants and reaction products have to adapt to their surroundings simultaneously, which reduces the efficiency of the algorithm. Recently, Maginn and co-workers studied the isomerization of xylene isomers in different confinements and showed that insertion of product molecules aligned to the location and orientation of the deleted reactant molecule increases the acceptance probability of the reaction trial move [223]. Maginn and co-workers used this semi-grand reaction move to study the adsorption of CO<sub>2</sub> in the reactive ionic liquid Triethyl(octyl)phosphonium 2-Cyanopyrrolide [221].

Inspired by the algorithm introduced in the previous chapter, a new formulation for RxMC combined with CFCMC is introduced (serial Rx/CFC). The crucial difference with the parallel Rx/CFC is that either fractional molecules of reactants or reaction products are present in the system. The chemical potentials of reactants/reaction products are directly obtained without using Widom’s test particle insertion (or related) method [224]. Therefore, one can directly check for the condition of chemical equilibrium.

This chapter is organized as follows. In section 2, the conventional RxMC ensemble and its combination with CFCMC are reviewed. Our formulation of RxMC with CFCMC (denoted by serial Rx/CFC) is introduced in section 3. The partition function, types of trial moves, and the computation of chemical potentials are also discussed in this section. Simulation

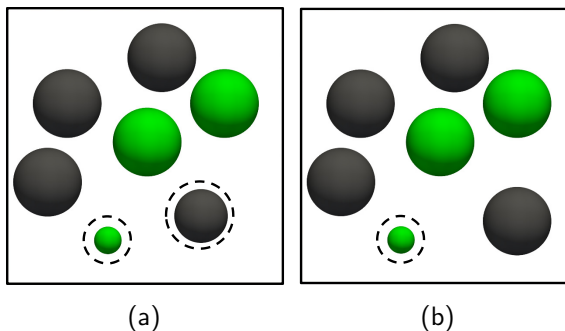


Figure 7.1: (a) Schematic representation of parallel Rx/CFC for the combination of RxMC with CFCMC (denoted by parallel Rx/CFC) [170]. The conventional RxMC is expanded with fractional molecules of each component participating in the reaction. The number of fractional molecules of each component is equal to its stoichiometric coefficient  $\nu_i$ . The coupling parameters for intermolecular interactions of fractional molecules of reactants and reaction products are constrained by  $\lambda_R + \lambda_P = 1$ . (b) Schematic representation of serial Rx/CFC for the combination of RxMC with CFCMC (the method described in this chapter). In serial Rx/CFC, either fractional molecules of reactants or fractional molecules of reaction products are present in the system. In both figures, we consider the reaction  $A \rightleftharpoons B$  in which A=green and B=black. The dashed spheres represent fractional molecules.

details and systems are described in section 4. In section 5, the performance of serial Rx/CFC is compared to conventional RxMC and parallel Rx/CFC for Lennard-Jones (LJ) molecules. We considered various model reactions and pressures for which ideal gas free energy changes are specified in advance. Our approach is also tested for the reaction of ammonia synthesis at various temperatures and pressures. Compared to parallel Rx/CFC, serial Rx/CFC is more efficient, faster and allows for the computation of chemical potentials of all components without any additional computation. Our findings are summarized in section 6. Additional details on the simulation technique are provided in the Appendix.

## 7.2 Conventional RxMC and parallel Rx/CFC

In RxMC simulations, the number of atoms is conserved and not the number of molecules of individual species [197]. Usually, the temperature is constant and either pressure or volume is imposed. The constant pressure version is more interesting for practical applications. In appendix, first the partition function and acceptance rules are derived for the constant volume case and extended to the constant pressure version by adding a term  $\exp[-\beta PV]$  to the partition function [38]. In this section, the partition function and acceptance rules are discussed in detail for the constant pressure version. In addition to Monte Carlo trial moves for thermalization and volume changes, attempts are made to remove reactants and insert reaction product molecules and vice versa. These are the so-called reaction trial moves. Here, for simplicity, we only consider systems with a single reaction as extension to systems with multiple reactions is straightforward [38, 154]. The partition function for the constant pressure version of conventional RxMC equals [197, 216]

$$Q_{\text{Conv},P} = \beta P \sum_{N_1=0}^{\infty} \dots \sum_{N_S=0}^{\infty} \int dV \exp[-\beta PV] \\ \exp \left[ \sum_{i=1}^S \left( \beta \mu_i N_i + N_i \ln \frac{V q_i}{\Lambda_i^3} - \ln N_i! \right) \right] \int ds^{N_{\text{total}}} \exp[-\beta U(s^{N_{\text{total}}})] \quad (7.1)$$

where  $S$  is the number of components,  $\beta = 1/(k_B T)$ ,  $k_B$  is the Boltzmann constant,  $s$  are reduced coordinates,  $V$  is the volume of the simulation box,  $P$  is the pressure,  $N_{\text{total}}$  is the total number of molecules in the simulation box, and  $U$  is the total potential energy.  $q_i$ ,  $\mu_i$ ,  $N_i$ , and  $\Lambda_i$  are the ideal gas partition function excluding the translational part, the chemical potential, the number of molecules, and the thermal wavelength of component (molecule type)  $i$ , respectively.  $q_i$  is related to the molar Gibbs free energy of formation by  $g_i^0 = -RT \ln (q_i/\beta P^0 \Lambda_i^3)$ , where  $P^0$  is the standard reference pressure. Details about methods used for the calculation of  $q_i$  are provided in appendix A.5. The ensemble of Eq. 7.1 is subject to the constraints that the total number of atoms of each type is constant and

that chemical reactions converting reactants into reaction products are in equilibrium. This sets limits on the values of  $\mu_i$ . Sampling of configurations in this ensemble requires: (1) sampling of the degrees of freedom of the interacting molecules (e.g. translation, rotation (for chain molecules), and sampling the internal configuration of molecules); (2) sampling the volume fluctuations; (3) sampling of chemical reactions subject to the constraint that the total number of atoms of each component is constant, as well as that the reaction is at chemical equilibrium. The latter is obtained by performing reaction trial moves. The reaction trial move is attempted to remove randomly selected reactants and insert reaction product molecules, simultaneously. According to the partition function of conventional RxMC (Eq. 7.1), the probabilities of being in the old and new configurations for the reaction trial move in the forward direction are

$$\begin{aligned} p_o &= \frac{\beta P}{Q_{\text{Conv}}} \exp[-\beta PV] \exp \left[ \sum_{i=1}^S \left( \beta \mu_i N_i + N_i \ln \frac{V q_i}{\Lambda_i^3} - \ln N_i! \right) \right] \exp[-\beta U_o] \\ p_n &= \frac{\beta P}{Q_{\text{Conv}}} \exp[-\beta PV] \exp \left[ \sum_{i=1}^R \left( \beta \mu_i (N_i - \nu_i) + (N_i - \nu_i) \ln \frac{V q_i}{\Lambda_i^3} - \ln(N_i - \nu_i)! \right) \right] \\ &\quad \exp \left[ \sum_{j=R+1}^S \left( \beta \mu_j (N_j + \nu_j) + (N_j + \nu_j) \ln \frac{V q_j}{\Lambda_j^3} - \ln(N_j + \nu_j)! \right) \right] \exp[-\beta U_n] \end{aligned} \quad (7.2)$$

where  $\nu_i$  is the stoichiometric coefficient of component  $i$  in the reaction. Here, n and o denote the new and old configurations, respectively. We choose the convention that  $\nu_i$  is positive if component  $i$  participates in the reaction and  $\nu_i$  is zero otherwise.  $R$  is the number of reactant components, and  $P$  is the number of reaction product components. As only systems with a single reaction where all components are either reactants or reaction products are considered here, one can write  $R + P = S$ . Therefore, the reaction product components are ranging from  $R + 1$  to  $S$  with  $S$  being the total number of components. The summation  $\sum_{i=1}^R$  is a sum over all reactant types and  $\sum_{j=R+1}^S$  is the sum over all reaction product types. Therefore, the

ratio of the probabilities of being in the new and old configurations equals

$$\frac{p_n}{p_o} = \exp \left[ -\beta \sum_{i=1}^R \mu_i \nu_i - \sum_{i=1}^R \nu_i \ln \frac{V q_i}{\Lambda_i^3} + \sum_{i=1}^R \ln \frac{N_i!}{(N_i - \nu_i)!} \right] \times \\ \exp \left[ \beta \sum_{j=R+1}^S \mu_j \nu_j + \sum_{j=R+1}^S \nu_j \ln \frac{V q_j}{\Lambda_j^3} + \sum_{j=R+1}^S \ln \frac{N_j!}{(N_j + \nu_j)!} \right] \times \exp [-\beta \Delta U] \quad (7.3)$$

here  $\Delta U = U_n - U_o$  is the total change in the potential energy of the system. Reaction equilibrium implies  $\sum_{i=1}^R \mu_i \nu_i = \sum_{j=R+1}^S \mu_j \nu_j$ . Consequently, the acceptance rule for the reaction trial move is [38, 197]

$$\text{acc}(o \rightarrow n) = \min \left[ 1, \left( \left[ \prod_{i=1}^R \left( \frac{V q_i}{\Lambda_i^3} \right)^{-\nu_i} \right] \times \left[ \prod_{j=R+1}^S \left( \frac{V q_j}{\Lambda_j^3} \right)^{\nu_j} \right] \times \right. \right. \\ \left. \left. \left( \prod_{i=1}^R \frac{N_i!}{(N_i - \nu_i)!} \times \prod_{j=R+1}^S \frac{N_j!}{(N_j + \nu_j)!} \times \exp [-\beta \Delta U] \right) \right) \right] \quad (7.4)$$

Due to simultaneous insertion of the molecules in a single step, the efficiency of this algorithm can be very low at high densities. This is also the case when Configurational-bias Monte Carlo is used for inserting/deleting molecules [219].

In parallel Rx/CFC [170], the conventional RxMC is expanded with fractional molecules of each component participating in the reaction (see Fig. 7.1a). The number of fractional molecules of each component is equal to its stoichiometric coefficient. Interactions of the fractional molecules are scaled with a coupling parameter  $\lambda_j$ . The value  $\lambda_j = 0$  corresponds to no interactions with the surrounding molecules (the fractional molecule acts as an ideal gas molecule), and  $\lambda_j = 1$  corresponds to full interactions with the surrounding molecules (the fractional molecule has the same interactions as whole molecules of the same component). There are two coupling parameters per reaction, one for all reactants ( $\lambda_R$ ) and one for all reaction products ( $\lambda_P$ ). The coupling parameters for the fractional molecules of reactants and reaction products are constrained by  $\lambda_R + \lambda_P = 1$ . Attempts

are made to change the coupling parameters by  $\lambda_{n,R} = \lambda_{o,R} + \Delta\lambda$  with  $\Delta\lambda \in [-\Delta\lambda_{\max}, +\Delta\lambda_{\max}]$ . Due to the constraint  $\lambda_R + \lambda_P = 1$ , the coupling parameter of the fractional molecules of reaction products changes according to  $\lambda_{n,P} = \lambda_{o,P} - \Delta\lambda$ . When  $\lambda_{n,R} > 1$  or  $\lambda_{n,R} < 0$ , an attempt is made to perform a chemical reaction. The acceptance rule for performing a chemical reaction in this ensemble is the same as Eq. 7.4. For more details, we refer the reader to the original publication by Maginn and co-worker [170].

## 7.3 Serial Rx/CFC

### 7.3.1 Partition function

In serial Rx/CFC, either fractional molecules of the reactants or reaction products are present in the system, in sharp contrast to parallel Rx/CFC where fractional molecules of both reactants and reaction products are always present (see Fig. 7.1b). Besides trial moves for thermalization and volume changes, there are three additional trial moves to facilitate the sampling of chemical reactions subject to the constraint that the total number of atoms of each component is constant, as well as chemical equilibrium. As derived in appendix A.1, the partition function for constant pressure of this ensemble equals (not yet taking into account the conservation of atoms)

$$\begin{aligned}
 Q_{\text{CFC},P} = \beta P \sum_{N_1=0}^{\infty} \dots \sum_{N_S=0}^{\infty} \sum_{\delta=0}^1 \int dV \exp[-\beta PV] \times \\
 \exp \left[ \beta \sum_{i=1}^R \mu_i (N_i + \nu_i \delta) + \sum_{i=1}^R (N_i + \nu_i \delta) \ln \frac{V q_i}{\Lambda_i^3} - \sum_{i=1}^R \ln N_i! \right] \times \\
 \exp \left[ \beta \sum_{j=R+1}^S \mu_j (N_j + \nu_j (1-\delta)) + \sum_{j=R+1}^S (N_j + \nu_j (1-\delta)) \ln \frac{V q_j}{\Lambda_j^3} - \sum_{j=R+1}^S \ln N_j! \right] \times \quad (7.5) \\
 \int_0^1 d\lambda \int ds^{N_{\text{int}}} \exp[-\beta U_{\text{int}}(s^{N_{\text{int}}})] \left( \prod_{i=1}^R \int ds_{\text{frac}}^{\nu_i} \exp[-\beta \delta U_{\text{frac},i}(s_{\text{frac}}^{\nu_i}, s^{N_{\text{int}}}, \lambda)] \right) \times \\
 \left( \prod_{j=R+1}^S \int ds_{\text{frac}}^{\nu_j} \exp[-\beta (1-\delta) U_{\text{frac},j}(s_{\text{frac}}^{\nu_j}, s^{N_{\text{int}}}, \lambda)] \right)
 \end{aligned}$$

$N_{\text{int}}$  is the total number of whole molecules (regardless the component type) and  $N_i$  is the number of whole molecules of component  $i$ . When  $\delta = 1$ , fractional molecules of reactants are present in the simulation box ( $\nu_i$  fractional molecule for component  $i$ ), and when  $\delta = 0$ , fractional molecules of reaction products are present. Here, a system with a single reaction is considered.  $U_{\text{int}}$  is the total internal energy of whole molecules and  $U_{\text{frac},i}$  is the interaction energy of fractional molecules of component  $i$  with the other molecules, including other fractional molecules. The interactions of the fractional molecules with the surroundings are such that  $\lambda = 0$  means no interactions and  $\lambda = 1$  means full interactions, and the value of  $\lambda$  is restricted to  $\lambda \in [0, 1]$ .

Since fractional molecules are always distinguishable from whole molecules, the term  $N_i!$  only counts for whole indistinguishable molecules. The main difference between Eq. A13 and Eq. 7.1 is the integration over  $\lambda$  in Eq. A13. This is an immediate consequence of expanding the conventional RxMC with fractional molecules. In Appendix A.1, we show that for systems without intermolecular interactions (ideal gas phase), the partition functions of Eq. A13 and Eq. 7.1 are proportional. Therefore, these ensembles result in identical average numbers of molecules for each component, provided that fractional molecules are not counted when computing ensemble averages. The fact that one should not count fractional molecules when computing the average number of molecules is in line with earlier studies in the Gibbs ensemble and in the grand-canonical ensemble [32, 191].

### 7.3.2 Trial moves

In addition to Monte Carlo trial moves for thermalization and volume changes, there are three trial moves in this ensemble to mimic the chemical reaction. A detailed description of these trial moves and the derivation of the acceptance rules is provided in Appendix A.1.

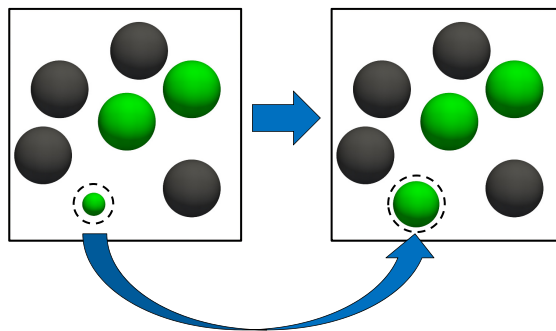


Figure 7.2: Schematic representation of the trial move attempting to change the coupling parameter  $\lambda$  for serial Rx/CFC. In this trial move,  $\delta$  and the positions of all molecules remain the same. We consider the reaction  $A \rightleftharpoons B$  in which  $A=\text{green}$  and  $B=\text{black}$ . The dashed spheres represent fractional molecules.

### Changing the value of $\lambda$

This trial move is used to change the value of  $\lambda$  either for reactants or reaction products, depending on the value of  $\delta$  (see Fig. 7.2). The value of  $\lambda$  is changed according to  $\lambda_n = \lambda_o + \Delta\lambda$  in which  $\Delta\lambda$  is a uniformly distributed random number between  $-\Delta\lambda_{\max}$  and  $+\Delta\lambda_{\max}$ . Note that  $\Delta\lambda_{\max}$  can be different for reactants and reaction products. When the new value of  $\lambda$  is not in the range  $\lambda \in [0, 1]$ , this trial move is automatically rejected. In this trial move, the value of  $\delta$ , all positions of molecules, and the number of whole molecules and fractional molecules remain the same. By changing the value of  $\lambda$ , only the interactions between the fractional molecules and other molecules are changed. In Appendix A.1, it is shown that the acceptance rule for this trial move is

$$\text{acc}(o \rightarrow n) = \min [1, \exp [-\beta \Delta U]] \quad (7.6)$$

in which  $\Delta U = U_n - U_o$  is the change in the total internal energy of the system.

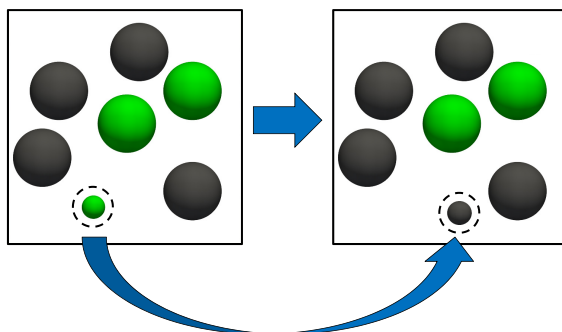


Figure 7.3: Schematic representation of the trial move attempting to perform the reaction for fractional molecules for serial Rx/CFC. In this trial move, the number of the whole molecules and also the value of  $\lambda$  are constant. We consider the reaction  $A \rightleftharpoons B$  in which  $A=\text{green}$  and  $B=\text{black}$ . The dashed spheres represent fractional molecules. The fractional molecule of  $A$  is removed and a fractional molecule of  $B$  is inserted at a randomly selected position.

### Reaction for fractional molecules

In this trial move, fractional molecules of reactants/reaction products are removed and fractional molecules of reaction products/reactants are inserted at random positions (see Fig. 7.3). In this trial move, essentially the value of  $\delta$  is changed, so if  $\delta_o = 1$  then  $\delta_n = 0$  and vice versa. The number of whole molecules and also the value of  $\lambda$  are constant. This trial move basically mimics a chemical reaction for the fractional molecules. Here, the acceptance rule for the forward reaction (reactants  $\rightarrow$  reaction products) is shown. The direction of the chemical reaction is defined by the value of  $\delta$  for the old configuration (if we have the fractional molecules of reactants or reaction products). In Appendix A.1, it is derived that the acceptance rule for converting the reactants into reaction products equals

$$\text{acc}(o \rightarrow n) = \min \left[ 1, \prod_{i=1}^R \left( \frac{V q_i}{\Lambda_i^3} \right)^{-\nu_i} \prod_{j=R+1}^S \left( \frac{V q_j}{\Lambda_j^3} \right)^{\nu_j} \exp [-\beta \Delta U] \right] \quad (7.7)$$

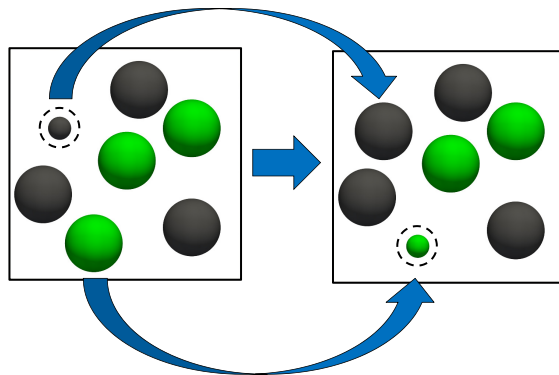


Figure 7.4: Schematic representation of the trial move attempting to perform the reaction for whole molecules for serial Rx/CFC. In this trial move, the value of  $\lambda$  and all positions of all molecules remain the same. We consider the reaction  $A \rightleftharpoons B$  in which  $A=\text{green}$  and  $B=\text{black}$ . The dashed spheres represent fractional molecules. The fractional molecule of  $A$  is transformed into a whole molecule of  $A$  while at the same time, a randomly selected whole molecule of  $B$  is transformed into a fractional molecule of  $B$ .

Since the number of whole molecules remains constant during this move, the terms  $\prod_{i=1}^R \frac{N_i!}{(N_i - \nu_i)!}$  and  $\prod_{j=R+1}^S \frac{N_j!}{(N_j + \nu_j)!}$  are not present in Eq. 7.7. The acceptance rule for the reverse reaction (reaction products  $\rightarrow$  reactants) simply follows by swapping the labels of the reactants and reaction products. The acceptance probability for this trial move is large when  $\lambda$  is small. The reason for this is that fractional molecules have very limited interactions with the surrounding molecules and therefore, the term  $\Delta U$  is nearly zero. For the limiting case of  $\lambda \downarrow 0$ , the acceptance rule reduces to

$$\text{acc}(o \rightarrow n) = \min \left[ 1, \prod_{i=1}^R \left( \frac{V q_i}{\Lambda_i^3} \right)^{-\nu_i} \prod_{j=R+1}^S \left( \frac{V q_j}{\Lambda_j^3} \right)^{\nu_j} \right] \quad (7.8)$$

### Reaction for whole molecules

In this trial move, fractional molecules of reactants/reaction products are transformed into whole molecules of reactants/reaction products, while simultaneously, randomly selected whole molecules of reaction products/reactants are transformed into fractional molecules of reaction products/reactants. In this trial move, all molecule positions and the value of  $\lambda$  stay the same. The value of  $\delta$  is changed as follows: if  $\delta_o = 1$  then  $\delta_n = 0$  and vice versa. This trial move is illustrated in Fig. 7.4 and can be seen as a reaction for whole molecules. In the forward reaction, whole molecules of reactants are transformed into fractional molecules, and fractional molecules of reaction products are turned into whole molecules. Essentially, the number of whole molecules of reactants is reduced and the number of whole molecules of reaction products is increased, according to their stoichiometric coefficients. Trial moves are automatically rejected when there are not enough whole molecules to turn into fractional molecules. Here, the acceptance rule for the forward reaction (reactants  $\rightarrow$  reaction products) is shown. The direction of the reaction eventually depends on the value of  $\delta$  for the old configuration (if we have fractional molecules of reactants or reaction products). As derived in Appendix A.1, the acceptance rule for this trial move is

$$\text{acc}(\text{o} \rightarrow \text{n}) = \min \left[ 1, \prod_{i=1}^R \frac{N_i!}{(N_i - \nu_i)!} \prod_{j=R+1}^S \frac{N_j!}{(N_j + \nu_j)!} \exp[-\beta \Delta U] \right] \quad (7.9)$$

in which  $\Delta U = U_n - U_o$  is the change in the total internal energy of the system including the interaction of fractional molecules as result of the trial move. The acceptance rule for the reverse reaction (reaction products  $\rightarrow$  reactants) simply follows by swapping the labels. Since the total number of whole and fractional molecules for each component remains constant, ideal gas partition functions are not present in Eq. 7.9. This trial move has a very high acceptance probability when the value of  $\lambda$  is close to 1. The reason for this is that fractional molecules have almost the same interactions as whole molecules and therefore, the term  $\Delta U$  is nearly zero. For the limiting

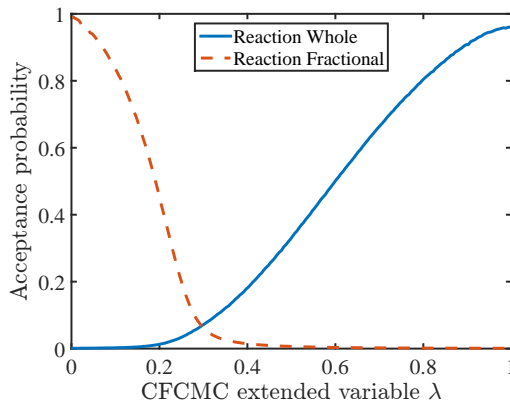


Figure 7.5: Acceptance probabilities for trial moves attempting to perform reactions for fractional molecules (dashed line, see Fig. 7.3), and for trial moves attempting to perform reactions for whole molecules (solid line, see Fig. 7.4), for serial Rx/CFC. Simulation conditions are: reduced temperature  $T = 2$ , and constant reduced pressure  $P = 3.0$ , for the reaction  $A \rightleftharpoons B$ . Similar results are obtained for the other reactions and at other conditions.

case of  $\lambda \uparrow 1$ , the acceptance rule reduces to

$$\text{acc}(o \rightarrow n) = \min \left[ 1, \prod_{i=1}^R \frac{N_i!}{(N_i - \nu_i)!}, \prod_{j=R+1}^S \frac{N_j!}{(N_j + \nu_j)!} \right] \quad (7.10)$$

### Volume changes

This trial move is only used for the case where the temperature and external pressure are imposed. In this trial move, the volume of the simulation box is changed while the number and relative coordinates of the whole molecules and fractional molecules stay the same. Here, the random walk is performed in  $V$  and not  $\ln(V)$  [38]. The acceptance rule for this trial move

is [38]

$$\text{acc}(\text{o} \rightarrow \text{n}) = \min \left[ 1, \left( \frac{V_n}{V_o} \right)^{\sum_{i=1}^R (N_i + \nu_i \delta) + \sum_{j=R+1}^S (N_j + \nu_j (1-\delta))} \times \exp [-\beta (\Delta U + P (V_n - V_o))] \right] \quad (7.11)$$

### Efficient selection of trial moves

As discussed in the previous section, the reaction trial move for fractional molecules has a very high acceptance probability at low values of  $\lambda$ , and the reaction trial move for the whole molecules has a very high acceptance probability at high values of  $\lambda$ . In Fig. 7.5, typical acceptance probabilities of these trial moves as a function of  $\lambda$  are shown. Therefore, one may attempt reaction trial moves for fractional molecules only at values of  $\lambda$  close to 0, and reaction trial moves for the whole molecules only at values of  $\lambda$  close to 1. In this way, each trial move is used where it is efficient and the overall efficiency of the algorithm is improved. This is done as follows: one can define a switching point for the value of  $\lambda$  ( $\lambda_{\text{sec}}$ ). The probabilities of selecting a trial move: thermalization, volume change, or changing the value of  $\lambda$  are always constant. For selection of the remaining trial moves one has a choice: selecting these with fixed probability, or always selecting the reaction trial move for fractional molecules (section 3.2.2) when  $\lambda < \lambda_{\text{sec}}$ , and always selecting the reaction trial move for whole molecules (section 3.2.3) when  $\lambda > \lambda_{\text{sec}}$ . In the latter approach, the reaction trial moves are selected when they have a higher acceptance probability. Since the value of  $\lambda$  remains constant during either of these trial moves, the probabilities for selecting the trial moves also remain constant. Therefore, the condition of detailed balance is not violated.

#### 7.3.3 Biasing the probability distribution $p(\lambda, \delta)$

It is important to bias the probability distribution of  $p(\lambda, \delta)$  ( $\delta$  indicates whether fractional molecules of reactants or reaction products are in the simulation box) in such a way that the sampled probability distributions

$p(\lambda, \delta)$  is flat and that it is equally likely to have the fractional molecules of reactants ( $\delta = 1$ ) or reaction products ( $\delta = 0$ ). By using an adequate biasing function, one can overcome the problem of being "stuck" in free energy minima and can easily diffuse through the  $\lambda$  space. This is obtained by multiplying the statistical weight of each system state by a factor  $\exp[W(\lambda, \delta)]$ . For parallel Rx/CFC [170], since fractional molecules of both reactants and reaction products are always present in the system, one would only need a one-dimensional weight function to obtain flat probability distribution of  $p(\lambda)$ . It is important to note that in serial Rx/CFC the weight function  $W(\lambda, \delta)$  is a two-dimensional function that depends both on  $\lambda$  and the identity of the fractional molecules ( $\delta$ ). By using this biased sampling, additional terms  $\exp[W(\lambda_n, \delta_n) - W(\lambda_o, \delta_o)]$  will be present in the acceptance rules of Eqs. 7.6, 7.7 and 7.9. For example, the acceptance rule for the trial move attempting to mimic a reaction for the fractional molecules (Eq. 7.7) will become

$$\text{acc}(o \rightarrow n) = \min \left[ 1, \prod_{i=1}^R \left( \frac{V q_i}{\Lambda_i^3} \right)^{-\nu_i} \prod_{j=R+1}^S \left( \frac{V q_j}{\Lambda_j^3} \right)^{\nu_j} \times \frac{\exp[-\beta \Delta U + W(\lambda, \delta_n) - W(\lambda, \delta_o)]}{\exp[-\beta \Delta U + W(\lambda, \delta_o) - W(\lambda, \delta_n)]} \right] \quad (7.12)$$

To remove this bias, the Boltzmann averages of any observable  $X$  should be computed using

$$\langle X \rangle_{\text{Boltzmann}} = \frac{\langle X \exp[-W(\lambda, \delta)] \rangle_{\text{biased}}}{\langle \exp[-W(\lambda, \delta)] \rangle_{\text{biased}}} \quad (7.13)$$

The weight function  $W(\lambda, \delta)$  can be obtained using the Wang-Landau algorithm [184, 185] or iteratively [170]. To compute ensemble averages corresponding to the conventional RxMC while performing simulation with serial Rx/CFC, one should exclude the contribution of fractional molecules. By doing this, one can analytically show that for an ideal gas case the ensemble averages computed using the serial Rx/CFC and the conventional RxMC are identical, see Appendix A.1. Including the contribution of the fractional molecules in the ensemble averages leads to small differences between the

ensemble averages compute in the serial Rx/CFC and those computed in the conventional RxMC [191].

### 7.3.4 Free energy calculations

In serial Rx/CFC, chemical potentials can be computed without any additional computational efforts. As shown in the appendix A.3, one can show that

$$\sum_{i=1}^R \nu_i \mu_i = -\frac{1}{\beta} \ln \left\langle \prod_{i=1}^R \left( \frac{q_i}{\Lambda_i^3 \rho_i} \right)^{\nu_i} \right\rangle - \frac{1}{\beta} \ln \left( \frac{p(\lambda \uparrow 1, \delta = 1)}{p(\lambda \downarrow 0, \delta = 1)} \right) \quad (7.14)$$

where  $q_i$  is the ideal gas partition function of component  $i$  excluding the translational part. One can obtain the sum of the chemical potentials of reaction products in a similar way. Eq. A58 allows for an independent check of reaction equilibria without any additional calculations (e.g. test molecules). The chemical potential of component  $i$  for a non-ideal gas equals [197, 198]

$$\mu_i = \frac{1}{\beta} \ln \frac{\beta P_0 \Lambda_i^3}{q_i} + \frac{1}{\beta} \ln \frac{y_i P \varphi_i}{P_0} \quad (7.15)$$

in which  $\varphi_i$  and  $y_i$  are the fugacity coefficient and mole fraction of component  $i$ , respectively.  $P_0$  is the reference pressure (1 bar) and  $P$  is the pressure of the mixture. For an ideal gas mixture we have  $\varphi_i = 1$ . The first term on the right hand side of Eq. 7.15 is the standard reference chemical potential ( $\mu_i^0(T)$ ) Therefore, we have

$$\sum_{i=1}^R \nu_i \mu_i = \frac{1}{\beta} \ln \left( \prod_{i=1}^R \left[ \frac{\beta \Lambda_i^3 y_i P \varphi_i}{q_i} \right]^{\nu_i} \right) \quad (7.16)$$

Combining this with Eq. A58 immediately leads to

$$\prod_{i=1}^R \varphi_i^{-\nu_i} = \frac{p(\lambda_R \uparrow 1)}{p(\lambda_R \downarrow 0)} \times \prod_{i=1}^R \left( \frac{\beta y_i P}{\rho_i} \right)^{\nu_i} \quad (7.17)$$

where  $\lambda_R = \lambda$  when we have the fractional molecules of reactants ( $\delta = 1$ ). In this equation,  $p(\lambda_R \uparrow 1)$  is the probability that  $\lambda_R$  approaches 1, and  $p(\lambda_R \downarrow 0)$  is the probability that  $\lambda_R$  approaches 0. To compute the chemical potential of individual components, one should couple the interactions of different components in a smart way. The two limiting cases are well defined: at  $\lambda = 0$ , fractional molecules of reactants (or reaction products) do not interact, and at  $\lambda = 1$ , fractional molecules of reactants have full interactions with the surrounding molecules. However, for intermediate values of  $\lambda$  one has a choice. One can choose different paths to scale the interactions of fractional molecules from no interactions to full interactions. The interactions can be scaled atom by atom, or molecule by molecule, or in any other way. By scaling the interactions of the fractional molecules of only one of the components from no interactions to full interactions when the value of  $\lambda$  is changed from 0 to  $A$  (see Figs. A1 and 7.6), one can write

$$\nu_i \mu_i = -\frac{1}{\beta} \ln \left( \frac{q_i}{\Lambda_i^3 \rho_i} \right)^{\nu_i} - \frac{1}{\beta} \ln \left( \frac{p(\lambda_R \uparrow A)}{p(\lambda_R \downarrow 0)} \right) \quad (7.18)$$

The first term on the right hand side accounts for the ideal gas part. The second term on the right hand side accounts for the excess part of the chemical potential (due to interactions with surrounding molecules). Similar to Eq. 7.17, one can write for  $\varphi_i$

$$\varphi_i^{-\nu_i} = \frac{p(\lambda_R \uparrow A)}{p(\lambda_R \downarrow 0)} \times \left( \frac{\beta y_i P}{\rho_i} \right)^{\nu_i} \quad (7.19)$$

When  $\nu_i > 1$  and interactions of fractional molecules are scaled sequentially (one by one), fractional molecules that have interactions with surrounding molecules later (at higher values of  $\lambda$ ) experience the effect of the fractional molecules which were inserted earlier (at lower values of  $\lambda$ ). For sufficiently large system sizes, this will not affect the calculated chemical potentials. However, for small system sizes there may be minor differences between the chemical potential of molecules that are inserted at lower values of  $\lambda$  and those inserted at higher values of  $\lambda$ . Although these differences are expected to be small, one should be aware of them.

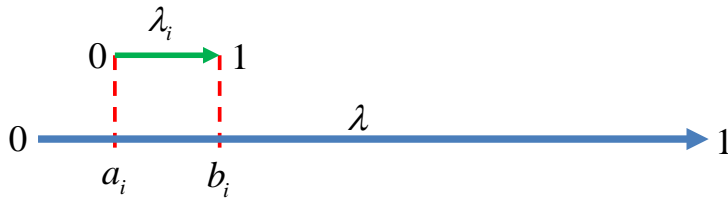


Figure 7.6: Schematic representation of the scaling of interactions for multiple fractional molecules. The interactions of molecule  $i$  are scaled such that  $\lambda_i = 0$  when  $\lambda = a_i$  and  $\lambda_i = 1$  when  $\lambda = b_i$ .

If the interactions are scaled molecule by molecule when  $\lambda$  is changed from 0 to 1, each fractional molecule  $i$  will have its own scaling parameter  $\lambda_i$ . The value of  $\lambda_i$  will be zero when  $\lambda = a_i$  and it will be 1 when  $\lambda = b_i$  this is shown schematically in Fig. 7.6. When two fractional molecules interact, the interactions are scaled according to minimum value of  $\lambda_i$  of the two molecules. Details on the scaled interactions are provided in Appendix A.6.

## 7.4 Simulation details

As a proof of principle, simulations are performed for different systems of LJ molecules. The ammonia synthesis reaction at various pressures (100-1000 bar) and temperatures (575-873K) is also considered as a practically important application. For different systems of LJ molecules, simulations are performed at constant pressure and temperature using conventional RxMC, parallel Rx/CFC [170], and serial Rx/CFC. Various model reactions of LJ molecules are studied. For these simulations, all properties are defined in reduced units. LJ interactions are truncated and shifted at  $2.5\sigma$ . The reduced temperature is set to  $T = 2.0$ , and simulations are always started with 400 molecules of component A. For simulations of LJ molecules using parallel Rx/CFC and serial Rx/CFC, the maximum molecule displacements, maximum volume change, and maximum change in the value of  $\lambda$  are set to

achieve 50% acceptance for these trial moves. For simulations using serial Rx/CFC, the switching point for the value of  $\lambda$  is set to  $\lambda_{\text{sec}} = 0.3$  (see section 3.2.4). In each Monte Carlo step, a trial move is selected at random with the following probabilities: 49.5% molecule displacements, 1% volume changes, and 49.5% reaction trial moves.

For the ammonia synthesis reaction, simulations are performed at constant pressure and temperature using serial Rx/CFC. All simulations start with a random configuration of 120 N<sub>2</sub>, 360 H<sub>2</sub> molecules, and no ammonia molecules. Fractional molecules are added to this configuration. All molecules are rigid and interact only by LJ and electrostatic interactions. Force field parameters for N<sub>2</sub>, H<sub>2</sub>, and NH<sub>3</sub> are taken from the literature [225–228]. The Wolf method is used to compute electrostatic interactions [229]. Details regarding the force field parameters, scaling of the electrostatic interactions, and the Wolf method are provided in Appendix A.6. The ideal gas partition functions for this system are listed in Appendix A.5. In Table A3, a detailed comparison is made between ideal gas partition functions from experiments and QM computations using Gaussian09 [230]. In each Monte Carlo step, a trial move is selected at random with the following probabilities: 33% molecule displacements, 33% molecule rotation, 1% volume changes, and 33% reaction trial moves. For the ammonia synthesis reaction, LJ interactions are switched on for  $\lambda \in [0, 0.9]$  and electrostatic interactions are switched on for  $\lambda \in [0.9, 1]$ .

For all simulations using parallel Rx/CFC and serial Rx/CFC, the weight function is determined using the Wang-Landau algorithm [184]. In serial Rx/CFC, the weight function  $W(\lambda, \delta)$  is determined such that the observed two-dimensional probability distribution  $p(\lambda, \delta)$  in the proposed ensemble is flat. 200 bins are used to store the probability distribution of  $\lambda$  for reactants or reaction products. All simulations are started with 0.2 million Monte Carlo cycles to equilibrate the system, followed by 1 million production trial moves. The number of Monte Carlo steps per cycle equals the total number of molecules initially in the system, with a minimum of 20.

LJ interactions of fractional molecules are scaled according to Eq. 6.1 [163]. In the conventional method and parallel Rx/CFC, there is only one type of reaction trial move. In this move reactants/reaction products are

remove and reaction productions/reactants are inserted. In contrast, serial Rx/CFC requires three types of trial moves for facilitating molecule transfers: 50% changes in the  $\lambda$  space (Fig. 7.2), 50% reaction for the fractional molecules (Fig. 7.3) when  $\lambda < \lambda_{\text{sec}}$ , or 50% reaction for the whole molecules (Fig. 7.4) when  $\lambda > \lambda_{\text{sec}}$ . In serial Rx/CFC, the chemical potentials are computed from Eq. A58. The contribution of fractional molecules are excluded while computing ensemble averages [191]. To compare the efficiencies of the three methods, a fair way to define the efficiency of each method is required. In this work, the efficiency for all three methods is defined as the number of accepted trial moves (either forward or backward) resulting in a change in the number of whole molecules due to the reaction, divided by the total number of reaction trial moves. For parallel Rx/CFC, this means: the number of accepted  $\lambda$  trial moves that resulted in  $\lambda_n > 1$  or  $\lambda_n < 0$ , divided by the total number of  $\lambda$  trial moves. For serial Rx/CFC, this means: the number of accepted reaction trial moves for whole molecules (Fig. 7.4) divided by the total number of all reaction trial moves, including changing the value of  $\lambda$ , reaction for fractional molecules, and reaction for whole molecules. Reaction trial moves in serial Rx/CFC are computationally cheaper compared to parallel Rx/CFC. This is due to the reduction in the number of fractional molecules and therefore the number of interacting molecule pairs is reduced. Simulations performed using serial Rx/CFC require less CPU time compared to similar simulations when parallel Rx/CFC is used. The CPU time depends on the programming of the algorithms, the compiler, and CPUs used to perform the calculations. In this paper, different approaches are only compared in terms of efficiency and not the CPU time. This can be considered as the worst-case scenario for serial Rx/CFC.

## 7.5 Results

To insure that serial Rx/CFC is implemented correctly, the equilibrium composition for different reactions of LJ molecules are computed and compared for the three methods. The LJ parameters and partition function for

Table 7.1: Interaction parameters (Lennard-Jones) and partition functions ( $q/\Lambda^3$ ) for different molecule types. Note that there are several molecule types with exactly the same interaction parameters. This was performed to show the effect of (in)distinguishability of the molecules in the reactions.

Molecule type	$\sigma$	$\epsilon$	$q/\Lambda^3$
A	1.0	1.0	0.002
B	1.0	1.0	0.002
C	1.1	0.9	0.002
D	1.0	1.0	0.02
E	1.1	0.9	0.02
F	1.0	1.0	0.02

LJ molecules used in this study are listed in Table 7.1. The equilibrium composition obtained with different methods at reduced pressures  $P = 0.3$ ,  $P = 1.0$ ,  $P = 3.0$  and,  $P = 5.0$  are shown in Tables 7.2 to 7.5, respectively. Equilibrium compositions obtained for the three methods are the same for all reactions and conditions (see Tables 7.2 to 7.5). This confirms the validity of the expressions used for the partition function and acceptance rules of serial Rx/CFC, and indicates that this method is implemented correctly.

The efficiencies of the three methods for different reactions are also shown in Tables 7.2 to 7.5. The conventional method has a very high efficiency for all reactions at the lowest pressure ( $P = 0.3$ ). Since in this case the density of the system is very low and therefore interactions between the molecules are limited, there is almost no energy penalty for the reaction trial moves and most of the attempts to perform reaction trial moves for whole molecules are accepted. Therefore, the method which attempts to directly replace the reactants with reaction products and vice versa has a high efficiency. For the conventional method, reaction trial moves for the whole molecules is the only reaction trial move and this trial move is accepted with a high probability for the low pressure case. As a result, this method has high efficiencies for this case. In parallel Rx/CFC [170], many trial moves are spent diffusing through the entire  $\lambda$ -space and less attempts

Table 7.2: Average number of molecules and density at equilibrium for different reactions for different methods. The efficiency is defined in Section 7.4. The reduced pressure and temperature are set to  $P = 0.3$  and  $T = 2.0$ , respectively. Simulations are started with 400 molecules of type A. The interaction parameters of different molecules are listed in Table 7.1. The numbers between brackets denote the uncertainty in the last digit.

Reaction	$\langle N_A \rangle$	$\langle N_{\text{Product } 1} \rangle$	$\langle N_{\text{Product } 2} \rangle$	$\langle \rho_{\text{tot}} \rangle$	Efficiency	Method
$A \rightleftharpoons B$	200.00(3)	200.00(3)		0.162(0)	0.40	Conventional
	199.99(7)	200.01(7)		0.161(0)	0.11	Parallel Rx/CFC
	199.98(6)	200.02(6)		0.161(0)	0.30	Serial Rx/CFC
$A \rightleftharpoons C$	206.62(2)	193.38(2)		0.155(0)	0.37	Conventional
	206.63(3)	193.37(2)		0.154(0)	0.098	Parallel Rx/CFC
	206.62(5)	193.38(5)		0.155(0)	0.30	Serial Rx/CFC
$A \rightleftharpoons 2D$	192.59(6)	414.8(2)		0.162(0)	0.26	Conventional
	192.27(6)	415.5(2)		0.161(0)	0.097	Parallel Rx/CFC
	192.36(4)	415.27(8)		0.161(0)	0.25	Serial Rx/CFC
$A \rightleftharpoons 2E$	202.75(5)	394.5(1)		0.153(0)	0.21	Conventional
	202.35(6)	395.3(2)		0.152(0)	0.086	Parallel Rx/CFC
	202.47(4)	395.06(8)		0.152(0)	0.25	Serial Rx/CFC
$A \rightleftharpoons D + F$	91.52(3)	308.48(3)	308.48(3)	0.162(0)	0.26	Conventional
	91.22(9)	308.78(9)	308.78(9)	0.161(0)	0.097	Parallel Rx/CFC
	91.33(3)	308.67(3)	308.67(3)	0.161(0)	0.25	Serial Rx/CFC
$A \rightleftharpoons D + E$	95.57(3)	304.43(3)	304.43(3)	0.156(0)	0.23	Conventional
	95.28(4)	304.72(4)	304.72(4)	0.155(0)	0.094	Parallel Rx/CFC
	95.39(2)	304.61(2)	304.61(2)	0.155(0)	0.25	Serial Rx/CFC

are made to perform a reaction. Therefore, this method has the lowest efficiency for the low pressure case. Already at  $P = 1.0$ , the efficiency of the conventional method is much lower than its efficiency at  $P = 0.3$ . At higher pressures ( $P = 3.0$ ,  $P = 5.0$ ), the efficiency of the conventional method drops below 0.01 even for the simplest reaction ( $A \rightleftharpoons B$ ). When the density is high, most of the reaction trial moves in the conventional method result in an overlap between the newly inserted molecules and molecules that are already in the system. Therefore, this move has very low acceptance probability. In this case, the efficiency of parallel Rx/CFC varies between 0.06 to 0.1 while the efficiency of serial Rx/CFC varies between 0.1 to 0.2 depending on the reaction. Due to the efficient use of the three trial moves in serial Rx/CFC, this method has a better performance compared to the

Table 7.3: Average number of molecules and density at equilibrium for different reactions for different methods. The efficiency is defined in Section 7.4. The reduced pressure and temperature are set to  $P = 1.0$  and  $T = 2.0$ . Simulations are started with 400 molecules of type A. The interaction parameters of different molecules are listed in Table 7.1. The numbers between brackets denote the uncertainty in the last digit.

Reaction	$\langle N_A \rangle$	$\langle N_{\text{Product } 1} \rangle$	$\langle N_{\text{Product } 2} \rangle$	$\langle \rho_{\text{tot}} \rangle$	Efficiency	Method
$A \rightleftharpoons B$	200.00(4)	200.00(4)		0.433(0)	0.077	Conventional
	200.0(2)	200.0(2)		0.431(0)	0.095	Parallel Rx/CFC
	200.01(8)	199.99(8)		0.432(0)	0.26	Serial Rx/CFC
$A \rightleftharpoons C$	226.48(4)	173.52(4)		0.392(0)	0.068	Conventional
	226.4(2)	173.6(2)		0.390(0)	0.079	Parallel Rx/CFC
	226.45(9)	173.55(9)		0.391(0)	0.26	Serial Rx/CFC
$A \rightleftharpoons 2D$	273.05(5)	253.89(9)		0.433(0)	0.017	Conventional
	272.8(2)	254.5(4)		0.430(0)	0.074	Parallel Rx/CFC
	272.8(2)	254.3(3)		0.431(0)	0.17	Serial Rx/CFC
$A \rightleftharpoons 2E$	300.57(6)	198.9(2)		0.395(0)	0.011	Conventional
	300.3(1)	199.4(2)		0.393(0)	0.059	Parallel Rx/CFC
	300.4(2)	199.3(3)		0.394(0)	0.17	Serial Rx/CFC
$A \rightleftharpoons D + F$	177.73(5)	222.27(5)	222.27(5)	0.433(0)	0.017	Conventional
	177.4(3)	222.6(3)	222.6(3)	0.431(0)	0.075	Parallel Rx/CFC
	177.5(2)	222.5(2)	222.5(2)	0.431(0)	0.17	Serial Rx/CFC
$A \rightleftharpoons D + E$	197.92(7)	202.08(7)	202.08(7)	0.401(0)	0.014	Conventional
	197.6(3)	202.4(3)	202.4(3)	0.399(0)	0.070	Parallel Rx/CFC
	197.6(2)	202.4(2)	202.4(2)	0.399(0)	0.17	Serial Rx/CFC

conventional method and parallel Rx/CFC.

In Fig. 7.7, the (unbiased) probability distributions  $p(\lambda, \delta)$  for two different reactions ( $A \rightleftharpoons B$ , and  $A \rightleftharpoons D + E$ ), and the weight functions to make  $p(\lambda, \delta)$  flat are shown. For the reaction  $A \rightleftharpoons B$ , the probability distributions and the weight functions for the reactants and reaction products are identical, as A and B have a similar interaction with the surrounding molecules. For the reaction  $A \rightleftharpoons D + E$ , one reactant molecule is replaced with two product molecules. For this reaction, the interactions of the first product molecule are scaled from no interactions (ideal gas molecule) to full interactions (whole molecule) when the value of  $\lambda$  is changed from 0 to  $\frac{1}{2}$ . For the second molecule, the interactions are scaled from no interactions (ideal gas molecule) to full interactions (whole molecule) when the

Table 7.4: Average number of molecules and density at equilibrium for different reactions for different methods. The efficiency is defined in Section 7.4. The reduced pressure and temperature are set to  $P = 3.0$  and  $T = 2.0$ , respectively. Simulations are started with 400 molecules of type A. The interaction parameters of different molecules are listed in Table 7.1. The numbers between brackets denote the uncertainty in the last digit.

Reaction	$\langle N_A \rangle$	$\langle N_{\text{Product } 1} \rangle$	$\langle N_{\text{Product } 2} \rangle$	$\langle \rho_{\text{tot}} \rangle$	Efficiency	Method
$A \rightleftharpoons B$	200.1(2)	199.9(2)		0.667(0)	$7 \cdot 10^{-3}$	Conventional
	199.9(4)	200.1(4)		0.665(0)	0.096	Parallel Rx/CFC
	199.9(2)	200.1(2)		0.667(0)	0.20	Serial Rx/CFC
$A \rightleftharpoons C$	268.7(2)	131.3(2)		0.614(0)	$5 \cdot 10^{-3}$	Conventional
	268.8(2)	131.2(2)		0.612(0)	0.076	Parallel Rx/CFC
	268.7(2)	131.3(2)		0.614(0)	0.20	Serial Rx/CFC
$A \rightleftharpoons 2D$	345.2(2)	109.5(4)		0.667(0)	$3 \cdot 10^{-4}$	Conventional
	345.0(3)	110.0(5)		0.665(0)	0.066	Parallel Rx/CFC
	344.8(4)	110.5(8)		0.666(0)	0.11	Serial Rx/CFC
$A \rightleftharpoons 2E$	373.0(2)	54.0(3)		0.646(0)	$1 \cdot 10^{-4}$	Conventional
	372.9(2)	54.1(3)		0.643(0)	0.051	Parallel Rx/CFC
	372.9(2)	54.3(4)		0.645(0)	0.11	Serial Rx/CFC
$A \rightleftharpoons D + F$	293.5(3)	106.5(3)	106.5(3)	0.667(0)	$3 \cdot 10^{-4}$	Conventional
	293.1(6)	106.9(6)	106.9(6)	0.665(0)	0.068	Parallel Rx/CFC
	293.3(5)	106.7(5)	106.7(5)	0.666(0)	0.11	Serial Rx/CFC
$A \rightleftharpoons D + E$	324.2(2)	75.8(2)	75.8(2)	0.641(0)	$2 \cdot 10^{-4}$	Conventional
	324.2(5)	75.8(5)	75.8(5)	0.638(0)	0.064	Parallel Rx/CFC
	324.1(4)	75.9(1)	75.9(1)	0.639(0)	0.11	Serial Rx/CFC

value of  $\lambda$  is changed from  $\frac{1}{2}$  to 1. This can also be clearly seen in the shape of the probability distribution of  $\lambda$  and the weight function of the reactant molecules. In this way, according to Eq. 7.18, one can obtain the excess chemical potential of the first reactant molecule using  $p(\lambda_R \downarrow 0)$  and  $p(\lambda_R \uparrow \frac{1}{2})$  and the excess chemical potential of the second reactant molecule using  $p(\lambda_R \downarrow \frac{1}{2})$  and  $p(\lambda_R \uparrow 1)$ . The values obtained for the excess chemical potential of the first and second reactant molecules were very close to each other. In Table 7.6, the sum of the total and excess chemical potentials times the stoichiometric coefficients are shown for the reactants and reaction products for different pressures and reactions. These values can only be directly computed in serial Rx/CFC according to Eq. A58. The data provided in Table 7.6 shows that for the reaction  $A \rightleftharpoons B$  where the reactant

Table 7.5: Average number of molecules and density at equilibrium for different reactions for different methods. The efficiency is defined in Section 7.4. The reduced pressure and temperature are set to  $P = 5.0$  and  $T = 2.0$ , respectively. Simulations are started with 400 molecules of type A. The interaction parameters of different molecules are listed in Table 7.1. The numbers between brackets denote the uncertainty in the last digit.

Reaction	$\langle N_A \rangle$	$\langle N_{\text{Product } 1} \rangle$	$\langle N_{\text{Product } 2} \rangle$	$\langle \rho_{\text{tot}} \rangle$	Efficiency	Method
$A \rightleftharpoons B$	199.8(3)	200.2(3)		0.766(0)	$1 \cdot 10^{-3}$	Conventional
	199(1)	201(1)		0.764(0)	0.096	Parallel Rx/CFC
	200.1(4)	199.9(4)		0.766(0)	0.20	Serial Rx/CFC
$A \rightleftharpoons C$	298.5(5)	101.5(5)		0.718(0)	$9 \cdot 10^{-4}$	Conventional
	298.5(8)	101.5(8)		0.716(0)	0.079	Parallel Rx/CFC
	298.6(4)	101.4(4)		0.718(0)	0.20	Serial Rx/CFC
$A \rightleftharpoons 2D$	372.5(3)	54.9(6)		0.766(0)	$3 \cdot 10^{-5}$	Conventional
	372.1(4)	55.8(7)		0.764(0)	0.063	Parallel Rx/CFC
	372.4(2)	55.2(4)		0.765(0)	0.11	Serial Rx/CFC
$A \rightleftharpoons 2E$	390.6(3)	18.8(5)		0.757(1)	$6 \cdot 10^{-6}$	Conventional
	390.6(2)	18.9(3)		0.755(0)	0.048	Parallel Rx/CFC
	390.5(2)	19.0(4)		0.756(0)	0.11	Serial Rx/CFC
$A \rightleftharpoons D + F$	345.2(5)	54.8(5)	54.8(2)	0.766(0)	$3 \cdot 10^{-5}$	Conventional
	345.4(6)	54.6(6)	54.6(6)	0.764(0)	0.067	Parallel Rx/CFC
	345.3(6)	54.7(6)	54.7(6)	0.765(0)	0.12	Serial Rx/CFC
$A \rightleftharpoons D + E$	368.1(6)	31.9(6)	31.9(6)	0.752(0)	$1 \cdot 10^{-5}$	Conventional
	368.2(4)	31.8(4)	31.8(4)	0.749(1)	0.063	Parallel Rx/CFC
	368.1(5)	31.9(5)	31.9(5)	0.751(0)	0.11	Serial Rx/CFC

and reaction products have identical LJ interactions, the values obtained for the chemical potentials of the reactants and reaction products are equal. Since molecules of A and B are identical (see Table 7.1), this is exactly what is expected. This case is included because it is trivial and can serve as an additional check on the implementation and on convergence of the simulation.

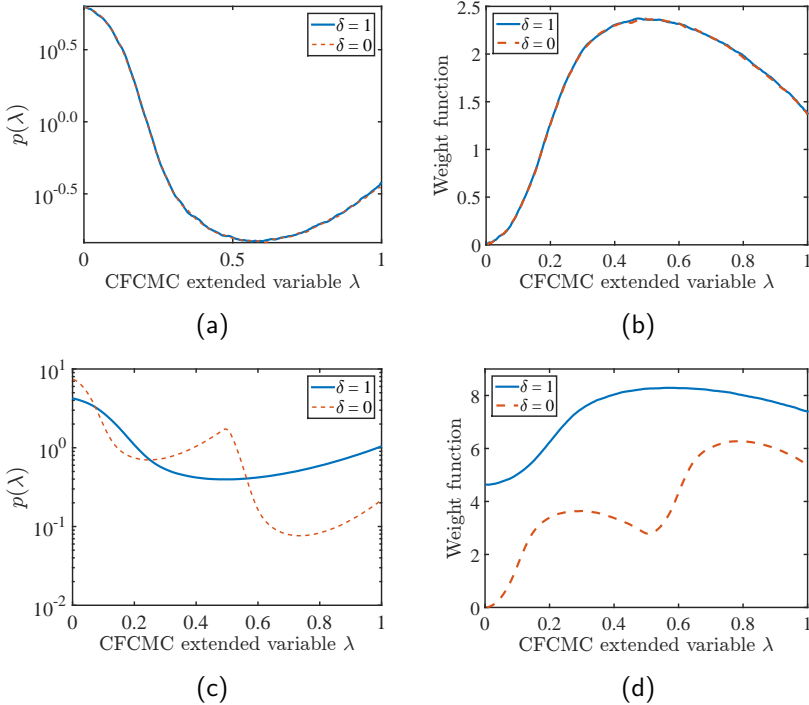


Figure 7.7: (a) and (c): Probability distributions  $p(\lambda, \delta)$  for reactants ( $\delta = 1$ ) and reactions products ( $\delta = 0$ ) for reaction (a)  $A \rightleftharpoons B$ , (c)  $A \rightleftharpoons D + E$  at a reduced temperature  $T = 2$ , and constant reduced pressure  $P = 3.0$ . (b) and (d): Weight functions (in units of  $k_B T$ ) to flatten the corresponding probability distributions of  $\lambda$  and to ensure that it is equally likely to have fractional molecules of reactants and reaction products for reactions (b)  $A \rightleftharpoons B$  (d)  $A \rightleftharpoons D + E$ .

It is verified that the computed excess chemical potentials are identical to those obtained from Widom's test particle insertion method in the conventional *NPT* ensemble at the same conditions (data not shown) [38]. For the reaction  $A \rightleftharpoons D + F$ , reaction products D and F have identical LJ interactions. Identical excess chemical potentials were obtained for D and F, while a fractional molecule of D was always inserted prior to an insertion of a fractional molecule of F.

Table 7.6: Chemical potentials of reactants and reaction products for different reactions of the Lennard-Jones system at different pressures obtained with serial Rx/CFC. The reduced temperature is set to  $T = 2.0$ . The interaction parameters of different molecules are listed in Table 7.1. The numbers between brackets denote the uncertainty in the last digit.

Reaction	$P$	$\sum_{\text{reactants}} \nu_i \mu_i^{\text{excess}}$	$\sum_{\text{reactants}} \nu_i \mu_i^{\text{tot}}$	$\sum_{\text{products}} \nu_i \mu_i^{\text{excess}}$	$\sum_{\text{products}} \nu_i \mu_i^{\text{tot}}$
$A \rightleftharpoons B$	0.3	-0.344(9)	7.036(9)	-0.344(6)	7.036(6)
	1.0	0.07(1)	9.42(1)	0.066(6)	9.421(6)
	3.0	2.73(1)	12.95(1)	2.727(6)	12.953(6)
	5.0	5.23(1)	15.74(1)	5.23(2)	15.73(1)
$A \rightleftharpoons C$	0.3	-0.265(8)	7.101(8)	-0.133(6)	7.101(6)
	1.0	0.25(1)	9.66(1)	0.79(1)	9.67(1)
	3.0	2.887(6)	13.541(6)	4.32(1)	13.53(1)
	5.0	5.35(2)	16.53(2)	7.51(2)	16.52(2)
$A \rightleftharpoons 2D$	0.3	-0.34(1)	6.13(1)	-0.68(1)	6.12(1)
	1.0	0.07(1)	9.49(1)	0.13(1)	9.48(1)
	3.0	2.73(1)	13.79(1)	5.43(4)	13.74(2)
	5.0	5.23(2)	16.84(2)	10.45(3)	16.74(2)
$A \rightleftharpoons 2E$	0.3	-0.240(9)	6.253(8)	-0.205(9)	6.245(9)
	1.0	0.247(8)	9.791(7)	1.553(9)	9.772(9)
	3.0	2.81(1)	14.08(1)	8.45(3)	13.98(1)
	5.0	5.25(3)	17.02(3)	14.78(8)	16.67(6)
$A \rightleftharpoons D + F$	0.3	-0.340(8)	4.319(8)	-0.68(1)	4.32(1)
	1.0	0.07(1)	8.30(2)	0.13(1)	8.29(1)
	3.0	2.724(9)	13.246(6)	5.44(2)	13.213(8)
	5.0	5.23(1)	16.57(1)	10.45(4)	16.52(2)
$A \rightleftharpoons D + E$	0.3	-0.270(7)	4.418(7)	-0.41(1)	4.43(1)
	1.0	0.220(9)	8.578(9)	0.96(1)	8.57(1)
	3.0	2.809(9)	13.573(9)	7.04(2)	13.528(6)
	5.0	5.27(2)	16.80(2)	12.69(6)	16.69(3)

It is instructive to repeat this test case for systems with a full LJ potential. The use of tail correction is dictated by legacy use of some force field like TraPPE, as these were developed using Monte Carlo methodology. It tries to approximate the “full” Lennard-Jones parameters using a finite (small) cutoff to keep computations tractable. However, for many other system, especially for use in MD, the discontinuity such a cutoff would create in the forces is problematic. In Appendix A.3, it is also shown that for the case of LJ molecules (truncated interactions and using analytic tail correction) identical values for the excess chemical potentials are obtained

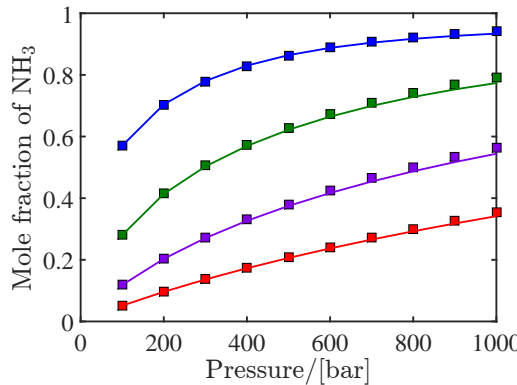


Figure 7.8: Mole fractions of ammonia at equilibrium obtained from serial Rx/CFC simulations (symbols), experiments (solid lines) [232] and, equation of state modeling using the Peng-Robinson equation of state (dashed lines) at 573K (blue), 673K (green), 773K (purple) and, 873K (red) as a function of pressure. All simulations start with a random configuration of 120 N<sub>2</sub>, 360 H<sub>2</sub> molecules, and no ammonium molecules.

from the serial RX/CFC, Widom's test particle insertion method in the conventional *NPT*, and EOS modeling using a full LJ potential [231]. Reaction equilibrium implies

$$\sum_{i=1}^R \mu_i \nu_i = \sum_{j=R+1}^S \mu_j \nu_j \quad (7.20)$$

It can be clearly seen that this condition is satisfied for all reactions at all pressures within the error bars. This indicates that simulations have reached the condition of chemical equilibrium, and one can trust the results obtained from the simulations. Moreover, one can directly compute the excess chemical potential of individual components according to Eq. 7.18. To test the suitability of serial Rx/CFC simulations for practical systems and molecules with partial charges, the ammonia synthesis reaction (N<sub>2</sub> + 3H<sub>2</sub> ⇌ 2NH<sub>3</sub>) is considered. Equilibrium compositions obtained from serial Rx/CFC are validated with the RASPA software [115, 116]. In Fig. 7.8, the mole frac-

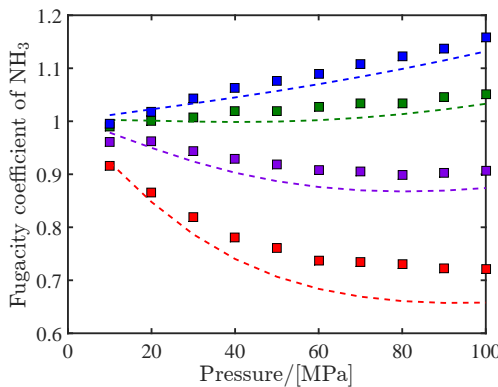


Figure 7.9: Fugacity coefficients of ammonia at equilibrium obtained from serial Rx/CFC simulations (symbols) and equation of state modeling using the Peng-Robinson equation of state (dashed lines) at 573K (blue), 673K (green), 773K (purple) and, 873K (red) as a function of pressure. All simulations start with a random configuration of 120 N<sub>2</sub>, 360 H<sub>2</sub> molecules, and no ammonium molecules.

tions of ammonia at equilibrium obtained from serial Rx/CFC simulations at different temperatures and pressures are compared with experimental results [232] and results using equation of state modeling (Peng-Robinson (PR) equation of state [233]). Excellent agreement is observed between the equilibrium mixture compositions obtained using the three different approaches. This validates the applicability of serial Rx/CFC for systems including molecules with electrostatic interactions. In Fig. 7.9, fugacity coefficients of ammonia at chemical equilibrium computed using serial Rx/CFC simulations are compared with the results of thermodynamic modeling (using the PR equation of state) at different temperatures and pressures. It is well-known that cubic equations of state fail to provide accurate estimates for the fugacity coefficient at very high pressures [234]. For pressures below 600 bar, fugacity coefficients computed using serial Rx/CFC simulations are in very good agreement with those calculated from equation of state modeling. No experimental data was found to compare with the values obtained for fugacity coefficients.

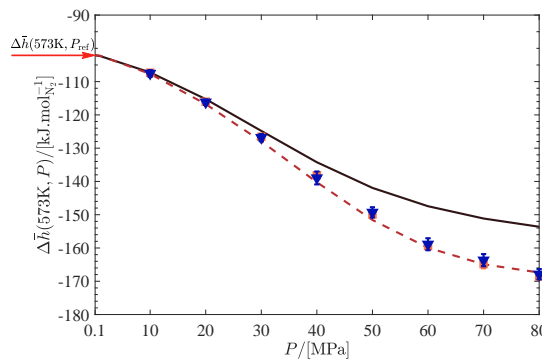


Figure 7.10: Computed reaction enthalpy of the Haber-Bosch process per mole of  $\text{N}_2$  at 573 K and pressure range of  $P = 10 \text{ MPa}$  to  $P = 80 \text{ MPa}$ . The arrow on the left indicates the value of the reaction enthalpy at standard reference pressure ( $P_{\text{ref}} = 1 \text{ bar}$ ). The compositions of the mixtures are obtained from equilibrium simulations of the Haber-Bosch reaction using serial Rx/CFC [147]. Different methods used to compute enthalpy of reaction: PR-EoS (solid line), PC-SAFT (dashed line), ND method (squares), CFCNPT ensemble (triangles). Raw data are listed in Table S12 of the Supporting Information.

Rahbari, Poursaeidesfahani, Vlugt, and co-workers have shown that by combining CFCMC and the original idea of Frenkel, Ciccotti, and co-workers [235, 236], one can compute partial molar excess enthalpies and partial molar volumes [237]. The contribution of the partial molar enthalpies to the reaction enthalpy of the Haber-Bosch process is significant at high pressures (up to 64% at a pressure of 80 MPa, relative to the reaction enthalpy at a pressure of 1 bar). This is shown in Fig. 7.10. At high pressures, the contribution of the partial molar excess enthalpies is not negligible for this reaction [237].

## 7.6 Conclusions

An improved formulation of the Reaction Ensemble combined with Continuous Fractional Component Monte Carlo is presented (serial Rx/CFC). The main difference between serial Rx/CFC and parallel Rx/CFC [170] is that in serial Rx/CFC, either the fractional molecules of the reactants or

the fractional molecules of the reaction products are present in the system. In serial Rx/CFC, there are three trial moves to facilitate a chemical reaction: (1) changing the value of  $\lambda$ ; (2) reaction for fractional molecules; (3) reaction for whole molecules. As a proof of principle, serial Rx/CFC is compared to the conventional formulation of RxMC and parallel Rx/CFC for systems of LJ molecules at different reduced pressures. Moreover, equilibrium mixture compositions obtained for the ammonia synthesis reaction using serial Rx/CFC are compared with experimental results and mixture compositions computed using equation of state modeling. The equilibrium compositions obtained with serial Rx/CFC are in excellent agreement with those obtained from the conventional RxMC and parallel Rx/CFC. For the ammonia synthesis reaction, excellent agreement between the results of serial Rx/CFC and experimental measured mixture compositions [232] was found as well. For systems at high pressures, the acceptance probability of the reaction trial move is improved by factor 2 to 3 (depending on the system under study) compared to parallel Rx/CFC. Serial Rx/CFC has the following advantages: (1) one directly obtains chemical potentials of all reactants and reaction products. These chemical potentials can directly be used as an independent check to ensure that chemical equilibrium is achieved; (2) independent biasing is applied to the fractional molecules of reactants and reaction products, therefore, the efficiency of the algorithm is increased; (3) changes in the maximum scaling parameter of intermolecular interactions can be chosen differently for reactants and reaction products. Serial Rx/CFC can be easily extended to molecules with intramolecular degrees of freedom. The trial moves of Fig. 7.3 can be performed by inserting fractional molecules at random positions with random orientations. The internal configuration of the molecule can be generated randomly or using the Rosenbluth scheme [38]. The trial moves of Fig. 7.4 can be performed by keeping the internal configuration of the molecule the same as in the old configuration. For ergodic sampling, trial moves that attempt to change the internal configuration of flexible molecules should be added to the MC method [38]. The serial Rx/CFC method could also be used for reactions involving ions. One can calculate the potential energy of periodic system with a net charge by placing a dummy charge at the center of charges. Al-

though it is difficult to interpret computed partial molar properties of ions (such as the chemical potential or the partial molar volume) [238], by using serial Rx/CFC one can still benefit from other advantages of the method such as efficient reaction trial moves.



# Appendix



In this Appendix, derivations of the expressions of the partition function and acceptance rules for the trial moves of the new formulation of the Reaction Ensemble Monte Carlo technique (RxMC) combined with the Continuous Fractional Component Monte Carlo technique (serial Rx/CFC) are presented. An expression for computing the chemical potential in the Gibbs ensemble for multicomponent mixtures is derived. This derivation is extended to arrive at an expression for chemical potentials in serial Rx/CFC. Details regarding the calculation of equilibrium mixture compositions by thermodynamic modelling using the Peng-Robinson equation of state are provided.

## A.1 Details on serial Rx/CFC

### A.1.1 Partition function of Serial Rx/CFC

In this section, we derive the partition function and acceptance rules for the constant volume version of serial Rx/CFC. In chapter 7 and appendix A.4, this is extended to the constant pressure version [38]. We start with the partition function of the Gibbs ensemble for a pure component with a single fractional molecule [132]:

$$\begin{aligned}
 Q_{\text{CFCMC}} = & \\
 & \frac{1}{\Lambda^{3(N_T+1)} N_T!} \sum_{i=1}^2 \sum_{N_1=0}^{N_T} \int_0^1 d\lambda \int_0^{V_T} dV_1 V_1^{N_1+\delta_{i,1}} (V_T - V_1)^{N_T-N_1+\delta_{i,2}} \\
 & \int ds^{N_1} \exp[-\beta U_{\text{int},1}(s^{N_1}, V_1)] \int ds^{N_T-N_1} \exp[-\beta U_{\text{int},2}(s^{N_T-N_1}, V_1)] \quad (\text{A1}) \\
 & \frac{N_T!}{N_1! (N_T - N_1)!} \left( \begin{array}{l} \delta_{i,1} \int ds_{\text{frac}}^1 \exp[-\beta U_{\text{frac},1}(s_{\text{frac}}^1, s^{N_1}, \lambda, V_1)] \\ + \delta_{i,2} \int ds_{\text{frac}}^2 \exp[-\beta U_{\text{frac},2}(s_{\text{frac}}^2, s^{N_T-N_1}, \lambda, V_1)] \end{array} \right)
 \end{aligned}$$

where  $\lambda$  is the scaling parameter with  $\lambda \in [0, 1]$ ,  $V_T$  is the total volume of the two boxes,  $V_1$  is the volume of box 1,  $N_T$  is the total number of whole

molecules in the two boxes,  $N_1$  is the number of whole molecules in box 1,  $U_{\text{int},i}$  is the total potential energy of whole molecules in box  $i$ , and  $U_{\text{frac},i}$  is the potential energy of the fractional molecule in box  $i$ . The fractional molecule can be either in box 1 ( $i = 1$ ,  $\delta_{i,1} = 1$ ,  $\delta_{i,2} = 0$ ) or in box 2 ( $i = 2$ ,  $\delta_{i,1} = 0$ ,  $\delta_{i,2} = 1$ ). When  $\lambda = 0$ , the fractional molecule has no interactions with surrounding molecules and when  $\lambda = 1$ , the fractional molecule has full interactions with surrounding molecules. To derive an expression for the partition function of the reaction ensemble, we consider the case where the volumes of the boxes are fixed and molecules in box 2 do not interact with each other (box 2 is an ideal gas). Later, we will take the limit that box 2 is infinitely large. In this case, the partition function  $Q_{\text{CFCMC}}$  becomes

$$Q_{\text{CFCMC}} = \frac{1}{\Lambda^{3(N_T+1)}} \sum_{\delta=0}^1 \sum_{N_1=0}^{N_T} \frac{V_1^{N_1+\delta} (V_T - V_1)^{N_T - N_1 + 1 - \delta}}{N_1! (N_T - N_1)!} \\ \int_0^1 d\lambda \int ds^{N_1} \exp[-\beta U_{\text{int},1}(s^{N_1})] \\ \left( \int ds_{\text{frac}}^1 \exp[-\beta \delta U_{\text{frac},1}(s_{\text{frac}}^1, s^{N_1}, \lambda)] \right) \quad (\text{A2})$$

where  $\delta = 1$  when the fractional molecule is in box 1 and otherwise  $\delta = 0$ . Next, we consider a system with multiple components. Each component has  $\nu_i$  fractional molecules ( $\nu_i > 0$ ). The fractional molecules of component  $i$  are either all in box 1 or in box 2. The interaction energy between fractional molecules themselves is included in the term  $U_{\text{frac},i}$ . Fractional molecules of type  $i$  are distinguishable from the whole molecules in box 1. Since there are no interactions between molecules in the ideal gas reservoir (box 2), fractional molecules are indistinguishable from whole molecules of the same component type in box 2.

In this case, we can write

$$\begin{aligned}
 Q_{\text{CFCMC}} = & \\
 & \sum_{N_1=0}^{N_{T,1}} \sum_{\delta_1=0}^1 \sum_{N_2=0}^{N_{T,2}} \sum_{\delta_2=0}^1 \dots \sum_{N_S=0}^{N_{T,S}} \sum_{\delta_S=0}^1 \prod_{i=1}^S \frac{V_1^{N_i + \nu_i \delta_i} (V_T - V_1)^{N_{T,i} + (1 - \delta_i) \nu_i - N_i}}{\Lambda_i^{3(N_{T,i} + \nu_i)} N_i! (N_{T,i} + (1 - \delta_i) \nu_i - N_i)!} \\
 & \int_0^1 d\lambda_1 \int_0^1 d\lambda_2 \dots \int_0^1 d\lambda_S \int ds^{N_{\text{int}}} \exp[-\beta U_{\text{int}}(s^{N_{\text{int}}})] \\
 & \left( \prod_{i=1}^S \int ds_{\text{frac}}^{\nu_i} \exp[-\beta \delta_i U_{\text{frac},i}(s_{\text{frac}}^{\nu_i}, s^{N_{\text{int}}}, \lambda_1, \dots, \lambda_S)] \right)
 \end{aligned} \tag{A3}$$

where  $S$  is the number of components,  $N_{T,i}$  is the total number of whole molecules of component  $i$  (in box 1 and box 2),  $N_{\text{int}}$  is the total number of whole molecules in box 1,  $N_i$  is the total number of whole molecules of type  $i$  in box 1.  $\delta_i = 1$  when the  $\nu_i$  fractional molecules of type  $i$  are in box 1, and  $\delta_i$  is zero otherwise. We assume that box 2 is very large and we want to express the term

$$\frac{(V_T - V_1)^{N_{T,i} + (1 - \delta_i) \nu_i - N_i}}{(N_{T,i} + (1 - \delta_i) \nu_i - N_i)!}$$

as a function of the chemical potential of component  $i$  in the reservoir. As  $V_T$  is much larger than  $V_1$  and  $N_T$  is much larger than  $N_1$ , we can write

$$\begin{aligned}
 (V_T - V_1)^{N_{T,i} + (1 - \delta_i) \nu_i - N_i} &\approx (V_T)^{N_{T,i} + (1 - \delta_i) \nu_i - N_i} \\
 &= (V_T)^{N_{T,i}} (V_T)^{(1 - \delta_i) \nu_i - N_i}
 \end{aligned} \tag{A4}$$

$$\begin{aligned}
 (N_{T,i} + (1 - \delta_i) \nu_i - N_i)! &\approx (N_{T,i})^{N_{T,i} + (1 - \delta_i) \nu_i - N_i} \\
 &= (N_{T,i})^{N_{T,i}} (N_{T,i})^{(1 - \delta_i) \nu_i - N_i}
 \end{aligned} \tag{A5}$$

Therefore, we can write

$$\begin{aligned} \frac{(V_T - V_1)^{N_{T,i} + (1-\delta_i)\nu_i - N_i}}{(N_{T,i} + (1 - \delta_i)\nu_i - N_i)!} &= \frac{(V_T)^{N_{T,i} + \nu_i} (V_T)^{-\delta_i\nu_i - N_i}}{(N_{T,i})^{N_{T,i} + \nu_i} (N_{T,i})^{-\delta_i\nu_i - N_i}} \\ &= (\text{constant}) \times \rho_i^{N_i + \delta_i\nu_i} \end{aligned} \quad (\text{A6})$$

where  $\rho_i = N_{T,i}/V_T$  is the number density of component  $i$  in box 2 (the ideal gas reservoir). When  $N_{T,i} \rightarrow \infty$ ,  $V_T \rightarrow \infty$ , and  $\rho_i$  is a finite number, we can replace the term

$$\frac{(V_T - V_1)^{N_{T,i} + (1-\delta_i)\nu_i - N_i}}{(N_{T,i} + (1 - \delta_i)\nu_i - N_i)!}$$

with  $\rho_i^{N_i + \nu_i\delta_i}$  and we can rewrite the corresponding partition function as

$$\begin{aligned} Q_{\text{CFCMC, GC}} &= \\ &\sum_{N_1=0}^{\infty} \sum_{\delta_1=0}^1 \sum_{N_2=0}^{\infty} \sum_{\delta_2=0}^1 \dots \sum_{N_S=0}^{\infty} \sum_{\delta_S=0}^1 \prod_{i=1}^S \frac{V_1^{N_i + \nu_i\delta_i} \rho_i^{N_i + \nu_i\delta_i} \Lambda_i^{3(N_i + \nu_i\delta_i)}}{\Lambda_i^{3(N_i + \nu_i\delta_i)} N_i!} \\ &\int_0^1 d\lambda_1 \int_0^1 d\lambda_2 \dots \int_0^1 d\lambda_S \int ds^{N_{\text{int}}} \exp[-\beta U_{\text{int}}(s^{N_{\text{int}}})] \\ &\left( \prod_{i=1}^S \int ds_{\text{frac}}^{\nu_i} \exp[-\beta \delta_i U_{\text{frac},i}(s_{\text{frac}}^{\nu_i}, s^{N_{\text{int}}}, \lambda_1, \dots, \lambda_S)] \right) \end{aligned} \quad (\text{A7})$$

Essentially, we have moved to the grand-canonical (GC) ensemble and the sums over the number of molecules run from 0 to  $\infty$ . Here, the subscript GC refers to grand-canonical and this is used to emphasise that the reaction ensemble is essentially a grand-canonical ensemble where the chemical

potentials of components are constant. For an ideal gas we have [197]

$$\begin{aligned}\mu_i &= \mu_i^\circ + \frac{1}{\beta} \ln \frac{\rho_i}{\beta P^\circ} \\ \mu_i^\circ &= -\frac{1}{\beta} \ln \left( \frac{q_i}{\beta P^\circ \Lambda_i^3} \right)\end{aligned}\quad (\text{A8})$$

where  $\mu_i^\circ$  is the reference chemical potential,  $P^\circ$  is the standard reference pressure ( $10^5$  Pa),  $\Lambda_i$  is thermal wavelength of component  $i$ .  $q_i$  is the ideal gas phase partition function of an isolated molecule of type  $i$  excluding the translational part [197]. See also Eq. 7.15. Therefore, we can write

$$\begin{aligned}\mu_i &= -\frac{1}{\beta} \ln \left( \frac{q_i}{\beta P^\circ \Lambda_i^3} \right) + \frac{1}{\beta} \ln \frac{\rho_i}{\beta P^\circ} \\ \exp [\beta \mu_i (N_i + \nu_i \delta_i)] &= \rho_i^{N_i + \nu_i \delta_i} \left( \frac{\Lambda_i^3}{q_i} \right)^{N_i + \nu_i \delta_i}\end{aligned}\quad (\text{A9})$$

and arrive at

$$\rho_i^{N_i + \nu_i \delta_i} \Lambda_i^{3(N_i + \nu_i \delta_i)} = \exp [\beta \mu_i (N_i + \nu_i \delta_i) + (N_i + \nu_i \delta_i) \ln q_i] \quad (\text{A10})$$

Substituting Eq. A10 into Eq. A7 yields

$$\begin{aligned}Q_{\text{CFCMC,GC}} &= \\ &\sum_{N_1=0}^{\infty} \sum_{\delta_1=0}^1 \sum_{N_2=0}^{\infty} \sum_{\delta_2=0}^1 \dots \sum_{N_S=0}^{\infty} \sum_{\delta_S=0}^1 \prod_{i=1}^S \frac{V_1^{N_i + \nu_i \delta_i} \exp [\beta \mu_i (N_i + \nu_i \delta_i) + (N_i + \nu_i \delta_i) \ln q_i]}{\Lambda_i^{3(N_i + \nu_i \delta_i)} N_i!} \\ &\int_0^1 d\lambda_1 \int_0^1 d\lambda_2 \dots \int_0^1 d\lambda_S \int ds^{N_{\text{int}}} \exp [-\beta U_{\text{int}}(s^{N_{\text{int}}})] \\ &\left( \prod_{i=1}^S \int ds_{\text{frac}}^{\nu_i} \exp [-\beta \delta_i U_{\text{frac},i}(s_{\text{frac}}^{\nu_i}, s^{N_{\text{int}}}, \lambda_1, \dots, \lambda_S)] \right)\end{aligned}\quad (\text{A11})$$

We can rearrange the partition function as follows:

$$\begin{aligned}
Q_{\text{CFCMC,GC}} = & \sum_{N_1=0}^{\infty} \sum_{\delta_1=0}^1 \sum_{N_2=0}^{\infty} \sum_{\delta_2=0}^1 \dots \sum_{N_S=0}^{\infty} \sum_{\delta_S=0}^1 \exp \left[ \beta \sum_{i=1}^S \mu_i (N_i + \nu_i \delta_i) + \sum_{i=1}^S (N_i + \nu_i \delta_i) \ln \frac{V q_i}{\Lambda_i^3} - \sum_{i=1}^S \ln N_i! \right] \\
& \int_0^1 d\lambda_1 \int_0^1 d\lambda_2 \dots \int_0^1 d\lambda_S \int ds^{N_{\text{int}}} \exp[-\beta U_{\text{int}}(s^{N_{\text{int}}})] \\
& \left( \prod_{i=1}^S \int ds_{\text{frac}}^{\nu_i} \exp[-\beta \delta_i U_{\text{frac},i}(s_{\text{frac}}^{\nu_i}, s^{N_{\text{int}}}, \lambda_1, \dots, \lambda_S)] \right)
\end{aligned} \tag{A12}$$

Next, we move to the reaction ensemble and divide the components into reactants ( $R$ ) and reaction products ( $P$ ). For simplicity, we only consider systems with a single reaction as extension to systems with multiple reactions is trivial. We consider the case that we either have fractional molecules of reactants ( $\delta = 1$ ) or fractional molecules of reaction products ( $\delta = 0$ ). The number of fractional molecules of component  $i$  equals the stoichiometric coefficient of component  $i$  ( $\nu_i > 0$ ) in the reaction or equals zero when a component does not participate in the reaction. For convenience, we defined the stoichiometric coefficient as non-negative numbers. This means that we have to specify whether a component type is a reactant, reaction product, or inert species. Instead of  $\lambda_i$  for each component, we have an overall  $\lambda$  for the system which translates to  $\lambda$  of individual fractional molecules. Eq. A12 then reduces to

$$\begin{aligned}
Q_{\text{CFCMC,GC}} = & \sum_{N_1=0}^{\infty} \dots \sum_{N_S=0}^{\infty} \sum_{\delta=0}^1 \exp \left[ \beta \sum_{i=1}^R \mu_i (N_i + \nu_i \delta) + \sum_{i=1}^R (N_i + \nu_i \delta) \ln \frac{V q_i}{\Lambda_i^3} - \sum_{i=1}^R \ln N_i! \right] \\
& \exp \left[ \beta \sum_{j=R+1}^S \mu_j (N_j + \nu_j(1-\delta)) + \sum_{j=R+1}^S (N_j + \nu_j(1-\delta)) \ln \frac{V q_j}{\Lambda_j^3} - \sum_{j=R+1}^S \ln N_j! \right] \\
& \int_0^1 d\lambda \int ds^{N_{\text{int}}} \exp[-\beta U_{\text{int}}(s^{N_{\text{int}}})] \left( \prod_{i=1}^R \int ds_{\text{frac}}^{\nu_i} \exp[-\beta \delta_i U_{\text{frac},i}(s_{\text{frac}}^{\nu_i}, s^{N_{\text{int}}}, \lambda)] \right) \\
& \left( \prod_{j=R+1}^S \int ds_{\text{frac}}^{\nu_j} \exp[-\beta(1-\delta) U_{\text{frac},j}(s_{\text{frac}}^{\nu_j}, s^{N_{\text{int}}}, \lambda)] \right)
\end{aligned} \tag{A13}$$

where  $R$  is the number of reactant components, and  $P$  is the number of reaction product components so  $R + P = S$ . Therefore, the number of reaction product components is ranging from  $R + 1$  to  $S$  with  $S$  being the total number of components.

### A.1.2 Partition function of the reaction ensemble with CFCMC for the ideal gas case

In the ideal gas case, molecules do not interact. Therefore, the energy terms in the partition functions of the conventional reaction ensemble and the reaction ensemble with CFCMC can be disregarded. The partition functions of the conventional reaction ensemble and the reaction ensemble with CFCMC for the ideal gas case are

$$Q_{\text{Conv}}^{\text{IG}} = \sum_{N_1=0}^{\infty} \dots \sum_{N_S=0}^{\infty} \exp \left[ \beta \sum_{i=1}^S \mu_i N_i + \sum_{i=1}^S N_i \ln \frac{V q_i}{\Lambda_i^3} - \sum_{i=1}^S \ln N_i! \right] \quad (\text{A14})$$

$$\begin{aligned} Q_{\text{CFCMC,GC}}^{\text{IG}} = & \\ & \sum_{N_1=0}^{\infty} \dots \sum_{N_S=0}^{\infty} \sum_{\delta=0}^1 \exp \left[ \beta \sum_{i=1}^R \mu_i (N_i + \nu_i \delta) + \sum_{i=1}^R (N_i + \nu_i \delta) \ln \frac{V q_i}{\Lambda_i^3} - \sum_{i=1}^R \ln N_i! \right] \times \\ & \exp \left[ \beta \sum_{j=R+1}^S \mu_j (N_j + \nu_j (1 - \delta)) + \sum_{j=R+1}^S (N_j + \nu_j (1 - \delta)) \ln \frac{V q_j}{\Lambda_j^3} - \sum_{j=R+1}^S \ln N_j! \right] \end{aligned} \quad (\text{A15})$$

One can separate the two cases  $\delta = 0$  and  $\delta = 1$ , and rewrite Eq. A15 as

$$\begin{aligned}
Q_{\text{CFCMC,GC}}^{\text{IG}} &= \\
&\sum_{N_1=0}^{\infty} \dots \sum_{N_S=0}^{\infty} \exp \left[ \beta \sum_{i=1}^R \mu_i N_i + \sum_{i=1}^R N_i \ln \frac{V q_i}{\Lambda_i^3} - \sum_{i=1}^R \ln N_i! \right] \times \\
&\exp \left[ \beta \sum_{j=R+1}^S \mu_j (N_j + \nu_j) + \sum_{j=R+1}^S (N_j + \nu_j) \ln \frac{V q_j}{\Lambda_j^3} - \sum_{j=R+1}^S \ln N_j! \right] + \\
&\exp \left[ \beta \sum_{i=1}^R \mu_i (N_i + \nu_i) + \sum_{i=1}^R (N_i + \nu_i) \ln \frac{V q_i}{\Lambda_i^3} - \sum_{i=1}^R \ln N_i! \right] \times \\
&\exp \left[ \beta \sum_{j=R+1}^S \mu_j N_j + \sum_{j=R+1}^S N_j \ln \frac{V q_j}{\Lambda_j^3} - \sum_{j=R+1}^S \ln N_j! \right] \quad (\text{A16}) \\
&= \sum_{N_1=0}^{\infty} \dots \sum_{N_S=0}^{\infty} \exp \left[ \beta \sum_{i=1}^R \mu_i N_i + \sum_{i=1}^R N_i \ln \frac{V q_i}{\Lambda_i^3} - \sum_{i=1}^R \ln N_i! \right] \times \\
&\exp \left[ \beta \sum_{j=R+1}^S \mu_j N_j + \sum_{j=R+1}^S N_j \ln \frac{V q_j}{\Lambda_j^3} - \sum_{j=R+1}^S \ln N_j! \right] \times \\
&\left[ \exp \left[ \beta \sum_{i=1}^R \mu_i \nu_i + \sum_{i=1}^R \nu_i \ln \frac{V q_i}{\Lambda_i^3} \right] + \exp \left[ \beta \sum_{j=R+1}^S \mu_j \nu_j + \sum_{j=R+1}^S \nu_j \ln \frac{V q_j}{\Lambda_j^3} \right] \right]
\end{aligned}$$

The last term is simply a constant for given values of  $\mu_i$ ,  $\Lambda_i$ , and  $q_i$  for all component. Therefore, we have

$$\begin{aligned}
Q_{\text{CFCMC,GC}}^{\text{IG}} &= \\
&\sum_{N_1=0}^{\infty} \dots \sum_{N_S=0}^{\infty} \exp \left[ \beta \sum_{i=1}^S \mu_i N_i + \sum_{i=1}^S N_i \ln \frac{V q_i}{\Lambda_i^3} - \sum_{i=1}^S \ln N_i! \right] \times \text{Constant} \quad (\text{A17}) \\
&= Q_{\text{Conv}}^{\text{IG}} \times \text{Constant}
\end{aligned}$$

Therefore, ensemble averages computed in the ensemble of Eq. A15 are identical to those computed in the ensemble of Eq. A14, provided that the quantity of which the ensemble average is computed does not depend on

$\lambda$  or  $\delta$ . By not counting fractional molecules when computing ensemble averages of the number of molecules of a component, one is guaranteed that the ensembles of Eqs. A14 and A15 yield the same results. It is therefore a natural choice not to count fractional molecules when computing ensemble averages for systems with intermolecular interactions.

### A.1.3 Trial moves and acceptance rules

Starting from the partition function of Eq. A13, we derive the acceptance rules for the trial moves of serial Rx/CFC. These trial move are also illustrated in Figs. 7.2 to 7.4.

### A.1.4 Changing the value of $\lambda$

This trial move is used to change the value of  $\lambda$  (see Fig. 7.2) while keeping  $\delta$  and all molecules positions constant. When the new  $\lambda$  is outside the interval  $[0,1]$ , this trial move is automatically rejected. In this trial move, the number of whole molecules and fractional molecules remains the same. By changing the value of  $\lambda$ , only the strength of interactions between the fractional molecules and the whole molecules are changed. Therefore, the probabilities of being in the old (o) and new (n) configurations are

$$\begin{aligned} p_o &= \frac{\exp[-\beta U_o]}{Q_{\text{CFCMC,GC}}} \exp \left[ \beta \sum_{i=1}^R \mu_i (N_i + \nu_i \delta) + \sum_{i=1}^R (N_i + \nu_i \delta) \ln \frac{V q_i}{\Lambda_i^3} - \sum_{i=1}^R \ln N_i! \right] \\ &\quad \exp \left[ \beta \sum_{j=R+1}^S \mu_j (N_j + \nu_j(1-\delta)) + \sum_{j=R+1}^S (N_j + \nu_j(1-\delta)) \ln \frac{V q_j}{\Lambda_j^3} - \sum_{j=R+1}^S \ln N_j! \right] \quad (\text{A18}) \\ p_n &= \frac{\exp[-\beta U_n]}{Q_{\text{CFCMC,GC}}} \exp \left[ \beta \sum_{i=1}^R \mu_i (N_i + \nu_i \delta) + \sum_{i=1}^R (N_i + \nu_i \delta) \ln \frac{V q_i}{\Lambda_i^3} - \sum_{i=1}^R \ln N_i! \right] \\ &\quad \exp \left[ \beta \sum_{j=R+1}^S \mu_j (N_j + \nu_j(1-\delta)) + \sum_{j=R+1}^S (N_j + \nu_j(1-\delta)) \ln \frac{V q_j}{\Lambda_j^3} - \sum_{j=R+1}^S \ln N_j! \right] \end{aligned}$$

where  $U_o$  and  $U_n$  are the total potential energies in the old and new configurations, respectively. Therefore the acceptance rule for this trial move is

$$\text{acc}(\text{o} \rightarrow \text{n}) = \min [1, \exp [-\beta \Delta U]] \quad (\text{A19})$$

in which  $\Delta U = U_{\text{n}} - U_{\text{o}}$ .

### A.1.5 Reaction for fractional molecules

In this trial move, the fractional molecules of reactants/reaction products are removed and fractional molecules of reaction/reactants are inserted at random positions (see Fig. 7.3). The number of whole molecules and also the value of  $\lambda$  are constant but the value of  $\delta$  changes. This trial move basically mimics the reaction for fractional molecules and is very efficient at low values of  $\lambda$ . Here, we derive the acceptance rule for the forward reaction (reactants  $\rightarrow$  reaction products). The acceptance rule for the reverse reaction (reaction products  $\rightarrow$  reactants) simply follows by swapping the labels. The direction of the reaction eventually depends on the value of  $\delta$  for the old configuration (if we have the fractional molecules of reactants or reaction products). The probabilities of being in the old (o) and new (n) configurations are

$$p_{\text{o}} = \frac{\exp[-\beta U_{\text{o}}]}{Q_{\text{CFCMC,GC}}} \exp \left[ \beta \sum_{i=1}^R \mu_i (N_i + \nu_i \delta_{\text{o}}) + \sum_{i=1}^R (N_i + \nu_i \delta_{\text{o}}) \ln \frac{V q_i}{\Lambda_i^3} - \sum_{i=1}^R \ln N_i! \right] \\ \exp \left[ \beta \sum_{j=R+1}^S \mu_j (N_j + \nu_j (1 - \delta_{\text{o}})) + \sum_{j=R+1}^S (N_j + \nu_j (1 - \delta_{\text{o}})) \ln \frac{V q_j}{\Lambda_j^3} - \sum_{j=R+1}^S \ln N_j! \right] \quad (\text{A20})$$

$$p_{\text{n}} = \frac{\exp[-\beta U_{\text{n}}]}{Q_{\text{CFCMC,GC}}} \exp \left[ \beta \sum_{i=1}^R \mu_i (N_i + \nu_i \delta_{\text{n}}) + \sum_{i=1}^R (N_i + \nu_i \delta_{\text{n}}) \ln \frac{V q_i}{\Lambda_i^3} - \sum_{i=1}^R \ln N_i! \right] \\ \exp \left[ \beta \sum_{j=R+1}^S \mu_j (N_j + \nu_j (1 - \delta_{\text{n}})) + \sum_{j=R+1}^S (N_j + \nu_j (1 - \delta_{\text{n}})) \ln \frac{V q_j}{\Lambda_j^3} - \sum_{j=R+1}^S \ln N_j! \right] \quad (\text{A21})$$

where we have used the notation  $\delta_{\text{n}}, \delta_{\text{o}}$  for the value of  $\delta$  in the new and old configurations, respectively. If  $\delta_{\text{o}} = 1$  then  $\delta_{\text{n}} = 0$  (and vice versa). For the forward reaction (reactants  $\rightarrow$  reaction products), we have  $\delta_{\text{o}} = 1$  and

$\delta_n = 0$ . Therefore, we can rewrite Eqs. A20 and A21 as

$$\begin{aligned} p_o &= \frac{\exp[-\beta U_o]}{Q_{CFCMC,GC}} \exp \left[ \beta \sum_{i=1}^R \mu_i (N_i + \nu_i) + \sum_{i=1}^R (N_i + \nu_i) \ln \frac{Vq_i}{\Lambda_i^3} - \sum_{i=1}^R \ln N_i! \right] \\ &\quad \exp \left[ \beta \sum_{j=R+1}^S \mu_j N_j + \sum_{j=R+1}^S N_j \ln \frac{Vq_j}{\Lambda_j^3} - \sum_{j=R+1}^S \ln N_j! \right] \end{aligned} \quad (\text{A22})$$

$$\begin{aligned} p_n &= \frac{\exp[-\beta U_n]}{Q_{CFCMC,GC}} \exp \left[ \beta \sum_{i=1}^R \mu_i N_i + \sum_{i=1}^R N_i \ln \frac{Vq_i}{\Lambda_i^3} - \sum_{i=1}^R \ln N_i! \right] \\ &\quad \exp \left[ \beta \sum_{j=R+1}^S \mu_j (N_j + \nu_j) + \sum_{j=R+1}^S (N_j + \nu_j) \ln \frac{Vq_j}{\Lambda_j^3} - \sum_{j=R+1}^S \ln N_j! \right] \end{aligned} \quad (\text{A23})$$

It is important to note that the number of whole molecules of each component does not change in this trial move. Therefore, we have

$$\begin{aligned} \frac{p_n}{p_o} &= \exp \left[ -\beta \sum_{i=1}^R \mu_i \nu_i - \sum_{i=1}^R \nu_i \ln \frac{Vq_i}{\Lambda_i^3} + \beta \sum_{j=R+1}^S \mu_j \nu_j + \sum_{j=R+1}^S \nu_j \ln \frac{Vq_j}{\Lambda_j^3} \right] \\ &\quad \times \exp [-\beta \Delta U] \end{aligned} \quad (\text{A24})$$

Reaction equilibrium implies  $\sum_{i=1}^R \mu_i \nu_i = \sum_{j=R+1}^S \mu_j \nu_j$ . Consequently, Eq. A24 reduces to

$$\frac{p_n}{p_o} = \exp \left[ - \sum_{i=1}^R \nu_i \ln \frac{Vq_i}{\Lambda_i^3} + \sum_{j=R+1}^S \nu_j \ln \frac{Vq_j}{\Lambda_j^3} \right] \times \exp [-\beta \Delta U] \quad (\text{A25})$$

Therefore the acceptance rule for this trial move is

$$\text{acc}(o \rightarrow n) = \min \left[ 1, \left[ \prod_{i=1}^R \left( \frac{Vq_i}{\Lambda_i^3} \right)^{-\nu_i} \right] \times \left[ \prod_{j=R+1}^S \left( \frac{Vq_j}{\Lambda_j^3} \right)^{\nu_j} \right] \times \exp [-\beta \Delta U] \right] \quad (\text{A26})$$

For the limiting case of  $\lambda \rightarrow 0$ , this acceptance rule reduces to

$$\text{acc}(\text{o} \rightarrow \text{n}) = \min \left[ 1, \left[ \prod_{i=1}^R \left( \frac{Vq_i}{\Lambda_i^3} \right)^{-\nu_i} \right] \times \left[ \prod_{j=R+1}^S \left( \frac{Vq_j}{\Lambda_j^3} \right)^{\nu_j} \right] \right] \quad (\text{A27})$$

### A.1.6 Reaction for whole molecules

In this trial move, the fractional molecules of reactants/reaction products are transformed into whole molecules of reactants/reaction products while at the same time, randomly selected whole molecules of reaction products/reactants are transformed into the fractional molecules of reaction products/reactants. All molecule positions stay the same. This trial move is illustrated in Fig. 7.4. The value of  $\lambda$  remains constant during this trial move and the value of  $\delta$  changes. This trial move can be seen as a reaction for whole molecules. In the forward reaction, whole molecule of reactants are transformed into fractional molecules and, at the same time, fractional molecules of reaction products are turned into whole molecules. Essentially, the number of whole molecules of reactants is reduced and the number of whole molecules of reaction products is increased, according to their stoichiometric coefficients. This trial move is very efficient when the value of  $\lambda$  is close to 1. Trial moves are automatically rejected when there are not enough whole molecules to turn into fractional molecules. Here, we derive the acceptance rule for the forward reaction (reactants  $\rightarrow$  reaction products), so the fractional molecules of the reaction products are converted into whole molecules, and  $\nu_i$  whole molecules of reactants are converted into fractional molecules. The acceptance rule for the reverse reaction (reaction products  $\rightarrow$  reactants) simply follows by swapping the labels. The direction of the reaction eventually depends on the value of  $\delta$  for the old configuration (if we have the fractional molecules of reactants or reaction products).

The probabilities of being in the old (o) and new (n) configurations are

$$p_o = \frac{\exp[-\beta U_o]}{Q_{\text{CFCMC,GC}}} \exp \left[ \beta \sum_{i=1}^R \mu_i (N_i + \nu_i \delta_o) + \sum_{i=1}^R (N_i + \nu_i \delta_o) \ln \frac{V q_i}{\Lambda_i^3} - \sum_{i=1}^R \ln N_i! \right] \\ \exp \left[ \beta \sum_{j=R+1}^S \mu_j (N_j + \nu_j(1 - \delta_o)) + \sum_{j=R+1}^S (N_j + \nu_j(1 - \delta_o)) \ln \frac{V q_j}{\Lambda_j^3} - \sum_{j=R+1}^S \ln N_j! \right] \quad (\text{A28})$$

$$p_n = \frac{\exp[-\beta U_n]}{Q_{\text{CFCMC,GC}}} \exp \left[ \beta \sum_{i=1}^R \mu_i (N_i - \nu_i + \nu_i \delta_n) + \sum_{i=1}^R (N_i - \nu_i + \nu_i \delta_n) \ln \frac{V q_i}{\Lambda_i^3} - \sum_{i=1}^R \ln (N_i - \nu_i)! \right] \\ \exp \left[ \beta \sum_{j=R+1}^S \mu_j (N_j + \nu_j + \nu_j(1 - \delta_n)) + \sum_{j=R+1}^S (N_j + \nu_j + \nu_j(1 - \delta_n)) \ln \frac{V q_j}{\Lambda_j^3} - \sum_{j=R+1}^S \ln (N_j + \nu_j)! \right] \quad (\text{A29})$$

For the forward reaction (reactants  $\rightarrow$  reaction products) we have  $\delta_o = 0$  and  $\delta_n = 1$ . Therefore, we can write

$$p_o = \frac{\exp[-\beta U_o]}{Q_{\text{CFCMC}}} \exp \left[ \beta \sum_{i=1}^R \mu_i N_i + \sum_{i=1}^R N_i \ln \frac{V q_i}{\Lambda_i^3} - \sum_{i=1}^R \ln N_i! \right] \\ \exp \left[ \beta \sum_{j=R+1}^S \mu_j (N_j + \nu_j) + \sum_{j=R+1}^S (N_j + \nu_j) \ln \frac{V q_j}{\Lambda_j^3} - \sum_{j=R+1}^S \ln N_j! \right] \quad (\text{A30})$$

$$p_n = \frac{\exp[-\beta U_n]}{Q_{\text{CFCMC}}} \exp \left[ \beta \sum_{i=1}^R \mu_i N_i + \sum_{i=1}^R N_i \ln \frac{V q_i}{\Lambda_i^3} - \sum_{i=1}^R \ln (N_i - \nu_i)! \right] \\ \exp \left[ \beta \sum_{j=R+1}^S \mu_j (N_j + \nu_j) + \sum_{j=R+1}^S (N_j + \nu_j) \ln \frac{V q_j}{\Lambda_j^3} - \sum_{j=R+1}^S \ln (N_j + \nu_j)! \right] \quad (\text{A31})$$

Since the total number of whole plus fractional molecules of each component remains constant in this trial move, the terms related to the chemical potential and ideal gas partition function are the same for the old and new

configurations. Therefore, we have

$$\frac{p_n}{p_o} = \exp \left[ \sum_{i=1}^R \ln \frac{N_i!}{(N_i - \nu_i)!} + \sum_{j=R+1}^S \ln \frac{N_j!}{(N_j + \nu_j)!} \right] \times \exp [-\beta \Delta U] \quad (\text{A32})$$

in which  $\Delta U = U_n - U_o$ . Therefore, the acceptance rule is

$$\text{acc}(o \rightarrow n) = \min \left[ 1, \prod_{i=1}^R \frac{N_i!}{(N_i - \nu_i)!} \times \prod_{j=R+1}^S \frac{N_j!}{(N_j + \nu_j)!} \times \exp [-\beta \Delta U] \right] \quad (\text{A33})$$

For the limiting case of  $\lambda \rightarrow 1$ , the acceptance rule reduces to

$$\text{acc}(o \rightarrow n) = \min \left[ 1, \prod_{i=1}^R \frac{N_i!}{(N_i - \nu_i)!} \times \prod_{j=R+1}^S \frac{N_j!}{(N_j + \nu_j)!} \right] \quad (\text{A34})$$

## A.2 Chemical potentials of mixtures in the conventional Gibbs ensemble

To assess the condition of chemical equilibria in the Rx/CFC ensemble, we should calculate the chemical potentials of all reactants and products. Here, we derive an expression for the calculation of chemical potentials of different components for a multicomponent mixtures in the NVT version of the conventional Gibbs ensemble. For the NPT version of the Gibbs ensemble, the derivation is similar and one can easily show that it leads to the same result. In the next section, the result of this derivation is used to derive an expression for each component in the Rx/CFC ensemble. We will follow the original derivation of Frenkel and Smit for the single-component Gibbs ensemble [177]. We start with the partition function of the conventional Gibbs ensemble of a mixture of  $S$  components [38]

$$Q_{\text{normal,GE}} = \sum_{N_1=0}^{N_{T,1}} \sum_{N_2=0}^{N_{T,2}} \dots \sum_{N_s=0}^{N_{T,S}} \int_0^{V_T} dV_1 \left( \prod_{i=1}^S \frac{V_1^{N_i} (V_T - V_1)^{N_{T,i} - N_i}}{\Lambda^{3N_{T,i}} N_i! (N_{T,i} - N_i)!} \right) \int ds^{N_{\text{total}}} \exp[-\beta U(s^{N_{\text{total}}}, V_1)] \quad (\text{A35})$$

The chemical potential of a component equals the partial derivative of the free energy with respect to the number of molecules of that component [38].

$$\mu_i = \left( \frac{\partial F}{\partial N_i} \right)_{V,T,N_j \neq i} \approx \frac{F_{N_{\text{total}}+1} - F_{N_{\text{total}}}}{1} \approx \frac{F_{N_{\text{total}}+\nu_i} - F_{N_{\text{total}}}}{\nu_i} \quad (\text{A36})$$

Therefore, when adding  $\nu_i$  molecules, we have

$$\nu_i \mu_i = F_{N_{\text{total}}+\nu_i} - F_{N_{\text{total}}} = \frac{-1}{\beta} \ln \left( \frac{Q_{N_{\text{total}}+\nu_i}}{Q_{N_{\text{total}}}} \right) \quad (\text{A37})$$

We can extend this to mixtures and write

$$\sum_{i=1}^R \nu_i \mu_i = \frac{-1}{\beta} \ln \left( \frac{Q_{N_{\text{total}} + \sum_{i=1}^R \nu_i}}{Q_{N_{\text{total}}}} \right) \quad (\text{A38})$$

In this case, we have

$$\begin{aligned} & Q_{N_{\text{total}} + \sum_{i=1}^R \nu_i} = \\ & \sum_{N_1=0}^{N_{T,1}+\nu_1} \dots \sum_{N_R=0}^{N_{T,R}+\nu_R} \dots \sum_{N_{R+1}=0}^{N_{T,R+1}} \dots \sum_{N_s=0}^{N_{T,S}} \int_0^{V_T} dV_1 \left( \prod_{i=R+1}^S \frac{V_1^{N_i} (V_T - V_1)^{N_{T,i}-N_i}}{\Lambda^{3N_{T,i}} N_i! (N_{T,i} - N_i)!} \right) \\ & \left( \prod_{i=1}^R \frac{V_1^{N_i} (V_T - V_1)^{N_{T,i}+\nu_i-N_i}}{\Lambda^{3(N_{T,i}+\nu_i)} N_i! (N_{T,i} + \nu_i - N_i)!} \right) \\ & \int ds^{N_{\text{total}} + \sum_{i=1}^R \nu_i} \exp[-\beta U(s^{N_{\text{total}} + \sum_{i=1}^R \nu_i}, V_1)] \end{aligned} \quad (\text{A39})$$

where  $\frac{Q_{N_{\text{total}} + \sum_{i=1}^R \nu_i}}{Q_{N_{\text{total}}}}$  is the partition function of Gibbs ensemble when for each reactant  $i$ ,  $\nu_i$  molecules of type  $i$  are added to the system. Therefore,

$$\frac{Q_{N_{\text{total}} + \sum_{i=1}^R \nu_i}}{Q_{N_{\text{total}}}} = \frac{1}{Q_{N_{\text{total}}}} \times \left( \begin{array}{l} \sum_{N_1=0}^{N_{T,1}+\nu_1} \dots \sum_{N_R=0}^{N_{T,R}+\nu_R} \dots \sum_{N_{R+1}=0}^{N_{T,R+1}} \dots \sum_{N_s=0}^{N_{T,S}} \int_0^{V_T} dV_1 \left( \prod_{i=R+1}^S \frac{V_1^{N_i} (V_T - V_1)^{N_{T,i} - N_i}}{\Lambda^{3N_{T,i}} N_i! (N_{T,i} - N_i)!} \right) \\ \left( \prod_{i=1}^R \frac{V_1^{N_i} (V_T - V_1)^{N_{T,i} + \nu_i - N_i}}{\Lambda^{3(N_{T,i} + \nu_i)} N_i! (N_{T,i} + \nu_i - N_i)!} \right) \\ \left( \int ds^{N_{\text{total}} + \sum_{i=1}^R \nu_i} \exp[-\beta U(s^{N_{\text{total}} + \sum_{i=1}^R \nu_i}, V_1)] \right) \end{array} \right) \quad (\text{A40})$$

Separating the terms  $N_i = 0$  to  $N_i = \nu_i - 1$  for reactants leads to [177]

$$\frac{Q_{N_{\text{total}} + \sum_{i=1}^R \nu_i}}{Q_{N_{\text{total}}}} = \frac{\left( \begin{array}{l} \sum_{N_1=\nu_1}^{N_{T,1}+\nu_1} \sum_{N_R=\nu_R}^{N_{T,R}+\nu_R} \dots \sum_{N_{R+1}=0}^{N_{T,R+1}} \dots \sum_{N_s=0}^{N_{T,S}} \int_0^{V_T} dV_1 \left( \prod_{i=R+1}^S \frac{V_1^{N_i} (V_T - V_1)^{N_{T,i} - N_i}}{\Lambda^{3N_{T,i}} N_i! (N_{T,i} - N_i)!} \right) \\ \left( \prod_{i=1}^R \frac{V_1^{N_i} (V_T - V_1)^{N_{T,i} + \nu_i - N_i}}{\Lambda^{3(N_{T,i} + \nu_i)} N_i! (N_{T,i} + \nu_i - N_i)!} \right) \\ \left( \int ds^{N_{\text{total}} + \sum_{i=1}^R \nu_i} \exp[-\beta U(s^{N_{\text{total}} + \sum_{i=1}^R \nu_i}, V_1)] \right) \end{array} \right)}{Q_{N_{\text{total}}}} + \frac{\left( \begin{array}{l} \sum_{N_1=0}^{\nu_1-1} \sum_{N_2=0}^{\nu_2-1} \dots \sum_{N_R=0}^{\nu_R-1} \dots \sum_{N_{R+1}=0}^{N_{T,R+1}} \dots \sum_{N_s=0}^{N_{T,S}} \int_0^{V_T} dV_1 \left( \prod_{i=R+1}^S \frac{V_1^{N_i} (V_T - V_1)^{N_{T,i} - N_i}}{\Lambda^{3N_{T,i}} N_i! (N_{T,i} - N_i)!} \right) \\ \left( \prod_{i=1}^R \frac{V_1^{N_i} (V_T - V_1)^{N_{T,i} + \nu_i - N_i}}{\Lambda^{3(N_{T,i} + \nu_i)} N_i! (N_{T,i} + \nu_i - N_i)!} \right) \\ \left( \int ds^{N_{\text{total}} + \sum_{i=1}^R \nu_i} \exp[-\beta U(s^{N_{\text{total}} + \sum_{i=1}^R \nu_i}, V_1)] \right) \end{array} \right)}{Q_{N_{\text{total}}}} \quad (\text{A41})$$

By re-indexing the sums, we obtain

$$\frac{Q_{N_{\text{total}} + \sum_{i=1}^R \nu_i}}{Q_{N_{\text{total}}}} = \frac{\left( \begin{array}{l} \sum_{N_1=0}^{N_{T,1}} \dots \sum_{N_s=0}^{N_{T,S}} \int_0^{V_T} dV_1 \left( \prod_{i=1}^S \frac{V_1^{N_i} (V_T - V_1)^{N_{T,i} - N_i}}{\Lambda^{3N_{T,i}} N_i! (N_{T,i} - N_i)!} \right) \\ \prod_{i=1}^R \left( \frac{\left( \frac{V_1}{\Lambda_i^3} \right)^{\nu_i}}{\frac{(N_i + \nu_i)!}{N_i!}} \exp[-\beta \sum_{j=1}^{\nu_i} \Delta U_{i,j}^+] \right) \\ \int ds^{N_{\text{total}}} \exp[-\beta U(s^{N_{\text{total}}}, V_1)] \end{array} \right)}{Q_{N_{\text{total}}}} + \frac{\left( \begin{array}{l} \sum_{N_1=0}^{\nu_1-1} \sum_{N_2=0}^{\nu_2-1} \dots \sum_{N_R=0}^{\nu_R-1} \dots \sum_{N_{R+1}=0}^{N_{T,R+1}} \dots \sum_{N_s=0}^{N_{T,S}} \int_0^{V_T} dV_1 \left( \prod_{i=R+1}^S \frac{V_1^{N_i} (V_T - V_1)^{N_{T,i} - N_i}}{\Lambda^{3N_{T,i}} N_i! (N_{T,i} - N_i)!} \right) \\ \left( \prod_{i=1}^R \frac{V_1^{N_i} (V_T - V_1)^{N_{T,i} + \nu_i - N_i}}{\Lambda^{3(N_{T,i} + \nu_i)} N_i! (N_{T,i} + \nu_i - N_i)!} \right) \\ \int ds^{N_{\text{total}} + \sum_{i=1}^R \nu_i} \exp[-\beta U(s^{N_{\text{total}} + \sum_{i=1}^R \nu_i}, V_1)] \end{array} \right)}{Q_{N_{\text{total}}}} \quad (\text{A42})$$

where  $\sum_{j=1}^{\nu_i} \Delta U_{i,j}^+$  is the total change in the potential energy of the system due to the addition of  $\nu_i$  molecules of component  $i$ . Here, the interaction with additional molecules that are already in the system are also included in  $\sum_{j=1}^{\nu_i} \Delta U_{i,j}^+$  (see Fig. A1). As the first term on the right hand side of Eq. A42 corresponds to an ensemble average in the conventional Gibbs ensemble, we

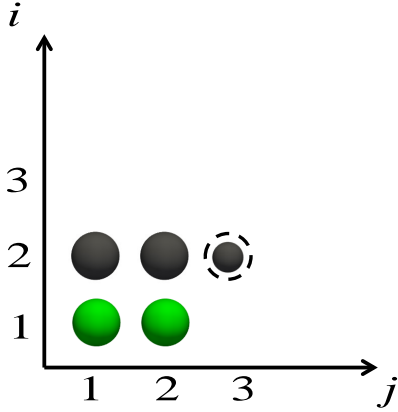


Figure A1: Schematic representation of the addition of reactant molecules. Here, we have  $\nu_1 = 2$  and  $\nu_2 = 3$ . The order of insertion of a molecule X is  $X_{11} \rightarrow X_{12} \rightarrow X_{21} \rightarrow X_{22} \rightarrow X_{23}$ . When a molecule  $X_{ij}$  is added, interactions with all whole molecules (also fractional molecules that were already added) are included in the term  $\Delta U_{i,j}^+$ . The corresponding changes in  $\lambda$  are shown in Fig. 7.6.

can write

$$\frac{Q_{N_{\text{total}} + \sum_{i=1}^R \nu_i}}{Q_{N_{\text{total}}}} = \left( \prod_{i=1}^R \frac{\left(\frac{V_1}{\Lambda_i^3}\right)^{\nu_i} \exp[-\beta \sum_{j=1}^{\nu_i} \Delta U_{i,j}^+]}{\frac{(N_i + \nu_i)!}{N_i!}} \right)_{\text{normal,GE}} + \\ \left( \sum_{N_1=0}^{\nu_1-1} \sum_{N_2=0}^{\nu_2-1} \dots \sum_{N_R=0}^{\nu_R-1} \dots \sum_{N_{R+1}=0}^{N_{T,R+1}} \dots \sum_{N_s=0}^{N_{T,S}} \int_0^{V_T} dV_1 \left( \prod_{i=R+1}^S \frac{V_1^{N_i} (V_T - V_1)^{N_{T,i} - N_i}}{\Lambda^{3N_{T,i}} N_i! (N_{T,i} - N_i)!} \right) \right. \\ \left( \prod_{i=1}^R \frac{V_1^{N_i} (V_T - V_1)^{N_{T,i} + \nu_i - N_i}}{\Lambda^{3(N_{T,i} + \nu_i)} N_i! (N_{T,i} + \nu_i - N_i)!} \right) \\ \left. \int ds^{N_{\text{total}} + \sum_{i=1}^R \nu_i} \exp[-\beta U(s^{N_{\text{total}} + \sum_{i=1}^R \nu_i}, V_1)] \right)_{Q_{N_{\text{total}}}} \quad (\text{A43})$$

where the last term corresponds to configurations where the numbers of molecules of reactants in box 1 are less than their stoichiometric coefficient. These configurations have very limited contribution to the statistical weight [38, 177] and therefore we can neglect this term. Therefore, we have

$$\frac{Q_{N_{\text{total}} + \sum_{i=1}^R \nu_i}}{Q_{N_{\text{total}}}} = \left\langle \prod_{i=1}^R \frac{\left(\frac{V_1}{\Lambda_i^3}\right)^{\nu_i} \exp[-\beta \sum_{j=1}^{\nu_i} \Delta U_{i,j}^+]}{\frac{(N_i + \nu_i)!}{N_i!}} \right\rangle_{\text{normal,GE}} \quad (\text{A44})$$

so that

$$\sum_{i=1}^R \nu_i \mu_i = \left\langle \prod_{i=1}^R \frac{\left(\frac{V_1}{\Lambda_i^3}\right)^{\nu_i} \exp[-\beta \sum_{j=1}^{\nu_i} \Delta U_{i,j}^+]}{\frac{(N_i + \nu_i)!}{N_i!}} \right\rangle_{\text{normal,GE}} \quad (\text{A45})$$

For  $R = 1$  and  $\nu_i = 1$ , we recover the original expression by Frenkel and Smit (see Eq. 6.20).

### A.3 Chemical potentials in serial Rx/CFCMC

Consider the reaction:



We start the derivation by not yet considering the contribution of internal degrees of freedom to the chemical potential of each component  $i$  (see Eq. 7.15), as we add these effects at the very end. We start again from the Gibbs ensemble where molecules only interact in box 1, and box 2 is an ideal gas reservoir (see section A.1).

$$Q_{\text{CFCMC}} = \sum_{N_1=0}^{N_{T,1}} \dots \sum_{N_S=0}^{N_{T,S}} \sum_{\delta=0}^1 \int_0^{V_T} dV_1 \left( \prod_{i=1}^R \frac{V_1^{N_i + \nu_i \delta} (V_T - V_1)^{N_{T,i} + (1-\delta)\nu_i - N_i}}{\Lambda_i^{3(N_{T,i} + \nu_i)} N_i! (N_{T,i} + (1-\delta)\nu_i - N_i)!} \right) \\ \left( \prod_{j=R+1}^S \frac{V_1^{N_j + \nu_j (1-\delta)} (V_T - V_1)^{N_{T,j} + \delta\nu_j - N_j}}{\Lambda_j^{3(N_{T,j} + \nu_j)} N_j! (N_{T,j} + \delta\nu_j - N_j)!} \right) \\ \int_0^1 d\lambda \int ds^{N_{\text{int}}} \exp[-\beta U_{\text{int}}(s^{N_{\text{int}}}, V_1)] \\ \left( \prod_{i=1}^R \int ds_{\text{frac}}^{\nu_i} \exp[-\beta \delta U_{\text{frac},i}(s_{\text{frac}}^{\nu_i}, s^{N_{\text{int}}}, \lambda, V_1)] \right) \\ \left( \prod_{j=R+1}^S \int ds_{\text{frac}}^{\nu_j} \exp[-\beta (1-\delta) U_{\text{frac},j}(s_{\text{frac}}^{\nu_j}, s^{N_{\text{int}}}, \lambda, V_1)] \right) \quad (\text{A46})$$

We can write

$$\left\langle \delta'_{\lambda=0, \delta=1} \frac{1}{\prod_{i=1}^R \left( \frac{V_1}{\Lambda_i^3} \right)^{\nu_i}} \right\rangle = \frac{1}{Q_{\text{CFCMC}}} \left( \begin{array}{l} \sum_{N_1=0}^{N_{T,1}} \dots \sum_{N_S=0}^{N_{T,S}} \int_0^{V_T} dV_1 \left( \prod_{i=1}^R \frac{V_1^{N_i + \nu_i} (V_T - V_1)^{N_{T,i} - N_i}}{\Lambda_i^{3(N_{T,i} + \nu_i)} N_i! (N_{T,i} - N_i)!} \right) \\ \times \left( \prod_{j=R+1}^S \frac{V_1^{N_j} (V_T - V_1)^{N_{T,j} + \nu_j - N_j}}{\Lambda_j^{3(N_{T,j} + \nu_j)} N_j! (N_{T,j} + \nu_j - N_j)!} \right) \\ \frac{1}{\prod_{i=1}^R \left( \frac{V_1}{\Lambda_i^3} \right)^{\nu_i}} \int ds^{N_{\text{int}}} \exp[-\beta U_{\text{int}}(s^{N_{\text{int}}}, V_1)] \end{array} \right) \quad (\text{A47})$$

$\delta'_{\lambda=0, \delta=1}$  equals one when  $\lambda = 0$  and  $\delta = 1$  and otherwise this term equals zero. When  $\delta = 1$ , all reactants have fractional molecules in box 1. Therefore,

$$\left\langle \delta'_{\lambda=0, \delta=1} \frac{1}{\prod_{i=1}^R \left( \frac{V_1}{\Lambda_i^3} \right)^{\nu_i}} \right\rangle = \frac{1}{Q_{\text{CFCMC}}} \left( \begin{array}{l} \sum_{N_1=0}^{N_{T,1}} \dots \sum_{N_S=0}^{N_{T,S}} \int_0^{V_T} dV_1 \left( \prod_{i=1}^R \frac{V_1^{N_i} (V_T - V_1)^{N_{T,i} - N_i}}{\Lambda_i^{3N_{T,i}} N_i! (N_{T,i} - N_i)!} \right) \\ \left( \prod_{j=R+1}^S \frac{V_1^{N_j} (V_T - V_1)^{N_{T,j} + \nu_j - N_j}}{\Lambda_j^{3(N_{T,j} + \nu_j)} N_j! (N_{T,j} + \nu_j - N_j)!} \right) \\ \int ds^{N_{\text{int}}} \exp[-\beta U_{\text{int}}(s^{N_{\text{int}}}, V_1)] \end{array} \right) \quad (\text{A48})$$

We can also write

$$\left\langle \delta'_{\lambda=1, \delta=1} \frac{1}{\prod_{i=1}^R \frac{(N_i + \nu_i)!}{N_i!}} \right\rangle = \frac{1}{Q_{\text{CFCMC}}} \left( \sum_{N_1=0}^{N_{T,1}} \dots \sum_{N_S=0}^{N_{T,S}} \frac{1}{\prod_{i=1}^R \frac{(N_i + \nu_i)!}{N_i!}} \int_0^{V_T} dV_1 \left( \prod_{i=1}^R \frac{V_1^{N_i + \nu_i} (V_T - V_1)^{N_{T,i} - N_i}}{\Lambda_i^{3(N_{T,i} + \nu_i)} N_i! (N_{T,j} - N_i)!} \right) \right. \\ \left. \prod_{j=R+1}^S \frac{V_1^{N_j} (V_T - V_1)^{N_{T,j} + \nu_j - N_j}}{\Lambda_j^{3(N_{T,j} + \nu_j)} N_j! (N_{T,j} + \nu_j - N_j)!} \int ds^{N_{\text{int}}} \exp[-\beta U_{\text{int}}(s^{N_{\text{int}}}, V_1)] \right. \\ \left. \left( \prod_{i=1}^R \int ds_{\text{frac}}^{\nu_i} \exp[-\beta U_{\text{frac},i}(s_{\text{frac}}^{\nu_i}, s^{N_{\text{int}}}, \lambda = 1, V_1)] \right) \right) \quad (\text{A49})$$

$$\left\langle \delta'_{\lambda=1, \delta=1} \frac{1}{\prod_{i=1}^R \frac{(N_i + \nu_i)!}{N_i!}} \right\rangle = \frac{1}{Q_{\text{CFCMC}}} \left( \sum_{N_1=0}^{N_{T,1}} \dots \sum_{N_S=0}^{N_{T,S}} \frac{\prod_{i=1}^R \left( \frac{V_1}{\Lambda_i^{3/2}} \right)^{\nu_i}}{\prod_{i=1}^R \frac{(N_i + \nu_i)!}{N_i!}} \int_0^{V_T} dV_1 \prod_{i=1}^R \frac{V_1^{N_i} (V_T - V_1)^{N_{T,i} - N_i}}{\Lambda_i^{3N_{T,i}} N_i! (N_{T,j} - N_i)!} \right. \\ \left. \left( \prod_{j=R+1}^S \frac{V_1^{N_j} (V_T - V_1)^{N_{T,j} + \nu_j - N_j}}{\Lambda_j^{3(N_{T,j} + \nu_j)} N_j! (N_{T,j} + \nu_j - N_j)!} \right) \int ds^{N_{\text{int}}} \exp[-\beta U_{\text{int}}(s^{N_{\text{int}}}, V_1)] \right. \\ \left. \left( \prod_{i=1}^R \int ds_{\text{frac}}^{\nu_i} \exp[-\beta U_{\text{frac},i}(s_{\text{frac}}^{\nu_i}, s^{N_{\text{int}}}, \lambda = 1, V_1)] \right) \right) \quad (\text{A50})$$

Here, fractional molecules is just like whole molecules and we can write

$$\left\langle \delta'_{\lambda=1,\delta=1} \frac{1}{\prod_{i=1}^R \frac{(N_i+\nu_i)!}{N_i!}} \right\rangle = \frac{1}{Q_{\text{CFCMC}}} \left( \sum_{N_1=0}^{N_{T,1}} \dots \sum_{N_S=0}^{N_{T,S}} \frac{\prod_{i=1}^R \left(\frac{V_1}{\Lambda_i^3}\right)^{\nu_i}}{\prod_{i=1}^R \frac{(N_i+\nu_i)!}{N_i!}} \int_0^{V_T} dV_1 \left( \prod_{i=1}^R \frac{V_1^{N_i} (V_T - V_1)^{N_{T,i}-N_i}}{\Lambda_i^{3N_{T,i}} N_i! (N_{T,j} - N_i)!} \right) \right. \\ \left. \left( \prod_{j=R+1}^S \frac{V_1^{N_j} (V_T - V_1)^{N_{T,j}+\nu_j-N_j}}{\Lambda_j^{3(N_{T,j}+\nu_j)} N_j! (N_{T,j} + \nu_j - N_j)!} \right) \left[ \prod_{i=1}^R \exp[-\beta \sum_{j=1}^{\nu_i} \Delta U_{i,j}^+] \right] \right) \\ \int ds^{N_{\text{int}}} \exp[-\beta U_{\text{int}}(s^{N_{\text{int}}}, V_1)] \quad (\text{A51})$$

By combining Eqs. A48 and A51, we can write:

$$\left\langle \delta'_{\lambda=1,\delta=1} \frac{1}{\prod_{i=1}^R \frac{(N_i+\nu_i)!}{N_i!}} \right\rangle = \left\langle \delta'_{\lambda=0,\delta=1} \frac{1}{\prod_{i=1}^R \left(\frac{V_1}{\Lambda_i^3}\right)^{\nu_i}} \right\rangle \\ \left( \sum_{N_1=0}^{N_{T,1}} \dots \sum_{N_S=0}^{N_{T,S}} \int_0^{V_T} dV_1 \left( \prod_{i=1}^R \frac{V_1^{N_i} (V_T - V_1)^{N_{T,i}-N_i}}{\Lambda_i^{3N_{T,i}} N_i! (N_{T,j} - N_i)!} \right) \right. \\ \left( \prod_{j=R+1}^S \frac{V_1^{N_j} (V_T - V_1)^{N_{T,j}+\nu_j-N_j}}{\Lambda_j^{3(N_{T,j}+\nu_j)} N_j! (N_{T,j} + \nu_j - N_j)!} \right) \\ \left. \left( \prod_{i=1}^R \left(\frac{V_1}{\Lambda_i^3}\right)^{\nu_i} \prod_{i=1}^R \exp[-\beta \sum_j^{\nu_i} \Delta U_{i,j}^+] \int ds^{N_{\text{int}}} \exp[-\beta U_{\text{int}}(s^{N_{\text{int}}}, V_1)] \right) \right) \\ \overline{\left( \sum_{N_1=0}^{N_{T,1}} \dots \sum_{N_S=0}^{N_{T,S}} \int_0^{V_T} dV_1 \left( \prod_{i=1}^R \frac{V_1^{N_i} (V_T - V_1)^{N_{T,i}-N_i}}{\Lambda_i^{3N_{T,i}} N_i! (N_{T,i} - N_i)!} \right) \right.} \\ \left( \prod_{j=R+1}^S \frac{V_1^{N_j} (V_T - V_1)^{N_{T,j}+\nu_j-N_j}}{\Lambda_j^{3(N_{T,j}+\nu_j)} N_j! (N_{T,j} + \nu_j - N_j)!} \right) \int ds^{N_{\text{int}}} \exp[-\beta U_{\text{int}}(s^{N_{\text{int}}}, V_1)] \quad (\text{A52})$$

This leads to

$$\frac{\left\langle \delta'_{\lambda=1,\delta=1} \frac{1}{\prod_{i=1}^R \frac{(N_i+\nu_i)!}{N_i!}} \right\rangle}{\left\langle \delta'_{\lambda=0,\delta=1} \frac{1}{\prod_{i=1}^R \left(\frac{V_1}{\Lambda_i^3}\right)^{\nu_i}} \right\rangle} = \left\langle \prod_{i=1}^R \frac{\left(\frac{V_1}{\Lambda_i^3}\right)^{\nu_i} \exp[-\beta \sum_{j=1}^{\nu_i} \Delta U_{i,j}^+]}{\frac{(N_i+\nu_i)!}{N_i!}} \right\rangle_{\text{normal,GE}} \quad (\text{A53})$$

Note that the right hand side of Eq. A53 is directly related to the chemical potential (see Eq. A45). If we assume that number of whole molecules and volume of the box are independent of the value of  $\lambda$ , we can write

$$\begin{aligned} \frac{\left\langle \delta'_{\lambda=1,\delta=1} \frac{1}{\prod_{i=1}^R \frac{(N_i+\nu_i)!}{N_i!}} \right\rangle}{\left\langle \delta'_{\lambda=0,\delta=1} \frac{1}{\prod_{i=1}^R \left(\frac{V_1}{\Lambda_i^3}\right)^{\nu_i}} \right\rangle} &\approx \left\langle \prod_{i=1}^R \frac{\left(\frac{V_1}{\Lambda_i^3}\right)^{\nu_i}}{\frac{(N_i+\nu_i)!}{N_i!}} \right\rangle \frac{\langle \delta'_{\lambda=1,\delta_1=1} \rangle}{\langle \delta'_{\lambda=0,\delta_1=1} \rangle} \\ &\approx \left\langle \prod_{i=1}^R \frac{\left(\frac{V_1}{\Lambda_i^3}\right)^{\nu_i} \exp[-\beta \sum_{j=1}^{\nu_i} \Delta U_{i,j}^+]}{\frac{(N_i+\nu_i)!}{N_i!}} \right\rangle_{\text{normal,GE}} = \sum_{i=1}^R \nu_i \mu_i \end{aligned} \quad (\text{A54})$$

which leads to

$$\begin{aligned} \frac{\left\langle \prod_{i=1}^R \frac{\left(\frac{V_1}{\Lambda_i^3}\right)^{\nu_i}}{\frac{(N_i+\nu_i)!}{N_i!}} \right\rangle p(\lambda_R \uparrow 1)}{p(\lambda_R \downarrow 0)} &\\ \approx \left\langle \prod_{i=1}^R \frac{\left(\frac{V_1}{\Lambda_i^3}\right)^{\nu_i} \exp[-\beta \sum_{j=1}^{\nu_i} \Delta U_{i,j}^+]}{\frac{(N_i+\nu_i)!}{N_i!}} \right\rangle_{\text{normal,GE}} &= \sum_{i=1}^R \nu_i \mu_i \end{aligned} \quad (\text{A55})$$

where  $\lambda_R = \lambda$  when we have the fractional molecules of reactants ( $\delta = 1$ ). In this equation,  $p(\lambda_R \uparrow 1)$  is the probability that  $\lambda_R$  approaches 1, and

$p(\lambda_R \downarrow 0)$  is the probability that  $\lambda_R$  approaches 0.

$$\left\langle \frac{\prod_{i=1}^R \left( \frac{V_1}{\Lambda_i^3} \right)^{\nu_i}}{\prod_{i=1}^R \frac{(N_i + \nu_i)!}{N_i!}} \right\rangle \approx \left\langle \frac{\left( \frac{V_1}{\Lambda_i^3} \right)^{\nu_i}}{\prod_{i=1}^R N_i^{\nu_i}} \right\rangle = \left\langle \prod_{i=1}^R \left( \frac{1}{\Lambda_i^3 \rho_i} \right)^{\nu_i} \right\rangle \quad (\text{A56})$$

where  $\rho_i$  is the number density of component  $i$ . The sum of chemical potentials of all reactants times their stoichiometric coefficients equals

$$\left\langle \prod_{i=1}^R \left( \frac{1}{\Lambda_i^3 \rho_i} \right)^{\nu_i} \right\rangle \frac{p(\lambda_R \uparrow 1)}{p(\lambda_R \downarrow 0)} \approx \left\langle \prod_{i=1}^R \frac{\left( \frac{V_1}{\Lambda_i^3} \right)^{\nu_i} \exp[-\beta \sum_{j=1}^{\nu_i} \Delta U_{i,j}^+]}{\frac{(N_i + \nu_i)!}{N_i!}} \right\rangle_{\text{normal,GE}} \quad (\text{A57})$$

At this point, it is important to note that so far we did not consider the internal contribution of the partition function of component  $i$ . The corrected expression including the correct reference state for the chemical potential of component  $i$  equals

$$\sum_{i=1}^R \nu_i \mu_i = -\frac{1}{\beta} \ln \left\langle \prod_{i=1}^R \left( \frac{q_i}{\Lambda_i^3 \rho_i} \right)^{\nu_i} \right\rangle - \frac{1}{\beta} \ln \left( \frac{p(\lambda_R \uparrow 1)}{p(\lambda_R \downarrow 0)} \right) \quad (\text{A58})$$

where  $q_i$  is the ideal gas partition function of component  $i$ , excluding the translational part [197]. Eq. A58 allows for an independent check of reaction equilibria without any additional calculations (e.g. Widom's test particle insertion method) [38]. By coupling the interactions of different components in smart way to the order parameter  $\lambda_R$ , we are able to compute the chemical potentials of all components participating in the reaction. If we only scale the interactions of the fractional molecule of one of the reactant components (for instance component  $i$ ) from no interactions to full interactions when  $\lambda \in \langle 0, A \rangle$ , we can write

$$\nu_i \mu_i = -\frac{1}{\beta} \ln \left( \frac{q_i}{\Lambda_i^3 \rho_i} \right)^{\nu_i} - \frac{1}{\beta} \ln \left( \frac{p(\lambda_R \uparrow A)}{p(\lambda_R \downarrow 0)} \right) \quad (\text{A59})$$

Table A1: Computed excess chemical potentials of Lennard-Jones particles (with analytic tail corrections [38, 183]) at different pressures obtained from serial RX/CFC and Widom's test particle insertion method [224] in the *NPT* ensemble are compared with values computed from the Equation Of State (EOS) from Kolafa and Nezbeda [231]. In the second column, the values obtained with the serial Rx/CFC method for the reaction  $A \rightleftharpoons B$  are shown. In the third column, values obtained from *NPT* simulations (400 particles) with Widom's test particle insertion method are shown [224]. The numbers between brackets denote the uncertainty in the last digit. All values are reported in dimensionless units. The cutoff radius was set to 2.5 in dimensionless units.  $T=2$  in reduced units.

$P$	Serial RX/CFC	Widom	EOS
1.0	-0.646(9)	-0.645(8)	-0.646
3.0	1.91(2)	1.91(3)	1.910
5.0	4.34(2)	4.37(4)	4.342

The first term on the right hand side accounts for the ideal gas part of the chemical potential including the internal degrees of freedom, and the second term account for the excess part of the chemical potential (due to the interactions of molecules with the surrounding). To validate Eq. A59, excess chemical potentials obtained from serial Rx/CFC for the reaction  $A \rightleftharpoons B$ , where A and B have identical interaction potentials, are compared with the values obtained from Widom's test particle insertion method [38, 183, 224] in the *NPT* ensemble and values computed from the equation of state of the Lennard-Jones interaction potential [231]. As shown in Table A1, values obtained from the three methods are in excellent agreement. The chemical potential of component  $i$  for a non-ideal gas equals [198] (see also Eq. 7.15)

$$\mu_i = \frac{1}{\beta} \ln \frac{\beta P_0 \Lambda_i^3}{q_i} + \frac{1}{\beta} \ln \frac{y_i P \varphi_i}{P_0} \quad (\text{A60})$$

in which  $\varphi_i$  and  $y_i$  are the fugacity coefficient and mole fraction of component  $i$ .  $P_0$  is the reference pressure (1 bar) and  $P$  is the pressure of the mixture.

Therefore, we have

$$\sum_{i=1}^R \nu_i \mu_i = \frac{1}{\beta} \ln \left( \prod_{i=1}^R \left[ \frac{\beta \Lambda_i^3 y_i P \varphi_i}{q_i} \right]^{\nu_i} \right) \quad (\text{A61})$$

Combining this with Eq. A58 immediately leads to

$$\prod_{i=1}^R \varphi_i^{-\nu_i} = \left( \frac{\beta y_i P}{\rho_i} \right)^{\nu_i} \frac{p(\lambda_R \uparrow 1)}{p(\lambda_R \downarrow 0)} \quad (\text{A62})$$

We define the term  $z_i$  by

$$z_i = \frac{\beta y_i P}{\rho_i} \quad (\text{A63})$$

Therefore, we can write for  $\varphi_i$

$$\varphi_i^{-\nu_i} = \frac{p(\lambda_R \uparrow A)}{p(\lambda_R \downarrow 0)} z_i^{\nu_i} \quad (\text{A64})$$

## A.4 Extension to constant pressure

In this section, we extend the expressions derived for the partition function and acceptance rules for the constant volume version of serial Rx/CFC to the constant pressure version by multiplying the partition function by a term  $\exp[-\beta PV]$  [38]. The partition function for the constant pressure version of serial Rx/CFC is therefore given by

$$\begin{aligned}
 Q_{\text{CFC,P}} = & \\
 & \beta P \sum_{N_1=0}^{\infty} \dots \sum_{N_S=0}^{\infty} \sum_{\delta=0}^1 \int dV \exp[-\beta PV] \exp \left[ \beta \sum_{i=1}^R \mu_i (N_i + \nu_i \delta) + \sum_{i=1}^R (N_i + \nu_i \delta) \ln \frac{V q_i}{\Lambda_i^3} - \sum_{i=1}^R \ln N_i! \right] \\
 & \exp \left[ \beta \sum_{j=R+1}^S \mu_j (N_j + \nu_j(1-\delta)) + \sum_{j=R+1}^S (N_j + \nu_j(1-\delta)) \ln \frac{V q_j}{\Lambda_j^3} - \sum_{j=R+1}^S \ln N_j! \right] \\
 & \int_0^1 d\lambda \int ds^{N_{\text{int}}} \exp[-\beta U_{\text{int}}(s^{N_{\text{int}}})] \left( \prod_{i=1}^R \int ds_{\text{frac}}^{\nu_i} \exp[-\beta \delta U_{\text{frac},i}(s_{\text{frac}}^{\nu_i}, s^{N_{\text{int}}}, \lambda)] \right) \\
 & \left( \prod_{j=R+1}^S \int ds_{\text{frac}}^{\nu_j} \exp[-\beta (1-\delta) U_{\text{frac},j}(s_{\text{frac}}^{\nu_j}, s^{N_{\text{int}}}, \lambda)] \right)
 \end{aligned} \tag{A65}$$

where  $P$  is the pressure of the system. The term  $\beta P$  is used to make the partition function dimensionless [38]. In the constant pressure version of the serial Rx/CFC method, the volume of the simulation box remains unchanged in all reaction trial moves. Therefore, the acceptance rules for these trial moves in the constant volume and constant pressure versions of serial Rx/CFC (Eqs. A19, A26 and A33) are identical. The only additional trial move in the constant pressure versions of serial Rx/CFC is the trial move to change the volume of the simulation box. In this trial move, the volume of the simulation box is changed while the number and relative coordinates of the whole molecules and fractional molecules stay the same. Here, the random walk is performed in  $V$  and not in  $\ln(V)$  [38]. The acceptance rule for this trial move is [38]

$$\text{acc}(o \rightarrow n) = \min \left[ 1, \left( \frac{V_n}{V_o} \right)^{\sum_{i=1}^R (N_i + \nu_i \delta) + \sum_{j=R+1}^S (N_j + \nu_j(1-\delta))} \exp[-\beta (\Delta U + P (V_n - V_o))] \right] \tag{A66}$$

As we assume that the probability distribution of  $\lambda$  does not depend on volume, the expression derived for the chemical potential for the constant volume version of serial Rx/CFC can also be used for the constant pressure version of the serial Rx/CFC method, as is the same for the conventional *NVT* and *NPT* Gibbs ensembles [38].

## A.5 Thermodynamic modeling of the ammonia synthesis reaction

The ammonia synthesis reaction is modelled using the Peng-Robinson Equation of State (PR-EoS) [233] and the mixture compositions at equilibrium are obtained for different temperatures and pressures. These results are compared to those obtained from serial Rx/CFC simulations. The equilibrium constant is only a function of temperature and here defined by [198]

$$K = \frac{\prod_{j=R+1}^S \left( q_j / \Lambda_j^3 \right)^{v_j}}{\prod_{i=1}^R \left( q_i / \Lambda_i^3 \right)^{v_i}} \quad (\text{A67})$$

where  $\Lambda_i$  is the de Broglie thermal wavelength of component  $i$ , and  $q_i$  is the ideal gas partition function excluding the translational part.  $q_i$  is related to the Gibbs free energy of formation by  $g_i^0 = -RT \ln(q_i / \beta P^0 \Lambda_i^3)$ .  $g_i^0$  can be found in JANAF thermochemical tables [239]. At equilibrium, the equilibrium constant is also provided by [198]

$$K = \frac{\prod_{j=R+1}^S \left( \frac{y_j P \varphi_j}{k_B T} \right)^{v_j}}{\prod_{i=1}^R \left( \frac{y_i P \varphi_i}{k_B T} \right)^{v_i}} \quad (\text{A68})$$

where  $P$  is the total pressure, and  $y_i$  and  $\varphi_i$  are the mole fraction and the fugacity coefficient of component  $i$ , respectively. For a non-linear polyatomic molecule, the ideal gas partition function excluding the translational part is [198]

$$\frac{q_i(T)}{\Lambda_i^3} = \left( \frac{2\pi M_i k_B T}{h^2} \right)^{3/2} \frac{\pi^{1/2}}{\sigma} \left( \frac{T^3}{\Theta_{\text{rot},A,i} \Theta_{\text{rot},B,i} \Theta_{\text{rot},C,i}} \right) \prod_{j=1}^{3n-6} \frac{1}{1 - \exp(-\Theta_{\text{vib},j,i}/T)} g_{e1,i} \exp[D_0/k_B T] \quad (\text{A69})$$

where  $\Theta_{\text{rot},A,i}$ ,  $\Theta_{\text{rot},B,i}$ , and  $\Theta_{\text{rot},C,i}$  are the characteristic rotational temperatures in terms of three principal moments of inertial [198].  $M_i$  is the molecular mass of component  $i$ ,  $\Theta_{\text{vib},j}$  is the characteristic vibrational temperature corresponding to normal mode  $j$ .  $D_0$  is the atomization energy at 0K.  $\sigma$  is the symmetry number of molecules of component  $i$ .  $h$  is the Planck constant.  $g_{e1,i}$  is the degeneracy of the electronic ground state, and  $k_B$  is the Boltzmann constant. As the atomization energies  $D_0$  appear in the exponential, small differences in  $D_0$  may lead to large differences in the computed partition functions. Deviations are observed between the experimental atomization energies and those obtained from the Gaussian09. These values are reported in Table A2. Table A3 summarizes the computed partition functions both based on experimental data from literature [198, 239] and quantum computations using Gaussian09 [230]. It is important to note that for the latter, the atomization energies from McQuarrie [198] were used, and not the ones computed from Gaussian09. Using the atomization energies computed from Gaussian09 results in equilibrium constants that are 5 times larger than experimentally measured equilibrium constants. In all QM computations, the optimized molecular structures for nitrogen, hydrogen and ammonia were obtained at the B3LYP level of theory with a 6-31G\*\* basis set. A frequency analysis was carried out on the optimized geometries to compute the partition functions.

Table A2: Experimental atomization energies [198] and atomization energies computed for nitrogen, hydrogen, ammonia using Gaussian09 using the B3LYP level of theory with a 6-31G\*\* basis set [230]

Component	$D_0$ / [kJ/mol]	
	McQuarrie	Gaussian
N <sub>2</sub>	941.6	917.6
H <sub>2</sub>	432.1	432.1
NH <sub>3</sub>	1158	1149.8

Table A3: Computed ideal gas partition functions of nitrogen, hydrogen, ammonia obtained as defined in appendix A.5. The reported values are based on experimental data [198, 239] and quantum computations using Gaussian09 (using B3LYP level of theory with a 6-31G\*\* basis set) [230]. It is important to note that for the values obtained from Gaussian09, the experimental atomization energies provided by McQuarrie [198] are used (see Table A2) and *NOT* the ones obtained from Gaussian09. One can easily see that using the atomization energies from Gaussian09 (as listed in Table A2) results in large deviations. For serial Rx/CFC simulations values reported in the first column (McQuarrie) are used.

T/K	$q/\text{Å}^3 [\text{N}_2]/[\text{Å}^{-3}]$			$q/\text{Å}^3 [\text{H}_2]/[\text{Å}^{-3}]$			$q/\text{Å}^3 [\text{NH}_3]/[\text{Å}^{-3}]$		
	McQuarrie	JANAF	Gaussian	McQuarrie	JANAF	Gaussian	McQuarrie	JANAF	Gaussian
573	$2.60 \cdot 10^{90}$	$2.63 \cdot 10^{90}$	$2.65 \cdot 10^{90}$	$6.46 \cdot 10^{40}$	$6.46 \cdot 10^{40}$	$5.95 \cdot 10^{40}$	$1.50 \cdot 10^{110}$	$1.44 \cdot 10^{110}$	$1.50 \cdot 10^{110}$
673	$6.89 \cdot 10^{77}$	$6.99 \cdot 10^{77}$	$6.99 \cdot 10^{77}$	$1.28 \cdot 10^{35}$	$1.35 \cdot 10^{35}$	$1.25 \cdot 10^{35}$	$5.42 \cdot 10^{94}$	$5.22 \cdot 10^{94}$	$5.42 \cdot 10^{94}$
773	$3.44 \cdot 10^{68}$	$3.50 \cdot 10^{68}$	$3.49 \cdot 10^{68}$	$8.28 \cdot 10^{30}$	$8.75 \cdot 10^{30}$	$8.09 \cdot 10^{30}$	$2.12 \cdot 10^{83}$	$2.05 \cdot 10^{83}$	$2.12 \cdot 10^{83}$
873	$2.42 \cdot 10^{61}$	$2.47 \cdot 10^{61}$	$2.77 \cdot 10^{61}$	$5.08 \cdot 10^{27}$	$5.36 \cdot 10^{27}$	$4.96 \cdot 10^{27}$	$3.65 \cdot 10^{74}$	$3.56 \cdot 10^{74}$	$3.65 \cdot 10^{74}$

For the ammonia synthesis reaction  $\text{N}_2 + 3\text{H}_2 \rightleftharpoons 2\text{NH}_3$ , the equilibrium constant of Eq. A68 becomes

$$K = \frac{(y_{\text{NH}_3} P \varphi_{\text{NH}_3})^2}{(y_{\text{N}_2} P \varphi_{\text{N}_2})(y_{\text{H}_2} P \varphi_{\text{H}_2})^3} (k_B T)^2 \quad (\text{A70})$$

The fugacity coefficients of ammonia, nitrogen and hydrogen can be obtained from the Peng-Robinson Equation of State [240]:

$$P = \frac{RT}{V - b} - \frac{a}{V(V + b) + b(V - b)} \quad (\text{A71})$$

$$\begin{aligned} \ln \varphi_i = & \frac{b_i}{b_m} (Z_m - 1) - \ln (Z_m - B_m) \\ & - \frac{A_m}{2\sqrt{2}B_m} \left( \frac{2 \sum_{k=1}^S y_k a_{ik}}{a_m} - \frac{b_i}{b} \right) \ln \left( \frac{Z_m + 2.414B_m}{Z_m - 0.414B_m} \right) \end{aligned} \quad (\text{A72})$$

$S$  is the number of components,  $Z_m$  is the compressibility factor and  $A_m$  and  $B_m$  are defined as [240, 241]

$$A_m = a_m(T) P / R^2 T^2, \quad B_m = b_m P / RT, \quad Z_m = PV / RT \quad (\text{A73})$$

$a_m$  and  $b_m$  are constants taking into account the molecular interactions in the mixture and co-volume, respectively. For mixtures,  $a$  and  $b$  in Eq. A71 are replaced by  $a_m$  and  $b_m$ , respectively. The van der Waals mixing rules are used to compute these values [240, 241]:

$$\begin{aligned} a_m &= \sum_{i=1}^S \sum_{j=i}^S x_i x_j a_{ij} \\ b_m &= \sum_{i=1}^S \sum_{j=i}^S x_i x_j b_{ij} \end{aligned} \quad (\text{A74})$$

where  $x_i$  is the mole fraction of component  $i$ . In the above equation,  $a_{ii}$  and  $b_{ii}$  correspond to pure component  $i$  and are defined as [240, 241]

$$\begin{aligned} a_{ii}(T) &= 0.4572 \frac{R^2 T_c^2}{P_c} \left[ 1 + (0.3746 + 1.5423\omega - 0.2699\omega^2) \left( 1 - T_r^{1/2} \right) \right]^2 \\ b_{ii} &= \frac{0.078RT_c}{P_c} \end{aligned} \quad (\text{A75})$$

$\omega$  is the acentric factor of the component which can be found in literature [242].  $T_c$  and  $P_c$  are the critical temperature and critical pressure of

Table A4: Critical temperatures ( $T_c$ ), pressures ( $P_c$ ) and acentric factors ( $\omega$ ) of the components used in the PR-EoS modeling [242].

Component	$T_c$ / [K]	$P_c$ / [Pa]	$\omega$
N <sub>2</sub>	126.19	3395800	0.0372
H <sub>2</sub>	33.14	1296400	-0.219
NH <sub>3</sub>	405.4	11333000	0.25601

the component, respectively. Critical points and acentric factors for nitrogen, hydrogen and ammonia are taken from the REFPROP database [243] and are listed in Table A4.  $a_{ij}$  and  $b_{ij}$  corresponds to unlike-interaction parameters and defined as

$$\begin{aligned} a_{ij} &= (a_{ii}a_{jj})^{1/2} (1 - k_{ij}) \\ b_{ij} &= \frac{(b_{ii} + b_{jj})}{2} \end{aligned} \quad (\text{A76})$$

$k_{ij}$  is the coupling interaction parameter. For a given temperature and pressure, the right hand side of Eq. A70 is defined by mixture compositions at equilibrium. To obtain the mixture compositions at equilibrium using the PR-EoS, the reaction is started with 3 moles of H<sub>2</sub> and 1 mole of N<sub>2</sub> and no ammonia. The reaction coordinate  $\varepsilon \in [0, 1]$  is defined as a measure of the extent of the reaction. The value 0 meaning the reaction has not taken place and the value 1 meaning all reactants are converted into reaction products. Knowing the initial composition, the mixture composition at equilibrium is defined by the value of  $\varepsilon$ , when equilibrium is reached. Using Eq. A70 and the Peng-Robinson equation of state, the value of  $\varepsilon$  can be found iteratively and this directly leads to the composition of the mixture at chemical equilibrium.

## A.6 Molecular interactions for modelling the ammonia synthesis reaction

For the Lennard-Jones interactions, the cutoff radius is set to 12.0 Å. The Lorentz-Berthelot mixing rules and analytical tail corrections are used [183]. For fractional molecules, Lennard-Jones interactions are scaled as:

$$u(r, \lambda_i) = \lambda_i 4\epsilon \left( \frac{1}{\left[ \frac{1}{2} (1 - \lambda_i)^2 + \left( \frac{r}{\sigma} \right)^6 \right]^2} - \frac{1}{\left[ \frac{1}{2} (1 - \lambda_i)^2 + \left( \frac{r}{\sigma} \right)^6 \right]} \right) \quad (\text{A77})$$

where  $\lambda_i$  is the scaling parameter for fractional molecule  $i$ . The value of  $\lambda_i$  will be zero when  $\lambda = a_i$  and it will be 1 when  $\lambda = b_i$ ; this is shown schematically in FIGURE X. When two fractional molecules interact, the interactions are scaled according to minimum of  $\lambda_i$  of the two molecules. The tail corrections energy for two atom types  $i$  and  $j$  equals [38]:

$$u_{\text{tail}}^{ij} = \frac{16\pi N_i N_j \epsilon_{ij}}{V} \left( \frac{\sigma_{ij}^{12}}{9r_{\text{cut}}^9} - \frac{\sigma_{ij}^6}{3r_{\text{cut}}^3} \right) \quad (\text{A78})$$

where  $N_i$  and  $N_j$  are the total number of atoms of type  $i$  and  $j$  in the simulation box,  $V$  is the volume of the simulation box and  $r_{\text{cut}}$  the cutoff radius. An atom of a fractional molecule is counted as  $\lambda$ . The total tail correction energy of the system is then:

$$U_{\text{tail, total}} = \frac{1}{2} \sum_{i=1}^M \sum_{j=1}^M u_{\text{tail}}^{ij}$$

where  $M$  is the number of different atom types and the factor  $\frac{1}{2}$  corrects for counting contributions double. Coulombic interactions are calculated with the Wolf method [229]. Here, also a cutoff radius of 12.0 Å is used and the damping parameter was set to  $\alpha = 0.10 \text{ \AA}^{-1}$ . In the Wolf method, Coulombic interactions are calculated in two parts.

The first part is a damped pairwise potential:

$$u(r) = \frac{q_i q_j}{4\pi\epsilon_0} \left( \frac{\operatorname{erfc}(\alpha r)}{r} - \frac{\operatorname{erfc}(\alpha r_{\text{cut}})}{r_{\text{cut}}} \right) \quad (\text{A79})$$

where  $\alpha$  is a damping parameter,  $r_{\text{cut}}$  the cutoff radius, and  $\operatorname{erfc}(x)$  is the complementary error function. These interactions should be calculated for all interacting atom pairs, both intermolecular and intramolecular. For fractional molecules, we use a slightly different form:

$$u(r, \lambda_i) = \frac{\lambda_i q_i q_j}{4\pi\epsilon_0} \left( \frac{\operatorname{erfc}(\alpha r)}{r + A(1 - \lambda_i)^2} - \frac{\operatorname{erfc}(\alpha r_{\text{cut}})}{r_{\text{cut}} + A(1 - \lambda_i)^2} \right) \quad (\text{A80})$$

where  $A=1/2$  Å. This ensures that for  $\lambda = 1$  we have the original interaction potential and for  $\lambda = 0$  interactions are switched off, and no singularities are present when  $\lambda \rightarrow 0$ . The second term is a correction term called the self term [229]:

$$u_{\text{self}} = -\frac{1}{4\pi\epsilon_0} \left( \frac{\operatorname{erfc}(\alpha r_{\text{cut}})}{2r_{\text{cut}}} + \frac{\alpha}{\sqrt{\pi}} \right) \sum_{i=1}^N q_i^2 \quad (\text{A81})$$

where the sum is over all atomic charges so that  $N$  is the total number of atoms in the system. Fractional molecules are included by substituting  $N$  by  $N + N_{\text{frac}}$  ( $N_{\text{frac}}$  is the total number of atoms of fractional molecules). For fractional molecules, the term  $q_i^2$  is replaced by  $\lambda_i q_i^2$ . Here we are considering only rigid molecules, therefore, we do not have any intramolecular Coulombic interactions. As the pairwise potential of Eq. A79 is also applied to intramolecular charge pairs, we should add an exclusion term similar to the Ewald summation [33, 244, 245]. The exclusion term is:

$$u_{\text{excl}} = -\frac{\lambda_i q_i q_j}{4\pi\epsilon_0(r + A(1 - \lambda_i))} \quad (\text{A82})$$

and it should be added for all intramolecular charge pairs.

By comparing the total electrostatic energy of several configurations using the Wolf method and the Ewald summation [38, 195], we verified that the electrostatic energies computed using the Wolf method are nearly identical and these two methods yield the same Vapour-Liquid Equilibria for different molecules [245].

Force field parameters used for ammonia, nitrogen and, hydrogen are listed in Table A5 [225–228]. Hydrogen is modeled by a single chargeless Lennard-Jones interaction site. For nitrogen, bond lengths and angles are:

- $d(N_{N_2}, M_{N_2}) = 0.55\text{\AA}$
- $d(N_{N_2}, N_{N_2}) = 1.10\text{\AA}$
- $\theta(N_{N_2}, M_{N_2}, N_{N_2}) = 180 \text{ deg}$

$M_{N_2}$  is a dummy site which only carries a partial charge and is located in between the two N atoms (see also Table A5). For ammonia, bond lengths and angles are:

- $d(N_{NH_3}, H_{NH_3}) = 1.012\text{\AA}$
- $d(N_{NH_3}, M_{NH_3}) = 0.080\text{\AA}$
- $\theta(H_{NH_3}, N_{NH_3}, H_{NH_3}) = 106.7 \text{ deg}$
- $\theta(H_{NH_3}, N_{NH_3}, M_{NH_3}) = 67.9 \text{ deg}$

$M_{NH_3}$  is a dummy site which only carries a partial charge and is located in outside the three H atoms (see also Table A5).

Table A5: Force field parameters (Lennard-Jones parameters, and partial charges of interaction sites) used for ammonia, nitrogen and, hydrogen [225–228]. The different interaction sites are defined in appendix A.6. Lennard-Jones interactions between unlike atoms are calculated using the Lorentz–Berthelot mixing rules [183].

Site	$\sigma$ /[\AA]	$\epsilon/k_B$ /[K]	$q$ /[e]
$N_{N_2}$	3.32	36.4	-0.40505
$M_{N_2}$	0.0	0.0	0.8101
$H_2$	2.915	38.0	0.0
$N_{NH_3}$	3.420	185.0	0.0
$H_{NH_3}$	0.0	0.0	0.410
$M_{NH_3}$	0.0	0.0	-1.230



# References

- (1) Ravindra, K.; Sokhi, R.; Grieken, R. V. Atmospheric polycyclic aromatic hydrocarbons: source attribution, emission factors and regulation. *Atmos. Environ.* **2008**, *42*, 2895–2921.
- (2) Mi, H.-H.; Lee, W.-J.; Chen, C.-B.; Yang, H.-H.; Wu, S.-J. Effect of fuel aromatic content on PAH emission from a heavy-duty diesel engine. *Chemosphere* **2000**, *41*, 1783–1790.
- (3) Baek, S.; Field, R.; Goldstone, M.; Kirk, P.; Lester, J.; Perry, R. A Review of atmospheric polycyclic aromatic hydrocarbons: sources, fate and behavior., English *Water, Air, Soil Pollut.* **1991**, *60*, 279–300.
- (4) Biswas, J.; Maxwell, I. E. Octane enhancement in fluid catalytic cracking: I. role of ZSM-5 addition and reactor temperature. *Appl. Catal.* **1990**, *58*, 1–18.
- (5) Karavalakis, G.; Short, D.; Vu, D.; Russell, R.; Hajbabaei, M.; Asa-Awuku, A.; Durbin, T. D. Evaluating the effects of aromatics content in gasoline on gaseous and particulate matter emissions from SI-PFI and SIDI vehicles. *Environ. Sci. Technol.* **2015**, *49*, 7021–7031.
- (6) Weisel, C. P. Benzene exposure: An overview of monitoring methods and their findings. *Chem. Biol. Interact.* **2010**, *184*, 58–66.
- (7) Morley, C. A Fundamentally based correlation between alkane structure and octane number. *Combust. Sci. Technol.* **1987**, *55*, 115–123.

- (8) Pasadakis, N.; Gaganis, V.; Foteinopoulos, C. Octane number prediction for gasoline blends. *Fuel Process. Technol.* **2006**, *87*, 505–509.
- (9) Rownaghi, A. A.; Rezaei, F.; Hedlund, J. Selective formation of light olefin by n-hexane cracking over HZSM-5: influence of crystal size and acid sites of nano-and micrometer-sized crystals. *Chem. Eng. J.* **2012**, *191*, 528–533.
- (10) Soualah, A; Lemberton, J.-L.; Pinard, L; Chater, M; Magnoux, P.; Moljord, K Hydroisomerization of long-chain n-alkanes on bifunctional Pt/zeolite catalysts: Effect of the zeolite structure on the product selectivity and on the reaction mechanism. *Appl. Catal. A* **2008**, *336*, 23–28.
- (11) Bouchy, C; Hastoy, G; Guillon, E; Martens, J. Fischer-Tropsch waxes upgrading via hydrocracking and selective hydroisomerization. *Oil & Gas Scie. Tech.* **2009**, *64*, 91–112.
- (12) Smit, B.; Maesen, T. L. M. Molecular simulations of zeolites: adsorption, diffusion, and shape selectivity. *Chem. Rev.* **2008**, *108*, 4125–4184.
- (13) Jae, J.; Tompsett, G. A.; Foster, A. J.; Hammond, K. D.; Auerbach, S. M.; Lobo, R. F.; Huber, G. W. Investigation into the shape selectivity of zeolite catalysts for biomass conversion. *J. Catal.* **2011**, *279*, 257–268.
- (14) Gomes, V. G.; Yee, K. W. Pressure swing adsorption for carbon dioxide sequestration from exhaust gases. *Sep. Purif. Technol.* **2002**, *28*, 161–171.
- (15) Yang, H.; Xu, Z.; Fan, M.; Gupta, R.; Slimane, R. B.; Bland, A. E.; Wright, I. Progress in carbon dioxide separation and capture: A review. *J. Environ. Sci.* **2008**, *20*, 14–27.
- (16) Li, J. R.; Kuppler, R. J.; Zhou, H.-C. Selective gas adsorption and separation in metal-organic frameworks. *Chem. Soc. Rev.* **2009**, *38*, 1477–1504.

- (17) Jensen, N. K.; Rufford, T. E.; Watson, G.; Zhang, D. K.; Chan, K. I.; May, E. F. Screening zeolites for gas separation applications involving methane, nitrogen, and carbon dioxide. *J. Chem. Eng. Data* **2012**, *57*, 106–113.
- (18) Earl, D. J.; Deem, M. W. Toward a database of hypothetical zeolite structures. *Ind. Eng. Chem. Res.* **2006**, *45*, 5449–5454.
- (19) Sircar, S.; Cao, D. V. Heat of adsorption. *Chem. Eng. Technol.* **2002**, *25*, 945–948.
- (20) Chen, D.-L.; Wang, N.; Xu, C.; Tu, G.; Zhu, W.; Krishna, R. A combined theoretical and experimental analysis on transient breakthroughs of  $C_2H_6/C_2H_4$  in fixed beds packed with ZIF-7. *Micropor. Mesopor. Mat.* **2015**, *208*, 55 –65.
- (21) Ghorai, S.; Pant, K. Equilibrium, kinetics and breakthrough studies for adsorption of fluoride on activated alumina. *Sep. Purif. Technol.* **2005**, *42*, 265 –271.
- (22) Shendalman, L. H.; Mitchell, J. E. A study of heatless adsorption in the model system  $CO_2$  in He, I. *Chem. Eng. Sci.* **1972**, *27*, 1449–1458.
- (23) Silva, J. A. C.; Ferreira, A.; Mendes, P. A. P.; Cunha, A. F.; Gleichmann, K.; Rodrigues, A. E. Adsorption equilibrium and dynamics of fixed bed adsorption of  $CH_4/N_2$  in binderless beads of 5A zeolite. *Ind. Eng. Chem. Res.* **2015**, *54*, 6390–6399.
- (24) Valdés-Solis, T.; Linders, M.; Kapteijn, F.; Marbán, G.; Fuertes, A. Adsorption and breakthrough performance of carbon-coated ceramic monoliths at low concentration of n-butane. *Chem. Eng. Sci.* **2004**, *59*, 2791 –2800.
- (25) Mason, J. A.; Sumida, K.; Herm, Z. R.; Krishna, R.; Long, J. R. Evaluating metal–organic frameworks for post-combustion carbon dioxide capture via temperature swing adsorption. *Energy Environ. Sci.* **2011**, *4*, 3030–3040.

- (26) Bloch, E. D.; Queen, W. L.; Krishna, R.; Zadrozny, J. M.; Brown, C. M.; Long, J. R. Hydrocarbon separations in a Metal-Organic Framework with open Iron(II) coordination sites. *Science* **2012**, *335*, 1606–1610.
- (27) Chowdhury, S.; Mishra, R.; Saha, P.; Kushwaha, P. Adsorption thermodynamics, kinetics and isosteric heat of adsorption of malachite green onto chemically modified rice husk. *Desalination* **2011**, *265*, 159 –168.
- (28) Sircar, S.; Mohr, R.; Ristic, C.; Rao, B. M. Isosteric heat of adsorption: theory and experiment. *J. Phys. Chem. B* **1999**, *103*, 6539–6546.
- (29) Schenk, M.; Vidal, S. L.; Vlugt, T. J. H.; Smit, B.; Krishna, R. Separation of alkane isomers by exploiting entropy effects during adsorption on silicalite-1: A Configurational-Bias Monte Carlo simulation study. *Langmuir* **2001**, *17*, 1558–1570.
- (30) Torres-Knoop, A.; Dubbeldam, D. Exploiting large-pore Metal-Organic Frameworks for separations through entropic molecular mechanisms. *Chem. Phys. Chem.* **2015**, *16*, 2046–2067.
- (31) Torres-Knoop, A.; Heinen, J.; Krishna, R.; Dubbeldam, D. Entropic separation of styrene/ethylbenzene mixtures by exploitation of subtle differences in molecular configurations in ordered crystalline nanoporous adsorbents. *Langmuir* **2015**, *31*, 3771–3778.
- (32) Torres-Knoop, A.; Poursaeidesfahani, A.; Vlugt, T. J. H.; Dubbeldam, D. Behavior of the enthalpy of adsorption in nanoporous materials close to saturation conditions. *J. Chem. Theory Comput.* **2017**, *13*, 3326–3339.
- (33) Vlugt, T. J. H.; García-Pérez, E.; Dubbeldam, D.; Ban, S.; Calero, S. Computing the heat of adsorption using molecular simulations: The effect of strong coulombic interactions. *J. Chem. Theory. Comput.* **2008**, *4*, 1107–1118.

- (34) Qiao, Z.; Torres-Knoop, A.; Dubbeldam, D.; Fairen-Jimenez, D.; Zhou, J.; Snurr, R. Q. Advanced Monte Carlo simulations of the adsorption of chiral alcohols in a homochiral Metal-Organic Framework. *AIChE J.* **2014**, *60*, 2324–2334.
- (35) Getman, R. B.; Bae, Y.-S.; Wilmer, C. E.; Snurr, R. Q. Review and analysis of molecular simulations of methane, hydrogen, and acetylene storage in Metal-Organic Frameworks. *Chem. Rev.* **2012**, *112*, 703–723.
- (36) Herm, Z. R.; Wiers, B. M.; Mason, J. A.; van Baten, J. M.; Hudson, M. R.; Zajdel, P.; Brown, C. M.; Masciocchi, N.; Krishna, R.; Long, J. R. Separation of hexane isomers in a Metal-Organic Framework with triangular channels. *Science* **2013**, *340*, 960–964.
- (37) Gutierrez-Sevillano, J. J.; Vicent-Luna, J. M.; Dubbeldam, D.; Calero, S. Molecular mechanisms for adsorption in Cu-BTC Metal-Organic Framework. *J. Phys. Chem. C* **2013**, *117*, 11357–11366.
- (38) Frenkel, D.; Smit, B., *Understanding molecular simulation: from algorithms to applications*, 2nd ed.; Academic Press: San Diego, California, 2002.
- (39) Svoboda, G. D.; Vynckier, E.; Debrabandere, B.; Froment, G. F. Single-event rate parameters for paraffin hydrocracking on a Pt/US-Y zeolite. *Ind. Eng. Chem. Res.* **1995**, *34*, 3793–3800.
- (40) Thybaut, J. W.; Marin, G. B. Kinetic modeling of the conversion of complex hydrocarbon feedstocks by acid catalysts. *Chem. Eng. Technol.* **2003**, *26*, 509–514.
- (41) Smit, B.; Maesen, T. L. M. Towards a molecular understanding of shape selectivity. *Nature* **2008**, *451*, 671–678.
- (42) Janda, A.; Vlaisavljevich, B.; Smit, B.; Lin, L.-C.; Bell, A. T. Effects of pore and cage topology on the thermodynamics of n-alkane adsorption at bronsted protons in zeolites at high temperature. *J. Phys. Chem. C* **2017**, *121*, 1618–1638.

- (43) Konno, H.; Okamura, T.; Kawahara, T.; Nakasaka, Y.; Tago, T.; Masuda, T. Kinetics of n-hexane cracking over ZSM-5 zeolites—effect of crystal size on effectiveness factor and catalyst lifetime. *Chem. Eng. J.* **2012**, *207*, 490–496.
- (44) Denayer, J. F.; Martens, J. A.; Jacobs, P. A.; Thybaut, J. W.; Marin, G. B.; Baron, G. Influence of the zeolite composition on the hydroisomerisation and hydrocracking of alkanes on Pt/USY zeolites: modelling of the reaction kinetics using an adsorption reaction approach. *Appl. Catal. A* **2003**, *246*, 17–28.
- (45) Martens, J.; Parton, R; Uytterhoeven, L; Jacobs, P.; Froment, G. Selective conversion of decane into branched isomers: A comparison of platinum/ZSM-22, platinum/ZSM-5 and platinum/USY zeolite catalysts. *Appl. Catal.* **1991**, *76*, 95–116.
- (46) Swisher, J. A.; Hansen, N.; Maesen, T.; Keil, F. J.; Smit, B.; Bell, A. T. Theoretical simulation of n-alkane cracking on zeolites. *J. Phys. Chem. C* **2010**, *114*, 10229–10239.
- (47) Martens, G.; Marin, G.; Martens, J.; Jacobs, P.; Baron, G. A fundamental kinetic model for hydrocracking of  $C_8$  to  $C_{12}$  alkanes on Pt/US-Y zeolites. *J. Catal.* **2000**, *195*, 253–267.
- (48) Steijns, M.; Froment, G. F. Hydroisomerization and hydrocracking. 3. Kinetic analysis of rate data for n-decane and n-dodecane. *Ind. Eng. Chem. Prod. Res. Dev.* **1981**, *20*, 660–668.
- (49) Vlugt, T. J. H.; Krishna, R.; Smit, B. Molecular simulations of adsorption isotherms for linear and branched alkanes and their mixtures in silicalite. *J. Phys. Chem. B* **1999**, *103*, 1102–1118.
- (50) Dickman, R.; Hall, C. K. High density Monte Carlo simulations of chain molecules: bulk equation of state and density profile near walls. *The Journal of Chemical Physics* **1988**, *89*, 3168–3174.
- (51) Dubbeldam, D.; Calero, S.; Vlugt, T. J. H. iRASPA: GPU-accelerated visualization software for materials scientists. *Mol. Sim.* **2018**, *44*, 653–676.

- (52) Torres-Knoop, A.; Krishna, R.; Dubbeldam, D. Separating xylene isomers by commensurate stacking of p-xylene within channels of MAF-X8. *Angew. Chem. Int.* **2014**, *53*, 7774–7778.
- (53) International Zeolite Association and Structure Commission and others, *Database of zeolite structures*; IZA Structure Commission: 2001.
- (54) Shi, W.; Maginn, E. J. Continuous Fractional Component Monte Carlo: An adaptive biasing method for open system atomistic simulations. *J. Chem. Theory Comput.* **2007**, *3*, 1451–1463.
- (55) Shi, W.; Maginn, E. J. Improvement in molecule exchange efficiency in Gibbs ensemble Monte Carlo: Development and implementation of the Continuous Fractional Component Move. *J. Comput. Chem.* **2008**, *29*, 2520–2530.
- (56) Foo, K.; Hameed, B. Insights into the modeling of adsorption isotherm systems. *Chem. Eng. J.* **2010**, *156*, 2 –10.
- (57) Serra-Crespo, P.; Berger, R.; Yang, W.; Gascon, J.; Kapteijn, F. Separation of CO<sub>2</sub> / CH<sub>4</sub> mixtures over NH<sub>2</sub>-MIL-53 An experimental and modelling study. *Chem. Eng. Sci.* **2015**, *124*, 96 –108.
- (58) Shafeeyan, M. S.; Daud, W. M. A. W.; Shamiri, A. A review of mathematical modeling of fixed-bed columns for carbon dioxide adsorption. *Chem. Eng. Res. Des.* **2014**, *92*, 961 –988.
- (59) Zhang, W.; Shan, Y.; Seidel-Morgenstern, A. Breakthrough curves and elution profiles of single solutes in case of adsorption isotherms with two inflection points. *J. Chromatogr. A* **2006**, *1107*, 216–225.
- (60) Lisec, O; Hugo, P; Seidel-Morgenstern, A Frontal analysis method to determine competitive adsorption isotherms. *J. Chromatogr. A.* **2001**, *908*, 19–34.
- (61) Seidel-Morgenstern, A. Experimental determination of single solute and competitive adsorption isotherms. *J. Chromatogr. A.* **2004**, *1037*, 255–272.

- (62) Rhee, H. K.; Aris, R.; Amundson, N. R. on the theory of multicomponent chromatography. *Philosophical Transactions of the Royal Society of London* **1970**, *267*, 419–455.
- (63) Helfferich, F. G.; Klein, G., *Multicomponent Chromatography*; Marcel Dekker: New York, 1970.
- (64) Wilson, J. N. A Theory of chromatography. *J. Amer. Chem. Soc.* **1940**, *62*, 1583–1591.
- (65) DeVault, D. The theory of chromatography. *J. Amer. Chem. Soc.* **1943**, *65*, 532–540.
- (66) Glueckauf, E Theory of chromatography. Part II. *J. Chem. Soci.* **1947**, *10*, 1302–1308.
- (67) Guiochon, G; Golshan-Shirazi, S; Katti, A. M., *Fundamentals of nonlinear and preparative chromatography*; Academic Press: Boston, 1994.
- (68) Rhee, H.-K.; Aris, R.; Amundson, N. R., *First-order partial differential equations, volume I, theory and application of single equations*; Prentice Hall Inc: Englewood Cliffs, NJ, 1986.
- (69) Rhee, H.-K.; Aris, R.; Amundson, N. R., *First-order partial differential equations, volume II, theory and application of single equations*; Prentice Hall Inc: Englewood Cliffs, NJ, 1989.
- (70) Tiscornia, I.; Valencia, S.; Corma, A.; Tellez, C.; Coronas, J.; Santamaria, J. Preparation of ITQ-29 (Al-free zeolite A) membranes. *Micropor. Mesoporo. Mat.* **2008**, *110*, 303 –309.
- (71) Palomino, M.; Corma, A.; Rey, F.; Valencia, S. New insights on CO<sub>2</sub>-Methane separation using LTA zeolites with different Si/Al ratios and a first comparison with MOFs. *Langmuir* **2010**, *26*, 1910–1917.
- (72) Van Miltenburg, A.; Gascon, J.; Zhu, W.; Kapteijn, F.; Moulijn, J. A. Propylene/propane mixture adsorption on faujasite sorbents. *Adsorption* **2008**, *14*, 309–321.
- (73) Ergun, S. Fluid flow through packed columns. *Chem. Eng. Prog.* **1952**, *48*, 89–94.

- (74) Gascon, J.; Blom, W.; van Miltenburg, A.; Ferreira, A.; Berger, R.; Kapteijn, F. Accelerated synthesis of all-silica DD3R and its performance in the separation of propylene/propane mixtures. *Micropor. Mesopor. Mat.* **2008**, *115*, 585–593.
- (75) Glueckauf, E. Theory of chromatography. Part 1. Formula for diffusion into spheres and their application to chromatography. *Trans. Faraday Soc.* **1955**, *51*, 1540–1551.
- (76) Hartzog, D. G.; Sircar, S. Sensitivity of PSA process performance to input variables. *Adsorption* **1995**, *1*, 133–151.
- (77) Ruthven, D. M., *Principles of adsorption and adsorption processes*; John Wiley & Sons: New York, 1984.
- (78) Sircar, S.; Hufton, J. R. Why does the linear driving force model for adsorption kinetics work? *Adsorption* **2000**, *6*, 137–147.
- (79) Myers, A. L.; Prausnitz, J. M. Thermodynamics of mixed-gas adsorption. *AIChE J.* **1965**, *11*, 121–127.
- (80) Hand, D. W.; Loper, S.; Ari, M.; Crittenden, J. C. Prediction of multicomponent adsorption equilibria using ideal adsorbed solution theory. *Environ. Sci. Technol.* **1985**, *19*, 1037–1043.
- (81) Kheifets, L.; Predtechenskaya, D. On the applicability of the theory of ideal adsorption solutions to equilibria in the N<sub>2</sub>-O<sub>2</sub>-zeolite NaX system., English *Russ. J. Phys. Chem.* **2006**, *80*, 196–199.
- (82) Krishna, R.; van Baten, J. M. Influence of segregated adsorption on mixture diffusion in DDR zeolite. *Chem. Phys. Lett.* **2007**, *446*, 344–349.
- (83) Krishna, R; Van Baten, J. M. Segregation effects in adsorption of CO<sub>2</sub>-containing mixtures and their consequences for separation selectivities in cage-type zeolites. *Sep. Purif. Technol.* **2008**, *61*, 414–423.
- (84) Walton, K. S.; Sholl, D. S. Predicting multicomponent adsorption: 50 years of the ideal adsorbed solution theory. *AIChE J.* **2015**, *61*, 2757–2762.

- (85) Yang, R. T., *Gas separation by adsorption processes*; Butterworth: Boston, 1997.
- (86) Moulijn, J. A.; Van Swaaij, W. P. M. The correlation of axial dispersion data for beds of small particles. *Chem. Eng. Sci.* **1976**, *31*, 845–847.
- (87) Schiesser, W. E., *The numerical method of lines: integration of partial differential equations*; Elsevier Bethlehem Pennsylvania: 2012.
- (88) Yu, H.; Wang, X.; Xu, C.; Chen, D.-L.; Zhu, W.; Krishna, R. Utilizing transient breakthroughs for evaluating the potential of Kureha carbon for CO<sub>2</sub> capture. *Chem. Eng. J.* **2015**, *269*, 135–147.
- (89) Knox, J. C.; Ebner, A. D.; LeVan, M. D.; Coker, R. F.; Ritter, J. A. Limitations of breakthrough curve analysis in fixed-bed adsorption. *Ind. Eng. Chem. Res.* **2016**, *55*, 4734–4748.
- (90) Hatzikioseyan, A; Tsezos, M; Mavituna, F Application of simplified rapid equilibrium models in simulating experimental breakthrough curves from fixed bed biosorption reactors. *Hydrometallurgy* **2001**, *59*, 395 –406.
- (91) Yoshida, H.; Kataoka, T.; Ruthven, D. M. Analytical solution of the breakthrough curve for rectangular isotherm systems. *Chem. Eng. Sci.* **1984**, *39*, 1489–1497.
- (92) Raghavan, N. S.; Ruthven, D. M. Numerical simulation of a fixed-bed adsorption column by the method of orthogonal collocation. *AIChE J.* **1983**, *29*, 922–925.
- (93) Gholami, M.; Talaie, M. R. Investigation of simplifying assumptions in mathematical modeling of natural gas dehydration using adsorption process and introduction of a new accurate LDF model. *Ind. Eng. Chem. Res.* **2010**, *49*, 838–846.
- (94) Funke, H. H.; Argo, A. M.; Falconer, J. L.; Noble, R. D. Separations of cyclic, branched, and linear hydrocarbon mixtures through silicalite membranes. *Ind. Eng. Chem. Res.* **1997**, *36*, 137–143.

- (95) Maesen, T. L. M.; Schenk, M.; Vlugt, T. J. H.; Smit, B. Differences between MFI- and MEL-Type zeolites in paraffin hydrocracking. *J. Catal.* **2001**, *203*, 281–291.
- (96) Denayer, J. F.; Souverijns, W.; Jacobs, P. A.; Martens, J. A.; Baron, G. V. High-temperature Low-pressure adsorption of branched C<sub>5</sub>-C<sub>8</sub> alkanes on zeolite Beta, ZSM-5, ZSM-22, zeolite Y, and Mordenite. *J. Phys. Chem. B* **1998**, *102*, 4588–4597.
- (97) Funke, H. H.; Kovalchick, M. G.; Falconer, J. L.; Noble, R. D. Separation of hydrocarbon isomer vapors with silicalite zeolite membranes. *Ind. Eng. Chem. Res.* **1996**, *35*, 1575–1582.
- (98) Krishna, R.; Smit, B.; Vlugt, T. J. H. Sorption-induced diffusion-selective separation of hydrocarbon isomers using silicalite. *J. Phys. Chem. A* **1998**, *102*, 7727–7730.
- (99) Vlugt, T. J. H.; Zhu, W.; Kapteijn, F.; Moulijn, J. A.; Smit, B.; Krishna, R. Adsorption of linear and branched alkanes in the zeolite silicalite-1. *J. Amer. Chem. Soc.* **1998**, *120*, 5599–5600.
- (100) Krishna, R.; Vlugt, T. J. H.; Smit, B. Influence of isotherm inflection on diffusion in silicalite. *Chem. Eng. Sci.* **1999**, *54*, 1751 –1757.
- (101) Smit, B.; Siepmann, J. I. Computer simulations of the energetics and siting of n-alkanes in zeolites. *J. Phys. Chem.* **1994**, *98*, 8442–8452.
- (102) Garberoglio, G.; Skouidas, A. I.; Johnson, J. K. Adsorption of gases in Metal Organic materials: comparison of simulations and experiments. *J. Phys. Chem. B* **2005**, *109*, 13094–13103.
- (103) Myers, A. L. Thermodynamics of adsorption in porous materials. *AIChE J.* **2002**, *48*, 145–160.
- (104) Janda, A.; Vlaisavljevich, B.; Lin, L.-C.; Mallikarjun Sharada, S.; Smit, B.; Head-Gordon, M.; Bell, A. T. Adsorption thermodynamics and intrinsic activation parameters for monomolecular cracking of n-alkanes on Bronsted acid sites in Zeolites. *J. Phys. Chem. C* **2015**, *119*, 10427–10438.

- (105) Dubbeldam, D.; Calero, S.; Vlugt, T. J. H.; Krishna, R.; Maesen, T. L. M.; Smit, B. United atom force field for alkanes in nanoporous materials. *J. Phys. Chem. B* **2004**, *108*, 12301–12313.
- (106) Rosenbluth, M. N.; Rosenbluth, A. W. Monte Carlo calculation of the average extension of molecular chains. *J. Chem. Phys.* **1955**, *23*, 356–359.
- (107) Duren, T.; Bae, Y.-S.; Snurr, R. Q. Using molecular simulation to characterise Metal-Organic Frameworks for adsorption applications. *Chem. Soc. Rev.* **2009**, *38*, 1237–1247.
- (108) Lee, S.-J.; Bae, Y.-S. Can Metal-Organic Frameworks attain New DOE targets for on-board methane storage by increasing methane heat of adsorption? *J. Phys. Chem. C* **2014**, *118*, 19833–19841.
- (109) Nicholson, D., *Computer simulation and The statistical mechanics of adsorption*; Academic Press: 1982.
- (110) Vuong, T.; Monson, P. A. Monte Carlo simulation studies of heats of adsorption in heterogeneous solids. *Langmuir* **1996**, *12*, 5425–5432.
- (111) Karavias, F.; Myers, A. L. Isosteric heats of multicomponent adsorption: thermodynamics and computer simulations. *Langmuir* **1991**, *7*, 3118–3126.
- (112) Vlugt, T. J. H.; Schenk, M. Influence of framework flexibility on the adsorption properties of hydrocarbons in the zeolite silicalite. *J. Phys. Chem. B* **2002**, *106*, 12757–12763.
- (113) Farrusseng, D.; Daniel, C.; Gaudillère, C.; Ravon, U.; Schuurman, Y.; Mirodatos, C.; Dubbeldam, D.; Frost, H.; Snurr, R. Heats of adsorption for Seven Gases in three Metal-Organic Frameworks: systematic comparison of experiment and simulation. *Langmuir* **2009**, *25*, 7383–7388.
- (114) Jiang, J.; Sandler, S. I.; Schenk, M.; Smit, B. Adsorption and separation of linear and branched alkanes on carbon nanotube bundles from Configurational-Bias Monte Carlo simulation. *Phys. Rev. B* **2005**, *72*, 45447–45457.

- (115) Dubbeldam, D.; Calero, S.; Ellis, D. E.; Snurr, R. Q. RASPA: Molecular simulation software for adsorption and diffusion in flexible nanoporous materials. *Mol. Simul.* **2015**, *1*–21.
- (116) Dubbeldam, D.; Torres-Knoop, A.; Walton, K. S. On the inner workings of Monte Carlo codes. *Mol. Sim.* **2013**, *39*, 1253–1292.
- (117) Sadrameli, S. Thermal/catalytic cracking of hydrocarbons for the production of olefins: A state-of-the-art review I: Thermal cracking review. *Fuel* **2015**, *140*, 102–115.
- (118) Thybaut, J.; Marin, G.; Baron, G.; Jacobs, P.; Martens, J. Alkene protonation enthalpy determination from fundamental kinetic modeling of alkane hydroconversion on Pt/H-(US) Y-zeolite. *J. Catal.* **2001**, *202*, 324–339.
- (119) Marcilly, C. R. Where and how shape selectivity of molecular sieves operates in refining and petrochemistry catalytic processes. *Top. Catal.* **2000**, *13*, 357–366.
- (120) Denayer, J. F.; Baron, G. V.; Vanbutsele, G.; Jacobs, P. A.; Martens, J. A. Modeling of adsorption and bifunctional conversion of n-alkanes on Pt/H-ZSM-22 zeolite catalyst. *Chem. Eng. Sci.* **1999**, *54*, 3553–3561.
- (121) Baltanas, M. A.; Froment, G. F. Computer generation of reaction networks and calculation of product distributions in the hydroisomerization and hydrocracking of paraffins on Pt-containing bifunctional catalysts. *Comput. Chem. Eng.* **1985**, *9*, 71–81.
- (122) Claude, M. C.; Martens, J. A. Monomethyl-branching of long n-alkanes in the range from decane to tetracosane on Pt/H-ZSM-22 bifunctional catalyst. *J. Catal.* **2000**, *190*, 39–48.
- (123) Janda, A.; Vlaisavljevich, B.; Lin, L.-C.; Smit, B.; Bell, A. T. Effects of zeolite structural confinement on adsorption thermodynamics and reaction kinetics for monomolecular cracking and dehydrogenation of n-butane. *J. Amer. Chem. Soc.* **2016**, *138*, 4739–4756.

- (124) Zecevic, J.; Vanbutsele, G.; de Jong, K. P.; Martens, J. A. Nanoscale intimacy in bifunctional catalysts for selective conversion of hydrocarbons. *Nature* **2015**, *528*, 245.
- (125) Potoff, J. J.; Siepmann, J. I. Vapor–liquid equilibria of mixtures containing alkanes, carbon dioxide, and nitrogen. *AIChE J.* **2001**, *47*, 1676–1682.
- (126) Martin, M. G.; Siepmann, J. I. Transferable potentials for phase equilibria. 1. United-atom description of n-alkanes. *J. Phys. Chem. B* **1998**, *102*, 2569–2577.
- (127) Siepmann, J. I.; Frenkel, D. Configurational bias Monte Carlo: a new sampling scheme for flexible chains. *Mol. Phys.* **1992**, *75*, 59–70.
- (128) Laso, M.; de Pablo, J. J.; Suter, U. W. Simulation of phase equilibria for chain molecules. *J. Comput. Phys.* **1992**, *97*, 2817–2819.
- (129) Torrie, G. M.; Valleau, J. P. Nonphysical sampling distributions in Monte Carlo free-energy estimation: Umbrella sampling. *J. Comput. Phys.* **1977**, *23*, 187–199.
- (130) Zhu, X.; Wu, L.; Magusin, P. C.; Mezari, B.; Hensen, E. J. On the synthesis of highly acidic nanolayered ZSM-5. *J. Catal.* **2015**, *327*, 10–21.
- (131) Hensen, E. J.; Poduval, D. G.; Ligthart, D. M.; van Veen, J. R.; Rigo, M. S. Quantification of strong Brønsted acid sites in aluminosilicates. *J. Phys. Chem. C* **2010**, *114*, 8363–8374.
- (132) Poursaeidesfahani, A.; Torres-Knoop, A.; Rigo, M.; Nair, N.; Dubbeldam, D.; Vlugt, T. J. H. Computation of the heat and entropy of adsorption in proximity of inflection points. *J. Phys. Chem. C* **2016**, *120*, 1727–1738.
- (133) Scott, D. W.; McCullough, J. P.; El-Sabban, M. Z., *The chemical thermodynamic properties of hydrocarbons and related substances*; US Government Printing Office Washington, DC: 1974.

- (134) Verheyen, E.; Jo, C.; Kurttepeli, M.; Vanbutsele, G.; Gobechiya, E.; Korányi, T. I.; Bals, S.; Van Tendeloo, G.; Ryoo, R.; Kirschhock, C. E. Molecular shape-selectivity of MFI zeolite nanosheets in n-decane isomerization and hydrocracking. *J. Catal.* **2013**, *300*, 70–80.
- (135) Vynckier, E; Froment, G. Modeling of the kinetics of complex processes based upon elementary steps. *Kinetic and thermodynamic lumping of multicomponent mixtures* **1991**, *10*, 131–61.
- (136) Jacob, S. M.; Gross, B.; Voltz, S. E.; Weekman, V. W. A lumping and reaction scheme for catalytic cracking. *AICHE J.* **1976**, *22*, 701–713.
- (137) Orochko, D.; Perezhigina, I. Y.; Rogov, S.; Rysakov, M.; Chernakova, G. Applied over-all kinetics of hydrocracking of heavy petroleum distillates. *Chemistry and Technology of Fuels and Oils* **1970**, *6*, 561–565.
- (138) Quader, S.; Singh, S.; Wiser, W.; Hill, G. Hydrocracking of petroleum oil. *J. Inst. Petrol* **1970**, *56*, 187.
- (139) Zhorov, Y. M.; Panchenk, G. M.; Tatarint, G. M.; Kuzmin, S. T.; Zenkovsk, S. M. Chemical scheme and structure of mathematical description of hydrocracking. *Iny. Chem. Eng.* **1971**, *11*, 256.
- (140) Kumar, H. Mechanistic kinetic modeling of the hydrocracking of complex feedstocks., Ph.D. Thesis, Texas A&M University, 2006.
- (141) Liguras, D. K.; Allen, D. T. Structural models for catalytic cracking; Model compound reactions. *Ind. Eng. Chem. Res.* **1989**, *28*.
- (142) Quann, R. J.; Jaffe, S. B. Structure-oriented lumping: describing the chemistry of complex hydrocarbon mixtures. *Ind. Eng. Chem. Res.* **1992**, *31*, 2483–2497.
- (143) Bai, P.; Tsapatsis, M.; Siepmann, J. I. TraPPE-zeo: Transferable Potentials for Phase Equilibria Force Field for All-Silica Zeolites. *J. Phys. Chem. C* **2013**, *117*, 24375–24387.
- (144) Houdayer, J. The wormhole move: A new algorithm for polymer simulations. *J. Comput. Phys.* **2002**, *116*, 1783–1787.

- (145) Siepmann, J. I. A method for the direct calculation of chemical potentials for dense chain systems. *Mol. Phys.* **1990**, *70*, 1145–1158.
- (146) Siepmann, J. I.; Karaborni, S.; Smit, B. Vapor-liquid equilibria of model alkanes. *J. Amer. Chem. Soc.* **1993**, *115*, 6454–6455.
- (147) Poursaeidesfahani, A.; de Lange, M. F.; Khodadadian, F.; Dubbel-dam, D.; Rigo, M.; Nair, N.; Vlugt, T. J. H. Product shape selectivity of MFI-type, MEL-type, and BEA-type zeolites in the catalytic hydroconversion of heptane. *J. Catal.* **2017**, *353*, 54–62.
- (148) Banaszak, B. J.; Faller, R.; de Pablo, J. J. Simulation of the effects of chain architecture on the sorption of ethylene in polyethylene. *The Journal of Chemical Physics* **2004**, *120*, 11304–11315.
- (149) Ramdin, M.; Vlugt, T. J. H.; de Loos, T. W. Solubility of CO<sub>2</sub> in the ionic liquids [TBMN][MeSO<sub>4</sub>] and [TBMP][MeSO<sub>4</sub>]. *J. Chem. Eng. Data* **2012**, *57*, 2275–2280.
- (150) Adams, D. Grand-canonical ensemble Monte Carlo for a Lennard-Jones fluid. *Mol. Phys.* **1975**, *29*, 307–311.
- (151) Panagiotopoulos, A. Z. Direct determination of phase coexistence properties of fluids by Monte Carlo simulation in a new ensemble. *Mol. Phys.* **1987**, *61*, 813–826.
- (152) Panagiotopoulos, A. In *Observation, prediction and simulation of phase transitions in complex fluids*, Baus, M., Rull, L., Ryckaert, J., Eds.; NATO ASI Series, Vol. 460; Springer Netherlands: 1995, pp 463–501.
- (153) Panagiotopoulos, A.; Quirke, N.; Stapleton, M.; Tildesley, D. Phase equilibria by simulation in the Gibbs ensemble: alternative derivation, generalization and application to mixture and membrane equilibria. *Mol. Phys.* **1988**, *63*, 527–545.

- (154) Balaji, S. P.; Gangarapu, S.; Ramdin, M.; Torres-Knoop, A.; Zuilhof, H.; Goetheer, E. L. V.; Dubbeldam, D.; Vlugt, T. J. H. Simulating the reactions of CO<sub>2</sub> in aqueous monoethanolamine solution by reaction ensemble Monte Carlo using the Continuous Fractional Component Method. *J. Chem. Theory Comput.* **2015**, *11*, 2661–2669.
- (155) Ross, M. A high-density fluid-perturbation theory based on an inverse 12th-power hard-sphere reference system. *J. Comput. Phys.* **1979**, *71*, 1567–1571.
- (156) Brenner, D. W. Empirical potential for hydrocarbons for use in simulating the chemical vapor deposition of diamond films. *Phys. Rev. B* **1990**, *42*, 9458.
- (157) Consta, S.; Vlugt, T. J. H.; Wijchers Hoeth, J.; Smit, B.; Frenkel, D. Recoil growth algorithm for chain molecules with continuous interactions. *Mol. Phys.* **1999**, *97*, 1243–1254.
- (158) Combe, N.; Vlugt, T. J. H.; Wolde, P. R. T.; Frenkel, D. Dynamic pruned-enriched Rosenbluth method. *Mol. Phys.* **2003**, *101*, 1675–1682.
- (159) Escobedo, F. A.; de Pablo, J. J. Monte Carlo simulation of the chemical potential of polymers in an expanded ensemble. *J. Comput. Phys.* **1995**, *103*, 2703–2710.
- (160) Lyubartsev, A. P.; Martsinovski, A. A.; Shevkunov, S. V.; Vorontsov-Velyaminov, P. N. New approach to Monte Carlo calculation of the free energy: Method of expanded ensembles. *J. Comput. Phys.* **1992**, *96*, 1776–1783.
- (161) Rane, K. S.; Murali, S.; Errington, J. R. Monte Carlo simulation methods for computing liquid-vapor saturation properties of model systems. *J. Chem. Theory Comput.* **2013**, *9*, 2552–2566.

- (162) Ramdin, M.; Balaji, S. P.; Torres-Knoop, A.; Dubbeldam, D.; de Loos, T. W.; Vlugt, T. J. H. Solubility of natural gas species in ionic liquids and commercial solvents: experiments and Monte Carlo simulations. *J. Chem. Eng. Data* **2015**, *60*, 3039–3045.
- (163) Maginn, E. J. Atomistic simulation of the thermodynamic and transport properties of ionic liquids. *Acc. Chem. Res.* **2007**, *40*, 1200–1207.
- (164) Kelkar, M. S.; Shi, W.; Maginn, E. J. Determining the accuracy of classical force fields for ionic liquids: Atomistic simulation of the thermodynamic and transport properties of 1-Ethyl-3-methylimidazolium Ethylsulfate ([emim][EtSO<sub>4</sub>]) and Its Mixtures with Water. *Ind. Eng. Chem. Res.* **2008**, *47*, 9115–9126.
- (165) Zhang, X.; Huo, F.; Liu, Z.; Wang, W.; Shi, W.; Maginn, E. J. Absorption of CO<sub>2</sub> in the ionic liquid 1-n-Hexyl-3-methylimidazolium Tris(pentafluoroethyl)trifluorophosphate ([hmim][FEP]): A molecular view by computer simulations. *J. Phys. Chem. B* **2009**, *113*, 7591–7598.
- (166) Chen, Q.; Balaji, S. P.; Ramdin, M.; Gutierrez-Sevillano, J. J.; Bardow, A.; Goetheer, E. L. V.; Vlugt, T. J. H. Validation of the CO<sub>2</sub>/N<sub>2</sub>O analogy using molecular simulation. *Ind. Eng. Chem. Res.* **2014**, *53*, 18081–18090.
- (167) Ramdin, M.; Balaji, S. P.; Vicent-Luna, J. M.; Gutierrez-Sevillano, J. J.; Calero, S.; de Loos, T. W.; Vlugt, T. J. H. Solubility of the precombustion gases CO<sub>2</sub>, CH<sub>4</sub>, CO, H<sub>2</sub>, N<sub>2</sub>, and H<sub>2</sub>S in the ionic liquid [bmim][Tf<sub>2</sub>N] from Monte Carlo simulations. *J. Phys. Chem. C* **2014**, *118*, 23599–23604.
- (168) Shi, W.; Siefert, N. S.; Morreale, B. D. Molecular simulations of CO<sub>2</sub>, H<sub>2</sub>, H<sub>2</sub>O, and H<sub>2</sub>S gas absorption into Hydrophobic Poly(dimethylsiloxane) (PDMS) solvent: solubility and surface tension. *J. Phys. Chem. C* **2015**, *119*, 19253–19265.

- (169) Torres-Knoop, A.; Balaji, S. P.; Vlugt, T. J. H.; Dubbeldam, D. A comparison of advanced Monte Carlo methods for open systems: CFCMC vs CBMC. *J. Chem. Theory Comput.* **2014**, *10*, 942–952.
- (170) Rosch, T. W.; Maginn, E. J. Reaction ensemble Monte Carlo simulation of complex molecular systems. *J. Chem. Theory Comput.* **2011**, *7*, 269–279.
- (171) Theodorou, D. N. Progress and outlook in Monte Carlo simulations. *Ind. Eng. Chem. Res.* **2010**, *49*, 3047–3058.
- (172) Neubauer, B.; Boutin, A.; Tavitian, B.; Fuchs, A. H. Gibbs ensemble simulations of vapour-liquid phase equilibria of cyclic alkanes. *Mol. Phys.* **1999**, *97*, 769–776.
- (173) De Pablo, J. J.; Prausnitz, J. M. Phase equilibria for fluid mixtures from Monte Carlo simulation. *Fluid Phase Equilib.* **1989**, *53*, 177–189.
- (174) Green, D. G.; Jackson, G.; de Miguel, E.; Rull, L. F. Vapor-liquid and liquid-liquid phase equilibria of mixtures containing square-well molecules by Gibbs ensemble Monte Carlo simulation. *J. Chem. Phys.* **1994**, *101*, 3190–3204.
- (175) Fetisov, E. O.; Siepmann, J. I. Prediction of vapor–liquid coexistence properties and critical points of polychlorinated biphenyls from Monte Carlo simulations with the TraPPE–EH force field. *J. Chem. Eng. Data* **2015**, *60*, 3039–3045.
- (176) Dinpajoooh, M.; Bai, P.; Allan, D. A.; Siepmann, J. I. Accurate and precise determination of critical properties from Gibbs ensemble Monte Carlo simulations. *J. Chem. Phys.* **2015**, *143*, 114113.
- (177) Smit, B.; Frenkel, D. Calculation of the chemical potential in the Gibbs ensemble. *Mol. Phys.* **1989**, *68*, 951–958.
- (178) Price, D. J.; Brooks, C. L. A modified TIP3P water potential for simulation with Ewald summation. *J. Chem. Phys.* **2004**, *121*, 10096–10103.

- (179) Shirts, M. R.; Pande, V. S. Solvation free energies of amino acid side chain analogs for common molecular mechanics water models. *J. Chem. Phys.* **2005**, *122*, 134508.
- (180) Pitera, J. W.; van Gunsteren, W. F. A comparison of non-bonded scaling approaches for free energy calculations. *Mol. Simul.* **2002**, *28*, 45–65.
- (181) Dejaegere, A.; Karplus, M. Analysis of coupling schemes in free energy simulations: A unified description of nonbonded contributions to solvation free energies. *J. Phys. Chem.* **1996**, *100*, 11148–11164.
- (182) Naden, L. N.; Pham, T. T.; Shirts, M. R. Linear basis function approach to efficient alchemical free energy calculations. 1. Removal of uncharged atomic sites. *J. Chem. Theory Comput.* **2014**, *10*, 1128–1149.
- (183) Allen, M. P.; Tildesley, D. J., *Computer simulation of liquids*; Oxford University Press: New York, 1989.
- (184) Wang, F.; Landau, D. P. Efficient, multiple-range random walk algorithm to calculate the density of states. *Phys. Rev. Lett.* **2001**, *86*, 2050–2053.
- (185) Poulain, P.; Calvo, F.; Antoine, R.; Broyer, M.; Dugourd, P. Performances of Wang-Landau algorithms for continuous systems. *Phys. Rev. E* **2006**, *73*, 56704.
- (186) Rull, L. F.; Jackson, G.; Smit, B. The condition of microscopic reversibility in Gibbs ensemble Monte Carlo simulations of phase equilibria. *Mol. Phys.* **1995**, *85*, 435–447.
- (187) Shah, J. K.; Maginn, E. J. A general and efficient Monte Carlo method for sampling intramolecular degrees of freedom of branched and cyclic molecules. *J. Chem. Phys.* **2011**, *135*, 134121.
- (188) Sepehri, A.; Loeffler, T. D.; Chen, B. Improving the efficiency of configurational-bias Monte Carlo: A density-guided method for generating bending angle trials for linear and branched molecules. *J. Chem. Phys.* **2014**, *141*, 074102.

- (189) Wilding, N. B.; Muller, M. Accurate measurements of the chemical potential of polymeric systems by Monte Carlo simulation. *J. Chem. Phys.* **1994**, *101*, 4324–4330.
- (190) Kofke, D. A. Free energy methods in molecular simulation. *Fluid Phase Equilib.* **2005**, *228-229*, 41–48.
- (191) Poursaeidesfahani, A.; Rahbari, A.; Torres-Knoop, A.; Dubbeldam, D.; Vlugt, T. J. H. Computation of thermodynamic properties in the Continuous Fractional Component Monte Carlo Gibbs ensemble. *Mol. Sim.* **2017**, *43*, 189–195.
- (192) De Miguel, E.; Jackson, G. The nature of the calculation of the pressure in molecular simulations of continuous models from volume perturbations. *J. Chem. Phys.* **2006**, *125*, 164109.
- (193) Gray, C. G.; Gubbins, K. E.; Joslin, C. G., *Theory of molecular fluids 2: Applications. international series of monographs on chemistry*; Oxford University Press, New York: 2011.
- (194) Poursaeidesfahani, A.; Torres-Knoop, A.; Dubbeldam, D.; Vlugt, T. J. H. Direct Free Energy Calculation in the Continuous Fractional Component Gibbs Ensemble. *J. Chem. Theory Comput.* **2016**, *12*, 1481–1490.
- (195) Ewald, P. P. Die Berechnung optischer und elektrostatischer Gitterpotentiale. *Ann. phys.* **1921**, *369*, 253–287.
- (196) Lynden-Bell, R.; Atamas, N.; Vasilyuk, A.; Hanke, C. Chemical potentials of water and organic solutes in imidazolium ionic liquids: a simulation study. *Mol. Phys.* **2002**, *100*, 3225–3229.
- (197) Turner, H. C.; Brennan, J. K.; Lisal, M.; Smith, W. R.; Johnson, K. J.; Gubbins, K. E. Simulation of chemical reaction equilibria by the reaction ensemble Monte Carlo method: a review. *Mol. Sim.* **2008**, *34*, 119–146.
- (198) McQuarrie, D. A.; Simon, J. D., *Physical Chemistry: a molecular approach*, 1st ed.; University Science Books: Sausalito, California, 1997.

- (199) Car, R.; Parrinello, M. Unified approach for molecular dynamics and density-functional theory. *Phys. Rev. Lett.* **1985**, *55*, 2471.
- (200) Laasonen, K.; Sprik, M; Parrinello, M; Car, R “Ab initio” liquid water. *J. Comput. Phys.* **1993**, *99*, 9080–9089.
- (201) Iannuzzi, M.; Laio, A.; Parrinello, M. Efficient exploration of reactive potential energy surfaces using Car-Parrinello molecular dynamics. *Phys. Rev. Lett.* **2003**, *90*, 238302.
- (202) Van Duin, A. C.; Dasgupta, S.; Lorant, F.; Goddard, W. A. ReaxFF: a reactive force field for hydrocarbons. *J. Phys. Chem. A* **2001**, *105*, 9396–9409.
- (203) Chenoweth, K.; van Duin, A. C.; Goddard, W. A. ReaxFF reactive force field for molecular dynamics simulations of hydrocarbon oxidation. *J. Phys. Chem. A* **2008**, *112*, 1040–1053.
- (204) Laio, A.; Gervasio, F. L. Metadynamics: a method to simulate rare events and reconstruct the free energy in biophysics, chemistry and material science. *Rep. Prog. Phys.* **2008**, *71*, 126601.
- (205) Bussi, G.; Laio, A.; Parrinello, M. Equilibrium free energies from nonequilibrium metadynamics. *Phys. Rev. Lett.* **2006**, *96*, 090601.
- (206) Barducci, A.; Bonomi, M.; Parrinello, M. Metadynamics. *Wiley Interdiscip. Rev. Comput. Mol. Sci.* **2011**, *1*, 826–843.
- (207) Dellago, C.; Bolhuis, P. G.; Csajka, F. S.; Chandler, D. Transition path sampling and the calculation of rate constants. *J. Comput. Phys.* **1998**, *108*, 1964–1977.
- (208) Bolhuis, P. G.; Dellago, C; Chandler, D Sampling ensembles of deterministic transition pathways. *Faraday Discuss.* **1998**, *110*, 421–436.
- (209) Bolhuis, P. G.; Chandler, D.; Dellago, C.; Geissler, P. L. Transition path sampling: Throwing ropes over rough mountain passes in the dark. *Annu. Rev. Phys. Chem.* **2002**, *53*, 291–318.
- (210) Rogal, J.; Bolhuis, P. G. Multiple state transition path sampling. *J. Comput. Phys.* **2008**, *129*, 12B609.

- (211) Van Erp, T. S.; Bolhuis, P. G. Elaborating transition interface sampling methods. *J. Comput. Phys.* **2005**, *205*, 157–181.
- (212) Moroni, D.; van Erp, T. S.; Bolhuis, P. G. Investigating rare events by transition interface sampling. *Physica A* **2004**, *340*, 395–401.
- (213) Moroni, D.; Bolhuis, P. G.; van Erp, T. S. Rate constants for diffusive processes by partial path sampling. *J. Comput. Phys.* **2004**, *120*, 4055–4065.
- (214) Moroni, D.; van Erp, T. S.; Bolhuis, P. G. Simultaneous computation of free energies and kinetics of rare events. *Phys. Rev. E* **2005**, *71*, 056709.
- (215) Smith, W.; Triska, B. The reaction ensemble method for the computer simulation of chemical and phase equilibria. I. Theory and basic examples. *J. Comput. Phys.* **1994**, *100*, 3019–3027.
- (216) Johnson, J. K.; Panagiotopoulos, A. Z.; Gubbins, K. E. Reactive canonical Monte Carlo: a new simulation technique for reacting or associating fluids. *Mol. Phys.* **1994**, *81*, 717–733.
- (217) Glotzer, S. C.; Stauffer, D.; Jan, N. Monte Carlo simulations of phase separation in chemically reactive binary mixtures. *Phys. Rev. Lett.* **1994**, *72*, 4109.
- (218) Johnson, J. K. Reactive canonical Monte Carlo. *Adv. Chem. Phys.* **1999**, *105*, 461–481.
- (219) Hansen, N.; Jakobtorweihen, S.; Keil, F. J. Reactive Monte Carlo and grand-canonical Monte Carlo simulations of the propene metathesis reaction system. *J. Comput. Phys.* **2005**, *122*, 164705.
- (220) Jakobtorweihen, S; Hansen, N; Keil, F. Combining reactive and configurational-bias Monte Carlo: Confinement influence on the propene metathesis reaction system in various zeolites. *J. Comput. Phys.* **2006**, *125*, 224709.

- (221) Mullen, R. G.; Corcelli, S. A.; Maginn, E. J. Reaction ensemble Monte Carlo simulations of CO<sub>2</sub> absorption in the reactive ionic liquid triethyl(octyl)phosphonium 2-cyanopyrrolide. *J. Phys. Chem. Lett.* **2018**, -, DOI:10.1021/acs.jpclett.8b02304, 5213–5218.
- (222) Combe, N.; Vlugt, T. J. H.; Wolde, P. R. T.; Frenkel, D. Dynamic pruned-enriched Rosenbluth method. *Mol. Phys.* **2003**, *101*, 1675–1682.
- (223) Mullen, R. G.; Maginn, E. J. Reaction Ensemble Monte Carlo Simulation of xylene isomerization in bulk phases and under confinement. *J. Chem. Theory Comput.* **2017**, *13*, 4054–4062.
- (224) Widom, B. Some topics in the theory of fluids. *J. Comput. Phys.* **1963**, *39*, 2808–2812.
- (225) Turner, C. H.; Johnson, J. K.; Gubbins, K. E. Effect of confinement on chemical reaction equilibria: The reactions 2NO ⇌ (NO)<sub>2</sub> and N<sub>2</sub>+ 3H<sub>2</sub> ⇌ 2NH<sub>3</sub> in carbon micropores. *J. Comput. Phys.* **2001**, *114*, 1851–1859.
- (226) Gao, J.; Xia, X.; George, T. F. Importance of bimolecular interactions in developing empirical potential functions for liquid ammonia. *J. Phys. Chem.* **1993**, *97*, 9241–9247.
- (227) Talbot, J; Tildesley, D.; Steele, W. Molecular-dynamics simulation of fluid N<sub>2</sub> adsorbed on a graphite surface. *Faraday Discuss.* **1985**, *80*, 91–105.
- (228) Murthy, C.; Singer, K; Klein, M.; McDonald, I. Pairwise additive effective potentials for nitrogen. *Mol. Phys.* **1980**, *41*, 1387–1399.
- (229) Wolf, D; Kebbinski, P; Phillipot, S.; Eggebrecht, J Exact method for the simulation of coulombic systems by spherically truncated, pairwise  $N^{-1}$  summation. *J. Comput. Phys.* **1999**, *110*, 8254–8282.
- (230) Frisch, M. J. et al. Gaussian 09, Revision C02., Gaussian Inc. Wallingford CT, 2016.

- (231) Kolafa, J.; Nezbeda, I. The Lennard-Jones fluid: an accurate analytic and theoretically-based equation of state. *Fluid Phase Equilib.* **1994**, *100*, 1–34.
- (232) Gillespie, L. J.; Beattie, J. A. The thermodynamic treatment of chemical equilibria in systems composed of real gases. I. An approximate equation for the mass action function applied to the existing data on the Haber equilibrium. *Phys. Rev.* **1930**, *36*, 743.
- (233) Peng, D.-Y.; Robinson, D. B. A new two-constant equation of state. *Ind. Eng. Chem. Fundam.* **1976**, *15*, 59–64.
- (234) Poling, B. E.; Prausnitz, J. M.; O'Connell, J. P., *The properties of gases and liquids*; McGraw-Hill, New York: 2001; Vol. 5.
- (235) Sindzingre, P.; Ciccotti, G.; Massobrio, C.; Frenkel, D. Partial enthalpies and related quantities in mixtures from computer simulation. *Chem. Phys. Lett.* **1987**, *136*, 35–41.
- (236) Sindzingre, P.; Massobrio, C.; Ciccotti, G.; Frenkel, D. Calculation of partial enthalpies of an argon-krypton mixture by NPT molecular dynamics. *Chem. Phys.* **1989**, *129*, 213–224.
- (237) Rahbari, A.; Hens, R.; Nikolaidis, I. K.; Poursaeidesfahani, A.; Ramdin, M.; Economou, I. G.; Moulton, O. A.; Dubbeldam, D.; Vlugt, T. J. H. Computation of partial molar properties using Continuous Fractional Component Monte Carlo. *Mol. Phys.* **2018**, *0*, 1–14.
- (238) Schnell, S. K.; Englebienne, P.; Simon, J.-M.; Krüger, P.; Balaji, S. P.; Kjelstrup, S.; Bedeaux, D.; Bardow, A.; Vlugt, T. J. H. How to apply the Kirkwood–Buff theory to individual species in salt solutions. *Chem. Phys. Lett.* **2013**, *582*, 154–157.
- (239) Chase, M. W.; Curnutt, J.; Prophet, H.; McDonald, R.; Syverud, A. JANAF thermochemical tables, 1975 supplement. *J. Phys. Chem. Ref. Data.* **1975**, *4*, 1–176.

- (240) Lin, C.-T.; Daubert, T. E. Estimation of partial molar volume and fugacity coefficient of components in mixtures from the soave and Peng-Robinson equations of state. *Ind. Eng. Chem. Process. Des. Dev.* **1980**, *19*, 51–59.
- (241) Kwak, T.; Mansoori, G. A. Van der Waals mixing rules for cubic equations of state. Applications for supercritical fluid extraction modelling. *Chem. Eng. Sci.* **1986**, *41*, 1303–1309.
- (242) Yaws, C. L., *Thermophysical properties of chemicals and hydrocarbons*, 2nd ed.; Gulf Professional Publishing: Oxford, UK, 2014.
- (243) Lemmon, E. W.; Huber, M. L.; McLinden, M. O. NIST reference fluid thermodynamic and transport properties—REFPROP. *NIST standard reference database* **2002**, *23*, v7.
- (244) Waibel, C.; Gross, J. Modification of the Wolf method and evaluation for molecular simulation of vapor–liquid equilibria. *J. Chem. Theory Comput.* **2018**, *14*, 2198–2206.
- (245) Hens, R.; Vlugt, T. J. H. Molecular simulation of Vapor–Liquid Equilibria using the Wolf method for electrostatic interactions. *J. Chem. Eng. Data* **2017**, *63*, 1096–1102.

# Summary

Separation and selective production of branched paraffins are among the most important and still challenging processes in the oil and gas industry. Addition of branched hydrocarbons can increase the octane number of a fuel without causing additional environmental concerns. Conversion of linear hydrocarbons into branched ones also improves the performance of lubricants at low temperatures. Zeolites are commonly used for separation of branched hydrocarbons and selective conversion of linear long chain hydrocarbons into shorter branched ones.

In the first part of this thesis, we considered adsorption-based separation process using zeolites. An efficient separation process should have a high capacity and selectivity and low energy consumption. Experimentally measured adsorption isotherms and breakthrough curves are used to assess the capacity and selectivity of adsorption-based separation processes. Adsorption isotherms are the outcome of static adsorption experiments, where the adsorbate and adsorbent are kept in contact for a long time until equilibrium is reached. The equilibrium loadings measured at constant temperature and various pressures are used to construct adsorption isotherms. In dynamic adsorption experiments, a fluid phase containing the adsorbate flows over a fixed bed of adsorbent. Breakthrough curves show the concentration of an adsorbate in the fluid phase at the outlet of the adsorption column as a function of time. The experimental procedure, from preparing a sample to analysing the results, can be very time consuming and expensive. Hence, it is not feasible to experimentally screen a large number of potential zeolites for a separation process. One of the most efficient ways to select an appro-

priate adsorbent and find the optimal operating conditions for an adsorption based separation is the modelling of the transient adsorption process. In chapter 2, we introduced a mathematical model to estimate the adsorption isotherms from the breakthrough curves. In general, breakthrough experiments are faster than equilibrium adsorption experiments. Using our approach, the number of required experiments is reduced significantly. We used Ideal Adsorption Solution Theory (IAST) which allows for obtaining single component adsorption isotherms from the breakthrough experiments performed for a gas mixture. This is a very important advantage since one can compute and predict mixture adsorption isotherms at any composition from pure component adsorption isotherms using IAST.

In addition to the capacity and selectivity, the energy consumption is also a very important parameter in design of a separation process. The energy consumption of a separation process is determined by the heats of adsorption of components present in the system. To improve the cost efficiency and separation capacity of a column, most of the industrial adsorption processes take place at high loading. As the heat of adsorption is a function of loading and composition of the adsorbed phase, reliable techniques are required which are capable of computing this thermodynamic property at high loadings. In chapter 3, we systematically investigated the effectiveness of the available methods for computing the heat and entropy of adsorption of hydrocarbons at high loadings. We showed that none of the conventional methods is appropriate for accurate computation of heat of adsorption near the saturation loading. We introduced the "Energy Slope" method for computing the heat of adsorption at high loading. In this method, the heat of adsorption is computed using the slope of the fitted curve describing the variations of the total internal energy of zeolite as a function of the loading. We showed that this method is capable of computing the heat of adsorption for pure components and different components in a mixture at all loadings.

In chapters 4 and 5, we considered the zeolite-based production of branched hydrocarbons. In this process, catalytic activity, selectivity, and product quality all critically depend on the pore topology of the zeolites. Zeolite shape selectivity can influence the adsorption, formation, and diffusion of certain reactants/products. This can result in vastly different product

---

distributions when different catalysts are used. In chapters 4, we combined our experimental observations and results obtained from molecular simulations to study the shape selective behaviour of zeolites. We considered the zeolite-based hydroconversion of heptane using three different zeolite catalysts with different pore sizes MFI-type (pore size $\approx$  4.7 Å), MEL-type (pore size $\approx$  5.2 Å), and BEA-type (pore size $\approx$  6 Å) zeolites. For all three catalysts, n-C<sub>7</sub> is isomerized to monobranched isomers which are further isomerized into dibranched isomers, and these dibranched molecules are converted into cracking products. More dibranched isomers and less cracking products are produced by BEA-type zeolite compared to MFI-type and MEL-type zeolites. Clear differences are observed in the distribution of dibranched isomers produced by different zeolites. We showed that product shape selectivity can explain the distribution of dibranched molecules while transition state shape selectivity fails to do so. For MFI-type and MEL-type zeolites, the dibranched molecule that has to overcome the lowest diffusion barrier is produced with a higher yield and the distribution of dimethylpentane molecules is determined by their diffusion rate. As BEA-type zeolite imposes no free energy barrier for diffusion of any of the dibranched isomers, the distribution of dibranched isomers is very close to the equilibrium distribution in the gas phase. In chapter 5, we identified the appropriate reaction network for the hydroconversion of heptane by large pore bifunctional zeolite catalysts. This is realized by analysing the product slates from the extensive set of experiments at various conditions and using different large pore zeolites. We showed that as the pore size increases, the equilibrium distribution of dibranched molecules is reached at a lower conversion of heptane. We introduced a reactor model to simulate a hydrocracker and estimated the rates of different reactions by minimizing the differences between the experimental and theoretical yields (obtained from the model) for different components. The excellent agreement between the modeling results and experimental data indicates that an appropriate reaction network and description of kinetics are used.

As mentioned above, industrial separation and selective production of branched hydrocarbons takes place at high loadings. However, most of the available molecular simulation technique are not capable of computing ther-

modynamic properties accurately at high loadings. This is mainly due to the low acceptance probability for the molecular exchanges. In general, the grand-canonical ensemble, Gibbs ensemble (GE), and reaction ensemble can be used for studying these processes. These simulations critically rely on a sufficient number of molecule exchanges to satisfy the conditions of chemical equilibria. In chapters 6 and 7, we introduced advanced simulation techniques with high acceptance probability for the molecule exchanges even for large molecules in dense systems. These algorithms can be used to explicitly simulate reactions for complex mixtures of hydrocarbons in the liquid phase or inside zeolites. We introduced serial GE/CFC and serial Rx/CFC to simulate phase equilibria and reaction equilibria, respectively. Although these ensembles are expanded with fractional molecules, we showed that properties identical to those in conventional ensembles can be computed in these ensembles. Compared to earlier CFCMC methods in the literature, the number of fractional molecules is reduced and the computational cost is significantly reduced. These techniques allow for direct calculation of chemical potential of all components without the use of Widom's test particles. This can be used to verify the conditions of chemical equilibria without any additional computation.

# Samenvatting

De scheiding en selectieve productie van vertakte alkanen is één van de belangrijkste en uitdagendste processen in de olie- en gasindustrie. Het toevoegen van vertakte koolwaterstoffen aan brandstoffen kan het octaangetal verhogen zonder bij te dragen aan nadelige effecten op de omgeving. Ook zorgt de omzetting van lineaire naar vertakte koolwaterstoffen voor een betere werking van smeermiddelen bij lage temperaturen. Zeolieten worden vaak gebruikt voor de scheiding van lineaire en vertakte koolwaterstoffen en de selectieve omzetting van lange lineaire koolwaterstoffen in kortere.

In het eerste deel van dit proefschrift kijken we naar scheidingsprocessen gebaseerd op adsorptie in zeolieten. Een efficiënt scheidingsproces heeft een hoge capaciteit en laag energieverbruik. Experimentele adsorptie isothermen en breakthrough curves worden gebruikt om de capaciteit en selectiviteit van scheidingsprocessen te beoordelen. adsorptie isothermen zijn het resultaat van statische experimenten waar het adsorptiemiddel en adsorbaat met elkaar in contact worden gehouden tot een evenwicht bereikt wordt. De adsorptie bij verschillende drukken wordt gebruikt om de adsorptie isotherm te bepalen. In dynamische experimenten stroomt een vloeistof of gas met het adsorbaat over het adsorptiemiddel. Breakthrough curves beschrijven de concentratie van het adsorbaat aan het eind van de adsorptiekolom als een functie van de tijd. Dit experimentele proces, van het prepareren van de samples tot het analyseren van de resultaten, kan veel tijd kosten en duur zijn. Daarom is het niet mogelijk om experimenteel een groot aantal zeolieten te screenen op hun toepasbaarheid in scheidingsprocessen. Een van de meest efficiënte methoden om een geschikt

adsorptiemiddel en optimale werkcondities te vinden voor een op adsorptie gebaseerd scheidingsproces is het modelleren van het transiënte adsorption process. In hoofdstuk 2 introduceren we een wiskundig model voor het voorspellen van de adsorptie isothermen uit de breakthrough curves. Over het algemeen zijn breakthrough experimenten sneller dan experimenten die zich richten op adsorptie evenwichten. Met onze aanpak is het aantal benodigde experimenten voor voorspelling van adsorptie isothermen een stuk lager. We gebruiken Ideal Adsorption Solution Theory (IAST), die het mogelijk maakt om te adsorptie isothermen van pure componenten te bepalen in breakthrough experimenten met gasmengsels. Dit is een groot voordeel omdat men met IAST en de adsorptie isothermen van pure componenten de adsorptie isothermen van mengsels kan berekenen en voorspellen.

Naast de capaciteit en selectiviteit is ook het energieverbruik een belangrijk aspect om rekening mee te houden in een scheidingsproces. Dit energieverbruik wordt mede bepaald door de adsorptiewarmte van de verschillende componenten. Om het energieverbruik laag en de capaciteit hoog te houden werken veel industriële adsorptieprocessen bij hoge belading. De adsorptiewarmte is afhankelijk van belading en samenstelling van het adsorbaat en dus zijn goede technieken en methoden nodig die deze grootheid kunnen berekenen. In hoofdstuk 3 hebben we systematisch de effectiviteit van verschillende methoden voor het bepalen van de adsorptie-entropie en adsorptiewarmte van koolwaterstoffen bij hoge belading bestudeerd. We laten zien dat nabij verzadiging geen van de conventionele methoden goed in staat zijn om de adsorptiewarmte nauwkeurig te berekenen. We hebben de zogenaamde “Energy Slope” methode om de adsorptiewarmte te berekenen bij hoge belading geïntroduceerd. In deze methode is de warmteabsorptie berekend door gebruik te maken van de helling van een gefitte functie die de totale interne energie van het zeoliet als functie van de belading beschrijft. We laten zien dat we met deze methode de adsorptiewarmte kunnen berekenen van pure componenten en mengsels bij elke belading.

In hoofdstukken 4 en 5 bekijken we de productie van vertakte koolwaterstoffen met het gebruik van zeolieten. De katalytische activiteit, selectiviteit en productkwaliteit van dit proces hangen sterk af van de grootte en vorm van de poriën van het gebruikte zeoliet. De zogenaamde shape selectivity

---

van het zeoliet kan van invloed zijn op de adsorptie, vorming en diffusie van bepaalde reactanten en reactie producten. Dit kan resulteren in grote verschillen in de opbrengst van gevormde producten bij het gebruik van verschillende katalysatoren. In hoofdstuk 4 combineren we experimentele bevindingen en resultaten uit simulaties om de shape selectivity van verschillende zeoliets te bestuderen. We beschouwen de hydroconversie van heptaan door het gebruik van drie verschillende zeoliets met verschillende poriegroottes: MFI-type (poriegrootte  $\approx 4.7 \text{ \AA}$ ), MEL-type (poriegrootte  $\approx 5.2 \text{ \AA}$ ), en BEA-type (poriegrootte  $\approx 6 \text{ \AA}$ ). In deze drie katalysatoren wordt n-C<sub>7</sub> omgezet in enkelvoudig vertakte isomeren die op hun beurt omgezet worden in dubbelvertakte isomeren en tenslotte in kraakproducten. In BEA-type zeoliets worden meer dubbelvertakte isomeren gevormd en minder kraakproducten in vergelijking met de MFI-type en MEL-type zeoliets. De opbrengst van de geproduceerde dubbelvertakte isomeren is duidelijk anders voor verschillende zeoliets. We laten zien dat dit verschil kan worden verklaard door shape selectivity, maar niet door transition state shape selectivity. In MFI-type en MEL-type zeoliets wordt het dubbelvertakte molecuul dat de laagste energiebarrière voor diffusie heeft het meest gevormd en wordt de opbrengst van dimethylpentaan moleculen bepaald door diffusiesnelheid van dimethylpentaan moleculen. Omdat BEA-type zeoliets geen energiebarrière heeft voor de diffusie van dubbelvertakte isomeren is de opbrengst van deze isomeren vrijwel identiek aan de opbrengst voor een (hypothetische) reactie in de gasfase. Door het analyseren van een groot aantal experimenten met verschillende zeoliets bij verschillende condities hebben we het reactienetwerk voor de hydroconversie van heptaan in large pore bifunctional-zeoliets gevonden. Dit wordt beschreven in hoofdstuk 5. We laten zien dat voor grotere poriën de evenwichtsverdeling van de dubbelvertakte moleculen wordt bereikt bij een lagere omzettingsgraad van heptaan. We introduceren een model dat de hydrocracker simuleert. In dit model worden de verschillen in opbrengst tussen experimenten en theorie voor verschillende componenten geminimaliseerd. Hierdoor kunnen de verschillende reactiesnelheden geschat worden. Vergelijkbare resultaten van simulaties en experimenten laten zien dat het gebruikte reactienetwerk en de beschrijving van de kinetiek correct zijn.

Zoals eerder beschreven vinden industriële scheidingsprocessen en selectieve productie plaats bij hoge belading. Echter, de meeste moleculaire simulatie methoden zijn niet geschikt voor het nauwkeurig berekenen van thermodynamische eigenschappen bij een hoge belading. Dit komt vooral door lage acceptatie kans van molecuuluitwisselingen. Over het algemeen worden het grootkanoniek ensemble, Gibbs ensemble (GE) en het reactie ensemble (Rx) gebruikt om dit soort processen te bestuderen. Bij deze simulatietechnieken is het belangrijk dat er veel moleculen worden uitgewisseld om tot een evenwicht te komen. In hoofdstukken 6 en 7 introduceren we geavanceerde simulatiemethoden om de efficiëntie van deze molecuuluitwisselingen te verhogen, zelfs voor grote moleculen bij hoge dichtheden. Deze algoritmen kunnen worden gebruikt om complexe mengsels van koolwaterstoffen te simuleren in de vloeibare fase of in zeolieten. Voor het simuleren van respectievelijk fase-evenwichten en reactie-evenwichten introduceren we de simulatietechnieken serial GE/CFC en serial Rx/CFC. Deze ensembles zijn uitgebreid door toevoeging van fractional moleculen en we laten zien dat eigenschappen van de conventionele ensembles ook in de nieuwe ensembles berekend kunnen worden. In vergelijking met eerdere CFCMC methoden is het aantal fractional moleculen minder en de computational cost een stuk lager. Met deze nieuwe technieken kan ook de chemische potentiaal van alle componenten direct worden berekend zonder gebruik te maken van zogenaamde testdeeltjes. Dit kan dan gebruikt worden om te bepalen of er een chemisch evenwicht bereikt is zonder dat verdere berekeningen nodig zijn.

# Conclusions

To reduce the harmful impacts of consumption of fossil fuels on the environment, there is need for cleaner fuels with high energy efficiency . Current fuels contain a considerable amount of toxic components such as sulfur and aromatics. Increasing the concentration of branched hydrocarbons with certain chain lengths can improve the efficiency and performance of the fuel without adding any toxic component. However, separation and selective production of branched hydrocarbons are still challenging processes in the oil and gas industries. Zeolites have favourable properties for adsorption-based separation and catalytic production of branched hydrocarbons. In the first part of this thesis, we focused on the adsorption-based separation processes using zeolites. Capacity, selectivity, and energy consumption during the desorption process are crucial for designing an efficient adsorption-based separation process. Adsorption isotherms and breakthrough curves are used to assess the capacity and selectivity of a separation process. Heats of adsorption determine the energy consumption of a process. We introduced an approach to estimate adsorption isotherms from breakthrough curves even without detailed knowledge regarding the mass transfer characteristics of the system. In this way, one only needs to measure breakthrough curves experimentally (which requires lower number of experiments compared to experimental measurements of adsorption isotherms) and obtain adsorption isotherms from our mathematical approach. This is applicable for mixture of gases and one can obtain the single component adsorption isotherms from breakthrough experiments performed for a mixture of gases. In contrast to the conventional equilibrium theory, our method is suitable for cases

with significantly eroded breakthrough curves. This is typically the case when their diffusion is slow (e.g. adsorption of branched hydrocarbons by zeolites). We also systematically compared the effectiveness of various simulation methods to compute the heat and entropy of adsorption at different loadings. To improve the cost efficiency of the process and separation capacity of the column, during the adsorption process, the adsorbent is filled up to high loadings. Therefore, heats of adsorption of all components are needed at high loadings. We showed that none of the conventional simulation methods discussed in chapter 3 exhibited a satisfactory performance at high loadings. We introduced the "Energy Slope" method which outperforms the other approaches in the computation of the heat and entropy of adsorption at high loadings. In this method, the heat and entropy of adsorption are estimated from the slope of the line fitted to the variation of the total internal energy of the system as a function of loading.

In chapters 4 and 5 of this thesis, we focused on the selective production of branched hydrocarbons from hydroconversion of longer chain hydrocarbons. Zeolite-based catalytic hydroconversion is the most effective technique for this process. In this process, structural details of the pores of the zeolite can lead to enhanced or reduced adsorption, formation, and diffusion of certain reactants or products. These effects are known as shape selectivity. Understanding the shape selective behaviour of zeolites is crucial for improving the design of current processes and choosing the best zeolite for a certain application. As this process takes place inside zeolites, it is very difficult to perform experiments that can provide molecular information about the shape selectivity of a zeolite. We combined molecular simulation and experiments to obtain information on the adsorption, transport, and reaction of hydrocarbons at the molecular scale. We computed the adsorption isotherms and free energy profiles of different heptane isomers within the pores of BEA-type, MFI-type, and MEL-type zeolites. We showed that product shape selectivity (diffusion of branched hydrocarbons) is the main source of sharp differences between the product distribution of these zeolites. We also showed that dibranched molecules produced from catalytic hydroconversion of heptane using BEA-type zeolite are distributed according to the equilibrium distribution. To investigate the importance of other types

of shape selectivity, we considered three large pore zeolites where product shape selectivity is less expected. We showed that as the pore size increases the equilibrium distribution of dibranched molecules is reached at a lower conversion of heptane. It should be mentioned that in reality alkenes (an not alkanes) are involved in the isomerization and cracking reactions catalyzed by zeolites. However, to simplify the models we did not distinguish between alkenes corresponding alkanes. However, the kinetics and thermodynamics of alkenes might also be important for better understanding of the catalytic hydroconversion of hydrocarbons.

In the last part of this thesis, we presented advanced simulation techniques that can be used to simulate zeolite-based separations and catalytic hydroconversion of hydrocarbons at high loadings. The main difficulty of current simulation methods is the low acceptance probability of the molecule exchanges. Therefore, long simulations are required and it is not easy to confirm weather simulations have reached equilibrium or not. Our techniques have higher acceptance probabilities for molecule exchanges, and chemical potentials of all components are directly computed without any additional computations. This can be used to verify the conditions of chemical equilibrium.



# Acknowledgements

I would like to thank Thijs and David, my promoter and supervisor, for all their help and support during these four years. I am very grateful for working with these two brilliant persons. Thijs gave me the freedom to collaborate with other groups and work on different topics. Our mutual love for science, passion for exploring new subjects, and his appreciation for a good scientific work motivated me through the course of my PhD. It didn't matter if it was day or night, if there was an interesting topic to discuss, Thijs was always available. His attention to details helped me in finalizing this thesis and other publications. David was always involved throughout the course of my PhD. His different point of view and approach for analyzing problems helped me tremendously. Maybe it was because of our little talks about football that I always saw David as a friend who was guiding me with his invaluable feedback. Without our lengthy scientific discussions with Thijs and David, including a great deal of agreements and disagreements, it was not possible to get close to what we have accomplished.

I would like to express my gratitude to Marcello Rigozzo and Erik Zuidema from Shell Technology Centre Amsterdam. This thesis benefited significantly from the experimental support and industrial insight provided by Marcello and Erik. I would also like to thank Shell Global Solutions B.V. for the financial support of this work.

All the collaborations that I had with people from different groups and universities made this journey far more interesting. I had a wonderful chance to collaborate with Prof. Freek Kaptijn. I am really grateful for this opportunity and the experimental and theoretical support that I received from

Freek. I would also like to thank Eduardo for the excellent experimental work, which made us capable of realizing the second chapter of this thesis. I would like to thank Ariana and Jurn from the university of Amsterdam for the fruitful discussions that we had in Delft and Amsterdam. Without the help from Ariana, it was not possible to complete chapter 5 of this thesis. I would like to thank Prof. Sofia Calero and all members of her group for the work we accomplished together on the adsorption of different component in MOFs.

I would like to thank all my colleagues at Process and Energy. Special thanks to Mirhosein for being one of the most helpful and honest people that I have ever seen. Thank you for being flexible and showing me that friendship can be important enough to worth sacrifices. I would like to thank Ahmadreza for all the collaborations and the works we did together. I want to thank you for being patient and appreciating our friendship above the work even when you did not like my way of working. I would like to thank Remco for helping not only for translating the summary of this thesis but also for his amazing work for developing the codes for CFCMC algorithms. I would like to thank Tim for being a very supportive friend. Without your help I don't know how I could manage the first days of my PhD with no knowledge about working with Linux and molecular simulation. I would like to thank Noura for all the nice moments that we had, for being so sweet and bringing the nicest sweets to the office. I would like to thank Sebastian for all the moments we shared in the train from Delft to Amsterdam and meeting we had at Shell. I would like to thank Vilburg for reminding me that work is not everything. I am grateful for having Gustavo in the building, without you we could not win against master students two times in a row.

I also would like to thank my office mates through these four years Lalit, Farnaz, Hirand, and Goerge. Together we went through success, frustration, cold days, and some very hot days in that office. Thank you for all the good experiences. Maryam, we started as office mates, but the extent of our friendship has grown exponentially. I am very thankful for all the collaborations, drinks, exercises, foods, discussions, laughs, and fights over the window.

I would also like to thank my friends. Pooriya, I have already missed our coffee breaks and our discussions from politics to sports to our personal lives. I want to thank you for different sports that we tried together: Ping-Pong, tennis, football, volleyball, boot camp, swimming, hiking, and I don't know how many more. Bijan, Thank you for showing me how to overcome my limitations and how to push the boundaries in life. Bijan and Pooriya, you showed me that real friends can have the most heated discussions and right after that drink and have fun. Amirali, your visit was the highlight of the last year of my PhD. I cannot imagine how we could manage the moving to the new house without your help. My dear Faidra, What a wonderful addition to my life. Fighting for my rights, expressing my happiness and sadness, caring for others, and enjoying a fair competition, these are just some examples of things I learned from you. Thank you for making me a better person. I cannot forget the amazing trip we had to Greece and staying at your parents' apartment. Giani, thank you for showing me that life is not just running from one stage to another. How amazing was the last match of Iran in the world cup that we watched together? Paula, my best Dutch friend, to me you are a symbol of hard work and perseverance, a strong independent Dutch woman.

I would like to dedicate this paragraph to thank my second family in the Netherlands. Saman, saying goodbye to you at the airport was one the most difficult moments of my PhD. At the same time, your strength, your determination, and your courage showed me that it is important to make a choice you believe is right, even though it is the most difficult one. Saman, the missing member of the three musketeers, you completed the best circle of friends that anyone can dream of, and you went missing again. I am very grateful for all the years we spent with each other all the happy and sad moments, travels, struggles, and memories. Shima, I was always amazed by the fact that you were happier for the happiness of others, you would never share your sadness with us with the intention to keep us happy, while you were always there for our sad moments. I would like to thank you for being patient, cheerful, and supportive. I would like to thank Farideh for being my second mother. You were always a role model for me showing me the importance of having discipline, working hard, and enjoying the life itself.

You always managed to be here for us whenever we needed you.

Arash, where should I begin to thank you? I don't think words can describe my appreciation of you being a part of my life. I know you for the better half of my life. I am grateful for having a friend/brother like you, not only during my PhD but since the time we went to the same high school. If it was not because of your encouragements and your consultation, I might have never pursued a PhD. You were the reason I never, not even for a second, felt alone in the Netherlands. I always knew that even if I lose everything, I will still have you, and I will be fine. In the last 15 years, you fought next to me in all battles in life. We shared the sweetness of victories and the bitterness of defeats. Whenever I was down to the ground, I saw your hand reaching out to me. You never lost your trust and faith in me, despite all the mistakes I made. Arash, I would like to thank you for showing me my flaws and helping me resolve them. I have learned, am learning, and will learn numerous life lessons from you. All the nights we studied until the next morning and all the nights we walked in cities around the world and talked- I cannot be more grateful for all these moments and all the support I received from you.

Mohamad, all these years that I have been away from home, you took care of my responsibilities. If it was not because of your sacrifices, I would not be able to study abroad. You are always cheerful no matter what life throws at you. Around you everything is different and life is more joyful. Thank you for being such a wonderful brother.

Maryam, you are the glue that keeps our family together. Thank you for being the kindest sister ever. Thank you for taking care of everyone and especially our mother, during the years that I have been away. You showed me that there is always time for family. You work, you study, you help Hamidreza, and still you find time to help Our mother and Mohamad.

Baba, I cannot imagine how many sacrifices you have made for our family. You have been working hard to provide the best conditions for us to live and study. I am very thankful for your support. Although it was not easy for you to pay for my study costs, you never doubted your decision and supported me with all you had.

At the end, I would like to thank the best mother in the world for teaching me patience and hope. My dearest mother, I would like to thank you for all the sacrifices you made so that we could live happily. I would like to thank you for being always by my side despite the illness and all the troubles. You are the best mother in the world.



# Curriculum Vitea

Ali Poursaeidesfahani was born on 27 March 1989 in Tehran, Iran. In 2012, he received his Bachelor of Science degree in Mechanical Engineering from the University of Tehran, Iran. He then moved to the Netherlands to continue his academic career abroad. At Delft University of Technology (TU Delft), he studied Mechanical Engineering, specializing in Process Technology. He completed his Master of Science in Sustainable Process and Energy Technology (SPET) in 2014. Immediately after his graduation, he joined the Engineering Thermodynamic group of Prof. dr. ir. T. J. H. Vlugt at Delft University of Technology as a PhD candidate, in collaboration with Dr. David Dubbeldam from the University of Amsterdam. During his PhD, he enjoyed plenty of collaborations with universities around the world including The Hong Kong University of Science & Technology (Hong Kong), Universidad Pablo de Olavide (Spain), Texas A&M University at Qatar (Qatar), Institute of Nanoscience and Nanotechnology (Greece), Eindhoven University of Technology (The Netherlands), and the University of Amsterdam (The Netherlands). His research focused on understanding the catalytic hydroconversion of linear hydrocarbons using zeolites as bifunctional catalysts. He combined experimental results, molecular simulations, and process modelling to understand the shape selective behaviour of different zeolites. He also developed new simulation techniques for open ensembles based on fractional molecules.



# List of Publications

Publication included in this thesis:

1. Poursaeidesfahani, A.; de Lange. M. F.; Khodadadian, F.; Dubbel-dam , D.; Rigutto, M.; Nair, A.; Vlugt, T. J. H.; Product shape selectivity of MFI-type, MEL-type, and BEA-type zeolites in the catalytic hydroconversion of heptane: *Journal of Catalysis*, 2017, 353, 54-62
2. Poursaeidesfahani, A.; Torres-Knoop, A.; Rigutto, M.; Nair, A.; Dubbeldam , D.; Vlugt, T. J. H.; Computation of the heat and entropy of adsorption in proximity of inflection points: *Journal of Physical Chemistry C*, 2016, 120, 1727-1738
3. Poursaeidesfahani, A.; Torres-Knoop, A.; Dubbeldam , D.; Vlugt, T. J. H.; Direct free energy calculation in the Continuous Fractional Component Gibbs Ensemble: *Journal of Chemical Theory and Computation*, 2016, 12, 1481-1490
4. Poursaeidesfahani, A.; Rahbari, A.; Torres-Knoop, A.; Dubbeldam, D.; Vlugt, T. J. H.; Computation of thermodynamic properties in the Continuous Fractional Component Monte Carlo Gibbs Ensemble: *Molecular Simulation*, 2016, 43, 189-195
5. Poursaeidesfahani, A.; Hens, R.; Rahbari, A.; Ramdin, M.; Dubbel-dam , D.; Vlugt, T. J. H.; Efficient application of Continuous Frac-

tional Component Monte Carlo in the Reaction Ensemble: *Journal of Chemical Theory and Computation*, 2017, 13, 4452-4466

6. Poursaeidesfahani, A.; Andres-Garcia, E.; de Lange, M.; Torres-Knoop, A.; Rigutto, M.; Nair, N.; Kapteijn, F.; Gascon, J.; Dubbeldam, D.; Vlugt, T. J. H.; Prediction of adsorption isotherms from breakthrough curves: *Microporous and Mesoporous Materials*, 2019, 277, 237-244.
7. Poursaeidesfahani, A.; Rigutto, M.; Nair, N.; Dubbeldam, D.; Vlugt, T. J. H.; Experimental and theoretical study of catalytic hydroconversion of heptane using large pore zeolite catalysts, in preparation.

Publication not included in this thesis:

1. Torres-Knoop, A.; Burtch, N. C.; Poursaeidesfahani, A.; Balaji, S. P.; Kools, R; Smit, F. X.; Walton, K. S.; Vlugt, T. J. H.; Dubbeldam , D.; Optimization of particle transfers in the Gibbs Ensemble for systems with strong and directional interactions using CBMC, CFCMC, and CB/CFCMC: *The Journal of Physical Chemistry C*, 2016, 120, 9148-9159
2. Khodadadian, F.; Poursaeidesfahani, A.; Li, Z.; van Ommen, J. R.; Stankiewicz, A. I.; Lakerveld, R.; Model-Based optimization of a photocatalytic reactor with Light-Emitting Diodes: *Chem. Engi. Tech.*, 2016, 39, 1946-1954
3. Torres-Knoop, A.; Poursaeidesfahani, A.; Dubbeldam, D.; Vlugt, T. J. H.; Behavior of the enthalpy of adsorption in nanoporous materials close to saturation conditions: *Journal of Chemical Theory and Computation*, 2017, 13, 3326-3339
4. Liu, C; Van Santen,R. A.; Poursaeidesfahani, Vlugt, T. J. H.; Hensen, E. J. H.; Hydride transfer versus deprotonation kinetics in the isobutane–propene alkylation reaction: A computational study: *ACS Catalysis*, 2017, 12, 8613-8627

5. Khodadadian, F.; de Boer, M. W.; Poursaeidesfahani, A.; van Ommen, J. R.; Stankiewicz, A. I.; Lakerveld, R.; Model-Based optimization of a photocatalytic reactor with Light-Emitting Diodes: Chemical Engineering Journal, 2018, 333, 456-466
6. Rahbari, A.; Hens, R.; Nikolaidis, I. K.; Poursaeidesfahani, A.; Ramdin, M.; Economou, I. G.; Moulton, O. A.; Dubbeldam , D.; Vlugt, T. J. H.; Computation of partial molar properties using Continuous Fractional Component Monte Carlo: Molecular Physics, 2018, 44, 1-14
7. Rahbari, A.; Poursaeidesfahani, A.; Torres-Knoop, A.; Dubbeldam , D.; Vlugt, T. J. H.; Chemical potentials of water, methanol, carbon dioxide and hydrogen sulphide at low temperatures using Continuous Fractional Component Gibbs Ensemble Monte Carlo: Molecular Simulation, 2018, 44, 405-414
8. Luna-Triguero, A.; Vicent-Luna, J. M.; Poursaeidesfahani, A.; Vlugt, T. J. H.; Sanchez-de-Armas, R.; Calero, S.; Improving olefin purification using Metal Organic Frameworks with open metal sites: ACS Applied Materials and Interfaces, 2018, 10, 16911-16917